UNIVERSITÀ DI PARMA

UNIVERSITÀ DEGLI STUDI DI PARMA

Dottorato di Ricerca in

Ingegneria Civile e Architettura

CICLO XXXI

Innovative monitoring instrumentations and methods for landslide risk management and mitigation

Coordinatore:
Chiar.mo Prof. Andrea Carpinteri

Tutore:
Chiar.mo Prof. Andrea Segalini

Dottorando:
Ing. Andrea Carri

Anni: 2015/2018

"Knowing, then, begins with the shattering of illusions, with disillusionment" … "Knowing means to penetrate through the surface, in order to arrive at the roots, and hence the causes; knowing means to "see" reality in its nakedness. Knowing does not mean to be in possession of the truth; it means to penetrate the surface and to strive critically and actively in order to approach truth even more closely"

Fromm E. – To Have or to Be

Table of Contents

List of Figures

List of Tables

List of Equations

List of Acronyms

The following list reports the main acronyms used during this thesis, which appear repeatedly or are not defined in the text. The index is not complete, due to the high number of variables present, in particular in Chapter 3. In this case, they are defined in their own section, just above the first appearance.

3G	3^{rd} Generation
4G	4^{th} Generation
ADC	Analog to Digital Converter
Ah	Ampere-hour
AIS	Automated Inclinometer System
a.s.l.	Above sea level
atm	Atmosphere
a_x	Acceleration recorded along x-axis
a_y	Acceleration recorded along y-axis
a_z	Acceleration recorded along z-axis
bit	Binary digit
c	Cohesion
C_{Ks}	Viscosity of the dashpot for Kelvin model
C_{Ms}	Viscosity of the dashpot for Maxwell model
CA	Canada
cm	centimetre
C0	Activation Criterion 0
C1	Activation Criterion 1
C2	Activation Criterion 2
C3	Activation Criterion 3
CP	Calculation Point
CPA	Corleto Perticara formation
Cv	Primary consolidation coefficient
d	Day
D.L.	Decreto Legge
D. Lgs.	Decreto Legislativo
DB	Database
dd/mm/yyyy	Day – Month - Year
DEM	Digital Elevation Model
DMS	Differential Monitoring of Stability
DPGV	Deformazioni Gravitative Profonde di Versante
d_w	Dimension of dataset window
E	Oedometric modulus
e.g.	Exempli gratia
Eq.	Equation
e_p	Electrical power
EWS	Early Warning System
f	Function
FDM	Finite Difference Method
Fig.	Figure
FLAC®	Fast Lagrangian Analysis of Continua
FP	False Positives

FQA	Factored Quaternion Algorithm
FS	Full Scale
FV	Fukuzono-Voight
FYN	Numidian Flysch
FYR	Red Flysch
G	Gauss
g (associated to acceleration)	Gravity acceleration
g (associated to weight)	Grams
g.l.	Ground level
GB-inSAR	Ground Based interferometric Synthetic Aperture Radar
GeS	Gestione Sportiva
GPRS	General Packet Radio Service
GPS	Global Positioning System
GRG	Generalized Reduced Gradient
GSM	Global System for Mobile communications
h	hours
HH:MM	Hours and Minutes
Hz	Hertz
i.e.	id est
Inc.	Incorporation
IoT	Internet of Things
IPI	In Place Inclinometer
IRT	Infrared Thermography
ISPRA	Istituto Superiore per la Protezione e la Ricerca Ambientale
IT	Italy
IVM	Inverse Velocity Method
K_{Ks}	Stiffness of the linear spring for Kelvin model
K_{Ms}	Stiffness of the linear spring for Maxwell model
kN	kiloNewton
kPa	kiloPascal
LAN	Local Area Network
Ltd	Limited
m	meter
mA	milliAmpere
MAD	Median Absolute Deviation
max	Maximum
mbar	millibar
MEMS	Micro Electro Mechanical System
mg	milli gravity acceleration
min	Minimum
mm	millimeter
MPa	MegaPascal
ms	millisecond
MUMS	Modular Underground Monitoring System
mV	milliVolt
m_x	Magnetic field recorded along x-axis
m_y	Magnetic field recorded along y-axis
m_z	Magnetic field recorded along z-axis

N.A.	Not Available
NE	North-East
NED	North-East-Down
NOAA	National Oceanic and Atmospheric Administration
NTC	Negative Temperature Coefficient
PAI	Piano per l’Assetto Idrogeologico
PC	Personal Computer
PI (associated to T_f)	Predictability Index
PI (measure unit)	Poiseuille
PLC	Programmable Logic Controller
PS	Persistent Scatter
PS-inSAR	Persistent Scatter interferometric Synthetic Aperture Radar
psi	Pound per Square Inch
PVC	Polyvinyl chloride
QR code	Quick Response code
R^2	Coefficient of Determination
RBD	Reliability Based Design
RMSE	Root Mean Square Error
RS232	Recommended Standard 232
RS485	Recommended Standard 485
s	second
S.r.l.	Società a Responsabilità Limitata
SAA	Shape Accel Array
SD card	Secure Digital card
SMS	Short Message Service
SoR	Segment of Relevance
SQL	Structured Query Language
SW	Software
t	Time
T_f	Time of Failure
t_r	Time period related to the providing of results
t_{sp}	Frequency of data transmission
t_{sp}	Sampling period
Tab.	Table
TBM	Tunnel Boring Machine
TDR	Time Domain Reflectometry
TL3DV	Tilt Link HR 3D V
TLV	Tilt Link V
UMTS	Universal Mobile Telecommunications System
USA	United States of America
V	Volt
v_n	Normalized velocity
vs	Versus
$v_{s_{30}}$	Velocity averaged over the top 30 m of soil
VW	Vibrating Wire
W	Watt
ψ	Heading angle
θ	Pitch angle

ϕ	Roll angle
ø	Friction angle
σ	Standard Deviation
μ	Mean
μg	micro gravity acceleration
°C	Celsius degrees

Introduction

> "***Every geotechnical design is to some extent hypothetical, and every construction job involving earth or rock runs the risk of encountering surprises. These circumstances are the inevitable result of working with materials created by nature" … "The inability of exploratory procedures to detect in advance all the possibly significant properties and conditions of natural materials requires the designer to make assumptions that may be at variance with reality.***"
>
> **Peck R. B. – Geotechnical instrumentation for monitoring field performance**

During last century, the large spread of human activities, urban areas and infrastructures, together with the abandonment of rural or mountains zones, faces an increment of landslide events and potentially dangerous scenarios. Due to their geographical and economical characteristics, some Countries were particularly involved in natural disasters and words like "Risk Management" and "Monitoring" have become very common, even if often not applied. In particular, as described in Chapter 1, Italy is particularly susceptible to this theme, with a worrying increment of catastrophic events, which caused several deaths and economical loss.

The scientific community has concentrated many efforts in the definition and calibration of predictive numerical models and forecasting risk analysis, associating these tools with Civil Protection guidelines and emergency procedures. Nevertheless, while numerous data are available in the hydraulic field, geotechnics is characterized by several uncertainties and a general lack of information. In fact the general evolution of technologies that regarded industry and everyday life do not cover geotechnical instrumentations, which often require an operator, have a very low sampling period and are inadequate for risk management purposes. Chapter 2 summarizes the traditional instrumentations available on the market, together with the innovative tools that have been developed in recent years. These tools permits the integration of numerous sensors and the detection of cause-effect relationships, greatly improving the monitoring process, even if characterized by considerable costs and a series of characteristics that do not cover the complete spectrum of monitoring needs. Therefore, there are some critical aspects related to their manufacturing that may influence the final result and applicability.

The increasing number of infrastructures has required to realize underground excavations or cross landslide areas. In this field, each design is hypothetical, due to the use of natural materials, underruns the risk of facing surprises and a "learn as you go" approach is often indispensable, with field observations and quantitative measurements.

This thesis concentrates on the study of a new automatic and innovative technology, developed starting from the knowledge regarding landslide and infrastructure achieved during last decades at University of Parma. Chapter 3 reports the general characteristics of the new tool, together with the evolution of installation method, definition of calibration procedures and hardware development. Software and Calculation principles are widely discussed, due to their innovation characteristics and introduction of Internet of Things (IoT) principles. A particular innovative aspect regards the application of theory related to airplanes navigation at geotechnical field, together with the definition of statistical algorithms. The latter, in particular, are able to automatically detect instrumental and spike noise, sensors malfunctions and data trend, in a self-learning philosophy, where the software, after a training period, knows how to elaborate the raw data. The aim of the new tool was to increment the knowledge about evolution of slopes, both for natural conditions and artificial changes. Another key aspect was the real time control of geotechnical structures and underground excavations, during both construction and exercise phases.

Chapter 4 concentrates on time of failure prediction methods, starting from those available in literature for rock or soil slopes and open pit mines. In particular, Fukuzono (Inverse Velocity) method has showed its efficacy in numerous case histories, despite its site-specific applicability. In order to overcome this restriction, a new generalized criterion is proposed starting from data of past events. The method is able to evaluate landslide Time of Failure for a wide range of landslide behaviors and characteristics. The result has permitted the creation of an abacus that forecast the landslide behavior approaching to failure. The second part of the chapter concentrates on the real time applicability, with the implementation of the method inside a self-learning algorithm. This solution requires to automatically detect the point of activation. For this purpose, an activation criteria is proposed.

Finally, Chapter 5 reports a series of case histories where the new tool has been tested and applied to geotechnical structures and landslides, showing the comparison with traditional instrumentations and numerical models. It has been possible to study the ability of prediction of the Time of Failure method described in Chapter 4, when used in conjunction with an Early Warning Monitoring System.

Chapter 1

RISK MANAGEMENT

1.1. Introduction

During recent years, risk term is increasingly mentioned, while there are no generally accepted definitions for the risk assessment (Fell 1994). In particular, risk assessment, related to the geotechnical field, generally indicates the magnitude and probability of occurrence of a landslide, which is the source of potential risk. The term Hazard is not related to the elements at risk, except for the cases where the construction of elements increases the probability of a landslide occurrence (Fell 1994). Fell (1994) defines the Risk Management starting from the Magnitude (M), which is the "*volume of the source landslide*". Probability (P) indicates the "*probability that a particular landslide occurs within a given period of time*", while Hazard (H) is a "*description of the magnitude and probability of occurrence of the landslide*" (Eq. [1.1]).

$$H = M * P \qquad [\ 1.1\ ]$$

Vulnerability (V) is the "*degree of loss to a given element or set of elements within the area affected by the landslide*" that varies on a scale between 0 (no damage) and 1 (total loss). Considering loss of life, vulnerability could be defined as "*the probability that a particular life (the element at risk) will be lost given that the landslide occurs*". Elements at risk (E) are "*the population, properties, and economic activities [...] in the area potentially affected by the landslide*". The total risk (R) is the "*expected number of lives lost or injured, damage to property, or loss of economic activity or environment*", as in Eq. [1.2].

$$R = E * P * V \qquad [\ 1.2\ ]$$

Risk management process plays a key role in the modern world, where the rapid increase of population and factories faces issues related to the availability of territory and the susceptibility to landslide phenomena, as well as other natural disasters, like floods, volcanic eruptions, earthquakes, etc.

1.2. Italian situation

After the Second World War, Italy has been characterized by the rapid development of urban areas, which now cover the 7.65% of the whole territory, starting from the 2.7% of the fifties (ISPRA, 2018). Population moved from the rural mountain areas, which now are often not manned, increasing their susceptibility to instability phenomena. In the European Union context, 2/3 of the identified landslides (ISPRA 2018) are in Italy, which has hilly areas on the 75% of the whole territory.

A first report made by ISPRA (Istituto Superiore per la Protezione e la Ricerca Ambientale) during 2007 identified 469,298 landslides that cover an area of about 20,000 km^2, which represents the 6.6% of the Italian territory (Tab. 1.1).

In particular, the term "*Landslide index*" (Fig. 1.2) is defined as the percentage of the landslide area over the whole area, while the "*Landslide index over mountain areas*" represents the percentage of the landslide area over the mountain areas for each region or autonomous province. Mountain areas (Fig. 1.1b) are defined as zones where the tilt is over 3° (Fig. 1.1a), considering 20x20 m DEM, or territories over 300 m of height. The more indicative parameters to be considered are the landslide area and the landslide index over mountain areas. The last one in particular highlights the presence of the landslides over the territory prone to landslides and could be considered as an indicator of susceptibility to this kind of phenomena.

Regions with a higher landslide index over mountain areas are Lombardia, Emilia Romagna, Marche, Valle d'Aosta and Piemonte (Fig. 1.4a), while ISPRA (2007) reports that data about Basilicata, Calabria and Sicilia are incomplete. The landslide index evaluated considering Italian provinces (Fig. 1.4b) highlights how every province (with the exclusion of only 7) has at least one gravitational phenomenon.

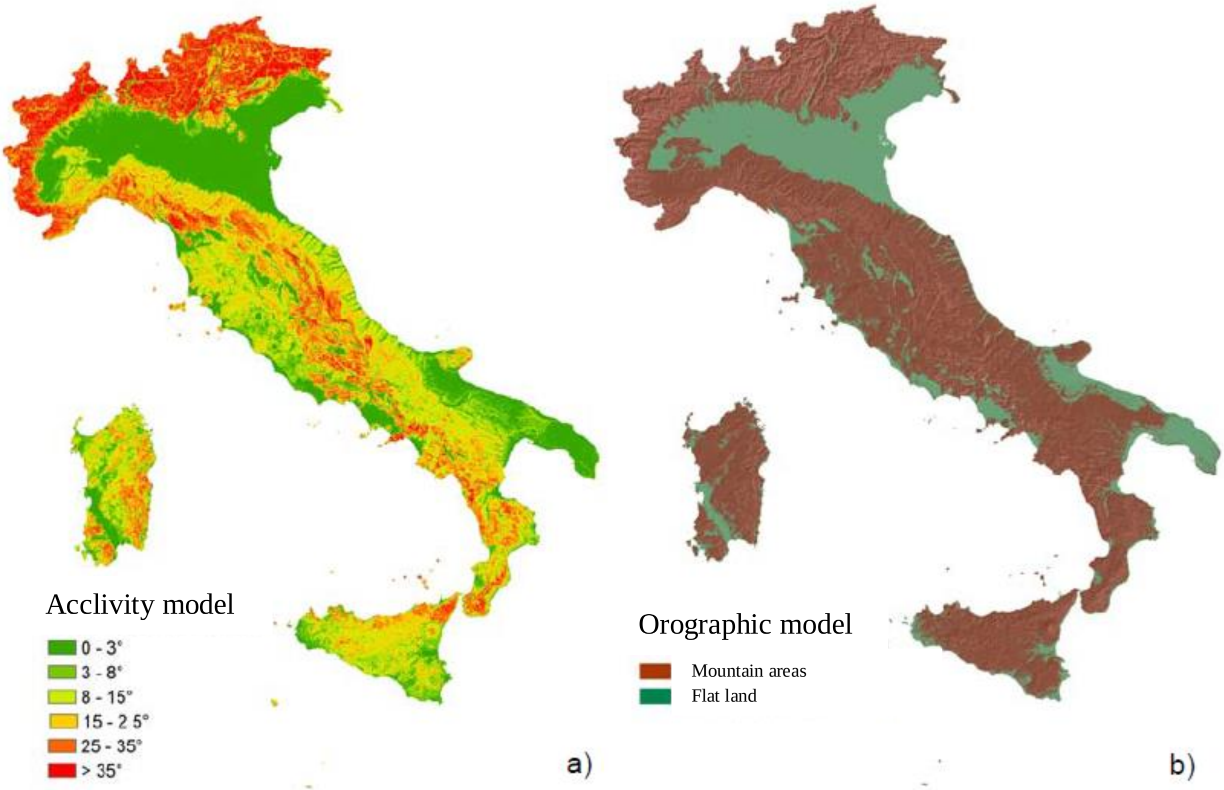

Fig. 1.1: a) Acclivity model and b) mountain areas in Italy (ISPRA 2007)

Tab. 1.1: Report about landslide in Italian regions (ISPRA 2007)

Region / autonomous province	Number of landslides [-]	Density of landslides [num/100 km^2]	Landslide area [km^2]	Landslide index [%]	Landslide index over mountain areas [%]
Piemonte	35,023	126	2,540	9.1	15.0
Valle d’Aosta	4,359	134	520	16.0	16.0
Lombardia	130,538	547	3,308	13.9	29.9
Bolzano	1,995	27	463	6.2	6.3
Trento	9,385	151	879	14.2	14.7
Veneto	9,476	52	223	1.2	3.1
Friuli Venezia Giulia	5,253	67	511	6.5	14.8
Liguria	7,515	139	425	7.9	8.1
Emilia Romagna	70,037	317	2,511	11.4	23.2
Toscana	29,208	127	1,035	4.5	5.6
Umbria	34,545	408	651	7.7	8.7
Marche	42,522	442	1,882	19.4	21.2
Lazio	10,548	61	398	2.0	3.0
Abruzzo	8,493	78	1,241	11.4	12.5
Molise	22,527	508	494	11.1	12.5
Campania	23,430	171	973	7.1	8.8
Puglia	843	4	85	0.4	1.0
Basilicata	9,004	90	298	3.0	3.6
Calabria	9,417	62	822	5.5	6.0
Sicilia	3,657	14	500	1.9	2.2
Sardegna	1,523	6	188	0.8	1.0
ITALY	**469,298**	**155**	**19,946**	**6.6**	**8.9**

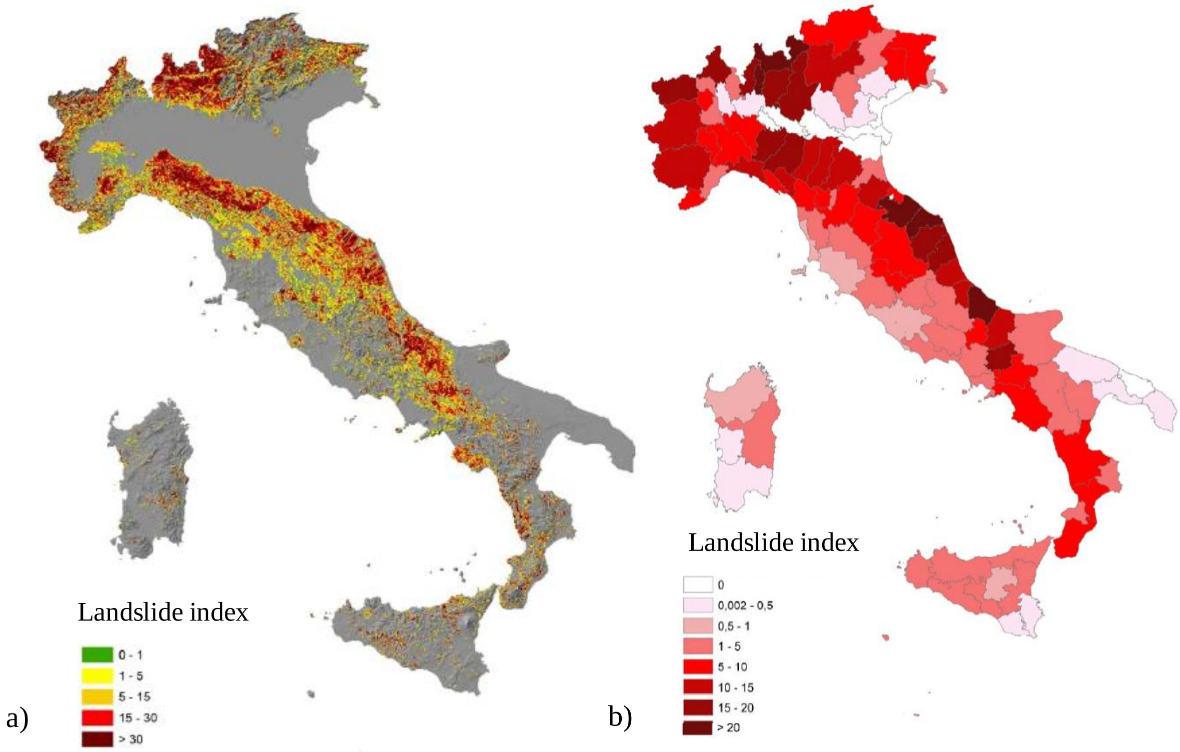

Fig. 1.2: a) Landslide index for the Italian territory and b) landslide index evaluated considering Italian provinces (ISPRA 2007)

In the Italian territory, the attention level is subdivided into four classes and defined considering the single common, as below:

- Very high: landslides intersect urban and/or industrial areas;
- High: landslides interact with highways, railways, roads, excavation areas, landfills or constructions sites;
- Medium: landslides insist on agricultural territories, woods, urban green areas or areas dedicated to sport and fun;
- Low: this category is defined for the common not interested by landslide phenomena.

The result of the study (Fig. 1.5) identifies that 5,596 commons, which represents the 69% of the Italian commons, are interested by landslide phenomena. 2,839 (51%) has a very high attention level, 1,691 (30%) a high attention level, 1,066 are in the medium class, while 2,505 are not interested by gravitational movements (ISPRA 2007).

A new updated report made by ISRPA during 2018 underlines the importance of risk management process. 620,808 landslides have been identified, covering an area that equals the 7.9% of the whole Italian territory. The data available are updated to 2017 for Umbria region, 2016 for Emilia Romagna, Friuli Venezia Giulia, Liguria, Piemonte, Sicilia, Valle d'Aosta regions and the autonomous province of Bolzano, 2015 for Toscana, 2014 for Basilicata and Lombardia, while data of 2007 have been considered for the other regions and the autonomous province of Trento. In particular, 1,281,970 people (2.2%) are subjected to landslide risk, while 6,183,364 (10.4%) are exposed to floods (ISPRA 2018). These numbers highly increase if we consider the factory and service fields (respectively 82,948 – 1.7% and 596,254 – 12.4%), the cultural heritage (11,712-5.8% and 31,137-15.3%) and buildings in general (550,723-3.8% and 1,351,578-9.3%). 538,034 (2.2%) Italian families are susceptible to landslide risk, while 2,648,499 (10.8%) are exposed to floods. The 91.1% of Italian commons are interested by floods or landslides, while 50,117 of 302,066 km^2 of the Italian territory, which represents the 16.6%, is mapped in the high risk classes. Therefore, the number of significant events (ISPRA 2018) has rapidly increased during the last few years, showing a worrying trend (Fig. 1.6). The definition of "significant events" regards landslides that caused dead, wounded, evacuated and damaged buildings, cultural assets, primary communication lines or infrastructures and service networks.

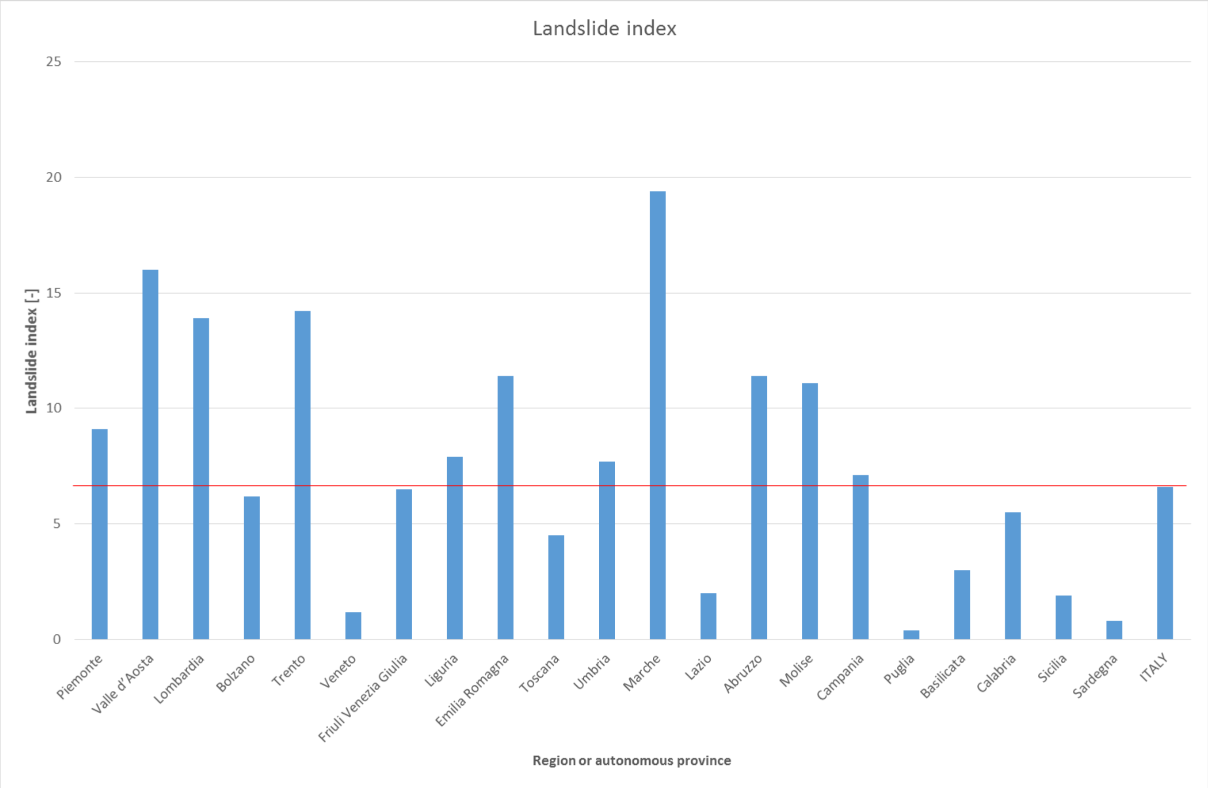

Fig. 1.3: Landslide index (source of the data: ISPRA 2007)

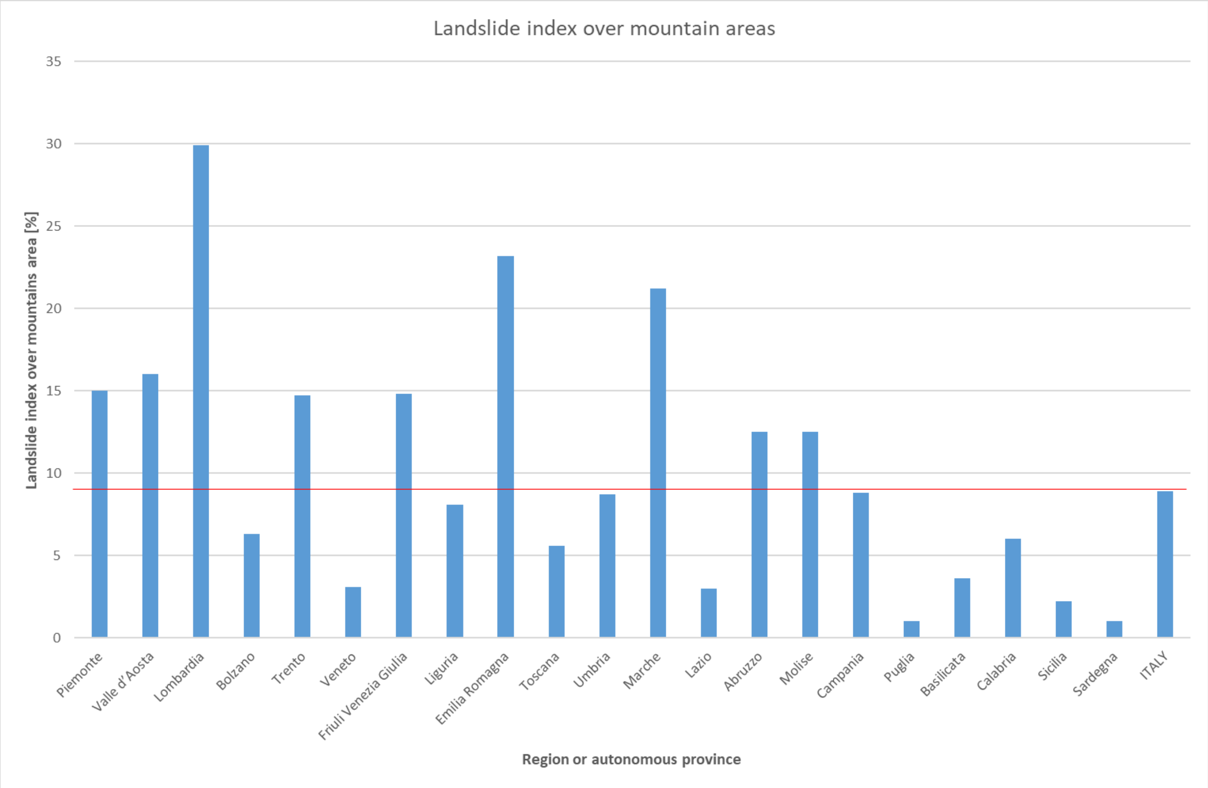

Fig. 1.4: Landslide index over mountain areas (source of the data: ISPRA 2007)

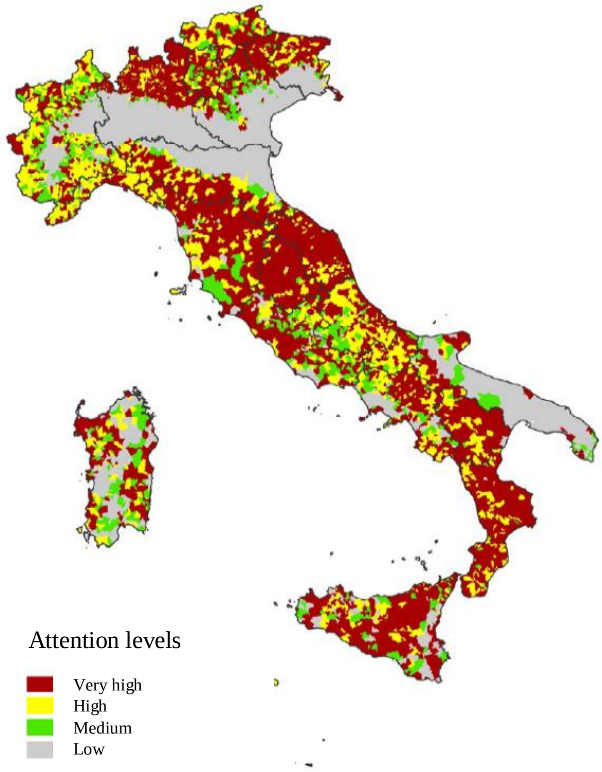

Fig. 1.5: Attention levels defined for each Italian common (ISPRA 2007)

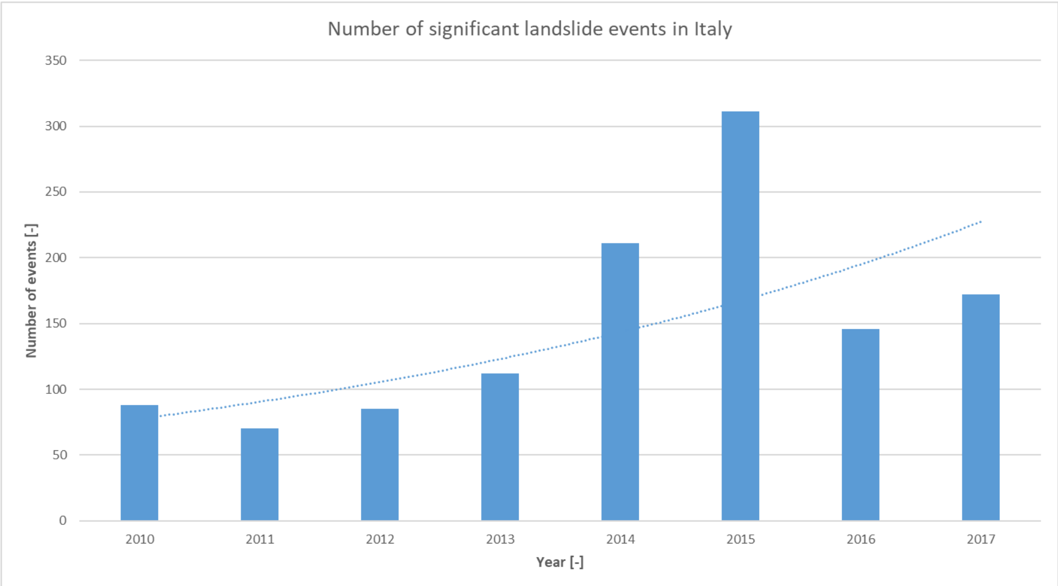

Fig. 1.6: Number of significant landslide events in Italy during recent years (data source: ISPRA 2018)

"Regio Decreto n. 3267" of 30 December 1923 could be considered as the first Italian law about landslide hazard, while the first law which considers natural phenomena during the urban planning is "Legge n. 183" of 18 May 1989. Nevertheless, this was not entirely applied until the facts of Sarno (5 of May 1998), which could be considered the turning point of the Italian Risk Management process. "D.L. n. 180" of 11 June 1998, then converted by "Legge 267/1998", accelerates the identification of risk areas for landslides and floods and the adoption of "Piano stralcio di bacino per l'Assetto Idrogeologico" (PAI), with the corresponding constraints and regulations for land use. In particular, PAI defines the ancient and the quiescent landslides, together with the areas that could be interested by the evolution of a landslide phenomenon, and the zones that are potentially susceptible to new dangerous events (Fig. 1.7a). Finally, "D. Lgs. 152/2006" represents the landmark of Italian legislation about environmental field.

The ISPRA report of 2018, based on PAI classification, shows that the 19.9% of the Italian territory is included inside landslide hazard areas, where the resident population amount is of 5,689,463 people (1,281,970 people live in very high or high landslide hazard areas, Fig. 1.8a). Fig. 1.7b analyses the landslide hazard defined by PAI together with the hydraulic hazard defined by "D. Lgs. 49/2010". Therefore, phenomenon like rock mass instabilities could also damage road and railways tunnels, as well as underground aqueduct pipes, causing water losses and sometimes shortages of water supply in several Italian major cities (Segalini et al, 2018b). This aspect is of fundamental importance and partly related to the increase of global temperature.

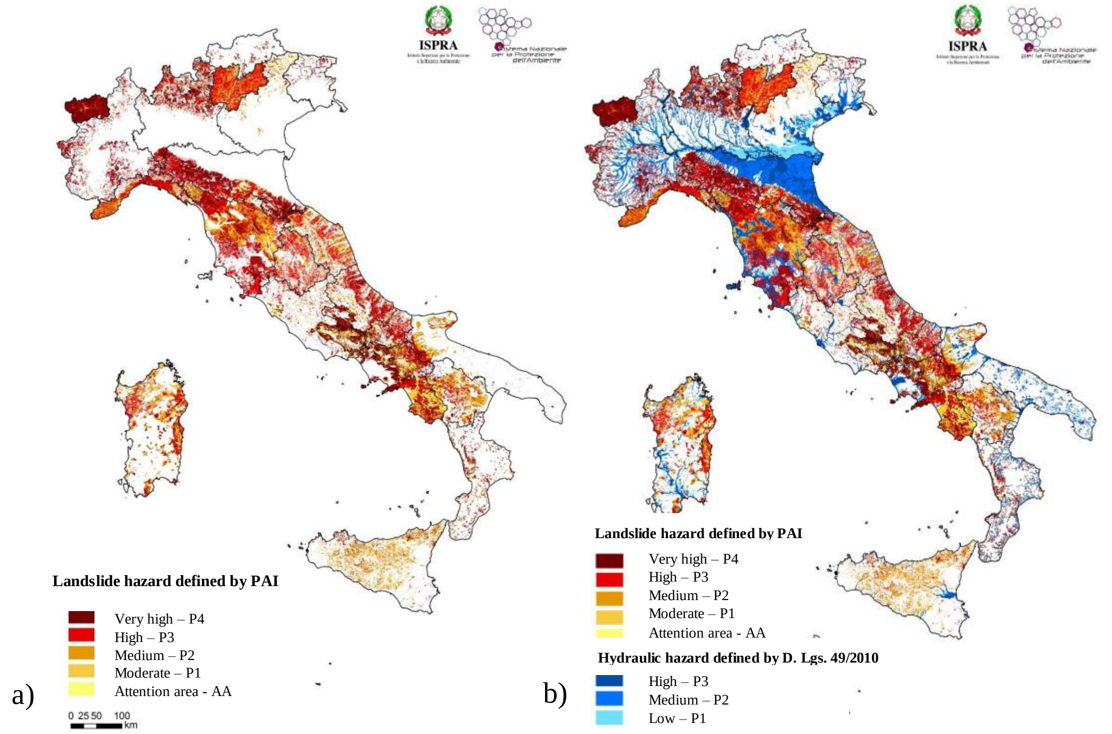

Fig. 1.7: a) Landslide hazard area defined by PAI and b) hydraulic hazard defined by D. Lgs. 49/2010 (source: ISPRA 2018)

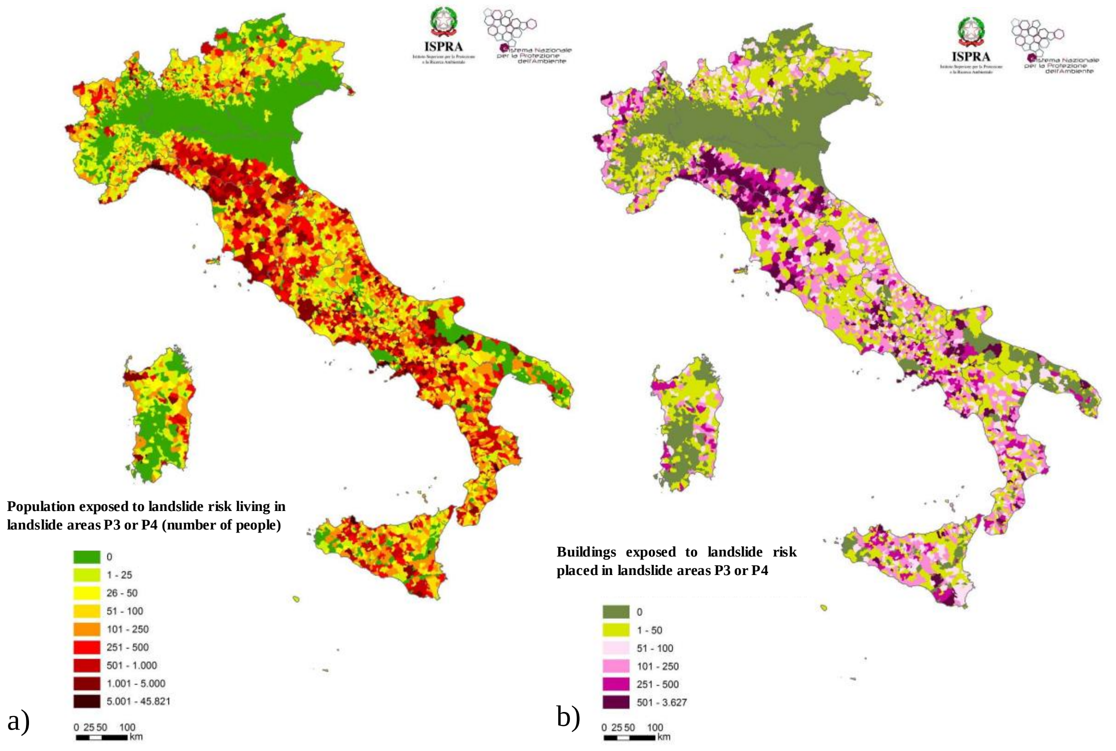

Fig. 1.8: a) Population and b) buildings exposed to landslide risk placed in landslide hazard areas P4 or P3 (source: ISPRA 2018)

The ISPRA report compares also the data about the population exposed to landslide or flood risk between 2015 and 2018, registering an increment equal to 4.7% in the first case (P3 and P4 areas) and of the 4.4% (P2 area) in the second. The result is influenced by the update or integration of mappings made by "Autorità di Bacino Distrettuali".

The situation of Italian infrastructures is another key point of the risk management process. In particular, the majority of the structural works were executed in the sixties or in the seventies, when techniques, materials and traffic were very different. The collapse of the Morandi Bridge (Fig. 1.9) in Genova, that caused 43 victims, is only one dramatic example of bridges (and infrastructures in general) situation.

Fig. 1.9: Collapse of the Morandi Bridge in Genova (14th August 2018)

1.3. Risk management

The results of this analysis highlight the need of adequate solutions at different levels, in order to increase the available information and knowledge about dangerous phenomena and cohabit with them. The responsibles of alert procedures should have clear and reliable results, evaluated and validated through statistical algorithms. Therefore, there is an increasing need for automated real time or near-real time solutions, together with the use of Early Warning Systems (EWSs), able to activate pre-alarm procedures and advise the authority in charge. Finally, the forecasting methods developed during recent years, based on numerical models or monitoring outcomes (like Fukuzono one as further discussed), require an adequate sampling period, not always assured by traditional monitoring instrumentations.

All the automated solutions discussed should not substitute the experts and/or the authorities in charge but help them to select the best practices and actions in a relatively short time, in order to give an adequate answer to warning signals.

This thesis investigates the monitoring process of landslides and geotechnical structures, concentrating on potentiality and weakness of available monitoring tools (Chapter 2). Then, study and applications of a new innovative monitoring system are presented (Chapter 3). The instrument was born with the goal to provide a solution to the mentioned issues and help the risk management process, together with a new landslide Time of Failure method, proposed in Chapter 4.

Chapter 2

STATE OF THE ART ABOUT MONITORING SYSTEMS

> ***"… field instrumentation is vital to the practice of geotechnics, in contrast to the practice of most other branches of engineering in which people have greater control over the materials with which they deal."***
>
> **Peck R. B. – Geotechnical instrumentation for monitoring field performance**

2.1. Introduction

The monitoring process is of fundamental importance in the practice of geotechnical (Dunnicliff 1988), natural hazard, risk mitigation, landslide surveys and construction works. The observational method introduced by Peck (1969) focuses its attention on a "learn as you go" philosophy, where monitoring and site investigations fill the gaps in the available information. A series of new geotechnical instrumentations have been introduced starting from the second half of 20th century, while the last 30 years have shown a constant appearance of new electrical instruments, together with the development of innovative technologies. In particular, the researches have focused their attention on automation and data processing, in order to activate the required emergency procedures with increasing confidence and reliability. The main source of information reported in this chapter is Segalini et al. 2017.

All the monitoring instrumentations are designed to measure directly or indirectly the physical entities of interest. Each measure is characterized by errors and uncertainties, which have to be defined and should not influence the parameters of interest. As an example, an inclinometer should have a casing and a mortar with the same deformability of the soil surrounding them. One of the most important features is the accuracy, defined as the difference between measured and "true" value. Accuracy could be interpreted as a description of systematic errors and it could be evaluated during the calibration procedure, by comparing the instrumental outcomes with the values recorded by an instrument of known accuracy. The result is expressed as a percentage of the full scale (%FS). The precision represents the repeatability of a measure and it is a description of random errors and statistical variability (Taylor 1999). An example of accuracy and precision is reported in Fig. 2.1.

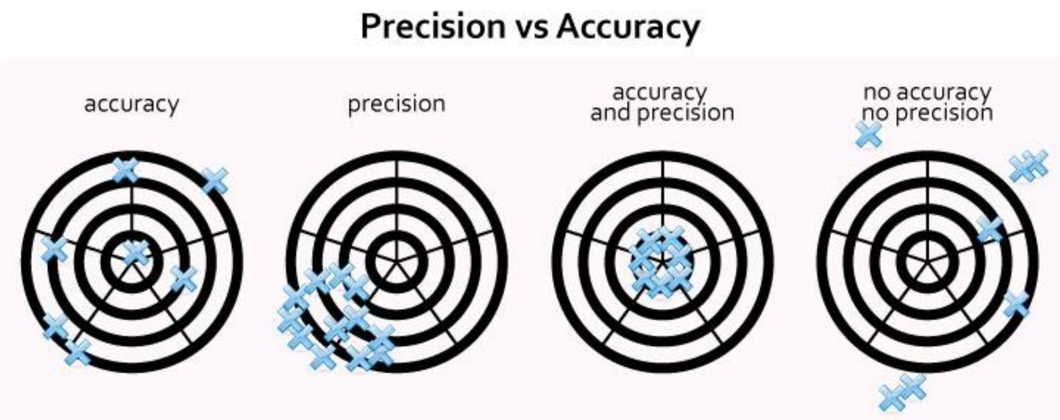

Fig. 2.1: Precision and accuracy

Resolution indicates the minimal scale division of the instrument. In the case of a digital instrumentation, the resolution is represented by the unit variation of the last number in the display or with the division between the full scale and the number of bit. For example, an accelerometer with a full scale of ± 2 g and a memory of 16 bit has a resolution represented by Eq. [2.1], where 1 bit stores the information about the sign.

$$\frac{2\,g}{2^{15}} = 6.1 * 10^{-5} g \qquad [\ 2.1\ ]$$

Sensitivity is the minimum value that the sensor could observe, i.e. the magnitude of input signal required to produce a specified output. It is important to specify that a high sensitivity does not imply a high accuracy or precision.

2.2. Plan of geotechnical monitoring

The importance of the monitoring data is strictly related to a correct plan, considering the typology of the data required, the sensor placement and the objectives. The mere installation of instruments, even of highest quality and reliability, can not guarantee a proper design and avoidance of problems. Unappropriated instruments located in unfavourable positions may provide confusing results or misleading indications. The cost is another very important task, which requires an accurate design of sensors layout. The installation of a huge number of instruments requires an adequate management platform and can cause confusion in the interpretation of results. On the other hand, the placement of only a few sensors, in order to save money, could generate a lack of relevant data and make the monitoring totally useless. As mentioned by Segalini et al. (2017), "*the role of monitoring instrumentation*" is to answer "*a specific question during the progression of construction or, in case of natural phenomena, indicate and follow the response of the geotechnical system, to the variation of external conditions*".

2.3. Monitoring of natural phenomena

The monitoring of natural phenomena investigates the stress-strain behaviour of materials involved whenever subjected to boundary conditions (pore pressure, rainfall, water level, temperature, etc.) and their variations along time. In the case of landslides, the choice of the most appropriate monitoring system should start from information about lithological and stratigraphic characteristics together with the instability phenomenon expected. Dealing with surface movements, it is necessary to define the displacement rate: some technics of remote sensing have issues finding the permanent scatters if the velocity is too high in relationship with the sampling period. The expected displacement velocity is a major task also referring to deep movements. If the landslide has a slow behaviour over time, it is necessary to use sensors with high accuracy, precision and repeatability, in order to detect physical values over instrumental noise. The goal of monitoring deserves some considerations: if the aim is to study and control the phenomenon evolution, data acquisition could be made by an operator (manual) or locally automated, with no necessity to immediately check the output and active alarm procedures. Vice versa, if the application is for EWS purposes, the measures require an automation and a high-speed data processing in order to validate the results and contact the responsible of monitoring if a threshold is overcome. The definition of the thresholds is related to the realization of a preliminary numerical model which should describe the potential phenomenon that may occur. The model has a series of uncertainties related to the typology of mathematical model used, the theoretical hypothesis involved, the lithology, the geometry, the input parameters (mechanical and deformation parameters, water level, position of the sliding surface, hydrogeological characteristics) and the intrinsic geotechnical variability. After a calibration period, the model requires a constant validation and updating process using the data of an automatic monitoring system, with statistical self-learning algorithms (Carri et al. 2017) able to identify anomalies in the raw data. This approach requires a training period at the beginning of the monitoring period, increasing its accuracy over time, together with the dataset. Monitoring of natural phenomena should interest also the pore pressure (also if negative), the rainfall, the water level, together with the atmospheric pressure, the humidity, the temperature, hydrographic levels and structural reinforcing elements, like rods or nails.

The automation of the monitoring system is strictly related to a correct design of the electric power, often guaranteed with solar panel and backup battery. It follows that, if the direct connection to the electrical line is not possible, the data logger must read instrumentation at a correct sample period, which has to respect the required frequency, compatible with the related risk, and power consumption. The sample period should increase if an accelerating phase is observed and then decrease its frequency if the slope shows no displacements or they are decelerating. If the rate is too high, a standard battery could run out of charge, especially during bad weather or night periods, and a consistent solar panel is required, with very high-cost and landscape impacts. The availability of a large amount of data is related to a long computing time and sometimes confusing results. On the contrary, low frequencies cause issues in the identification of triggering factors.

The monitoring planning process ends with the definition of physical entities to be measured, the positions of the sensors, the sample periods, the data management system and the most appropriate instruments to achieve the best compromise between results and cost-effectiveness.

2.4. Monitoring of geotechnical structures

Geotechnical structures include retaining structures, superficial or deep foundations, piles, bulkheads, wells and all the civil structures that have a strong interaction with natural materials at a shallow depth. The aim of the monitoring process is the compatibility check between the design outcomes and the effective response of the structure during construction. The designer should indicate the best positions for the instrumentations and the physical entities to be monitored, together with the expected magnitude values or their variability range, in order to correctly apply the observational method (Peck 1969). The designer or the responsible of the monitoring should also identify alert and alarm thresholds relating to the compatibility of deformations with the structure. In this field, it is quite often necessary to transfer data and achieve information rapidly. Consequently an automated system is required, together with a management platform, especially when a huge number of sensors are installed. The technician responsible of data control and interpretation should find and evaluate all the results in the same place, with clear and dynamic representations. This aspect plays a key role in the monitoring process because instruments offer important indications of what is going on, that are useless if the responsible for decision does not receive and analyse them. It is always important to remember that a huge number of installed sensors permits a more extensive control, introducing on the other hand the theme of the correct choice of meaningful and useful information for each construction or exercise phase of the opera. Data management platforms could work on a local or remote server, using radio or telephonic lines. In the second case, a web platform with controlled access permits to view the results at every time and from every part of the world, using a device connected to internet line. The opportunity of remote data storage guarantees also easier maintenance works or correction of software bugs, while a private and local server, often inaccessible from outside, requires the visit of a technician at the site, losing time and money. Due to the criticality of data transmission, it is appropriate to have a local storage and backup of the data inside the data logger, preserving the raw data. In the case of a complex site, where cables could interfere with works or instrumentations cover a large area, it is possible to transmit information provided by sensors installed to a master data logger using Wi-Fi or Radio Smart Mesh networks.

2.5. Monitoring of underground excavations

Underground excavations include deep tunnels, mines, underground deposits and all the structures that have a strong interaction with natural materials at consistent depths. The application field of monitoring has similar finality with respect to the previously described one. In addition, it is determinant to identify the behaviour of the natural surround materials at a certain distance from the excavation (Lunardi 1988), verifying or correcting design hypothesis about mechanical and/or hydraulic behaviour. The activation of the monitoring system at the surround of the structure should be performed in advance of the beginning of works, in order to define the undisturbed behaviour of the area and its modification after the excavation and construction processes. It is also necessary to monitor existing structures, if present, which could be damaged by works. This aspect has also the purpose to demonstrate the consistency (or not) of recriminated irreparable breakages that may occur

by the owners of the nearby facilities. It is worth nothing that sometimes properties have already some damages not related to construction works and the excavation could be a pretext to earn some money.
The field of application could require also the acoustic, vibration and environmental monitoring, related to the possible presence of gas and/or dust. Due to the high frequency of acquisition, it is often not possible to operate the vibration monitoring with traditional data loggers and a specific control unit is required.

2.6. Traditional instrumentation

The term traditional instrumentations generally indicates tools that have been available on the market since the second half of the last century. The instruments could be analogic or digital, manual or automated, and are generally characterized by a simple conversion between raw data and results. The sensor is generally one, at most integrated with a thermometer. The technology and the installation procedures are well known and available on the market from numerous different companies.
This sub-paragraph briefly summarizes the main traditional tools, organized on the physical quantities to be monitored.

2.6.1. Measure of deformation

Manual Inclinometer

Inclinometers monitor differential deformations of the soil or geotechnical structures (like diaphragms walls, dams, tunnels, etc.), finding the position of the potential sliding surface. They first appeared in the 50s (Fowler 2013) at Harvard University, while the installation of the first grooved casing took place in 1954.
The instrument measures rotations at specified points and consequently calculates the horizontal deformations (i.e. it is not possible to record rigid translations). It is also possible to use horizontal tools in order to monitor settlements. The system is generally constituted by a circular deformable ABS casing (Fig. 2.2a) with two pairs of guides. The pipe is inserted inside a borehole or the geotechnical structure to be monitored and coupled with the surrounding environment with rigid or semi-rigid materials, like cement, bentonite, gravel or sand. The measure is executed with a probe (Fig. 2.2b), with a cylindrical body and two carts, which is inserted inside the ABS casing. A transportable control unit placed on the ground collects data from the probe.

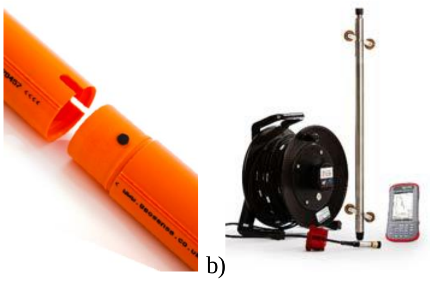

a) b)

Fig. 2.2 a) ABS casing and b) inclinometer probe with control unit (source: Geosense Ltd)

The operator generally samples the borehole along two orthogonal directions, defined as A and B, executing two conjugate measures for each of them, rotating the probe after the first one. The operation applies a hardware filter, based on the same principle of XLR audio cables, where the instrumental noise could be evaluated and deleted transmitting the same input signal with an opposite polarity. Displacements are finally calculated using simple trigonometric formulas along the two directions, starting from the bottom of the borehole and cumulating the single steps of measure. Sensors used are 2D MEMS (Micro Electro Mechanical System) or Servo-Accelerometers. The second ones have a great sensibility, accuracy and precision, together with a consistent price. The application is suggested when it is necessary to monitor very small deformations. MEMSs have lower technical features, implying a really cheaper cost.
The instrumentation requires an operator and could be reused in numerous places. Results are available through a stand-alone software or a mobile application.

In Place Inclinometer

In Place Inclinometer (IPI) is based on the same principle of manual inclinometer (Fig. 2.3). They have been introduced in the early 80s (Fowler 2013). They usually use 2D MEMS sensors, are fixed at a specified depth and are automated. The tool is able to provide only the local tilt angle or movement at a specified depth and it is not possible to have cumulative displacements. Before installation, it is important to know the places where the movements may occur. It is difficult to interpret the relevance and significance of this kind of results, which are not representative of the situation along the whole vertical borehole. Using them as a manual inclinometer leads to misleading information.

Fig. 2.3: In Place Inclinometer (source: Earth System S.r.l.)

Slip Indicator system

Slip Indicator (Fig. 2.4) is a flexible pipe with base plate, inserted inside a borehole. Using indicator probes attached to a support rope, it is possible to determine the position of the sliding surface.

Fig. 2.4: Slip Indicator system (source: Geosense Ltd)

Pendulum system

Pendulum (Fig. 2.5) is used to monitor the tilt or rotation of concrete dams, bridges and high rise buildings with very accurate and precise measures. It is possible to read the instrument manually or automatically. It is able to detect the X, Y and Z movements observing displacements relative to a stainless steel wire.

Fig. 2.5: Pendulum (source: Geosense Ltd)

Tilt Meter

Tilt Meter (Fig. 2.6) could be equipped with 1D/2D MEMS or electrolytic cell and measures rotations at a single location in structure or terrains, with respect to the planes which are perpendicular to the base unit. The sensor is bond or bolt to a structure and read with a cable or wireless. They have a good precision and low cost but are very sensible to temperature variations, requiring a thermal correction. A very similar application (sometimes defined as *Tilt Beam*) consists in the measure of differential movements of precast concrete in tunnel lining excavated thorough a Tunnel Boring Machine (TBM).

Fig. 2.6: Tilt Meter (source: Earth System S.r.l.)

Magnetic Extensometer

The Magnetic Extensometer (Fig. 2.7) is designed to monitor settlements or heave in excavations, embankments or foundations. The system is composed of a pipe that includes magnetic targets. The probe reads the relative position of the magnetic targets, identifying if a settlement occurred and its amount.

Fig. 2.7: Magnetic Extensometer (source: Geosense Ltd)

Settlement Gauge

Settlement Gauge (Fig. 2.8) monitors soil settlements and deformations measuring the variations of distance between two or more points in one single direction. Fiberglass or aluminium rods are installed in hollow boreholes, fixing one end with cement, while the other is free to move through a ring fixed at the surface. Here there is an electrical transducer that records pitch variations between the points.

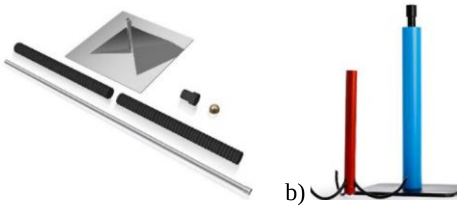

a) b)

Fig. 2.8: a) Elements that compose a Settlement Gauge (source: Earth System S.r.l) and b) rod settlement system (Geosense Ltd)

Liquid Settlement system

The Liquid Settlement system is able to measure settlements or lifts in soils or geotechnical structures, exploiting the properties of a fluid. The system is composed of a liquid-filled tubing and a vibrating wire pressure transducer. It could be manual or automated, fixed (Fig. 2.9a) or removable (Fig. 2.9b).

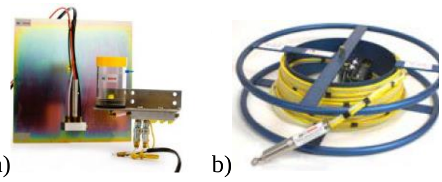

a) b)

Fig. 2.9: a) Fixed or b) removable Liquid Settlement system (source: Geosense Ltd)

Extensometer

Extensometer (Fig. 2.10a) measures the longitudinal deformation in numerous applications, as the monitoring of rock masses, settlements, soil displacements, geotechnical structures. They usually consist of a vibrating wire displacement sensor encased in a sealed body, which could be one-dimensional or triaxle. If used as a measuring anchor (Fig. 2.10b), they can determine also the load exerted on rock bolts (Geosense Ltd), measuring the changes in length due to extension or compression and knowing the constitutive laws and the dimensional characteristics of the element to be monitored. There are two main kinds of extensometers that differ according to the operating principles. The first one is the Extensometer Bridge, which looks like a steel section bar with a square cross section, instrumented on each side with a Wheatstone bridge extensometer. The measure of deformations is related to the strain resistance variation. The second one is the vibrating wire transducer, which is like a hollow tube, fitted inside a steel wire bound to the ends and an electromagnet placed in the middle that can swing the cable. When a deformation occurs, the length of the steel wire varies and the frequency of vibrations modifies accordingly. The deformation is measured indirectly, evaluating the variation of the wire vibration.

a) b)

Fig. 2.10: a) Extensometer and b) measuring anchor (source: Earth System S.r.l. and Geosense Ltd)

Wire Extensometer (Wire Deformeter)

Wire Extensometer is designed to monitor the changes in distance between two anchor points, connected with a stainless steel wire. The anchor could have a distance up to dozens of meters. Sensors are vibrating wire or potentiometers. The application regards structural joints, landslides and movements of the rock mass.

Fig. 2.11: Wire Extensometer (source: Earth System S.r.l.)

Crack Meter

Crack Meter is designed to monitor the change of fractures aperture that may occur in structures or rock masses. The instrument could be optical (Fig. 2.12a), mechanical (Fig. 2.12b) or electrical (Fig. 2.12c). Optical and mechanical typologies require an operator, while the electrical is automated, using potentiometer or vibrating wire transducers connected to a data logger. Optical Crack Meter has two plastic elements fixed at the end of the fracture, parallel one to each other, allowing the measure of displacements along two perpendicular directions. Mechanical Crack Meter could be mono-axial or triaxle. The mono-axial consists of a steel rod which is orthogonal to the fracture direction, fixed to one end and free to move on the other. The displacement is measured using a comparator. The triaxle is composed by a square section prism and an external frame with three singular comparators, permitting to monitor 3D movements (Ferrero et al. 2011). The electrical sensor has a linear displacement transducer with two anchors that are fixed to the crack sides. It could also be 3D, as mechanical crack meter.

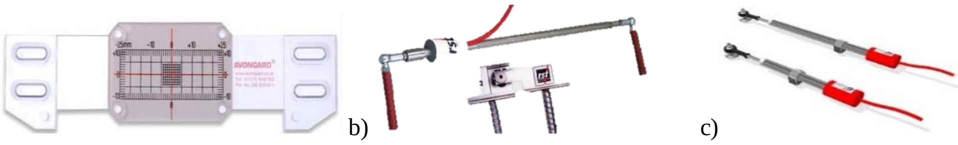

a) b) c)

Fig. 2.12: a) Optical, b) Mechanical and c) Electrical Crack Meter (source: Dusense LLC, rst Ltd, Earth System S.r.l.)

Multipoint Borehole Extensometer

The Borehole Rod Extensometer (Fig. 2.13) is used for the monitoring of underground excavations or slope to measure deformations of the rock mass or soil along a radial direction. The instrument measures and locates settlements, displacements and deformations of soil and rock. It is composed of a reference head and one or more holes anchors, placed at a known distance from the plate and connected to the head with rigid or flexible rods, which can move inside sleeves. If the soil or the rock deforms, the anchor changes its position and the rods slide through the head of the instrument, providing the magnitude of the movement.

Fig. 2.13: Multipoint Borehole Extensometer (source: Earth System S.r.l.)

Joint Meter

Joint Meter monitors joints of mass concrete structure and consists of two parts: a socket and the main body. The socket (Geosense Ltd) is secured to the form and embedded into the block to be constructed. The form is then removed and the gauge is screwed into the socket and embedded in the concrete, before the concreting of adjacent block.

Fig. 2.14: Joint meter (source: Geosense Ltd)

Fibre Optic Inclinometer

During recent years, numerous Fibre Optic Inclinometers (Fig. 2.15) have been studied by several authors (Nilsson et al. 2007, Lee et al. 2012, Minardo et al. 2014).

Fig. 2.15: Fibre optic inclinometer (TBT Scietech Ltd)

They enable long distance transmission in hazardous environments without signal loss. Contrarily to the increasing number of scientific articles about this theme, the system does not hit the market for many reasons, related to the price of the control unit, the possibility for some typologies to measure only cumulated displacements and other factors.

2.6.2. Measure of water level and pore pressure

Casagrande piezometer

The Casagrande piezometer (Fig. 2.16) has usually a solid casing down the whole depth of the borehole, with a screened casing in the area of pore pressure measure. The sealing of the case is obtained using bentonite, clay or concrete in order to prevent the contamination of the water level with other aquifers. In the case of an unconfined aquifer, the registered water level do not represent the exact value of water table, in particular if there is a significant vertical component of the flow velocity. If artesian conditions confine the aquifer, water level (Mayne et al. 2011) indicates the pore pressure in the aquifer but not necessarily the water table.

Fig. 2.16: Casagrande piezometer (source: Earth System S.r.l.)

Open Standpipe piezometer

Open Standpipe piezometer (Fig. 2.17) is composed with a riser pipe and a filter tip, backfilled with sand and a bentonite seal above. The pore water flows inside the standpipe reaching a pressure equilibrium, which represents the pore pressure of the soil. It could be manual or automated, sometimes including a thermometer.

Fig. 2.17: Open Standpipe piezometer (source: Geosense Ltd)

Electrical pressure transducer

Electrical pressure transducer is automatic and could be pneumatic (Fig. 2.18a) vibrating wire (Fig. 2.18b) or strain gauge (Fig. 2.18c). It registers the pore pressure (and sometimes also the temperature) as an electrical signal. Piezometers are isolated inside a single aquifer and cabled to the ground surface, where a data logger collects data (this could also be a portable readout unit). If numerous sensors are present, usually each piezometer has its own cable. Some companies provide a single cable for the array. If compared to Casagrande piezometer, electrical pressure transducer has a quicker time of response.

a) b) c)

Fig. 2.18: a) Pneumatic, b) Electrical and c) Strain Gauge piezometers (source: Geosense Ltd and Earth System S.r.l.)

Water Level Meter

Water Level Meter (Fig. 2.19) is composed of a removable probe that an operator could use to detect water level and temperature inside a borehole. It consists of a stainless steel probe with a specially designed conductive probe in order to minimise displacement errors (Geosense Ltd).

Fig. 2.19: Water Level Meter (source: Geosense Ltd)

2.6.3. Measure of stresses

Load Cell

Load Cell measures the load applied to the monitored element. It is electrical and constituted by a metal body (stainless steel or aluminium) to which it is possible to apply some extensometers. The number of extensometers is usually four in the configuration of Wheatstone bridge or vibrating wire sensors. It is possible to measure indirectly the force applied to the instrument by knowing the variation of electrical resistance measured in the extensometers.

Fig. 2.20: Load Cell (source: Earth System S.r.l.)

Pressure Cell

Pressure Cell records the intensity and distribution of pressure applied to the monitored element. The instrument could be hydraulic or a membrane cell. The hydraulic has two circular or rectangular plates, welded together with a chamber, filled with oil and connected to a transducer. The second typology reads the deflection of a membrane with an electrical resistance or a vibrating wire transducer. The choice between the two possibilities depends on the required precision, signal stability and temperature sensitivity.

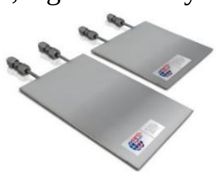

Fig. 2.21: Pressure Cell (source: Earth System S.r.l.)

2.7. Innovative instrumentation

The term innovative instrumentation is used in this chapter to describe the digital instrumentations that have been developed during the last 20 years, based on new technologies and innovations in the electronic and

electromagnetic fields. Many sensors have been adapted as a derivation from other broader and more profitable markets, like automotive, smartphone and consumer electronic. Some of the new tools are patented and distributed worldwide by a single company, while others have more than one manufacturer. The introduction of the Reliability Based Design (RBD) with Eurocodes has given a boost to the observational approach (Peck 1969), increasing the contractors demands for the verification of works during both construction and exercise phases. At the same time, the increasing attention on risk management theme and risk scenarios occurred after the facts of Sarno has required a daily or hourly monitoring frequency able to provide more complete and immediate answers. This is economically and operatively not sustainable with traditional tools. The innovative instrumentations are often a combination of traditional sensors along a single array able to measure multi-parametric physical entities.
This sub-paragraph briefly summarizes the most known innovative tools, organized on direct or indirect measures.

2.7.1. Direct measures

Automated Inclinometer System (AIS)

Automated Inclinometer System (AIS) is an automatic mechanized inclinometer (Fig. 2.22) designed by CNR-IRPI of Turin (IT) in 1992 and then redesigned and patented in 2008 (Lollino et al. 2008) to operate by remote control of a unit microprocessor (Lollino 1992, Lollino et al. 2002, 2006). The system is composed by an electrical control unit, a 2D servo-accelerometer or MEMS sensor and an electric motor with an encoder, able to drive the probe in the inclinometer casing and control the position of the sensor inside the borehole. The probe is automatically lowered at the bottom of the hole and then ascends at predefined depths to execute the measures and save them on a local memory, placed near the sensor. The system is designed to monitor a single or two opposite (0°-180°) guides and works with a battery. AIS measurement speed is about 30 seconds per meter, with measuring intervals of 50 cm (Allasia et al. 2018). At the end of the sampling phase, data are transmitted to the control unit through a local wireless network. Data logger is positioned at the ground surface and powered with solar panels. Here the system elaborates the results and sends them to a remotely PC to activate the alert procedures and process the consequent analysis. A 2.5 mm Dyneema® cable guarantees the mechanical resistance. The system could be used for the monitoring of landslides and geotechnical structures, like proper and diaphragms walls and underground excavations during both construction and exercise phases.

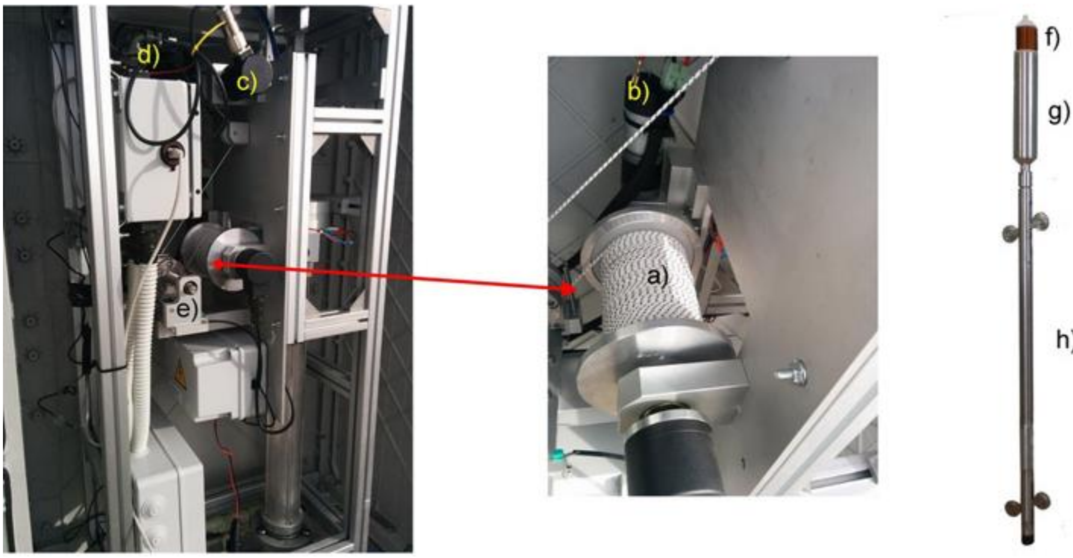

Fig. 2.22: AIS system, composed by a) 2.5 mm Dyneema® cable, b) engine for the rolling up and unrolling of the cable, c) high precision encoder, d) embedded PC, e) cable distribution system, f) inductive charging system, g) battery, h) probe (source: CNR-IRPI)

Differential Monitoring of Stability (DMS®)

Differential Monitoring of Stability (DMS®) has been a patented instrumentation (since 2013) designed and produced since 2001 by CSG S.r.l., an Italian company founded in 1997. A series of steel rigid modules (Fig.

2.23) compose the column. Each module has its own sensor and it is connected to the others using joints with 2 or 3 degrees of freedom (Cardellini and Osimani, 2008), preserving the azimuth. Integrated sensors are 2D MEMS, piezometers, extensometers (used to monitor vertical displacement), digital compass, 3D high frequency MEMS, thermometers. Control unit automatically collects data from DMS column through RS485 protocol and it can send warnings to the responsible of monitoring through GSM, GPRS, LAN or Wi-Fi lines, SMS or direct calls. The power consumption could vary between 90 and 150 mA. The system is powered through a 12 V battery and solar panel or with the direct connection to the electrical line. A proprietary stand-alone or online software calculates and represents the results, using trigonometry for the evaluation of displacements.
Different versions of the product are available, depending on the application. They are classified as DMS 2D Slide, DMS 2D Slope, DMS 2D Rock, DMS 2D GV, DMS 3D Multipacker and DMS 3D Plus. The following lines briefly summarize the main technical features of the monitoring system related to the various available tools, reporting the worst and the best characteristics for every single aspect.

The length of each module could be 1 or 1.5 m and the maximum total length could vary between 60 and 250 m, depending on the application. The range of 2D MEMS could vary between 10° and 45° (the installation for rock mass stability monitoring could be 360°). The repeatability and resolutions are related to the price and could vary respectively between ±0.002° ÷ ±0.05° and ±0.001° ÷ ±0.01°. The extensometer has a range of 0÷100 mm, with a resolution of 0.01 mm. The range of Piezometer starts from 30 up to 250 psi, with a repeatability of 0.2 mV and a resolution of 0.02 psi. The vibration accelerometer has a full range of ±2 or ±3 g. The thermometer has a range of -50 °C ÷ +130 °C with a resolution of 0.1 °C. The digital compass has a resolution of ±1°.

Fig. 2.23: DMS system (Source: CSG S.r.l.)

The tool can monitor in near-real time the deformations of landslides or geotechnical structures, together with temperatures, water levels and accelerations related to earthquakes or earth vibrations. At the end of monitoring the instrumentation could be fully or partially retrieved. Fields of application are slow moving landslides, DPGV, geotechnical structures, rock mass stability (CSG S.r.l.).

Shape Accel Array (SAA)
Shape Accel Array (SAA) is a patented geotechnical instrumentation device that has been developed by Rensselaer Polytechnic Institute (USA) and Measurand Inc. (CA) since 2006. The system (Fig. 2.24) looks like an array of jointed flexible tubes equipped with 3D high frequency MEMS and thermometer sensors, spaced 200, 305, 500 or 1000 mm, depending on the applications (Dasenbrock 2010).

Fig. 2.24: SAA system (Source: Measurand Inc.)

The connection between each tube preserves the azimuth. Displacements are evaluated using trigonometry and the known geometry of the array. Control unit (Campbell Scientific CR300) automatically queries sensors in near-real time through RS232 protocol and SAA232 interface, periodically uploading results on a web-platform. The system is able to send warning messages via e-mails or text messages if thresholds are exceeded. The power consumption could vary between 1.8 and 4.2 mA for each segment. The system is powered through a 12 V battery and a 50 W solar panel or with the direct connection to the electrical line.
The different available versions of the product are classified as SAAV, SAAF, SAAX and SAASCAN. As in the previous paragraph, the following lines briefly summarize the main technical features of the monitoring system, reporting the worst and the best characteristics for every aspect.

The length of each module could vary between 0.2 and 1 m and the maximum total length is 100 or 150 m, depending on the application. The range of 3D MEMS could vary between 30° and 180°. The resolutions is declared between ±0.000278° ÷ ±0.00056°, with a differential displacement accuracy of ±1.5 mm over 32 m of cumulated displacements (Bennett 2010). If reported to resolution per meter, it could be estimated as ±0.047 mm/m only if we assume that the error is equally distributed over local displacements: this is not generally true, due to the fact that the propagation of errors in inclinometric measures tends to compensate itself because they could be in opposite directions. The accuracy for absolute shape is of ±10 mm for 32 m, with a resolution of ±0.5 mm for the same length. The dynamic acceleration measurement of vibration has a range of ±1.7 g, with a frequency of 50 Hz. The system is declared waterproof and able to resist a pressure of 2000 kPa. The azimuth error in joints is estimated between ±0.01° and ±0.25°.

The tool can monitor in near-real time the deformations of unstable slopes, civil engineering structures, mines and underground excavations, drill-hole shapes (Measurand Inc.). At the end of monitoring the instrumentation could be retrieved.

2.7.2. Indirect measures

The indirect measures are remote systems that use sensors placed far from the monitored area. This kind of instruments could be terrestrial, aerial or satellite and monitor the surface of the soil over large areas. This characteristic is very useful to identify heterogeneous behaviours of the landslide, despite it is not possible to recognize the sliding surface.

Total Station

The mechanized topographic survey (Fig. 2.25) measures the shift of interest points over large areas along time. The system is based on a total station, a robotic automatic collimation on reflective prisms installed at the points of interest and a distance meter. Through the collimation of the prisms, it is possible to return their positions and displacements over time, referring to a predefined reference system. The tool has to be installed in a stable area.

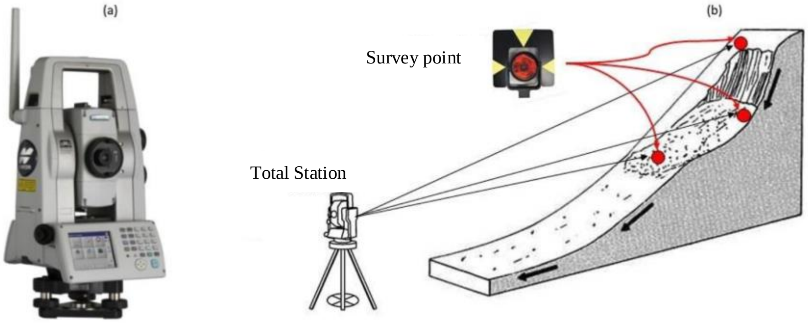

Fig. 2.25: a) Total Station and b) recognition of survey points along the slope (Source: ELEDIA Research Center)

Terrestrial and aerial photogrammetry

Photogrammetry is a prominent technique based on the recognition of the same points on at least a couple of 2D photos, made through calibrated terrestrial (Fig. 2.26a) or aerial (Fig. 2.26b) cameras. The spatial position of the representative points is obtained through the use of two central perspectives of the same object, using two projection centres (as in Ferrero et al. 2011, Curtaz et al. 2013, Roncella et al. 2014, Roncella and Forlani 2015, Scaioni et al. 2015).

Fig. 2.26: a) Terrestrial photogrammetry and b) drone for aerial photogrammetry (Source: Airvision)

Laser Scanner

Laser Scanner (Fig. 2.27) automatically scans the surface of interest generating a point cloud and reproducing the three-dimensional model of detected objects (Margottini et al. 2015). The distances from the objects are calculated using the laser impulse time of flight. It is possible to define information about distance, horizontal and vertical angles for each point, with respect to the instrument. By comparing recreated models at different times it is possible to know the deformations eventually occurred.

Fig. 2.27: Terrestrial Laser Scanner (Source: Leica Geosystems AG)

Terrestrial Interferometry (GB-inSAR)

Ground-Based interferometric Synthetic Aperture Radar (GB-inSAR) is a technique for the remote monitoring of surface deformations concerning large portions of territory (Beninati et al. 2015, Mazzanti et al. 2015, Crosta et al. 2017). The technique is based on the use of a radar sensor installed on a terrestrial platform. The device (Fig. 2.28) moves along a track, which is orthogonal to the direction of expected displacements, and acquires images that have to be compared. The result is a series of pictures at different times that can be processed, defining a map of shifts by comparing the phase differences of the same pixels in the different images. The number of pixels is closely related to the distance between the radar and the monitored scenario.

Fig. 2.28: GB-inSAR system (Source: IDS GeoRadar S.r.l.)

Satellite Interferometry (PS-inSAR)

Persistent Scatter interferometry (PS-inSAR) has the same operative principle of GB-inSAR and permits to monitor the subsidence, working with satellite images and their phase difference (Fig. 2.29). The technology finds objects (defined as Persistent Scatters) in the image area that produces a constant and characteristic radar reflection over time. The number and distribution of PS depend on the site and could be difficult to find in vegetated areas. Moreover, the sample period varies depending on the satellite used. Sentinel-1a and Sentinel-1b offer a revisiting time of 6 days (Raspini et al. 2018), which is suitable for a preliminary survey but not consistent for an Early Warning System, considering also the processing time of results.

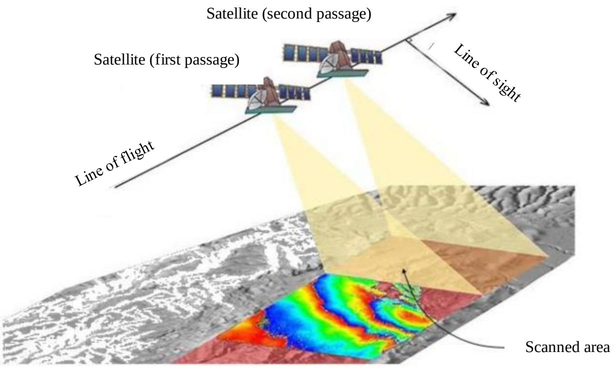

Fig. 2.29: PS-inSAR (Source: Geoscience Australia)

InfraRed Thermography (IRT)

InfraRed Thermography (IRT) is a non-destructive technique applied to the monitoring of natural slopes, rock masses and civil structures (Martino and Mazzanti 2014). The technology is based on the survey through thermocouples of thermal energy emitted by monitored objects. In this way, it is possible to describe the water circulation within granular or rocky soils and the presence of discontinuity in the surface layers. In the field of civil structures, thermography is used to detect any water infiltration, injury or anomaly in the structure.

Fig. 2.30: Infrared camera (Source: FLIR systems Inc.)

2.8. Comparison between inclinometers

The following table (Tab. 2.1) summarizes the main technical features of traditional inclinometers (manual probe and IPI) or piezometers and innovative multi-parametric tools (DMS, SAA, etc.), as declared in the data sheets. Each characteristic is expressed as a range, reporting the lower and the better value for the system. In particular, MUMS inclinometer is introduced (the tool will be further discussed in Chapter 3). In order to compare the different physical entities (degrees, gravity acceleration, etc.) that characterize the tilt sensors, repeatability and resolution are evaluated also as millimetres per meter.

Tab. 2.1: Comparison between technical features of traditional and innovative instrumentations

Instrumentation	Min. Step of Measures [m]	Max. total Length [m]	Tilt sensor (MEMS, Electrolytic Cell, Servo-Accelerometer)				Piezometer			High Frequency Accelerometer [g]	Thermometer	
			Number of axes	Measuring Range	Resolution	Repeatability	Measuring Range [kPa]	Resolution [kPa]	Repeatability [kPa]		Resolution [°C]	Range [°C]
Manual Probe[1,5]	0.50	500[5]	1D – 2D	±15° ÷ ±30°[1,5]	±0.0013° [5] 0.020 •,[1] ÷ ± 0.023[5] mm/m	±0.030[5] mm/m	-	-	-	-	-	-
Traditional Piezometers[1]	-	-	-	-	-	-	0.04 ÷ 173 0.517 ÷ 2068 0.35 ÷ 700	0.04 ÷ 0.35	0.07	-	N.A.	-20 ÷ +80 -40 ÷ +125
IPI[1,2,3,4]	1.00 ÷ 2.00	1200[1]	2D	±10° ÷ ±30°	±0.0004° ÷ ±0.0210° ±0.007 ÷ ±0.367[1,2,3] mm/m	±0.001° ÷ 0.020° ±0.030 ÷ 0.300 mm/m	-	-	-	-	±1.0000	-40 ÷ +85 -40 ÷ +125
AIS[6]	0.50 (standard) 0.05 (custom)	140	2D	±15° ÷ ±45°	±0.017 ÷ ±0.070 mm/m	±0.005 ÷ ±0.008 mm	-	-	-	-	-	-
DMS[7]	1.00 ÷ 1.50	60 ÷ 250	2D	±10° ÷ ±45°	±0.0010° ÷ ±0.0100° ±0.020 ÷ 0.180 mm/m	±0.002° ÷ 0.050° ±0.035 ÷ 0.873 mm/m	207 ÷ 1379	13.79	0.20 mV	±2.0 ÷ ±3.0	±0.1000	-50 ÷ +130
SAA[8]	0.20	100 ÷ 150	3D	±30° ÷ ±180°	±0.0003° ÷ ±0.0056° ±0.001 ÷ 0.002 mm/m	N.A.	-	-	-	±1.7	N.A.	N.A.
MUMS	0.30	130[†]	3D	±360°	±0.020 mm/m (Electrolytic) ÷ ±0.244 mm/m (MEMS)	0.020 mm/m	0 ÷ 1000	0.03	0.50	-	±0.0078	-55 ÷ +150

[1] source Earth System S.r.l.
[2] source Geosense Ltd
[3] source rst Instruments Ltd
[4] source SISGEO S.r.l.
[5] source Geokon Inc.
[6] source CNR-Irpi
[7] source CSG S.r.l.
[8] source Measurand Inc.
[*] The maximum total length characteristic could not be expressed for IPI, due to the instrumentation nature;
[†] There is not a maximum total length for MUMS array. The only physical limit is related to the number of sensors, which is 255. The deeper array that has been installed is 130 m long;
[•] The data refers to a Servo-Accelerometer inclinometer system.

Chapter 3

> ***"Measure what is measurable, and make measurable what is not so."***
>
> **Galilei G.**

MUMS MONITORING SYSTEMS

3.1. Introduction

Modular Underground Monitoring System (MUMS) is a patented automatic inclinometer composed by several nodes (defined as Links, Fig. 3.1) located at custom distances along a single chain. They are linked by an aramid fibre and a quadrupole electrical cables (Segalini and Carini 2013). The array is automated and collects multi-parametric data from each link through a remotely controlled data logger and RS485 communication protocol. The working principle of the system is quite complex and it is represented in Fig. 3.2.

Fig. 3.1: Link of a MUMS chain

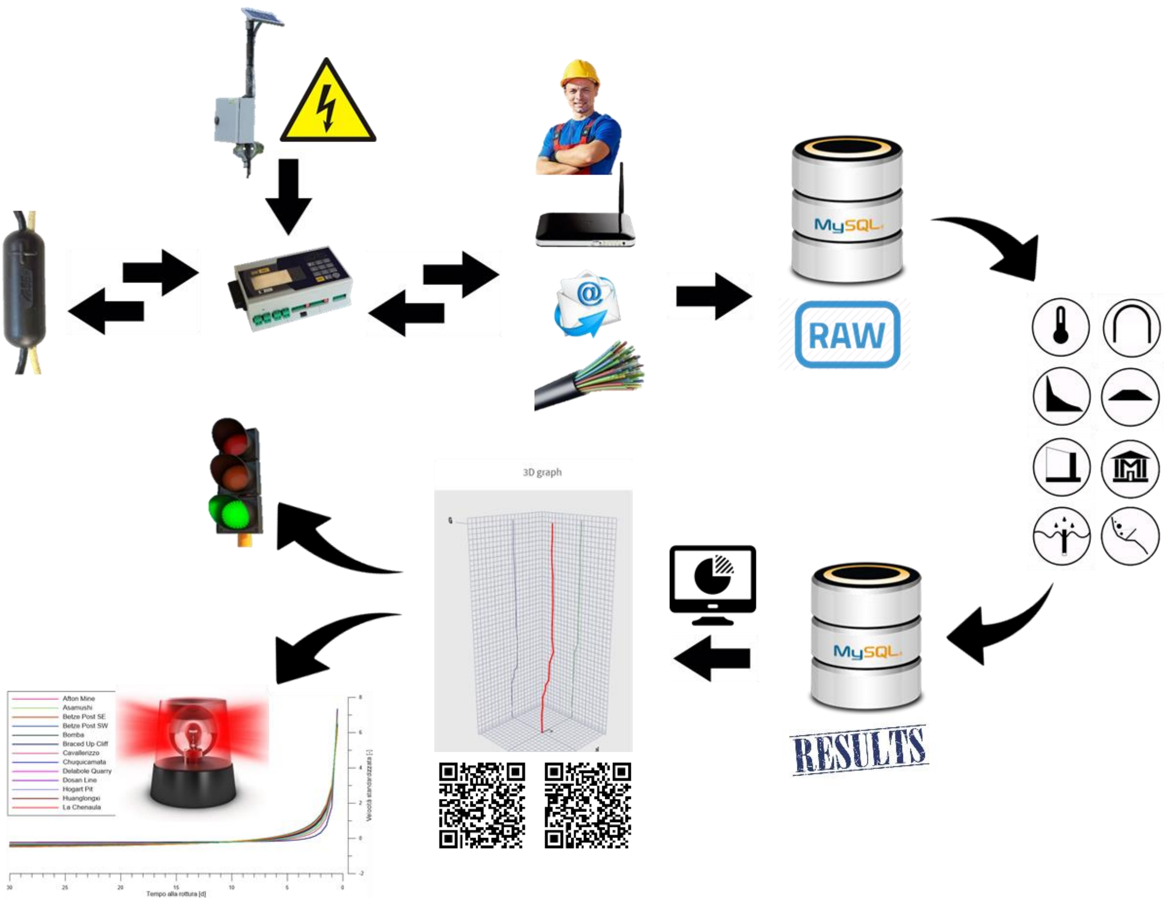

Fig. 3.2: MUMS system

Control unit queries sensors at the specified sample period, making 64 readings and saving the mean in an external SD card. This operation is able to apply a first filter on the raw dataset and remove uncertainties in the measure. Moreover, the data logger could record traditional sensors described in Chapter 2.6, based on 4-20 mA, mV/V, 0-10 V, 0-5 V, NTC and VW signals. Control unit is powered with a 12 V 7 Ah battery and a 5 W solar panel or the direct connection to the electrical line, whenever possible. In particular, the low electrical consumption permits to highly reduce the technical features of the solar panel, if compared to other innovative systems previously described in Chapter 2.7.1, saving money and reducing environmental impact. The data transmission generally exploits the 4G, 3G or GPRS line with a UMTS router. Dealing with underground excavations, it is also possible to use fibre optics leading to a local elaboration centre, or an operator, which has only to copy the content of the SD card and send it to the main server for the following elaboration. Raw data (electrical signals) are then stored in a safe DB, with multiple daily backups, and automatically elaborated, using a specific algorithm able to convert them into physical units, remove spike noises and accidental errors and calculate the final results (as described in the following paragraphs). Then, the outcomes of interest are represented through a dynamic and intuitive web platform with secure controlled access. This passage is of fundamental importance. As described in Chapter 2.2, the installation of a huge number of instruments requires an adequate management platform which has to simplify the accessibility and interpretation of results (some examples are accessible through the QR codes of Fig. 3.2). The last passage of the management system is the activation of alert or alarm messages to the authority responsible for the monitoring. This task is extensively discussed in Chapters 4 and 5.3.
The spacing between links could variate accordingly to the monitoring needs and budget available, while the external diameter of every node is 37 mm. Thanks to its flexibility, the system could be inserted inside an old inclinometer casing where the traditional probes could not pass due to excessive deformations. Paragraph 3.2 describes the sensors that could equip each array.
Like similar systems, the tool provides differential displacements related to a reference reading (as discussed in Chapter 3.3), while it is not able to detect absolute positions, which require a dedicated calibration procedure. Each link needs about one second to be read along the three axes, resulting in two seconds for each meter (considering an interspace of 50 cm between sensors). As a comparison, AIS spends 30 seconds per meter for a single guide, while an operator with a manual probe takes about 1 minute, considering the 0° and 180° measures on the two axes. For the manual system, the time to reach and get back from the site should be considered too.
As mentioned in the previous Chapter, traditional inclinometers casings present two pair of guides in order to cumulate the measures along the vertical, while innovative instrumentations like SAA or DMS are equipped with mechanical joints. This configuration requires particular attention during the installation procedure (in particular for SAA system) and could lead to errors and uncertainties, related to the spiralling of the instrumentations or incorrect assembly (Segalini and Carini 2013). MUMS follows a different philosophy, where every sensor has its own reference system and exploits a 3D magnetometer to reconstruct the space position of nodes. Like the resultant gravity acceleration vector, also the Earth's magnetic field is a known variable (Campbell 1997) which could be used to verify the instrumental measures.

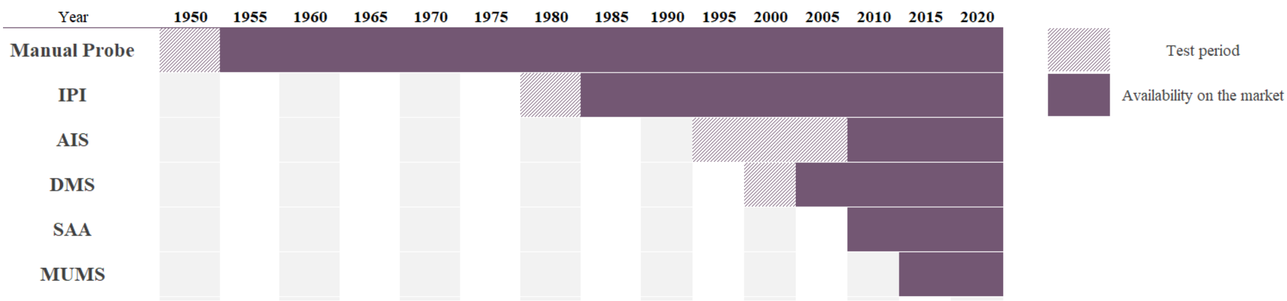

Fig. 3.3: Development of inclinometers along time

The instrumentation was born in 2011 with the idea to replace traditional measurement procedures (Segalini et al. 2011), improve the results or the applicability of innovative technologies and give a new tool to the monitoring responsible (Fig. 3.3). In particular, the design of the new system has focused its attention on some critical aspects that characterize the available inclinometers measures:

- Remove the presence of the operator on-site. This aspect has some advantages:
  - It consequently reduces the uncertainties related to his work;
  - It saves time and money;
  - The sampling is always possible, even when the site is not accessible;
- Overcome the traditional instrumentations, with the following advantages:
  - The reading frequency is higher and, together with the collection of multi-parameter data, permits a direct correlation between displacements and triggering factors;
  - The huge number of data permits to apply statistic in order to validate the results;
  - Have an operating Early Warning System;
- Improve the already existing innovative tools on the following tasks:
  - Remove any rigid mechanical connection between sensors, reducing uncertainties due to spiralling and creating a flexible instrumentation;
  - Create a lighter tool, easier to carry on site and to be installed;
  - Develop a cheaper instrumentation, more accessible for the market;
  - Change the elaboration philosophy, removing any closed-box hardware filter in order to store the raw data and apply statistical tools. Having the raw data available, it is always possible to study new algorithms and re-calculate the past events. Moreover, in this way scientists have the complete control of accuracy and repeatability, deleting any closed box process. Hardware filters are developed by the sensor providers and often unknown also for the producer and seller of the instrumentation;
  - Study a new redundant double sensor exploiting different technologies, able to be installed at the same depth and independently calculate the resulting displacement;
  - Reduce the electrical consumption in order to use smaller solar panels and reduce the impact on the landscape;
- Introduce new tools for landslide risk management and underground excavation processes, like:
  - A new method for the Time of Failure prediction, based on instrumental outcomes of different nature (local versus cumulative displacements) at different depths;
  - Create new automatic instrumentations for the monitoring of convergences and deformations of the rock mass in tunnelling, both during excavation and exercise phases;
  - Apply the Internet of Things (IoT) approach that characterizes the 4th Industrial Revolution to the geotechnical field.

The inclinometer has been designed as non-removable. It remains in place after the critical monitoring period, in order to continue the survey also after potentially dangerous events. MUMS has been available on the market since 2013, commercialized by ASE S.r.l., a Spin Off of the University of Parma founded for this specific purpose. The rapid development of the new technology (Fig. 3.4) certifies the necessity of the tool, demanded by construction companies, public and private agencies for the management of the territory and authorities for the safety control of roads.

“Vertical Array” has been the first version of the product, able to monitor landslides and geotechnical structures. During recent years, the tool has been subjected to a series of improvements and new fields of applicability (Fig. 3.5) and now (2018) could monitor settlements (Horizontal Array), temperatures for geothermal applications (Therm Array), water levels and pore pressures (Piezo Array), convergence (Cir Array), radial deformations inside the rock mass (Rad Array). Future developments will regard the monitoring of rockfall barriers (RockFall Safety Network), the environmental monitoring of museums (Musa) and the measure of pre-convergence (PreConv Array).

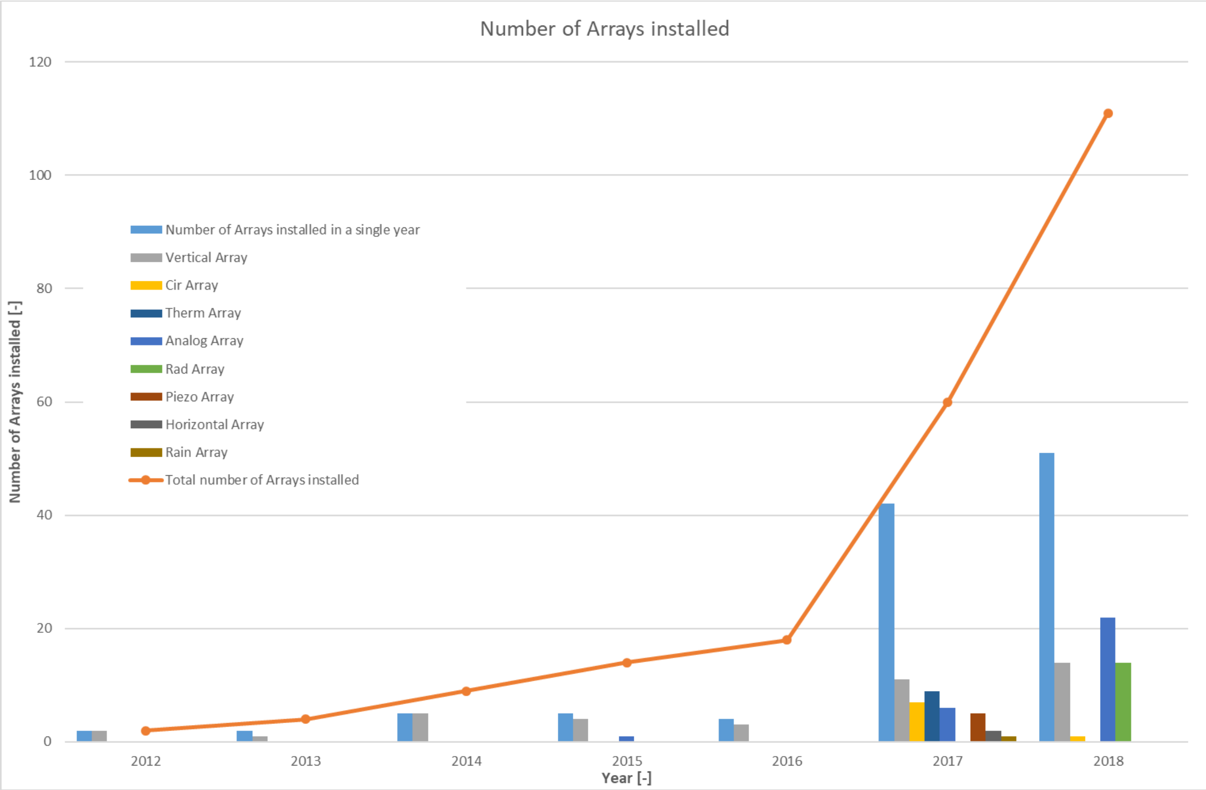

Fig. 3.4: Number of sensors installed on 22nd of October 2018

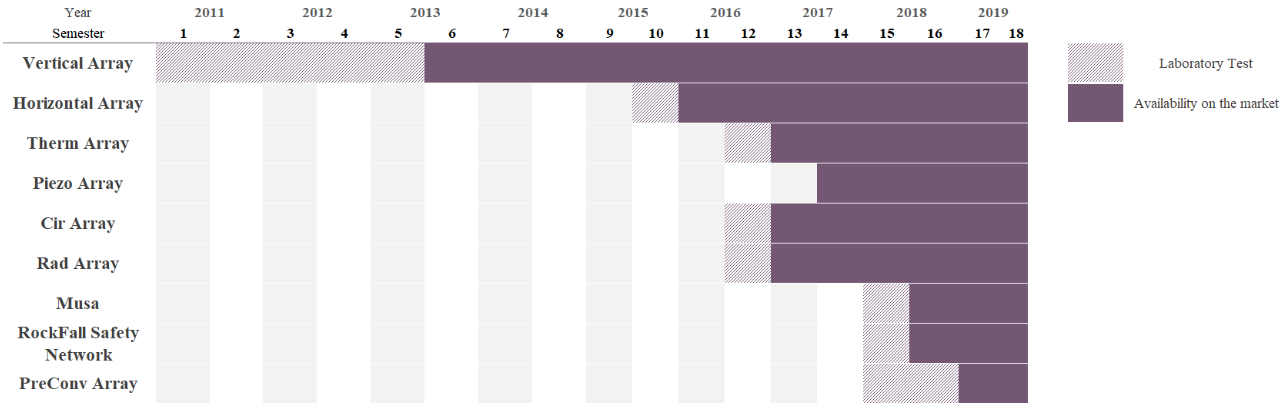

Fig. 3.5: MUMS system application fields

3.2. Sensors available and calibration procedures

This paragraph briefly summarizes the sensors available at the end of August 2018, focusing the attention on main technical features, applications and calibration procedures, which differ for each kind of sensor. During this thesis, standard calibration procedures have been developed for every Link, in order to guarantee the best results and fit the requested monitoring reliability, repeatability, thermal and long-term stability. This paragraph describes the operative principles and equations that govern the algorithm of *TarCal* software, specifically designed for the calibration purpose. In particular, *TarCal* is able to calculate all the calibration parameters with a series of easy and user-friendly passages, write them into the database, and create plots and tables for the Certificate of Calibration. The following sections are subdivided in accordance with the sensors.

3.2.1. Tilt Link V

Tilt Link V sensor (Fig. 3.6) is equipped with 3D MEMS (accelerometer, magnetometer and thermometer) and designed to monitor differential displacements along a vertical borehole, with an evaluation of settlements occurred. The calculation principle is indirect and the results are obtained using the tilt recorded by the accelerometer together with the direction provided by the magnetometer. Tilt Link V is not able to record rigid translations, like any other gravity based sensor.
In this thesis two different MEMS sensors are described. The first one (MEMS 1.0) has a resolution of12 bit, while the second (MEMS 2.0) has 14 bit. Tab. 3.1 summarizes the main features of both sensors.

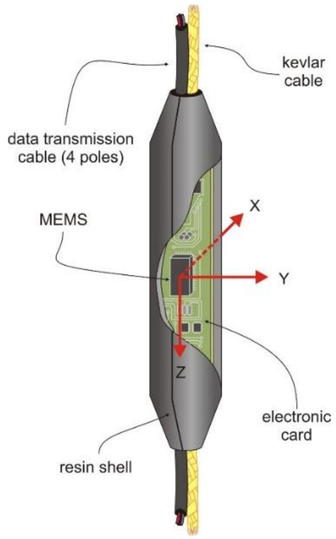

Fig. 3.6: Tilt Link V sensor, equipped with 3D MEMS

Tab. 3.1: Main features of MEMS 1.0 and MEMS 2.0

	MEMS 1.0	MEMS 2.0
Linear acceleration measurement range	±2 g	±2 g
Linear acceleration sensitivity	1 mg/ADC	0.244 mg/ADC
Linear acceleration sensitivity change vs. temperature	±0.01 %/°C	±0.008 %/°C
Zero-g level offset accuracy	±60 mg	±20 mg
Zero-g level change versus temperature	±0.5 mg/°C	±0.15 mg/°C
Acceleration noise density	220 μg/$\sqrt{Hz}$	126 μg/$\sqrt{Hz}$
Magnetic field measurement range	±1.3 G	±12 G
Magnetic gain	1100 ADC/G for X and Y axes 980 ADC/G for Z axis	1000 ADC/G for X, Y and Z axes
Magnetic resolution	2 mG	1 mG
Temperature sensor change vs. temperature	0.125 °C/ADC	0.96 °C/ADC
Operative temperature range	- 40 ÷ +85 °C	- 40 ÷ +85 °C

The calibration procedure reconstructs a matrix of 15 parameters for each node, as described below. The parameters are respectively:

- g_{x_j}: acceleration gain of node *j* *x* instrumental axis;
- g_{xT_j}: gain of the accelerometer thermal correction along the *x*-axis of node *j*;
- o_{xT_j}: thermal offset along the *x*-axis of node *j*;
- g_{y_j}: acceleration gain of node *j* *y* instrumental axis;
- g_{yT_j}: gain of the accelerometer thermal correction along the *y*-axis of node *j*;
- o_{yT_j}: thermal offset along the *y*-axis of node *j*;
- g_{z_j}: acceleration gain of node *j* *z* instrumental axis;
- g_{zT_j}: gain of the accelerometer thermal correction along the *z*-axis of node *j*;

- o_{zT_j}: thermal offset along the *z*-axis of node *j*;
- g_{M_j}: magnetic field gain of node *j* *x*, *y* and *z* instrumental axes;
- o_{Mx_j}: magnetic offset of node *j* *x* instrumental axis;
- o_{My_j}: magnetic offset of node *j* *y* instrumental axis;
- o_{Mz_j}: magnetic offset of node *j* *z* instrumental axis;
- m_j: temperature gain of node *j*;
- q_j: temperature offset of node *j*.

Accelerometers

The accelerometers of Tilt Link V (MEMS based) sensor are calibrated inside a thermal chamber, controlled through a PLC processor. The Array lies inside a dodecahedron (Fig. 3.7) specifically designed to host 70 nodes. The PLC reads each link at 24 different positions for 10 temperatures. Thanks to the fact that MEMS is 3D, it is possible to estimate the calibration parameters using a linear regression. Gravity acceleration is a known variable and the norm of the three components of instrumental axes has to provide that specific value. It is possible to estimate the first 6 calibration parameters $g_{x_{j,t}}$, $i_{x_{j,t}}$, $g_{y_{j,t}}$, $i_{y_{j,t}}$, $g_{z_{j,t}}$, $i_{z_{j,t}}$ by searching the minimum value of $\varepsilon_{j,t}$, as in Equation [3.1].

$$\varepsilon_{j,t} = \sum_{a=1}^{24}\left[G_v - \sqrt{\left(g_{x_{j,t}}a'_{x_{j,a}} + i_{x_{j,t}}\right)^2 + \left(g_{y_{j,t}}a'_{y_{j,a}} + i_{y_{j,t}}\right)^2 + \left(g_{z_{j,t}}a'_{z_{j,a}} + i_{z_{j,t}}\right)^2}\right] \quad [\ 3.1\ ]$$

Where:

- G_v is the gravity acceleration vector (known variable), expressed in g (1 g = 9.80665 m/s^2);
- $g_{x_{j,t}}$ is the acceleration gain of node *j* *x* axis at temperature *t*;
- $a'_{x_{j,a}}$ is the electrical value (ADC points) of gravity acceleration along instrumental axis *x* for node *j* recorded during the reading *a*;
- i_{x_j} is the intercept gain of instrumental *x* axes for node *j* at temperature *t*;
- $\varepsilon_{j,t}$ is the sum of residuals for node *j* at temperature *t*. This value has to be minimized using the linear regression, changing the six calibration parameters.

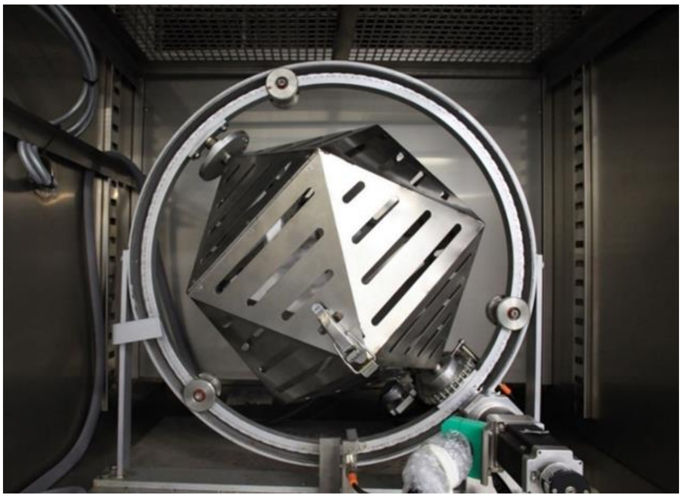

Fig. 3.7: Dodecahedron specifically designed for the calibration of 3D MEMS accelerometers

Once obtained the six parameters at each temperature *t*, gain values of node *j* (g_{x_j}, g_{y_j}, g_{z_j}) are obtained through the following set of Equations.

The first step (Equation [3.2]) identifies the maximum offset $g_{x_{j,t_M}}$ of the acceleration gain dataset for each instrumental axis. This value is removed from the data set.

$$g_{x_{j,t_M}} = max \begin{bmatrix} g_{x_{j,t_1}} - \frac{\sum_{i=1}^{10} g_{x_{j,t_i}}}{10} \\ \vdots \\ g_{x_{j,t_{10}}} - \frac{\sum_{i=1}^{10} g_{x_{j,t_i}}}{10} \end{bmatrix} \quad [\ 3.2\ ]$$

Where:

- $g_{x_{j,t_M}}$ is the maximum offset of the acceleration gain dataset made of ten temperatures, related to node *j x* instrumental axis;
- $g_{x_{j,t_i}}$ is the acceleration gain of node *j x* instrumental axis at temperature t_i.

The second step applies the Equation [3.2] to the remaining dataset, removing the secondary maximum.
At this point, it is possible to apply the Equation [3.3] to the matrix of eight gain parameters for that specific instrumental axis and node. The result is the acceleration gain parameter for one of the three instrumental axes of node *j*.

$$g_{x_j} = \frac{\left(\sum_{i=1}^{8} g_{x_{j,t_i}}\right)}{8} \quad [\ 3.3\ ]$$

Where:

- $g_{x_{j,t_i}}$ is the acceleration gain of node *j x* instrumental axes for at temperature t_i;
- g_{x_j} is the acceleration gain of *x* instrumental axes for node *j*.

The thermal correction of accelerometers is obtained applying three different linear regressions to the datasets represented respectively by $i_{x_{j,t}}$, $i_{y_{j,t}}$ and $i_{z_{j,t}}$ parameters, considered as *y* variables, and known temperatures, as *x* variables. g_{xT_j} and o_{xT_j} represent respectively the angular coefficient and the intercept of the regression.
The conversion from raw data to physical units, together with the thermal correction, is represented by the Equation [3.4].

$$a_{x_j} = g_{x_j} a'_{x_j} + g_{xT_j} T'_j + o_{xT_j} \quad [\ 3.4\ ]$$

Where:

- a_{x_j} is the value of gravity acceleration expressed in physical units (referred to acceleration vector *g*), on the *x*-axis (referred to the instrumental reference system) of node *j*;
- g_{x_j} is the acceleration gain of instrumental axis *x* for node *j*;
- a'_{x_j} is the raw value of gravity acceleration, expressed in electrical units, on the *x*-axis (referred to the instrumental reference system) of node *j*;
- g_{xT_j} is the gain of the thermal correction along the *x*-axis of node *j*;
- T'_j is the raw value of temperature, expressed in electrical units, of node *j*;
- o_{xT_j} is the thermal offset along the *x*-axis of node *j*.

The final dataset of accelerometer calibration parameters is represented by the following 9 values: g_{x_j}, g_{xT_j}, o_{xT_j}, g_{y_j}, g_{yT_j}, o_{yT_j}, g_{z_j}, g_{zT_j}, o_{zT_j}.
The described procedure is not valid to estimate the absolute position of sensors in the space and it is optimized for differential values. This mean that the physical entity does not exactly represent the position of the node, but its changing along time is perfectly identified.
As an example, if we consider the *z* axis of a vertical node, the acceleration should be 1 g. The value returned

by the calibrated sensor could be 0.98 g. If the accelerometer rotates of 0.15 g, the new value returned is 0.83 g (instead of 0.85 g). The difference between the two instrumental records (the differential rotation) is 0.15 g in both cases. The application of the sensors does not require the establishment of an absolute position in the space, while the goal of the monitoring is the definition of displacements starting from a reference reading.

Magnetometers
The calibration of magnetometers is based on the same principles of accelerometers. The resultant vector of magnetic field in a specific area is known and provided by online services, like for example the website of NOAA (National Oceanic and Atmospheric Administration). The gain of the linear correlation is provided (and verified) by the producer, while it is necessary to estimate the offset. To do so, it is important to find a free zone where there are not external disturbing electromagnetic sources. Then, it is possible to estimate the offset applying 24 distinct positions and collecting magnetic data for each of them. The linear regression (Eq. [3.5]) permits to estimate o_{Mx_j}, o_{My_j} and o_{Mz_j} by minimizing ε_j.

$$\varepsilon_j = \sum_{a=1}^{24}\left[M_v - \sqrt{\left[g_{M_j}\left(m'_{x_{j,a}} - o_{Mx_j}\right)\right]^2 + \left[g_{M_j}\left(m'_{y_{j,a}} - o_{My_j}\right)\right]^2 + \left[g_{M_j}\left(m'_{z_{j,a}} - o_{Mz_j}\right)\right]^2}\right] \qquad [\ 3.5\ ]$$

Where:

- M_v is the earth magnetic field (known variable);
- g_{M_j} is the gain of magnetic field (constant for the three axes);
- $m'_{x_{j,a}}$ is the electrical value (ADC points) of magnetic field along node *j* *x* instrumental axis recorded during reading a;
- o_{Mx_j} is the magnetic offset of node *j* *x* instrumental axis;
- ε_j is the sum of node *j* residuals. This value has to be minimized using the linear regression, changing the three calibration parameters.

The conversion from raw data to physical units is expressed through the following equation:

$$m_{x_j} = g_{M_j} m'_{x_j} + o_{Mx_j} \qquad [\ 3.6\ ]$$

Where:

- m_{x_j} is the value of magnetic field expressed in physical units, on the *x*-axis (referred to the instrumental reference system) of node *j*;
- g_{M_j} is the gain of magnetic field (constant for the three axis);
- m'_{x_j} is the raw value of magnetic field, expressed in electrical units, on the *x*-axis (referred to the instrumental reference system) of node *j*;
- o_{Mx_j} is the magnetic offset of *x* instrumental axes for node *j*.

Thermometers
The thermometers are calibrated inside the thermal chamber together with the accelerometers. It is possible to estimate a gain and an offset to convert the raw data into physical units, reading each sensor 24 times for each step and repeating the operation for a total of 10 temperatures. The first step wants to obtain a reliable electrical value for temperature. This is calculated as the mean of the 24 recorded temperatures (this number is related to the estimation of accelerometer coefficients) as in Equation [3.7].

$$T'_j = \frac{\sum_{i=1}^{24} T'_{i,j}}{24} \qquad [\ 3.7\ ]$$

Where:

- $T'_{i,j}$ is the raw temperature value of node *j* recorded at position *i*, expressed in electrical units;

- T'_j is the raw temperature value of node j, expressed in electrical units.

The calibration parameters for each node are the gain m_j and the offset q_j, as Eq. [3.8].

$$T_j = m_j \, T'_j + q_j \qquad [\ 3.8\ ]$$

Where:

- T_j is the value of node j temperature, expressed in Celsius degrees;
- T'_j is the raw value of node j temperature, expressed in electrical units;
- m_j is the gain of node j temperature;
- q_j is the offset of node j temperature.

3.2.2. Tilt Link HR 3D V

Tilt Link HR 3D V sensor (Fig. 3.8) is equipped with 3D MEMS (accelerometer, magnetometer and thermometer) and 2D electrolytic cell. It is designed to monitor a wide range (starting from hundredths of millimetres) of differential displacements along a vertical borehole, with an evaluation of settlements occurred. The calculation principle is indirect and results are obtained using the tilt provided by the accelerometer of MEMS or the information of electro-level and the direction of movement, recorded by the magnetometer. Like Tilt Link V, Tilt Link HR 3D V is not able to record rigid translations. Tab. 3.2 summarizes the main characteristics of electrolytic cell.

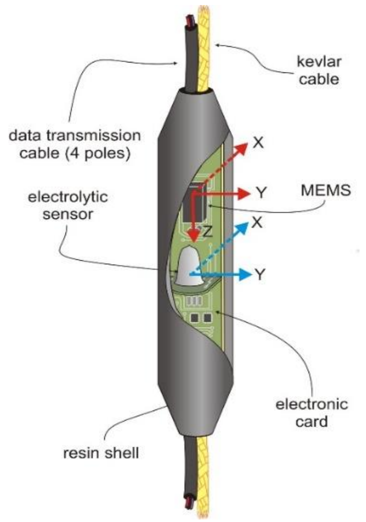

Fig. 3.8: Tilt Link HR 3D V sensor, equipped with 3D MEMS and 2D electrolytic cell

The calibration procedure reconstruct a matrix of 19 parameters for each node, as described below. The parameters are respectively:

- g_{x_j}: acceleration gain of node j x instrumental axis - MEMS;
- g_{xT_j}: gain of the accelerometer thermal correction along the x-axis of node j - MEMS;
- o_{xT_j}: thermal offset along the x-axis of node j - MEMS;
- g_{y_j}: acceleration gain of node j y instrumental axis - MEMS;
- g_{yT_j}: gain of the accelerometer thermal correction along the y-axis of node j - MEMS;
- o_{yT_j}: thermal offset along the y-axis of node j - MEMS;
- g_{z_j}: acceleration gain of node j z instrumental axis - MEMS;
- g_{zT_j}: gain of the accelerometer thermal correction along the z-axis of node j - MEMS;
- o_{zT_j}: thermal offset along the z-axis of node j - MEMS;
- g_{M_j}: magnetic field gain of node j x, y and z instrumental axes - MEMS;

- o_{Mx_j}: magnetic offset of node *j* *x* instrumental axis - MEMS;
- o_{My_j}: magnetic offset of node *j* *y* instrumental axis - MEMS;
- o_{Mz_j}: magnetic offset of node *j* *z* instrumental axis - MEMS;
- m_j: temperature gain of node *j* - MEMS;
- q_j: temperature offset of node *j* - MEMS;
- gE_{x_j}: gain of node *j* *x* instrumental axis - Electrolytic Cell;
- gE_{y_j}: gain of node *j* *y* instrumental axis - Electrolytic Cell;
- mE_j: temperature gain of node *j* - Electrolytic Cell;
- qE_j: temperature offset of node *j* - Electrolytic Cell.

Tab. 3.2: Main technical features of the 2D electrolytic cell

	Electrolytic cell
Range	±25°
Resolution	< 0.003°
Repeatability	±0.1°
Temperature coefficient Null Scale	 20 arc seconds/°C 0.1 %/°C
Operative temperature range	- 40 ÷ +85 °C

The calibration procedure of MEMS (Accelerometers, Magnetometers and Thermometers) is exactly the same described for Tilt Link V.

Gain of Electrolytic Cell

gE_{x_j} and gE_{y_j} gain parameters of electrolytic cell are evaluated using a specifically designed calibration machine. The tool is composed by a rigid bar that can rotate around a pin. Links are vertically fixed to this bar. A calibrated level gives information about the absolute tilt angle with respect to the horizontal. Each node is read at 9 different positions, starting from 20° tilt degrees on the left to 20° tilt degrees on the right, with steps of 5°. Due to the fact that the electrolytic cell is extremely sensible to vibrations and requires a couple of seconds to stabilize itself, each position is sampled three times and then the meaning value (Eq. [3.9]) is considered for the linear regression. This shrewdness permits to recognize disturbs related to external factors, like for example the walk of an operator inside the room or the opening of a door during the measure.

$$\alpha'_{x_j}{}^{p} = \frac{\sum_{i=1}^{3} \alpha'_{x_{i,j}}{}^{p}}{3} \qquad [\ 3.9\ ]$$

Where:

- $\alpha'_{x_{i,j}}{}^{p}$ is the reading *i* of the tilt angle, expressed in electrical units (ADC points), along *x* instrumental axis, for the position *p* of node *j*;
- $\alpha'_{x_j}{}^{p}$ is the mean value of the tilt angle, expressed in electrical units (ADC points), along *x* instrumental axis, for the position *p* of node *j*.

The gE_{x_j} and gE_{y_j} gain parameters are obtained through a linear regression applied to the data set represented by $\alpha'_{x_j}{}^{p}$ (angles expressed as electrical units) as *x*, and $\alpha_{x_j}{}^{p}$ (angles expressed as physical units) as *y*. The formulation used by the software is the Eq. [3.10].

$$\alpha_{x_j} = gE_{x_j}\,\alpha'_{x_j} \qquad [\ 3.10\ ]$$

Where:

- α'_{x_j} is the the tilt angle, as electrical units (ADC points), along *x* instrumental axis of node *j*;

- α_{x_j} is the the tilt angle, expressed in physical units (Degrees), along *x* instrumental axis of node j;
- gE_{x_j} is the gain of *x* instrumental axis of node j.

Thermometers of Electrolytic Cell

The thermometers of Electrolytic Cell are calibrated inside the thermal chamber together with the thermometers of MEMS, exploiting the same principle. The gain and the offset are evaluated through a linear regression. Each sensor is read 24 times for each temperature, for a total of 10 temperatures. After evaluating a reliable electrical value for temperature, calculated as the mean of recorded temperatures (Eq. [3.7]), the linear regression is applied to the data set represented by temperatures T'_j (expressed as electrical values) as x variable, and temperatures T_j (physical units), expressed as y variable.

The calibration parameters for each node are the gain mE_j and the offset qE_j, as in Eq. [3.11].

$$T_j = mE_j\, T'_j + qE_j \qquad [\ 3.11\ ]$$

Where:

- T_j is the temperature value of node j, expressed in Celsius degrees;
- T'_j is the raw temperature value of node j, expressed in electrical units;
- mE_j is the temperature gain of node j;
- qE_j is the temperature offset of node j.

3.2.3. Piezo Link

Piezo Link (Fig. 3.9) is an absolute pressure sensor, designed to monitor the pore pressure and the water level, if coupled with the information provided by Baro Link.

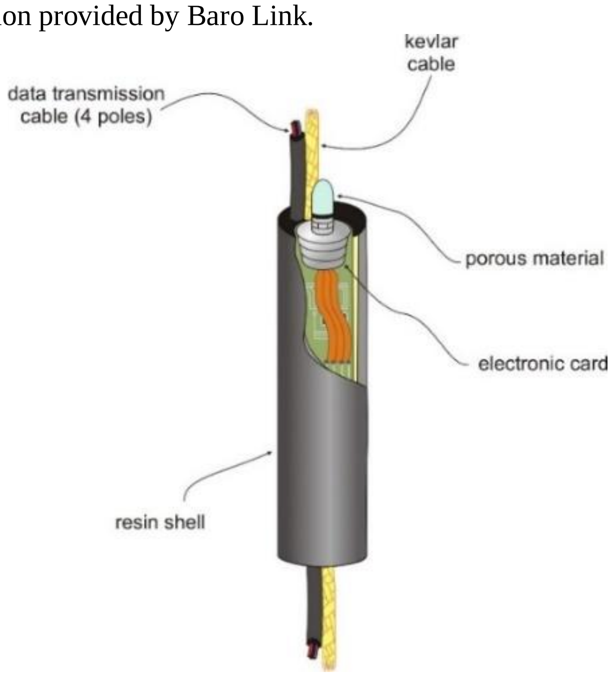

Fig. 3.9: Piezo Link sensor

The sensor is equipped also with a thermometer, installed in the electronic board. In this thesis, two versions of the product are discussed. The first one (Piezo Link 1.0) has a maximum operative range of 3.5 bar, while the second one (Piezo Link 2.0) reaches 10 bar. Other characteristics are reported in Tab. 3.3.

The calibration procedure reconstruct a matrix of 4 parameters for each node, as described below. The parameters are respectively:

- gP_j: pore pressure gain of node j;
- oP_j: pore pressure offset of node j;

- mP_j: temperature gain of node j;
- qP_j: temperature offset of node j.

Tab. 3.3: Data sheet features of Piezo Link 1.0 and Piezo Link 2.0

	Piezometer 1.0	Piezometer 2.0
Measure range	0 ÷ 3.5 bar	0 ÷ 10 bar
Proof pressure	7 bar	15 bar
Zero offset	±1 mV (Typ.) ±2 mV (Max.)	±1 mV (Typ.) ±2 mV (Max.)
Non-linearity	±0.1 % FS (Typ.) ±0.2 % FS (Max.)	±0.2 % FS (Typ.) ±0.25 % FS (Max.)
Repeatability	±0.01 % FS (Typ.) ±0.075 % FS (Max.)	±0.05 % FS (Typ.) ±0.075 % FS (Max.)
Hysteresis	±0.01 % FS (Typ.) ±0.075 % FS (Max.)	±0.05 % FS (Typ.) ±0.075 % FS (Max.)
Long term stability	±0.1 % FS/year	±0.1 % FS/year
Thermal effects		
Offset	±0.3 % FS (Typ.) ±0.75 % FS (Max.)	±0.75 % FS (Typ.) ±1.00 % FS (Max.)
Span	±0.5 % FS (Typ.) ±0.75 % FS (Max.)	±0.75 % FS (Typ.) ±1.00 % FS (Max.)
Weight	290 g	50 g
Operative temperature range	- 40 ÷ +85 °C	- 40 ÷ +125 °C

Pore pressure gain and offset

The calibration procedure requires to place the sensor inside a specifically designed autoclave (Fig. 3.10) with controlled pressure. It is possible to obtain gP_j and oP_j parameters with a linear regression by reading the pressure at different stages, then adding the contribution of atmospheric pressure. The conversion into physical units is expressed in Eq. [3.12].

$$P_{mBar_j} = gP_j \, P'_{ADC_j} + oP_j \qquad [\ 3.12\ ]$$

Where:

- P'_{ADC_j} is the pore pressure of node j, expressed in electrical units (ADC points);
- P_{mBar_j} is the pore pressure of node j, expressed in physical units (mbar);
- gP_j: pore pressure gain of node j;
- oP_j: pore pressure offset of node j.

Fig. 3.10: Autoclave used for the calibration of piezometers

Thermometer gain and offset

The thermometer of Piezo Link is calibrated inside the thermal chamber together with the thermometers of MEMS, exploiting the same principle. Gain and offset are evaluated through a linear regression. Each sensor is read 24 times for each temperature, for a total of 10 temperatures. After evaluating a reliable electrical value, calculated as the mean of recorded temperatures (Eq. [3.7]), the linear regression is applied to the data set represented by temperatures T'_j (expressed as electrical values), as x variable, and temperatures T_j (physical units), expressed as y variable.

The calibration parameters for each node are the gain mP_j and the offset qP_j, as in [3.13].

$$T_j = mP_j \, T'_j + qP_j \tag{3.13}$$

Where:

- T_j is the temperature value of node j, expressed in Celsius degrees;
- T'_j is the raw temperature value of node j, expressed in electrical units;
- mP_j is the temperature gain of node j;
- qP_j is the temperature offset of node j.

3.2.4. Baro Link

Baro Link (Fig. 3.11) is an absolute pressure sensor, designed to monitor the atmospheric pressure and compensate the absolute pore pressure recorded by Piezo Link, in order to define the water level. The sensor has a thermometer too, installed on the electronic board. Tab. 3.4 summarizes the main characteristics of the Barometer.

Fig. 3.11: Baro Link

Tab. 3.4: Main features of Baro Link sensor

	Baro Link
Measure range	0.6 ÷ 1.1 bar
Accuracy	±1.5 % FS
Proof pressure	2 bar
Burst pressure	3 bar
Response delay	0.5 ms
Weight	33 g
Operative temperature range	- 20 ÷ +85 °C

The calibration procedure reconstruct a matrix of 4 parameters for each node, as described below. The parameters are respectively:

- gB_j: atmospheric pressure gain of node j;
- oB_j: atmospheric pressure offset of node j;
- mB_j: temperature gain of node j;
- qB_j: temperature offset of node j.

Atmospheric pressure gain and offset

The calibration procedure requires to inflate a known temperature inside the sensor with a pump and a closed system. Repeating the operation at least 5 times, gB_j and oB_j parameters are obtained with a linear regression. The conversion into physical units is expressed by Eq. [3.14].

$$AP_{mBar_j} = gB_j \, AP'_{ADC_j} + oB_j \qquad [\ 3.14\ ]$$

Where:

- AP'_{ADC_j} is the atmospheric pressure of node j, expressed in electrical units (ADC points);
- AP_{mBar_j} is the atmospheric pressure of node j, expressed in physical units (mbar);
- gB_j: atmospheric pressure gain of node j;
- oB_j: atmospheric pressure offset of node j.

Thermometer gain and offset

Baro Link thermometer is calibrated by reading at least 5 different known temperatures, then applying a linear regression to the data set. mB_j and qB_j are the calibration parameters for each node, as in Eq. [3.15].

$$T_j = mB_j \, T'_j + qB_j \qquad [\ 3.15\ ]$$

Where:

- T_j is the temperature value of node j, expressed in Celsius degrees;
- T'_j is the raw temperature value of node j, expressed in electrical units;
- mB_j is the temperature gain of node j;
- qB_j is the temperature offset of node j.

3.2.5. Therm Link HR

Therm Link HR (Fig. 3.12) is a high-resolution thermometer designed to monitor the variation of temperature with high precision (±0.0078°C) and repeatability. Tab. 3.5 reports the technical specification of the sensor.

Fig. 3.12: Therm Link HR

The calibration procedure reconstructs a matrix of 2 parameters for each node:

- mT_j: temperature gain of node j;
- qT_j: temperature offset of node j.

Due to high precision of sensors, they are calibrated using a known temperature thermal bath inside an isolated chamber. Three values are collected for each temperature and only the mean is considered for the following linear regression, applied to the dataset represented by temperatures T'_j (expressed as electrical values) as *x* variable, and temperatures T_j (physical units), expressed as *y* variable.

The calibration parameters for each node are the gain mT_j and the offset qT_j, as in Eq. [3.16].

$$T_j = mT_j \, T'_j + qT_j \qquad [\ 3.16\ ]$$

Where:

- T_j is the temperature value of node j, expressed in Celsius degrees;

- T'_j is the raw temperature value of node j, expressed in electrical units;
- mT_j is the temperature gain of node j;
- qT_j is the temperature offset of node j.

Tab. 3.5: Main features of Therm Link HR

	Therm Link HR
Measure range	-55 ÷ +150 °C
Accuracy	± 0.4 °C
Resolution	0.0078 °C
Hysteresis	± 0.002 °C
Repeatability	± 0.015 °C
Weight	200 g

3.2.6. Tilt Link H

Tilt Link H sensor (Fig. 3.13) is equipped with 3D MEMS (accelerometer and thermometer) and designed to monitor differential displacements along a horizontal string, with an evaluation of settlements occurred. The calculation principle is indirect and the results are obtained using the variation of the gravity acceleration along time.

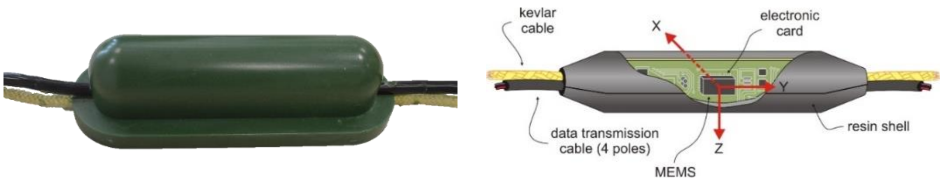

Fig. 3.13: Tilt Link H sensor, equipped with 3D MEMS

The calibration procedure is equal with respect to Tilt Link V sensor, excluding the magnetometer. The result is a matrix of 11 parameters for each node, as described below. The parameters are respectively:

- g_{x_j}: x instrumental axis acceleration gain of node j;
- g_{xT_j}: gain of the accelerometer thermal correction along the x-axis of node j;
- o_{xT_j}: thermal offset along the x-axis of node j;
- g_{y_j}: y instrumental axis acceleration gain of node j;
- g_{yT_j}: gain of the accelerometer thermal correction along the y-axis of node j;
- o_{yT_j}: thermal offset along the y-axis of node j;
- g_{z_j}: z instrumental axis acceleration gain of node j;
- g_{zT_j}: gain of the accelerometer thermal correction along the z-axis of node j;
- o_{zT_j}: thermal offset along the z-axis of node j;
- m_j: temperature gain of node j;
- q_j: temperature offset of node j.

3.2.7. Tilt Link HR 3D H

Tilt Link HR 3D H (Fig. 3.14) represents the horizontal version of Tilt Link HR 3D V, designed to monitor settlements with MEMS and electrolytic cell sensors.

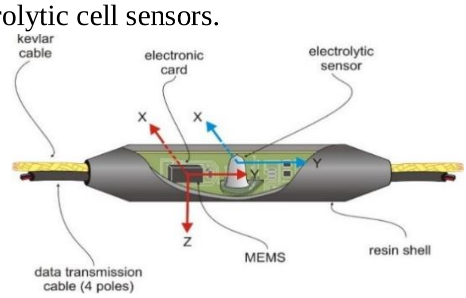

Fig. 3.14: Tilt Link HR 3D H sensor, equipped with 3D MEMS and 2D electrolytic cell

The calibration procedure reconstruct a matrix of 15 parameters for each node, as described below. The parameters are respectively:

- g_{x_j}: *x* instrumental axis acceleration gain of node *j* - MEMS;
- g_{xT_j}: gain of the accelerometer thermal correction along the *x*-axis of node *j* - MEMS;
- o_{xT_j}: thermal offset along the *x*-axis of node *j* - MEMS;
- g_{y_j}: *y* instrumental axis acceleration gain of node *j* - MEMS;
- g_{yT_j}: gain of the accelerometer thermal correction along the *y*-axis of node *j* - MEMS;
- o_{yT_j}: thermal offset along the *y*-axis of node *j* - MEMS;
- g_{z_j}: *z* instrumental axis acceleration gain of node *j* - MEMS;
- g_{zT_j}: gain of the accelerometer thermal correction along the *z*-axis of node *j* - MEMS;
- o_{zT_j}: thermal offset along the *z*-axis of node *j* - MEMS;
- m_j: temperature gain of node *j* - MEMS;
- q_j: temperature offset of node *j* - MEMS;
- gE_{x_j}: gain of node *j x* instrumental axis - Electrolytic Cell;
- gE_{y_j}: gain of node *j y* instrumental axis - Electrolytic Cell;
- mE_j: temperature gain of node *j* - Electrolytic Cell;
- qE_j: temperature offset of node *j* - Electrolytic Cell.

The calibration procedure of MEMS (Accelerometers, Magnetometers and Thermometers) is exactly the same described for Tilt Link V.

3.2.8. Tunnel Link

Tunnel Link (Fig. 3.15) is the evolution of Tilt Link V, designed for the monitoring of convergence during construction and exercise phases in underground excavations. Sensor is equipped with 3D MEMS and every node is linked through a fiberglass rod and a connection in order to preserve the alignment. Tunnel Link is not able to record rigid translations, like any other gravity based sensor. Tab. 3.6 summarizes the main technical features of MEMS accelerometer and thermometer.

The calibration procedure is equal with respect to Tilt Link V sensor, excluding the magnetometer and the fact that the calibration took place before the resin injection. The result is a matrix of 11 parameters for each node, as described below:

- g_{x_j}: *x* instrumental axis acceleration gain of node *j*;
- g_{xT_j}: gain of the accelerometer thermal correction along the *x*-axis of node *j*;
- o_{xT_j}: thermal offset along the *x*-axis of node *j*;
- g_{y_j}: *y* instrumental axis acceleration gain of node *j*;
- g_{yT_j}: gain of the accelerometer thermal correction along the *y*-axis of node *j*;
- o_{yT_j}: thermal offset along the *y*-axis of node *j*;
- g_{z_j}: *z* instrumental axis acceleration gain of node *j*;
- g_{zT_j}: gain of the accelerometer thermal correction along the *z*-axis of node *j*;
- o_{zT_j}: thermal offset along the *z*-axis of node *j*;
- m_j: temperature gain of node *j*;
- q_j: temperature offset of node *j*.

Tab. 3.6: Technical features of Tunnel Link sensor

	MEMS 2.0
Linear acceleration measurement range	±2 g
Linear acceleration sensitivity	0.244 mg/ADC
Linear acceleration sensitivity change vs. temperature	±0.008 %/°C
Zero-g level offset accuracy	±20 mg
Zero-g level change versus temperature	±0.15 mg/°C
Acceleration noise density	126 μg/$\sqrt{Hz}$
Magnetic field measurement range	±12 G
Magnetic gain	1000 ADC/G for X, Y and Z axes
Magnetic resolution	1 mG
Temperature sensor change vs. temperature	0.96 °C/ADC
Operative temperature range	- 40 ÷ +85 °C

Fig. 3.15: Tunnel Link sensor installed on site

3.2.9. Radial Link

Radial Link (Fig. 3.16) is the complementary of Tunnel Link, designed to monitor the deformations some meters inside the rock mass during both construction and exercise phases. Sensor is equipped with 3D MEMS and every node is linked through a fiberglass rod and a connection in order to preserve the alignment. Technical features are the same as Tunnel Link.

Fig. 3.16: Rad Array installed together with a Multi-Point Rod Extensometer

The calibration procedure follows the same principles as Tunnel Link, resulting in a matrix of 11 parameters for each node, as described below:

- g_{x_j}: x instrumental axis acceleration gain of node j;
- g_{xT_j}: gain of the accelerometer thermal correction along the x-axis of node j;
- o_{xT_j}: thermal offset along the x-axis of node j;
- g_{y_j}: y instrumental axis acceleration gain of node j;
- g_{yT_j}: gain of the accelerometer thermal correction along the y-axis of node j;
- o_{yT_j}: thermal offset along the y-axis of node j;

- g_{z_j}: *z* instrumental axis acceleration gain of node *j*;
- g_{zT_j}: gain of the accelerometer thermal correction along the *z*-axis of node *j*;
- o_{zT_j}: thermal offset along the *z*-axis of node *j*;
- m_j: temperature gain of node *j*;
- q_j: temperature offset of node *j*.

3.3. Installation procedure

The installation of geotechnical instrumentations is as important as the sensors itself (Segalini et al. 2017). Unappropriated installation procedures cause misleading results, related to many causes, consequently reducing precision and accuracy of the selected tools. For this reason, the study related to this thesis has concentrated part of the work on a new installation method for Vertical Array, evolved starting from the outcomes of the first on-site MUMS installations.

Spaggiari (2015) was the first to study and improve the installation procedure of the first commercialized MUMS system (Fig. 3.17), starting from the laboratory and in situ test results. During her master degree thesis at University of Parma, a standard procedure was defined, based on the following passages.

Fig. 3.17: First installation procedure of MUMS system

I. Execution of the borehole, with a diameter that could range between 110 and 160 mm, and insertion of a temporary casing to sustain the excavation during the installation procedure (a);
II. In situ preparation of the piezometer, using a non-woven fabric full of sand as a filter (b and c) and fixing the porous stone inside a recipient full of water (d);
III. Insertion of MUMS array together with a PVC pipe (e);
IV. Removal of the first 1.5 m portion of the temporary casing and PVC pipe, and cementation of the deeper part of the borehole (f);
V. Progressive removal of the temporary casing (at steps that could vary between 1.5 and 3 m) and insertion of the gravel (g). In order to avoid empty spaces, it is necessary to have gravel with a small diameter. It is necessary to protect the electrical and Kevlar cables at every removal of the temporary

casing, fixing them at the internal portion of the PVC pipe. This operation has to be repeated until the complete filling of the borehole;

VI. Placement of the control unit (h);

VII. Placement of the solar panel (i).

The deeper part of the array, which should be installed in a stable zone, was cemented using a mixture composed by bentonite (15%), cement (10%) and water (75%). The use of gravel with small diameter (less than 4 mm) wanted to remove the behaviour observed during the test installations, where through the first month of monitoring it was possible to observe consistent displacements related to the relative movement of grains. In order to avoid empty spaces, gravel was inserted from the bottom at steps of 1.5 meters, using the temporary PVC pipe.

The described installation procedure represents an improvement in terms of borehole stabilization, adherence to the ground, data stability during the first period. In spite of this, the installation procedure required a very long time (some hours for array with a total length less than 50 m), attention and expertise by the installer. The result was a couple of Arrays damaged during installation procedure, due to inappropriate behaviours of the operators. Moreover, the case study of Baveno highlighted the consequences of an incorrect placement of the filling material. In fact, during the installation procedure the operator badly estimated the required quantity of small size gravel and ignored the presence of cavity in the rock mass. Once removed the external temporary casing, the Array lowered of about 2 meters. For this reason it was necessary to carefully recover it after some hours of hard work (Fig. 3.18) and refill the borehole with gravel.

Fig. 3.18: Recovering of the array after an incorrect installation procedure

After six months, during the first rainy event a consistent displacement has been recorded (Fig. 3.19) and an alarm procedure was activated. After a site inspection (Fig. 3.20), it was clear that the rain washed the filling material from the ground level to a depth of 13 meters and the Array was free to move inside the borehole. Therefore, the lack of traction granted by the Kevlar rope at the top caused the lowering of the instrumentation.

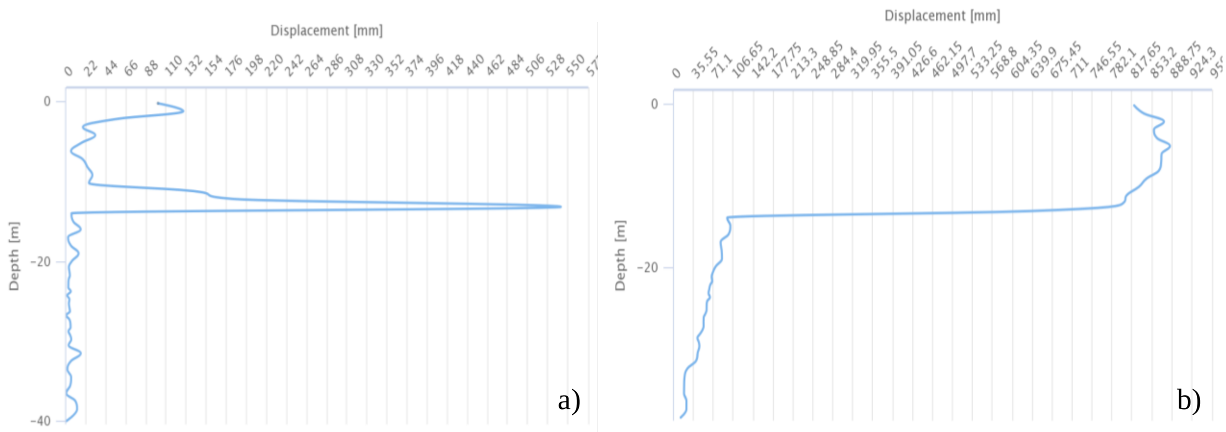

Fig. 3.19: a) Local and b) Cumulative displacements recorded after the first rainy event

Fig. 3.20: Site inspection at Baveno, after the event occurred on December 2017

The case study suggested to investigate a new installation method, able to simplify the whole procedure, reducing time and sources of error, together with the preservation of data quality, ensuring the correct traction of the Kevlar rope.

The new installation method, developed starting from Baveno outcomes, is described below and has been successfully applied to 19 case histories.

Fig. 3.21: Appearance of the chain-anchor connection system

The array (with a diameter per node of 37 mm) is inserted inside a plastic pipe with an internal diameter of 40 mm at the factory. Then, the bottom portion of the aramid fibre rope is fixed at an eyebolt, screwed to a threaded bar. The bar crosses a stopper and terminates with another eyebolt, where the anchor is fixed (Fig. 3.21). The aramid fibre cable is fixed at a spring at the top. This one is connected to a threaded bar exploiting a carabineer. The threaded bar crosses the top stopper and it is used to tension the whole system. The array is then placed on a bobbin and sent to the site.
Once the instrumentation is on site, the operator has to verify the functionality first, through a data collecting test, in order to exclude any damage that may happen during the shipping. Then it is necessary to drop down the vertical inside the borehole (Fig. 3.22a), which has to be larger than 50 mm (external diameter of the plastic pipe). It follows the installation of a temporary support system (Fig. 3.22b) just above the borehole, composed by two steel bars that must be driven inside the soil until they are stable. At this point it is necessary to secure the top of the aramid fibre cable to one of the steel bars in order to prevent the accident fall of MUMS inside

the open borehole. The device used for the injection of cementation mortar could be joined to the outside of the plastic pipe and lowered down together with the instrumentation. If the water level is high enough to prevent the insertion of the system due to its buoyancy, some small holes can be drilled in the lower portion of the plastic pipe, in order to let the water percolate inside. It is possible to calculate the buoyancy thrust according to the borehole characteristics and Vertical Array features.

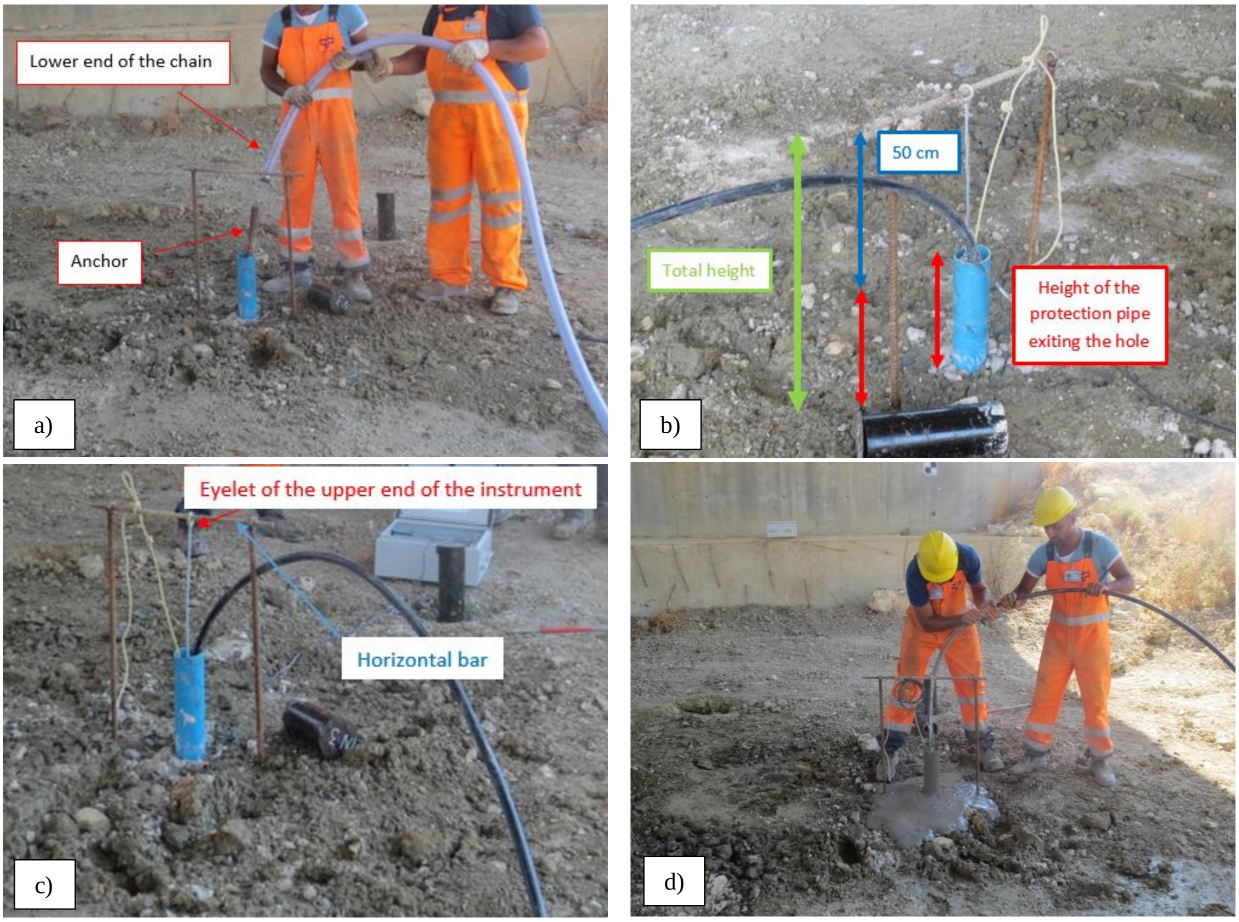

Fig. 3.22: New installation procedure of Vertical Array MUMS system

Once the instrument is properly inserted in the borehole, the upper metal ring of MUMS is run through a third steel bar (Fig. 3.22c) that is, in turn, inserted horizontally into the two buttonholes of the support system. After the correct positioning of the array in its final position, it is appropriate to make a second data collecting test, in order to avoid any malfunction that may occurred during the lowering procedure. If the array is not equipped with pore pressure sensors, it is possible to proceed with the infilling of the interspace between the flexible preservation pipe and the borehole (or the PVC casing when present). The infilling material must be chosen according to the specific installation and aim of the monitoring. Suggested infilling materials are clean coarse sand or small gravel, with a maximum diameter of 3-4 mm. It is possible to use mortar if expected displacements are lower than 3 cm/m. If the application regards geotechnical structures, mortar or concrete should be used. In any case, it is suggested to proceed with the injection of mortar for the infilling of the first 1-2 meters of the borehole at the MUMS fixed end (Fig. 3.22d). This would prevent the lower end of the Vertical Array from moving or being pulled away from its original position, compromising the interpretation of the monitoring results. Above the first 1-2 meters, starting from the bottom of the chain, the infilling can proceed with the selected material.

Once the infilling has been carried out completely, it is necessary to screw the two bolts located on the threaded bar at the upper end of the chain until the plastic cap is reached, in order to block the internal sliding of the sensors with respect to the external pipe (Fig. 3.23). This procedure should be done controlling that the spring located inside the flexible protection pipe is slightly pulled (i.e. the entire Vertical Array is in traction). The tension can be increased by pulling the thread bar by hand while screwing in the two bolts a little more.

Fig. 3.23: Once Vertical Array is placed inside the borehole, it is necessary to screw the bolts along the bar until they reach the plug

The correct final position of the support portal should be adapted by driving its vertical bars into the ground as appropriate. It is suggested to leave the support portal in place for at least two weeks after the installation or until the cement has completed the first phase of hydration and is hard enough to support the MUMS in place. This interval of time is particularly important when the selected material is sand or gravel, in order to assure that the whole borehole has been properly infilled and no voids were left along the borehole. If this happens, any delayed subsidence of the infilling material would cause the Vertical Array to be pulled downward if not supported, modifying its original position. For this reason, where possible, it is suggested to check the stability of the infilling by pouring water from the top of the borehole. At the end of the installation, after the suggested two weeks and the appropriate verification, the supporting portal can be removed and the threaded bar cut to a length that can be fitted inside the inspection well encasing that should be installed around the upper portion of the Vertical Array. The upper end of the aramid fibre rope should be left inside the inspection well, free to move and slip inside the upper plastic cap through the appropriate hole, in case of slope/structure consistent deformation.

If a pore pressure sensor is present, it is prepared at the factory (the first MUMS installation procedure required to prepare the sensor in place). The porous stone is placed on the Piezo Link inside a recipient full of water, in order to avoid air bubbles, and then node is inserted inside the plastic pipe in the required position. Sensor is isolated from the rest of the vertical by injecting a water-resistant resin above and below the Link. The portion of the plastic pipe around the piezometer is drilled and, during the installation procedure, is filled with sand pillows, permitting the water circulation. The procedure to be followed (Fig. 3.24) is similar to that normally used for the installation of electric piezometers, in order to ensure the appropriate insulation of the water horizons (where there is more than one aquifer level).

With regard to the infilling phase of the instrument, it is recommended to proceed as follows (for each piezometer along the array):

I. Infilling of the selected material from the bottom of the hole up to z + 1.50 cm, where z indicates the depth of the piezometer;

II. Creation of a lower cap with bentonite in granules with an approximate height of 1 m;

III. Infilling of sand in the borehole surrounding the piezometer sensor for a length of approximately 1 m (starting from z + 0.5 m up to z - 0.5 m);

IV. Creation of an upper cap with bentonite in granules with an approximate height of 1 m;

V. Infilling with the material of choice until completion of the borehole.

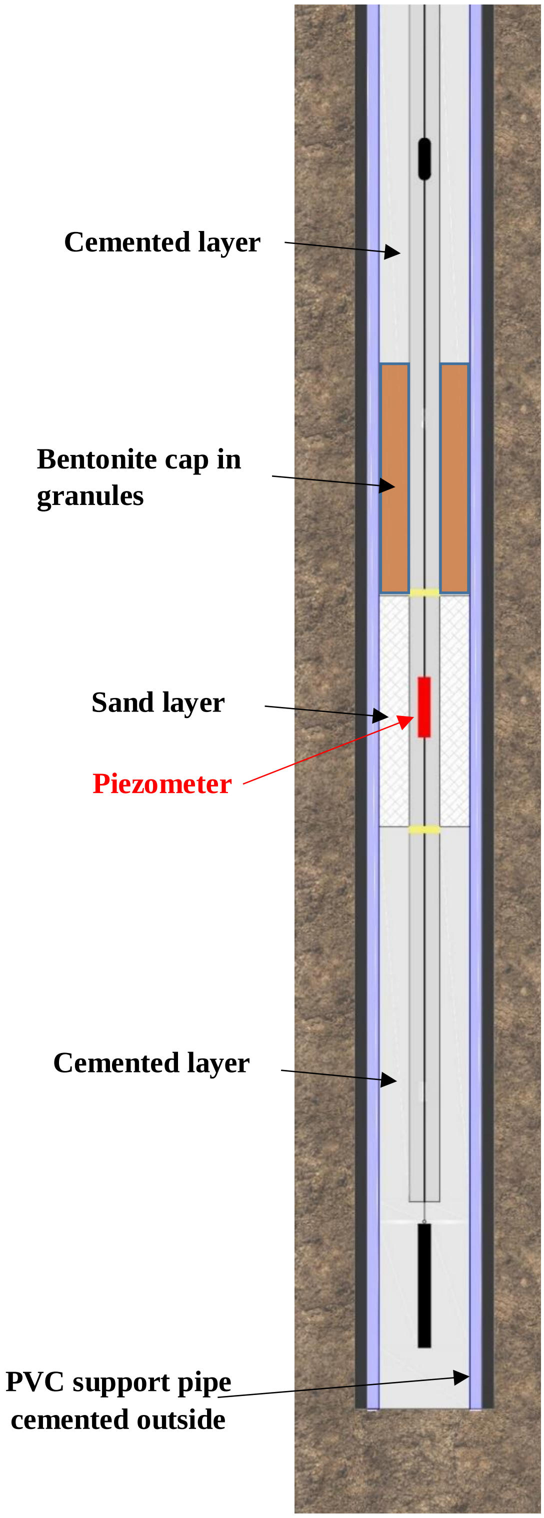

Fig. 3.24: Installation on site of pore pressure sensor

The infilling procedure should be followed also during the installation of the eventual PVC pipe, when it is inserted in the borehole in order to preserve it and facilitate the MUMS installation. In this case, the sand pillow and the lower and upper bentonite caps must be created around the PVC pipe as well.

The described system permits a very easy and rapid installation (an array of 50 m requires a maximum of 10 minutes to be operative), improving adherence to the ground. When a displacement occurs, the instrumentation follows the movement and the spring extends itself up to 50 cm, increasing the duration of the array over time and the major displacement which is possible to identify.

Data recorded (Fig. 3.26) after the installation shows a behaviour well known in literature and reported in numerous monitoring recommendations books, regarding the definition of the zero measurement for surveys with traditional inclinometer. In particular, it should be considered that the first period of monitoring is often taken as a reference for the subsequent measurements and it is commonly carried out with increased sample period, in order to provide a reliable datum of instrumental noise. Fig. 3.25 shows the theoretical expected behaviour of displacement recorded using a manual probe or an IPI during the first days after the installation (X axis represents the time, while Y reports the displacement). In particular, after the installation period (4) and the first measure (1), a stabilization period (5) is often observed, with movement that reduces along time. When stabilization occurs, it is possible to define the zero reading (2) followed by the baseline measurement interval (6), which should be far from expected displacements or construction phases. For this reason, it is very important to install the monitoring device taking into account the amount of time that is required for the installation and stabilization periods. When the landslide activates, it is possible to define the reference measurement (3), followed by the monitoring period (7) of interest (rainy season or construction phase).

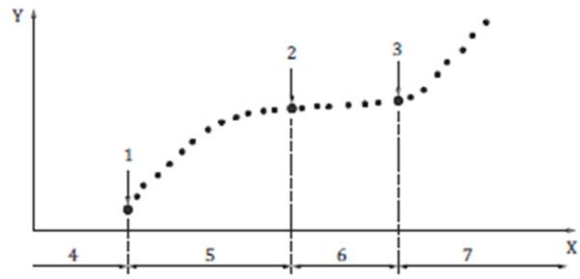

Fig. 3.25: Definition of distinct measuring points during a geotechnical monitoring project in the period up to and including the construction phase (source: ISO 18674-1:2015)

The example reported in Fig. 3.26, taken from three different MUMS case histories, highlights the stabilization period (5) in red, where it has been recorded 1 cm of movement during 5 days (a), 2 mm during 1 day (b) or 4 mm during 1 month (c). The stabilization is then followed by the zero reading (in blue) to be considered (2) and the period (green) of the baseline measures (6), where it is possible to define the repeatability of the sensor installed and the instrumental noise. In the case c) it is possible to identify also the reference measurement (3) in yellow and the monitoring period of interest (7), in light blue. As observed, the stabilization period and amount of displacements differ depending on the installation, site characteristics, surrounding and infilling materials. The identification of reference measurement could be related to the expertise of the technician or to a mathematical relationship that compares the local slope of the tangent line (derivative of the function at the marked point) with the slope of the baseline measure.

The Vertical Array installed with the new method perfectly reproduces the behaviour represented in Fig. 3.26, giving all the necessaries information to the monitoring responsible, as the definition of the zero and reference readings and the baseline measure values.

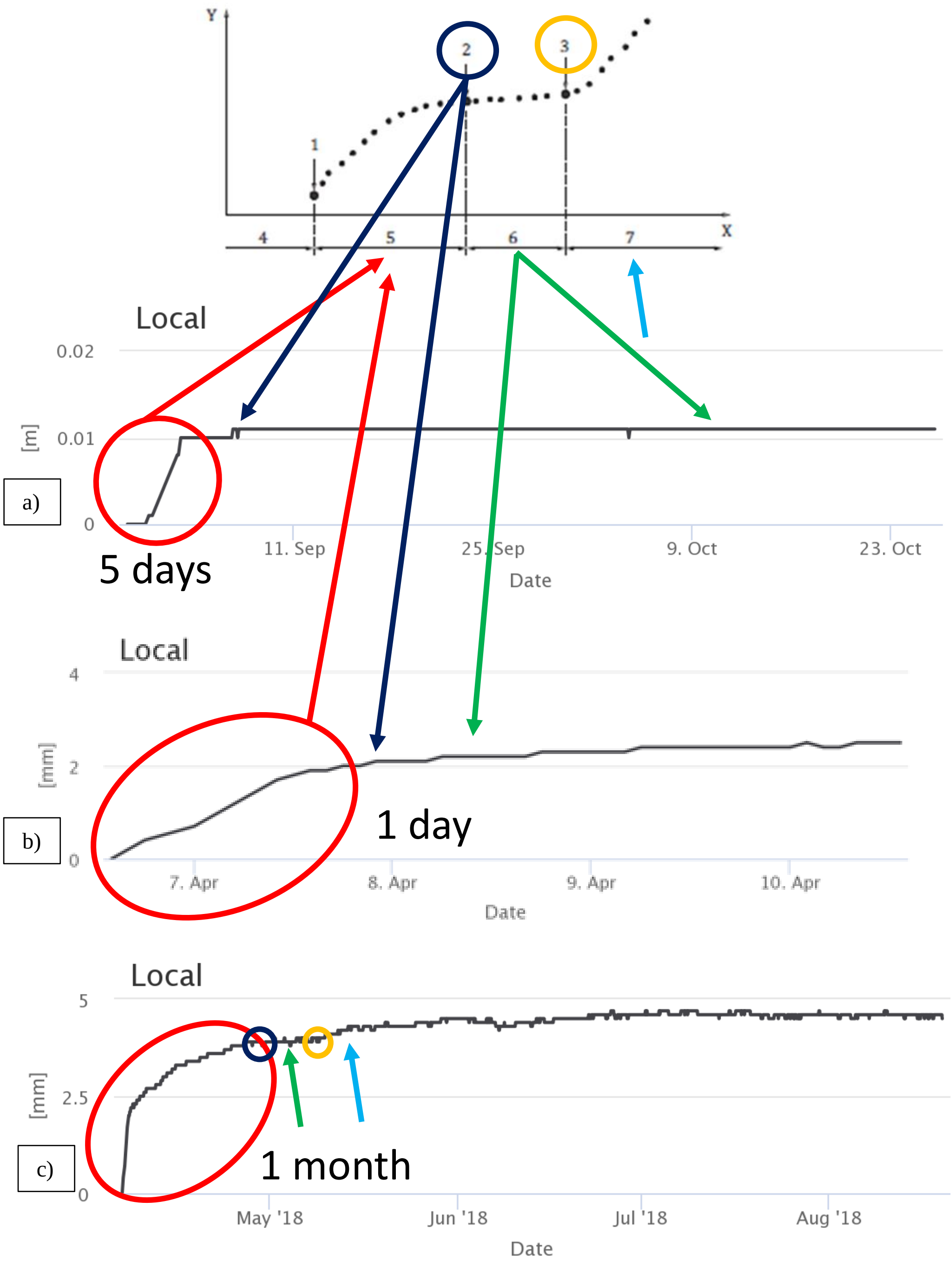

Fig. 3.26: Definition of distinct measuring points during a geotechnical monitoring project in the period up to and including the construction phase (source: ISO 18674-1:2015) and a), b) and c) MUMS data from three different on-site applications

3.4. Calculation principles

Calculation principle of traditional inclinometer is based on the rigid connection of the lower part of the casing to a stable area. Generally, one month after the placing of the casing, the vertical is sampled for the first time, which constitutes the “zero reading”, used as the reference measurement for all the subsequent surveys. The operator lowers the test probe, verifying the accessibility of the whole borehole. Then, he inserts the probe at the end of the borehole starting from the A groove, retrieving then the instrument at about 50 or 100 cm intervals (the reference targets are usually placed on the signal cable and allow an error of about 1÷5 cm), waiting for temperature stabilization and reading the sensor. Once reached the ground, the operator firstly repeats this operation by rotating the probe of 180° (applying the so-called “hardware filter”), then he lowers the test probe inside B groove, placed at 90° with respect to A, and samples the vertical (0° and 180°) for a total of 4 readings along the same borehole.

MUMS system calculation principle is based on the combination of information provided by the accelerometers and the magnetometers. The 3D accelerometers reconstruct the position of the instrument with respect to the vertical, identifying the change of tilt between two measures along every instrumental axis. The 3D magnetometers detect the dip direction and its variation along time with respect to the Earth magnetic field using the flight convention attitude (Tait-Bryan angles), as in Fig. 3.29. In this way, every sensor has its own reference system, which is roto-translated to the Earth reference system. This assumption permits to lower the instrumentation without paying attention to its orientation (like for example SAA or DMS systems), which is reconstructed later. Some scientists criticize this operating principle, highlighting the possible lower precision of the magnetometer, related to external influencing factors like magnetic disturbances. About this theme, it should not be forgotten that, for example, the SAA system requires to know the displacement direction in advance and to put one instrumental axis in that direction. Which is the error introduced by the operator during the lowering of the instrumentation? And what is the precision of mechanical joints? The same theme could be considered also for the DMS system. Joints are tested in the laboratory, but nobody could assure that they have the same performances once placed in the underground. Finally, the following task should be considered:

- Thanks to the 3D axes system, the instrumental resultant could be compared to the known magnetic field, observing the presence of constant (offsets) or variable magnetic disturbing effects. In case of constant effects, they could be corrected by applying the hard iron compensation;
- By considering the displacements starting from a reference reading, constant disturbing effects along time are reduced;
- If the site is highly disturbed, it is possible to install an array where aramid fibre cable is replaced by fiberglass rods and connections, designed for the monitoring of underground excavations. This technology, used for example for the monitoring of geotechnical structures, permits to have the same reference system for all the sensors composing the array, with an alignment error of about 1°-3° from bottom to the top.

The nodes remain inside the ground for the whole duration of the monitoring (Segalini et al. 2011) and will be lost at the end of it. The fixed position of the sensor for the whole monitoring period is very important and avoids the inaccuracies of a repositioning operation, like the case of manual probe or IPI, when it is necessary to remove and then reinsert it.

3.4.1. Standard inclinometer device

During the survey with the manual probe, data logger registers the two rotation angles with respect to the vertical, for each measurement depth. Starting from the known distances between measurement points, it is possible to evaluate the displacement of sensors, referring to the “zero reading” at depth *d* (Eq. [3.17]).

$$\begin{cases}\alpha_{A_{t,d}} = \alpha'_{A_{t,d}} - \alpha'_{A_{0d}} \\ \alpha_{B_{t,d}} = \alpha'_{B_{t,d}} - \alpha'_{B_{0d}}\end{cases} \qquad \begin{cases}\Delta s_{A_{t,d}} = L_d \sin \alpha_{A_{t,d}} \\ \Delta s_{B_{t,d}} = L_d \sin \alpha_{B_{t,d}}\end{cases} \qquad [\ 3.17\ ]$$

Where:

- $\alpha'_{A_{t,d}}$ is the absolute tilt angle with respect to the vertical of groove *A* at depth *d* and time *t*;
- $\alpha'_{A_{0d}}$ is the reference absolute tilt angle with respect to the vertical of groove *A* at depth *d* at the beginning of the monitoring period;
- $\alpha_{A_{d,t}}$ is the change in tilt of groove *A* at depth *d* and time *t*;
- L_d is the measurement step at depth *d*;
- $\Delta s_{A_{d,t}}$ is the differential local displacement of groove *A* at depth *d* and time *t*.

The differential local displacement resultant vector ($\Delta s_{R_{d,t}}$) at depth *d*, time *t*, is obtained through Eq. [3.18].

$$\Delta s_{R_{d,t}} = \sqrt{\Delta s_{A_{d,t}}{}^2 + \Delta s_{B_{d,t}}{}^2} \qquad [\ 3.18\ ]$$

The cumulative displacements along grooves *A* ($\Delta S_{A_{d,t}}$) and *B* ($\Delta S_{B_{d,t}}$) and resultant vector ($\Delta S_{R_{d},t}$) are expressed by Equations [3.19] and [3.20] respectively.

$$\Delta S_{A_{d,t}} = \sum_{i=1}^{d} \Delta s_{A_{i,t}}$$
$$\Delta S_{B_{d,t}} = \sum_{i=1}^{d} \Delta s_{B_{i,t}} \qquad [\ 3.19\ ]$$

$$\Delta S_{R_{d,t}} = \sqrt{\Delta S_{A_{d,t}}{}^2 + \Delta S_{B_{d,t}}{}^2} \qquad [\ 3.20\ ]$$

The azimuth (heading) angle at depth *d* and time *t* is expressed by the Equation [3.21] and represented in Fig. 3.27.

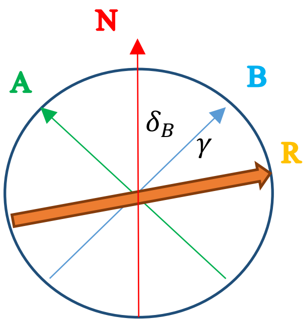

Fig. 3.27: Heading angle evaluated starting from displacement components of grooves A and B

$$\gamma_{d,t} = \tan^{-1}\frac{\Delta S_{A_{d,t}}}{\Delta S_{B_{d,t}}}$$
$$\rho_{d,t} = \gamma_{d,t} + \delta_B \qquad [\ 3.21\ ]$$

Where:

- $\rho_{d,t}$ is the azimuth of the cumulative displacements at depth *d* and time *t*;
- δ_B is the dip direction of groove B;
- $\Delta S_{A_{d,t}}$ and $\Delta S_{B_{d,t}}$ are the cumulative displacements at depth *d* and time *t*, along *A* and *B* grooves respectively.

3.4.2. MUMS system

As the traditional inclinometer, the deeper and terminal part of the MUMS system has to be inserted in a stable portion of the ground, which is considered the starting reference point for the calculation of displacements. In addition, the distance between two sensors is considered as a rigid segment and should not vary along time. In the past, this hypothesis was guaranteed by the filling of the borehole with gravel: when a movement occurred, the traction exerted on the aramid fibre cable conserved the distance between nodes, due to the fact that the lower one was cemented. In the new installation method, the working principle is the same, while the traction is guaranteed by the anchor and the spring, tensioned using the threaded bar system described in Chapter 3.3.

Definition of Segment of Relevance and Calculation Point

Due to the fact that the distance between nodes can be chosen according to the precision required and budget available, every sensor has its own Segment of Relevance, considered as rigid, and Calculation Point. In the case of Tilt Link V, the Segment of Relevance (Fig. 3.28) starts from the middle point between the considered Link and the previous one and terminates in the medium position between the considered Link and the following one.

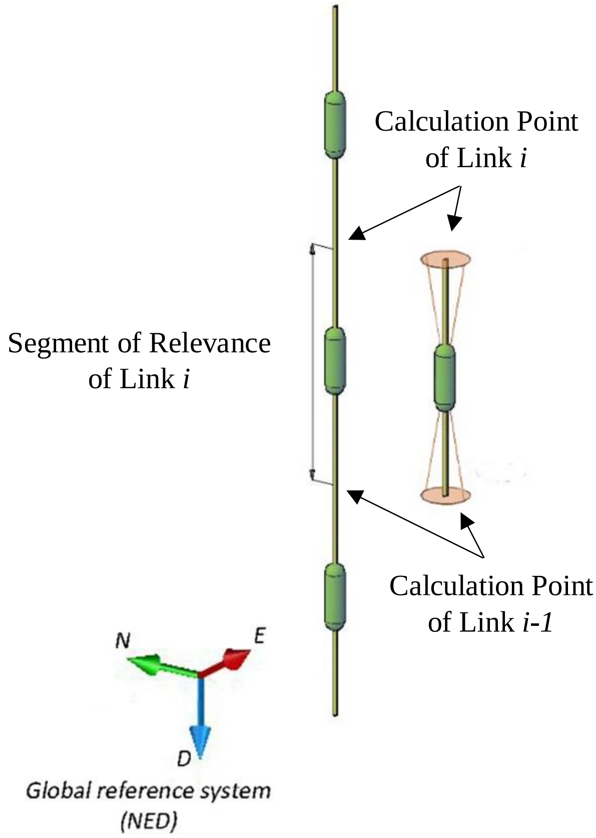

Fig. 3.28: Segment of Relevance and Calculation Point

The first node has a Segment of Relevance expressed by Eq. [3.22], where the depth is considered as positive.

$$SoR_1 = Z_{anchor} - \frac{Z_1 + Z_2}{2} \qquad [\ 3.22\ ]$$

Where:

- SoR_1 is the Segment of Relevance of Link 1;
- Z_{anchor} is the depth of the anchor (considered as the fixed point for the calculation process);
- Z_1 is the depth of Link 1 at the reference reading.

Segments of Relevance for Links that range from the second to the *n-1* are expressed by Eq. [3.23], while the last node (*n*) has a SoR expressed by Eq. [3.24].

$$SoR_i = \left|\frac{Z_i + Z_{i-1}}{2}\right| - \left|\frac{Z_i + Z_{i+1}}{2}\right| \qquad [\ 3.23\ ]$$

$$SoR_n = \frac{z_n + z_{n-1}}{2} \qquad [\ 3.24\ ]$$

During the period of this thesis, some application required to place the last node not at the ground level but at a certain depth, in order to monitor a specific band of the landslide. In this specific case, SoR_n is expressed by Eq. [3.25].

$$SoR_n = \frac{Z_n + Z_{n-1}}{2} - \frac{Z_n + CP_n}{2} \qquad [\ 3.25\ ]$$

Where CP_n is the required Calculation Point of node *n*, i.e. the translation of the ground level to the more superficial monitored depth.

The Calculation Point is placed at the end of every Segment of Relevance (Fig. 3.28), starting from the bottom of the borehole to the top. The Calculation Point of the anchor is placed at the same depth of the anchor itself, which must be in a stable portion of the slope. CP_1 (Calculation Point of Link 1) is expressed by Eq. [3.26], by cumulating the depth of the anchor with the Segment of Relevance of the first Link.

$$CP_1 = CP_{anchor} + SoR_1 \qquad [\ 3.26\ ]$$

The Calculation Points of the following nodes are expressed by Eq. [3.27] simply cumulating the CP of the previous Link with the SoR of the considered sensor.

$$CP_i = CP_{i-1} + SoR_i \qquad [\ 3.27\ ]$$

If electrolytic cells are present together with MEMS (Tilt Link HR 3D V), the Segment of Relevance could be evaluated in two different ways, due to the fact that some sensors may be equipped with only 3D MEMS (TLV). If all the sensors are Tilt Link HR 3D V (TL3DV), the calculation principle of SoR is the same described above. If some parts of the vertical are equipped with TL3DV and others only with TLV, the SoRs are evaluated considering only the MEMS sensors and reproducing them for the electrolytic cells. An example is reported in Tab. 3.7, where CP_n is required at a depth of 6.5 m.

Tab. 3.7: Example of Segments of Relevance and Calculation Points determination

Node Number [-]	Sensor	Depth [m from ground level]	Segment of Relevance [m]	Calculation Point [m from ground level]
-	Anchor	10	-	10.00
1	Tilt Link V	9.75	0.50	9.50
2	Tilt Link V	9.25	0.75	8.75
3-4	Tilt Link HR 3D V	8.25	1.00	7.75
5	Tilt Link V	7.25	0.75	7.00
6-7	Tilt Link HR 3D V	6.75	0.50	6.50

Horizontal Array has exactly the same working principle, with some minor differences:

- The depth along a vertical plane turns into the length over a horizontal plane;
- The first Link has the minimum length, while the first node of Vertical Array is at the maximum depth;
- The SoR_1 of the first sensor is expressed by Eq. [3.28], while the Eq. [3.23] should be simply multiplied for -1;
- The SoR_n considers the Eq. [3.29].

$$SoR_1 = \frac{l_1 + l_2}{2} \qquad [\ 3.28\ ]$$

$$SoR_n = l_n + \frac{l_n - l_{n-1}}{2} - \frac{l_{n-1} + l_n}{2} \qquad [\ 3.29\ ]$$

Aircraft angles convention

After defining Segment of Relevance and Calculation Point, the calculation differs according to the considered sensor. In particular, MEMS processing starts with the acquisition of the three components of gravity acceleration and magnetic field, coupled with the temperature information, and orients the body with 3-degrees of freedom using an algorithm called FQA (Factored Quaternion Algorithm) (Yun et al. 2008). Raw data are converted into physical units using Eq. [3.4], [3.6] and [3.8], then aircraft principle of calculation is applied. This one defines a device body coordinate (Fig. 3.29) using pitch, roll and heading angles (Segalini et al. 2011). Pitch is defined as the angle between X_b axis and the horizontal plane (positive if the movement is upwards), while roll is the angle between Y_b axis and the horizontal (positive if the movement is downwards). Finally, heading is represented by the angle between X_b axis and the magnetic North, measured in a clockwise direction, when viewed from the top. When a MEMS sensor is perfectly vertical, pitch and roll angles equal zero, while heading is evaluated through the components (X_h and Y_h) of the magnetic field measured by magnetic sensor axes X_M and Y_M. FQA is not applicable to situations in which relatively large linear accelerations due to dynamic motion are present (Yun et al. 2008).

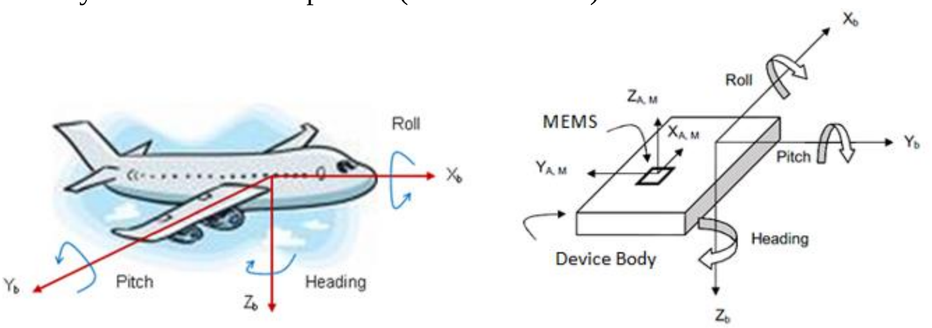

Fig. 3.29: Aircraft convention and MEMS device body (Source: STMicroelectronics, Modified)

The output quaternion of FQA is able to detect every possible system orientation referring to NED (North-East-Down) reference system x_e-y_e-z_e starting from the body reference system x_b-y_b-z_b. Sensor orientation x_s-y_s-z_s should also be considered, while during manufacturing process it is carefully aligned to rigid body reference system. The two reference systems differ for a constant (ε_s), which is accounted as a systematic error (Eq. [3.30]).

$$\begin{aligned} x_s - x_b &= \varepsilon_s \\ y_s - y_b &= \varepsilon_s \\ z_s - z_b &= \varepsilon_s \end{aligned} \qquad [\ 3.30\ ]$$

This paragraph briefly summarizes the work of Yun et al. (2008), which is the calculation principle of MUMS algorithm.

Quaternion rotation operator

According to Euler's theorem of finite rotations, a sequence of rotations in space could always be described as the rotation of a single axis of a certain angle. Once defined the rotation angle β and the 3D unit vector u, which expresses the rotation axis (Eq. [3.31]), it is possible to define the Euler parameters q_0, q_1, q_2, q_3, as in Eq. [3.32] and [3.33].

$$u = \begin{bmatrix} u_1 \\ u_2 \\ u_3 \end{bmatrix} \qquad [\ 3.31\ ]$$

$$q_0 = \cos\left(\frac{\beta}{2}\right) \qquad [\ 3.32\ ]$$

$$\begin{bmatrix} q_1 \\ q_2 \\ q_3 \end{bmatrix} = u \sin\left(\frac{\beta}{2}\right) = \begin{bmatrix} u_1 \\ u_2 \\ u_3 \end{bmatrix} \sin\left(\frac{\beta}{2}\right) \qquad [\ 3.33\ ]$$

An arbitrary rotation could be described with 3 independent parameters. It follows that the four Euler parameters should respect the Eq. [3.34] and could be described as a unit quaternion $q = (q_0\ q_1\ q_2\ q_3)$, where q_0 is the real part and $[q_1\ q_2\ q_3]^T$ the vector part.

$$q_0^2 + q_1^2 + q_2^2 + q_3^2 = 1 \qquad [\ 3.34\ ]$$

Thanks to the unit quaternion, it is possible to apply rotations in the 3D space. After defining any 3D vector $v = [v_1\ v_2\ v_3]^T$, Eq. [3.35] provides a vector v', which results from the rotation of v around u axis of an angle β.

$$v' = qvq^{-1} \qquad [\ 3.35\ ]$$

All the described multiplication are quaternion multiplications, v and v' are quaternion vectors with real parts that equal 0, while q^{-1} is the inverse quaternion of q.

Pitch calculation using Quaternions

A rigid body could be oriented by rotating itself first around its z_b axis of an angle ψ (heading), then around y_b axis of an angle θ (pitch) and finally around x_b axis of an angle ϕ (roll). A quaternion which considers only the pitch is based on the assumption that, when a rigid body is moving with a constant speed and orientation, an accelerometer records only the gravity. In this way, a_x depends only on the pitch. As an example, if the body is moving along an horizontal plane, we have the results of Eq. [3.36]. If this body rotates of an angle ψ, a_x shows the same value, resulting independent from heading. If the body rotates of an angle θ, it is possible to have the results of Eq. [3.37], where $g = 9.81$ m/s^2.

$$\begin{aligned} a_x &= 0 \\ a_y &= 0 \\ a_z &= -g \end{aligned} \qquad [\ 3.36\ ]$$

$$\begin{aligned} a_x &= g \sin\theta \\ a_y &= 0 \\ a_z &= -g\cos\theta \end{aligned} \qquad [\ 3.37\ ]$$

As a convention, it is useful to normalize acceleration and magnetic field values to unit vectors (Eq. [3.38], where $|a|$ is the norm of acceleration vector).

$$\bar{a} = \frac{a}{|a|} = \begin{bmatrix} \bar{a}_x \\ \bar{a}_y \\ \bar{a}_z \end{bmatrix} \qquad [\ 3.38\ ]$$

It follows the Eq. [3.39] and consequently the Eq. [3.40], where θ is always positive. Pitch is defined in the $-\frac{\pi}{2} \le \theta \le \frac{\pi}{2}$ interval, where the cosine is positive.

$$\bar{a}_x = \frac{a_x}{|a|} = \frac{a_x}{|g|} = \frac{g\sin\theta}{g} = \sin\theta \qquad [\ 3.39\ ]$$

$$\cos\theta = \sqrt{1 - \sin\theta^2} \qquad [\ 3.40\ ]$$

In order to obtain the quaternions expressed in Eq. [3.32] and [3.33] it is necessary to use bisection goniometric formulations (Eq. [3.41]), where sign is defined by $\sin\theta$. The result is the pitch quaternion q_p, as in Eq. [3.42].

$$\sin\frac{\theta}{2} = \pm\sqrt{\frac{1-\cos\theta}{2}}$$
$$\cos\frac{\theta}{2} = \sqrt{\frac{1+\cos\theta}{2}} \qquad [\ 3.41\ ]$$

$$q_p = \cos\frac{\theta}{2}(1\ 0\ 0\ 0) + \sin\frac{\theta}{2}(0\ 0\ 1\ 0) \qquad [\ 3.42\ ]$$

Roll calculation using Quaternions
If roll equals 0, a_z is expressed through Eq. [3.37]. A change in the heading does not influence the result, which instead varies following a change in the roll. In particular, a general formula that relates a_y, a_z and roll is reported in Eq. [3.43].

$$a_y = -g\cos\theta\sin\phi$$
$$a_z = -g\cos\theta\cos\phi \qquad [\ 3.43\ ]$$

If $\cos\theta \neq 0$, it is possible to write the Eq. [3.44] and [3.45] ($\cos\theta = 0$ if x_s is vertical. In this specific case it is not possible to define the roll angle, which is assumed equal to 0). As a convention, $-\pi < \phi \leq \pi$.

$$\sin\phi = -\frac{\bar{a}_y}{\cos\theta} \qquad [\ 3.44\ ]$$

$$\cos\phi = -\frac{\bar{a}_z}{\cos\theta} \qquad [\ 3.45\ ]$$

Using equations similar to Eq. [3.41], it is possible to define the roll quaternion q_r, as in Eq. [3.46].

$$q_r = \cos\frac{\phi}{2}(1\ 0\ 0\ 0) + \sin\frac{\phi}{2}(0\ 1\ 0\ 0) \qquad [\ 3.46\ ]$$

If $\phi = \pi$, $\sin\frac{\phi}{2} = \pm 1$. A correction should be applied, considering the results as positive.

Heading calculation using Quaternions
The calculation of heading has no effects on pitch and roll evaluation. For this reason, it could be calculated at the end, using the information of pitch and roll to rotate the magnetic field vector expressed in the sensor reference system $\bar{m}_b$ into an intermediate terrestrial reference system, as in Eq. [3.47]

$$m_e = q_e\, q_r\, m_b\, {q_r}^{-1}\, {q_e}^{-1} \qquad [\ 3.47\ ]$$

Where $m_b = (0\ m_{b_x}\ m_{b_y}\ m_{b_z})$ and $m_e = (0\ m_{e_x}\ m_{e_y}\ m_{e_z})$. If there are not measure errors, m_e equals M_e, except the heading rotation, where $M_e = \left[M_{e_x}\ M_{e_y}\ M_{e_z}\right]$ is the local magnetic field vector. In particular, the complete relation is expressed through Eq. [3.48].

$$\begin{bmatrix} M_{e_x} \\ M_{e_y} \end{bmatrix} = \begin{bmatrix} \cos\psi & -\sin\psi \\ \sin\psi & \cos\psi \end{bmatrix} \begin{bmatrix} m_{e_x} \\ m_{e_y} \end{bmatrix}$$
$$M_{e_z} = m_{e_z} \qquad [\ 3.48\ ]$$

Experimental data highlight that, in case of magnetic interferences or measure errors, M_{e_x} and M_{e_y} could differ in length. For this reason, it is necessary to apply a normalization process that regards the horizontal plane, as in Eq. [3.49], where $\bar{M}_e$ and $\bar{m}_e$ are the local magnetic field vectors in the earth and sensor reference systems respectively.

$$\bar{M}_e = \begin{bmatrix} \bar{M}_{e_x} \\ \bar{M}_{e_y} \end{bmatrix} = \frac{1}{\sqrt{{M_{e_x}}^2 + {M_{e_y}}^2}} \begin{bmatrix} M_{e_x} \\ M_{e_y} \end{bmatrix}$$
$$\bar{m}_e = \begin{bmatrix} \bar{m}_{e_x} \\ \bar{m}_{e_y} \end{bmatrix} = \frac{1}{\sqrt{{m_{e_x}}^2 + {m_{e_y}}^2}} \begin{bmatrix} m_{e_x} \\ m_{e_y} \end{bmatrix} \qquad [\ 3.49\ ]$$

The Eq. [3.48] could then be expressed as in Eq. [3.50]. The consequence is Eq. [3.51], where heading is defined in the interval $-\pi < \psi \le \pi$. Applying goniometric formulas, it is possible to determine (Eq. [3.52]) the heading quaternion q_h.

$$\begin{bmatrix} \bar{M}_{e_x} \\ \bar{M}_{e_y} \end{bmatrix} = \begin{bmatrix} \cos\psi & -\sin\psi \\ \sin\psi & \cos\psi \end{bmatrix} \begin{bmatrix} \bar{m}_{e_x} \\ \bar{m}_{e_y} \end{bmatrix}$$
$$\bar{M}_{e_z} = \bar{m}_{e_z} \qquad [\ 3.50\ ]$$

$$\begin{bmatrix} \cos\psi \\ \sin\psi \end{bmatrix} = \begin{bmatrix} \bar{m}_{e_x} & \bar{m}_{e_y} \\ -\bar{m}_{e_y} & \bar{m}_{e_x} \end{bmatrix} \begin{bmatrix} \bar{M}_{e_x} \\ \bar{M}_{e_y} \end{bmatrix} \qquad [\ 3.51\ ]$$

$$q_h = \cos\frac{\psi}{2}(1\ 0\ 0\ 0) + \sin\frac{\psi}{2}(0\ 0\ 0\ 1) \qquad [\ 3.52\ ]$$

Orientation of a rigid body using quaternions
Thanks to pitch, roll and heading quaternions, it is possible to define the orientation of sensor (body) reference system with respect to the Earth reference system, as in Eq. [3.53].

$$\hat{q} = q_h\ q_p\ q_r \qquad [\ 3.53\ ]$$

The algorithm uses the acceleration and magnetic field data as input, producing the output $\hat{q}$. Quaternions are not subjected to singularity, but the algorithm uses angles in order to represent the 3D result. For this reason, the FQA is subjected to singularities that have to be solved, as every representation based on 3 parameters and 3 degrees of freedom.

Singularities
FQA has a singularity if $\theta = \frac{\pi}{2}$ and consequently $\cos\theta = 0$ in Eq. [3.44] and [3.45]. For this reason, the value of pitch angle should be verified and corrected if $\cos\theta < \epsilon$, using Eq. [3.54], where ϵ is a positive constant ($\epsilon \to 0$) and $\bar{a}$ and m_b are rotated along y_b axis of an angle α.

$$\bar{a}_{offset} = q_\alpha\ \bar{a}\ {q_\alpha}^{-1}$$
$$m_{b_{offset}} = q_\alpha\ m_b\ {q_\alpha}^{-1} \qquad [\ 3.54\ ]$$

Where q_α is the rotation quaternion expressed as $q_\alpha = \cos\frac{\alpha}{2}(1\ 0\ 0\ 0) + \sin(0\ 0\ 1\ 0)$.

An alternative method consists of inverting the rotations order by applying the rotation θ along y_b, followed by the rotation ψ along z_b. The change in the operations order produces a distinct result and the singularity happens for a different angle. Of course, this method requires various formulations for the evaluation of pitch, roll and heading quaternions.

MEMS calculation completion

Due to the convention of accelerometer signs, the normalized value recorded is positive if it points in the Earth gravity direction. For this reason, it should be noted that it is necessary to apply some sign corrections in order to preserve a right-hand convention and a correspondence between accelerometers and magnetometers components, as in Eq. [3.55].

$$\begin{aligned} Z_A &= -Z_A \\ X_M &= -X_M \\ Y_M &= -Y_M \end{aligned} \qquad [\ 3.55\ ]$$

The displacement vector of every Link (Fig. 3.30) is obtained starting from the quaternion $\hat{q}$ and applying the Eq. [3.56], where $q_v = [0\ 0\ 0\ SoR_i]$.

$$q_{v_R} = \hat{q}\ q_v\ \hat{q}^{-1} \qquad [\ 3.56\ ]$$

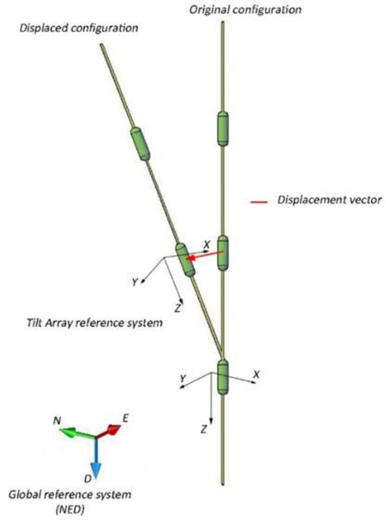

Fig. 3.30: Displacement vector between two consecutive sensor readings

In particular, the local displacements (not cumulated over space and time) along *x* ($d_{X_{i,a}}$), *y* ($d_{Y_{i,a}}$), and *z* ($d_{Z_{i,a}}$), directions are expressed in Eq. [3.57].

$$\begin{aligned} d_{X_{i,a}} &= q_{v_R}(2) \\ d_{Y_{i,a}} &= q_{v_R}(3) \\ d_{Z_{i,a}} &= q_{v_R}(4) \end{aligned} \qquad [\ 3.57\ ]$$

The evaluation of *X* local displacement of Link *i* at time *j* is executed through the Eq. [3.58].

$$X_{L_{i,j}} = \sum_{a=1}^{j} d_{X_{i,a}} + S_{X_i} \qquad [\ 3.58\ ]$$

Where:

- $d_{X_{i,a}}$ is the differential local displacement of Link *i*, between time *a* and *a-1*, along North (+) – South (-) direction;
- S_{X_i} is the local displacement of Link *i* along North-South direction at time *a*, evaluated starting from the zero reading. If the software considers all the dataset and *a* = *t* = *0*, $S_{X_i} = 0$;
- $X_{L_{i,j}}$ is the differential local displacement of Link *i* along North-South direction at time *j*, referred to the zero reading.

In the same way, the evaluation of Y local displacement of Link i at time j is executed through Eq. [3.59], while the calculation of settlements is executed through Eq. [3.60].

$$Y_{L_{i,j}} = \sum_{a=1}^{j} d_{EO_{i,a}} + S_{Y_i} \qquad [\ 3.59\ ]$$

$$Z_{L_{i,j}} = \sum_{a=1}^{j} d_{Z_{i,a}} + S_{Z_i} \qquad [\ 3.60\ ]$$

Where $Y_{L_{i,j}}$ is the differential local displacement of Link i along East (+) – West (-) direction and $Z_{L_{i,j}}$ is the settlement of node i at time j over the vertical direction, referred to the zero reading.

The calculation of $H_{L_{i,j}}$, local displacement resultant vector over the horizontal plane (represented by X and Y axes), is expressed through Eq. [3.61].

$$H_{L_{i,j}} = \sqrt{X_{L_{i,j}}^2 + Y_{L_{i,j}}^2} \qquad [\ 3.61\ ]$$

The determination of X and Y cumulative displacements of Link i at time j is executed through the set of Equations [3.62], while the depth Z of node i at time j is expressed by Eq. [3.63], starting from the depth of the Calculation Point of the same node at the zero reading ($Z_{i,R}$). Eq. [3.64] is the formula for the resultant vector of cumulative displacements over the horizontal plane.

$$X_{i,j} = \sum_{a=1}^{i} X_{L_{aj}} \qquad Y_{i,j} = \sum_{a=1}^{i} Y_{L_{aj}} \qquad [\ 3.62\ ]$$

$$Z_{i,j} = \sum_{a=1}^{i} Z_{L_{i,j}} + Z_{i,R} \qquad [\ 3.63\ ]$$

$$H_{i,j} = \sqrt{X_{i,j}^2 + Y_{i,j}^2} \qquad [\ 3.64\ ]$$

The algorithm calculates the local and cumulative displacement rate ($v_{L_{i,j}}$ and $v_{i,j}$ respectively in Eq. [3.65]) and acceleration ($a_{L_{i,j}}$and $a_{i,j}$ respectively in Eq. [3.66]) of the resultant vector over horizontal plane H represented by X and Y.

$$v_{L_{i,j},d} = \frac{H_{L_{i,j},d} - H_{L_{i,j},d-1}}{t_d - t_{d-1}} \qquad v_{i,j,d} = \frac{H_{i,j,d} - H_{i,j,d-1}}{t_d - t_{d-1}} \qquad [\ 3.65\ ]$$

$$a_{L_{i,j},d} = \frac{v_{L_{i,j},d} - v_{L_{i,j},d-1}}{t_d - t_{d-1}} \qquad a_{i,j,d} = \frac{v_{i,j,d} - v_{i,j,d-1}}{t_d - t_{d-1}} \qquad [\ 3.66\ ]$$

Where:

- $v_{L_{i,j},d}$ is the local displacement rate of $H_{L_{i,j}}$, expressed as meters per day, evaluated between day *d* and day *d-1*;
- $v_{i,j,d}$ is the cumulative displacement rate of $H_{i,j}$, expressed as meters per day, evaluated between day *d* and day *d-1*;
- $a_{L_{i,j},d}$ is the local acceleration of $H_{L_{i,j}}$, expressed as meters per day, evaluated between day *d* and day *d-1*;
- $a_{i,j,d}$ is the cumulative displacement rate of $H_{i,j}$, expressed as meters per day, evaluated between day *d* and day *d-1*.

Heading is calculated through Eq. [3.67] which does not consider the sign of $X_{i,j}$. Then, it is necessary to eventually correct it with the possible cases that may happen, reported in Tab. 3.8.

$$\rho_{i,j} = \cos^{-1}\frac{|X_{i,j}|}{H_{i,j}} * \frac{180}{\pi} \qquad [\ 3.67\ ]$$

Tab. 3.8: Correction of the heading considering $X_{i,j}$ and $Y_{i,j}$ signs

$X_{i,j}$	$Y_{i,j}$	Corrected $\rho_{i,j}$
Positive	Positive	$\rho_{i,j}$
Negative	Positive	$180° - \rho_{i,j}$
Negative	Negative	$180° + \rho_{i,j}$
Positive	Negative	$360° - \rho_{i,j}$
0	Negative	270°
0	Positive	90°
Positive	0	0°
Negative	0	180°

As an example, we could consider a sensor experiencing a local displacement on 30th of June 2018 over North-South direction (cumulated over time) of 5 mm at the maximum depth, 2 mm on the following Link, while the third node did not record any displacement. If at the date of 1st July 2018 Link 1 records a displacement on North-South direction of 0.1 mm at 9 AM, 0 mm at 4 PM and 0.2 mm at 11 PM, Link 2 highlights a movement of 2 mm only in the last sample time and Link 3 shows 3 mm of displacement between 9 AM and 4 PM, we have the following set of matrices.

$$d_x = \begin{vmatrix} 0.1 & 0.0 & 0.2 \\ 0.0 & 0.0 & 2.0 \\ 0.0 & 3.0 & 0.0 \end{vmatrix} \qquad d_Y = \begin{vmatrix} 0.0 & 0.0 & 0.0 \\ 0.1 & 4.0 & 0.2 \\ 0.0 & 2.2 & 1.0 \end{vmatrix}$$

$$\sum_{a=1}^{j} d_{X_{i,a}} = \begin{vmatrix} 0.1 & 0.1 & 0.3 \\ 0.0 & 0.0 & 2.0 \\ 0.0 & 3.0 & 3.0 \end{vmatrix} \qquad \sum_{a=1}^{j} d_{Y_{i,a}} = \begin{vmatrix} 0.0 & 0.0 & 0.0 \\ 0.1 & 4.1 & 4.3 \\ 0.0 & 2.2 & 3.2 \end{vmatrix}$$

$$S_X = \begin{vmatrix} 5.0 \\ 2.0 \\ 0.0 \end{vmatrix} \qquad S_Y = \begin{vmatrix} 0.5 \\ 0.2 \\ 0.4 \end{vmatrix}$$

$$X_{L_{i,j}} = \begin{vmatrix} 5.0 & 5.1 & 5.1 & 5.3 \\ 2.0 & 2.0 & 2.0 & 4.0 \\ 0.0 & 0.0 & 3.0 & 3.0 \end{vmatrix} \qquad Y_{L_{i,j}} = \begin{vmatrix} 0.5 & 0.5 & 0.5 & 0.5 \\ 0.2 & 0.3 & 4.3 & 4.5 \\ 0.4 & 0.4 & 2.6 & 3.6 \end{vmatrix}$$

$$H_{L_{i,j}} = \begin{vmatrix} 5.0 & 5.1 & 5.1 & 5.3 \\ 2.0 & 2.0 & 4.7 & 6.0 \\ 0.4 & 0.4 & 4.0 & 4.7 \end{vmatrix}$$

$$X_{i,j} = \begin{vmatrix} 5.0 & 5.1 & 5.1 & 5.3 \\ 7.0 & 7.1 & 7.1 & 9.3 \\ 7.0 & 7.1 & 10.1 & 12.3 \end{vmatrix} \qquad Y_{i,j} = \begin{vmatrix} 0.5 & 0.5 & 0.5 & 0.5 \\ 0.7 & 0.8 & 4.8 & 5.0 \\ 1.1 & 1.2 & 7.4 & 8.6 \end{vmatrix}$$

$$H_{i,j} = \begin{vmatrix} 5.0 & 5.1 & 5.1 & 5.3 \\ 7.0 & 7.1 & 8.6 & 10.6 \\ 7.1 & 7.2 & 12.5 & 15.0 \end{vmatrix}$$

$$\rho_{i,j} = \begin{vmatrix} 0 & 0 & 0 & 0 \\ 0 & 0 & 34 & 29 \\ 10 & 10 & 36 & 35 \end{vmatrix}$$

$$v_{L_{i,j}} = \begin{vmatrix} d-1 & d-0.5 & d & d+0.75 \\ 0.0 & 0.0 & 0.1 & 0.2 \\ 0.0 & 0.0 & 2.7 & 3.2 \\ 0.0 & 0.0 & 3.6 & 3.4 \end{vmatrix} \qquad v_{i,j} = \begin{vmatrix} d-1 & d-0.5 & d & d+0.75 \\ 0.0 & 0.0 & 0.1 & 0.2 \\ 0.0 & 0.0 & 1.3 & 2.4 \\ 0.0 & 0.0 & 3.4 & 6.2 \end{vmatrix}$$

$$a_{L_{i,j}} = \begin{vmatrix} d-1 & d-0.5 & d & d+0.75 \\ 0.0 & 0.0 & 0.0 & 0.2 \\ 0.0 & 0.0 & 0.0 & 2.6 \\ 0.0 & 0.0 & 0.0 & 2.7 \end{vmatrix} \qquad a_{i,j} = \begin{vmatrix} d-1 & d-0.5 & d & d+0.75 \\ 0.0 & 0.0 & 0.0 & 0.2 \\ 0.0 & 0.0 & 0.0 & 2.4 \\ 0.0 & 0.0 & 0.0 & 6.2 \end{vmatrix}$$

Electrolytic Cell calculation

The evaluation of displacement starting from electrolytic cell data is easier than MEMS sensor. In particular, the movements could be evaluated in two different ways: by using the magnetometer of MEMS or cumulating the information along electrolytic cell instrumental axes x and y. In particular, the second possibility requires to previously align every node preserving the azimuth with a mechanical system. In the first case, the algorithm evaluates the heading angle using the magnetic field recorded along MEMS instrumental axes x and y, starting from the hypothesis that the two axes are orthogonal one to each other and that the magnetometer works like a compass. Considering the situation of Fig. 3.31 where N_g and E_g are North and East axes in the Earth geographic reference system respectively, N_m and E_m are North and East axes in the Earth magnetic reference system and $X-Y$ is the instrumental reference system. If we do not consider the magnetic declination angle β and we refer the results to the Earth magnetic reference system, we have the situation of Fig. 3.32, where α is the angle between North magnetic field and Y instrumental axis.

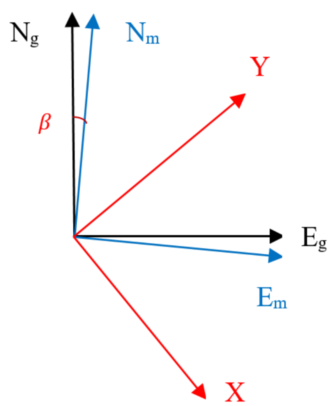

Fig. 3.31: Earth geographic (dark line), Earth magnetic (blue line) and instrumental (line in red) reference systems

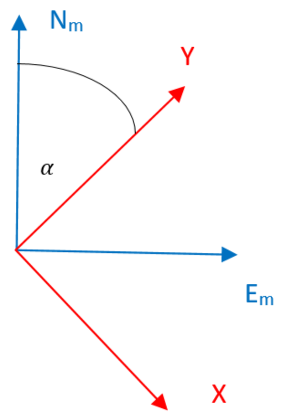

Fig. 3.32: Earth Magnetic reference system and instrumental reference system

At this point, it is necessary to consider different possibilities, based on the sign of magnetic field recorded along *x* and *y* instrumental axes.

I) $m_y > 0, m_x > 0$

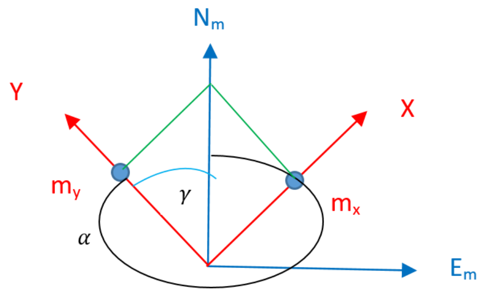

Fig. 3.33: Detection of Earth magnetic field along instrumental axes, with $m_y > 0$ and $m_x > 0$

Starting from Fig. 3.33, it is possible to determine the set of Eq. [3.68]. The Eq. [3.69] is obtained by dividing the second equation with the first. Then α is evaluated through the Eq. [3.70].

$$\begin{cases} m_y = N_m * \cos\gamma \\ m_x = N_m * \sin\gamma \end{cases} \quad [\ 3.68\ ]$$

$$\frac{m_x}{m_y} = \tan\gamma \quad [\ 3.69\ ]$$

$$\alpha(°) = 360 - \tan^{-1}\left(\frac{m_x}{m_y}\right) * \frac{180}{\pi} \quad [\ 3.70\ ]$$

II) $m_y > 0, m_x < 0$

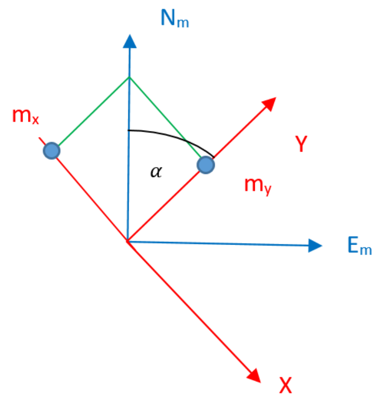

Fig. 3.34: Detection of Earth magnetic field along instrumental axes, with $m_y > 0$ and $m_x < 0$

This case is similar to the previous one and the result is expressed in the following set of equations.

$$\begin{cases} m_y = N_m * \cos\alpha \\ m_x = -N_m * \sin\alpha \end{cases} \qquad [\ 3.71\ ]$$

$$\frac{m_x}{m_y} = -\tan\alpha \qquad [\ 3.72\ ]$$

$$\alpha(°) = \tan^{-1}\left(-\frac{m_x}{m_y}\right) * \frac{180}{\pi} \qquad [\ 3.73\ ]$$

III) $m_y < 0, m_x < 0$

The situation of Fig. 3.35 is governed by the Eq. [3.68], which leads to Eq. [3.70].

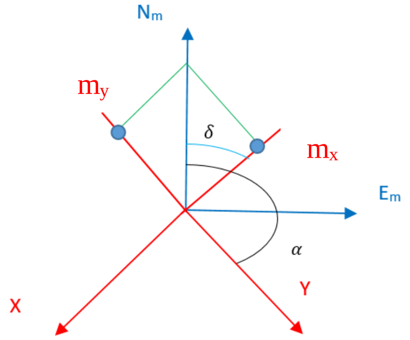

Fig. 3.35: Detection of Earth magnetic field along instrumental axes, with $m_y < 0$ and $m_x < 0$

$$\begin{cases} m_x = -N_m * \cos\delta \\ m_y = -N_m * \sin\delta \end{cases} \qquad [\ 3.74\ ]$$

$$\frac{m_y}{m_x} = \tan\delta \qquad [\ 3.75\ ]$$

$$\alpha(°) = 90 + \tan^{-1}\left(\frac{m_y}{m_x}\right) * \frac{180}{\pi} \qquad [\ 3.76\ ]$$

IV) $m_y < 0, m_x > 0$

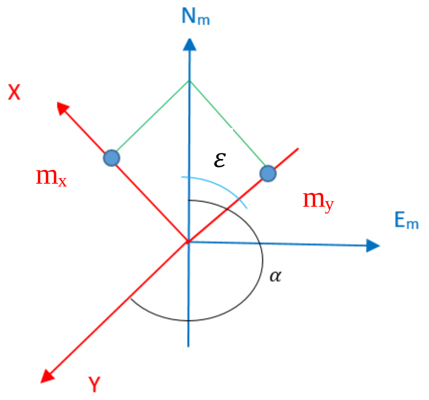

Fig. 3.36: Detection of Earth magnetic field along instrumental axes, with $m_y < 0$ and $m_x > 0$

The case of Fig. 3.36 leads to Eq. [3.79].

$$\begin{cases} m_y = -N_m * \cos\varepsilon \\ m_x = N_m * \sin\varepsilon \end{cases} \qquad [\ 3.77\ ]$$

$$\frac{m_x}{m_y} = -\tan\varepsilon \qquad [\ 3.78\ ]$$

$$\alpha(°) = 180 + \tan^{-1}\left(-\frac{m_x}{m_y}\right) * \frac{180}{\pi} \qquad [\ 3.79\ ]$$

V) $m_y = 0, m_x > 0$

If $m_y = 0$, it is possible to determine α only observing the sign of m_x, as in Eq. [3.81] and Eq. [3.83].

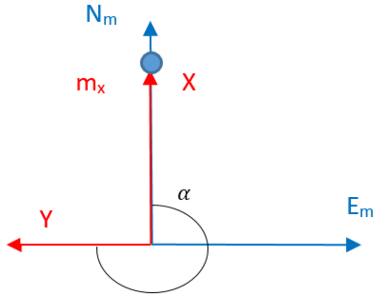

Fig. 3.37: Detection of Earth magnetic field along instrumental axes, with $m_y = 0$ and $m_x > 0$

$$\begin{cases} m_y = 0 \\ m_x = N_m \end{cases} \qquad [\ 3.80\ ]$$

$$\alpha(°) = 270 \qquad [\ 3.81\ ]$$

VI) $m_y = 0, m_x < 0$

$$\begin{cases} m_y = 0 \\ m_x = -N_m \end{cases} \qquad [\ 3.82\ ]$$

$$\alpha(°) = 90 \qquad [\ 3.83\ ]$$

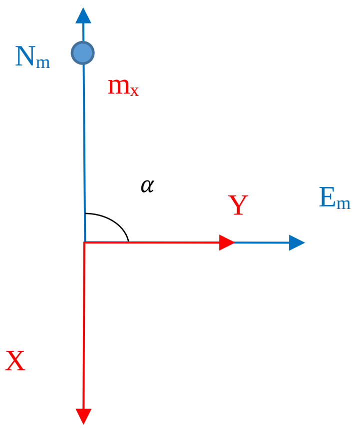

Fig. 3.38: Detection of Earth magnetic field along instrumental axes, with $m_y = 0$ and $m_x < 0$

VII) $m_y > 0, m_x = 0$

Like cases V) and VI), if $m_x = 0$, α is determined only observing the sign of m_y, as in Equations [3.85] and [3.87].

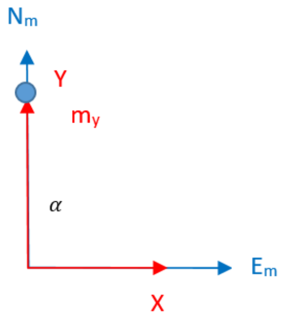

Fig. 3.39: Detection of Earth magnetic field along instrumental axes, with $m_y > 0$ and $m_x = 0$

$$\begin{cases} m_x = 0 \\ m_y = N_m \end{cases} \quad [\ 3.84\ ]$$

$$\alpha(°) = 0 \quad [\ 3.85\ ]$$

VIII) $m_y < 0, m_x = 0$

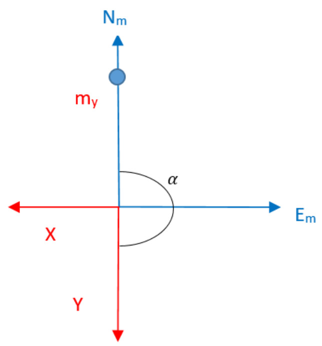

Fig. 3.40: Detection of Earth magnetic field along instrumental axes, with $m_y < 0$ and $m_x = 0$

$$\begin{cases} m_x = 0 \\ m_y = -N_m \end{cases} \quad [\ 3.86\ ]$$

$$\alpha(°) = 180 \quad [\ 3.87\ ]$$

The number of equations could be highly reduced if we consider α as the angle between Earth magnetic North and X instrumental axis, as described below.

I) $m_y > 0$

$$\alpha(°) = 90 - \tan^{-1}\left(\frac{m_x}{m_y}\right) * \frac{180}{\pi} \quad [\ 3.88\ ]$$

II) $m_y < 0$

$$\alpha(°) = 270 - \tan^{-1}\left(\frac{m_x}{m_y}\right) \quad [\ 3.89\ ]$$

III) $m_y = 0, m_x > 0$

$$\alpha(°) = 0 \quad [\ 3.90\ ]$$

IV) $m_y = 0, m_x < 0$

$$\alpha(°) = 180 \quad [\ 3.91\ ]$$

Case I) includes cases I), II) and III) of the previous method, as reported below.

$m_y > 0, m_x > 0$ $$\alpha(°) = 90 - \gamma = 90 - \tan^{-1}\left(\frac{m_x}{m_y}\right) * \frac{180}{\pi}$$ [3.92]

$m_y > 0, m_x < 0$ $$\alpha(°) = 90 + \tan^{-1}\left(-\frac{m_x}{m_y}\right) * \frac{180}{\pi} = 90 - \tan^{-1}\left(\frac{m_x}{m_y}\right) * \frac{180}{\pi}$$ [3.93]

$m_y > 0, m_x = 0$ $$\alpha(°) = 90 - \tan^{-1}\left(\frac{m_x}{m_y}\right) * \frac{180}{\pi} = 90$$ [3.94]

In the same way, case II) includes the cases IV), V) and VI) of the previous method.

$m_y < 0, m_x > 0$ $$\alpha(°) = 270 + \varepsilon = 270 + \tan^{-1}\left(-\frac{m_x}{m_y}\right) * \frac{180}{\pi} = 270 - \tan^{-1}\left(\frac{m_x}{m_y}\right)$$ [3.95]

$m_y < 0, m_x < 0$ $$\alpha(°) = 180 + \delta = 180 + \tan^{-1}\left(\frac{m_y}{m_x}\right) * \frac{180}{\pi} = 270 - \tan^{-1}\left(\frac{m_x}{m_y}\right)$$ [3.96]

$m_y < 0, m_x = 0$ $$\alpha(°) = 270 + \varepsilon = 270 + \tan^{-1}\left(-\frac{m_x}{m_y}\right) * \frac{180}{\pi} = 270$$ [3.97]

It is possible to evaluate the local displacements (cumulated over time) along North ($N_{Lx_{i,j}}$) and East ($E_{Lx_{i,j}}$) magnetic Earth directions due to the tilt angle recorded by *x* instrumental axis ($\varphi_{x_{i,j}}$) of node *i* at the date *j*, using Eq. [3.98] (if $\sin\left(\varphi_{x_{i,j}}\right) \geq 0$) or Eq. [3.99] ($\sin\left(\varphi_{x_{i,j}}\right) < 0$).

$$\begin{aligned} N_{Lx_{i,j}} &= SoR_i * \sin\left(\varphi_{x_{i,j}}\right) * \cos\alpha \\ E_{Lx_{i,j}} &= -SoR_i * \sin\left(\varphi_{x_{i,j}}\right) * \sin\alpha \end{aligned}$$ [3.98]

$$\begin{aligned} N_{Lx_{i,j}} &= -SoR_i * \sin\left(\varphi_{x_{i,j}}\right) * \cos\alpha \\ E_{Lx_{i,j}} &= SoR_i * \sin\left(\varphi_{x_{i,j}}\right) * \sin\alpha \end{aligned}$$ [3.99]

The local settlements due to the tilt of *x* instrumental axis are evaluated through the Eq. [3.99].

$$Z_{Lx_{i,j}} = SoR_i - SoR_i * \cos\left(\varphi_{x_{i,j}}\right)$$ [3.99]

In the same way, it is possible to obtain the Eq. [3.100] ($\sin\left(\varphi_{y_{i,j}}\right) \geq 0$) or the Eq. [3.101] ($\sin\left(\varphi_{y_{i,j}}\right) < 0$) considering the tilt angle recorded by *y* instrumental axis ($\varphi_{y_{i,j}}$), , while settlements are evaluated through the Eq. [3.102].

$$N_{Ly_{i,j}} = SoR_i * \sin\left(\varphi_{y_{i,j}}\right) * \sin\alpha$$
$$E_{Ly_{i,j}} = SoR_i * \sin\left(\varphi_{y_{i,j}}\right) * \cos\alpha \qquad [\ 3.100\ ]$$

$$N_{Ly_{i,j}} = -SoR_i * \sin\left(\varphi_{y_{i,j}}\right) * \sin\alpha$$
$$E_{Ly_{ij,}} = -SoR_i * \sin\left(\varphi_{y_{i,j}}\right) * \cos\alpha \qquad [\ 3.101\ ]$$

$$Z_{Ly_{i,j}} = SoR_i - SoR_i * \cos\left(\varphi_{y_{i,j}}\right) \qquad [\ 3.102\ ]$$

Finally, the local displacements (not cumulated over time) along North and East magnetic Earth directions of node *i* at the date *j*, are obtained through the Eq. [3.103], while the local settlement $Z_{L_{i,j}}$ is evaluated by considering the maximum between the two estimated settlements $Z_{Lx_{i,j}}$ and $Z_{Ly_{i,j}}$.

$$N_{L_{i,j}} = N_{Lx_{i,j}} + N_{Ly_{i,j}}$$
$$E_{L_{i,j}} = E_{Lx_{i,j}} + E_{Ly_{i,j}} \qquad [\ 3.103\ ]$$

If the MEMS sensor is not present and nodes are aligned, it is possible to calculate the displacements along *X*-*Y* instrumental reference system and then refer the results to Earth Magnetic reference system, if the azimuth of *X* or *Y* instrumental axis is known. In particular, the local displacements and the local settlements are evaluated through the Eq. [3.115] and Eq. [3.116] respectively.

$$X_{L_{i,j}} = SoR_i * \sin\left(\varphi_{x_{i,j}}\right)$$
$$Y_{L_{i,j}} = SoR_i * \sin\left(\varphi_{y_{i,j}}\right) \qquad [\ 3.104\ ]$$

$$Z_{Lx_{i,j}} = SoR_i - SoR_i * \cos\left(\varphi_{x_{i,j}}\right)$$
$$Z_{Ly_{i,j}} = SoR_i - SoR_i * \cos\left(\varphi_{y_{i,j}}\right) \qquad [\ 3.105\ ]$$

The Eq. [3.117] represent the rotation of instrumental reference system to obtain the Earth magnetic reference system, where α is the heading angle of *Y* instrumental axis.

$$N_{L_{i,j}} = Y_{L_{i,j}} * \cos\alpha - X_{L_{i,j}} * \sin\alpha$$
$$E_{L_{i,j}} = Y_{L_{i,j}} * \sin\alpha + X_{L_{i,j}} * \cos\alpha \qquad [\ 3.106\ ]$$

The cumulative displacements over time and space along North and East directions, the local and cumulative displacements in the maximum grade direction, the resulting azimuth, the local and cumulative displacements ratio as well as the local and cumulative accelerations are evaluated with the same set of equations previously described, which start from Eq. [3.61] and terminates with Eq. [3.67].

Settlements calculation

The evaluation of settlement along a horizontal direction is obtained using one single instrumental axis of Tilt Link H (MEMS) or Tilt Link HR 3D H (MEMS and electrolytic cell) sensors. The local settlement $Z_{L_{i,j}}$ (cumulated over time) of node *i* at the date *j* is obtained through Eq. [3.107], while the local variation of Link position over the horizontal plane is estimated using Eq. [3.108].

$$Z_{L_{i,j}} = SoR_i * \sin(\varphi_{i,j}) \quad [\ 3.107\ ]$$

$$X_{L_{i,j}} = SoR_i * \cos(\varphi_{i,j}) \quad [\ 3.108\ ]$$

Finally, the determination of cumulative displacement of Link *i* at time *j* is executed through the Eq. [3.110], while the position of node over the horizontal plane is defined by the Eq. [3.109].

$$X_{i,j} = \sum_{a=1}^{i} X_{L_{a,j}} \quad [\ 3.109\ ]$$

$$Z_{i,j} = \sum_{a=1}^{i} Z_{L_{a,j}} \quad [\ 3.110\ ]$$

Finally, the algorithm calculates also the local ($v_{L_{i,j},d}$, $a_{L_{i,j},d}$) and cumulative ($a_{L_{i,j},d}$, $a_{i,j,d}$) displacements ratio (Eq. [3.65]) and accelerations (Eq. [3.66]) of settlements.

$$v_{L_{i,j},d} = \frac{Z_{L_{i,j},d} - Z_{L_{i,j},d-1}}{t_d - t_{d-1}}$$

$$v_{i,j,d} = \frac{Z_{i,j,d} - Z_{i,j,d-1}}{t_d - t_{d-1}} \quad [\ 3.111\ ]$$

$$a_{L_{i,j},d} = \frac{v_{L_{i,j},d} - v_{L_{i,j},d-1}}{t_d - t_{d-1}}$$

$$a_{i,j,d} = \frac{v_{i,j,d} - v_{i,j,d-1}}{t_d - t_{d-1}} \quad [\ 3.112\ ]$$

Where:

- $v_{L_{i,j},d}$ is the local displacement rate of $Z_{L_{i,j},d}$, expressed as meters per day, evaluated between day *d* and day *d-1*;
- $v_{i,j,d}$ is the cumulative displacement rate of $Z_{i,j}$, expressed as meters per day, evaluated between day *d* and day *d-1*;
- $a_{L_{i,j},d}$ is the local acceleration of $Z_{L_{i,j}}$, expressed as meters per day, evaluated between day *d* and day *d-1*;
- $a_{i,j,d}$ is the cumulative displacement rate of $Z_{i,j}$, expressed as meters per day, evaluated between day *d* and day *d-1*.

Water Level calculation

The calculation of water level is quite simple and it is based on the difference between the absolute pore pressure recorded by the piezometer (P_{piezo}) and the atmospheric pressure registered by the barometer (P_{atm}). In particular, after defining the height of the water table (h_{H_2O}) over the piezometer (Eq. [3.113], where P_{piezo} and P_{atm} are expressed using Pascal), the depth of the water table (d_{H2O}) is calculated through Eq. [3.114], where d_{piezo} is the depth of the piezometer sensor (as a negative value).

$$h_{H_2O} = \frac{P_{piezo} - P_{atm}}{9806} \qquad [\ 3.113\ ]$$

$$d_{H2O} = d_{piezo} + h_{H2O} \qquad [\ 3.114\ ]$$

3.4.3. Self-check controls

When dealing with automated tools, it is of fundamental importance to determine self-check data controls able to recognize malfunctions, spike noises, inaccuracies and every disturbing factor which could influence the elaboration. Dealing with geotechnical instrumentations, it is quite difficult to find articles in literature about this key aspect. The scientific community often concentrates on the inaccuracies of numerical models, forgetting to investigate the significance of monitoring datum. During this thesis and the creation of MUMS algorithm, multi-level automated controls have been defined. They monitor the value of index physical entities, as reported below:

I. Recognition of spike noise
II. Coherence of gravity acceleration vector
III. Variability of gravity acceleration vector
IV. Coherence of magnetic field vector
V. Variability of magnetic field vector
VI. Coherence of node temperature
VII. Running average
VIII. Recognition of instrumental noise
IX. Recognition of not-operating sensors

Recognition of spike noise

Spike noise or impulse noise is an electrical disturb related to sharp and sudden disorder in the signal that may occur in a single measure often related to external factors. Spike noises are recognized using statistical tools over a specific dataset. In particular, it is possible to evaluate the variability of a univariate sample of quantitative data using the Scaled Median Absolute Deviation (MAD). MAD (Hoaglin et al 1983) represents a measure of the statistical dispersion and it is defined as the median of the absolute deviations from the data's median, as in Eq. [3.115]. MAD is a robust statistic, more resilient to outliers than the standard deviation. In fact, standard deviation evaluates the squared distance from the mean, weighting heavier large deviations than Median Absolute Deviation.

The removal of accelerometer spike noise is fundamental in some applications, like for example tunnelling and underground excavations in general. In this case, the vibrations induced by works could highly influence the single data-point, resulting in a well identifiable outlier.

$$\begin{gathered} MAD = c * median(|X_i - median(X)|) \\ c = \frac{-1}{\sqrt{2} * erfc^{-1}\left(\frac{3}{2}\right)} \\ erfc(x) = \frac{2}{\sqrt{\pi}\int_x^{\infty} e^{-t^2}dt} = 1 - erf(x) \\ erf(x) = \frac{2}{\sqrt{\pi}}\int_0^x e^{-t^2}dt \end{gathered} \qquad [\ 3.115\ ]$$

Where:

- X_i is the datum to be evaluated;
- $erfc(x)$ is the complementary error function;
- $erf(x)$ is the error function (Glaisher 1871).

The algorithm, introduced for Tunnel Link and Radial Link sensors, is applied also to landslide sector for both accelerometer and magnetometer data. In this specific field of application, spikes could be related to earthquakes or traffic vibrations and, if not highlighted, may activate alarms. It is quite important to underline that the recognition of spike noises shows high performances if the dataset is centred. For this reason, the calculation of the last part of data sample is not 100% validated until its time window is fully centred. The validation may occur some hours later and it is strictly related to the number of points considered, the sample period and the data transmission frequency. If for example we have the situation represented in Fig. 3.41, with a sample period of 10 minutes, a dataset of 11 elements and a data transmission frequency of 30 minutes, the complete validation of the considered raw data (red line) occurs one hour and 15 minutes later.

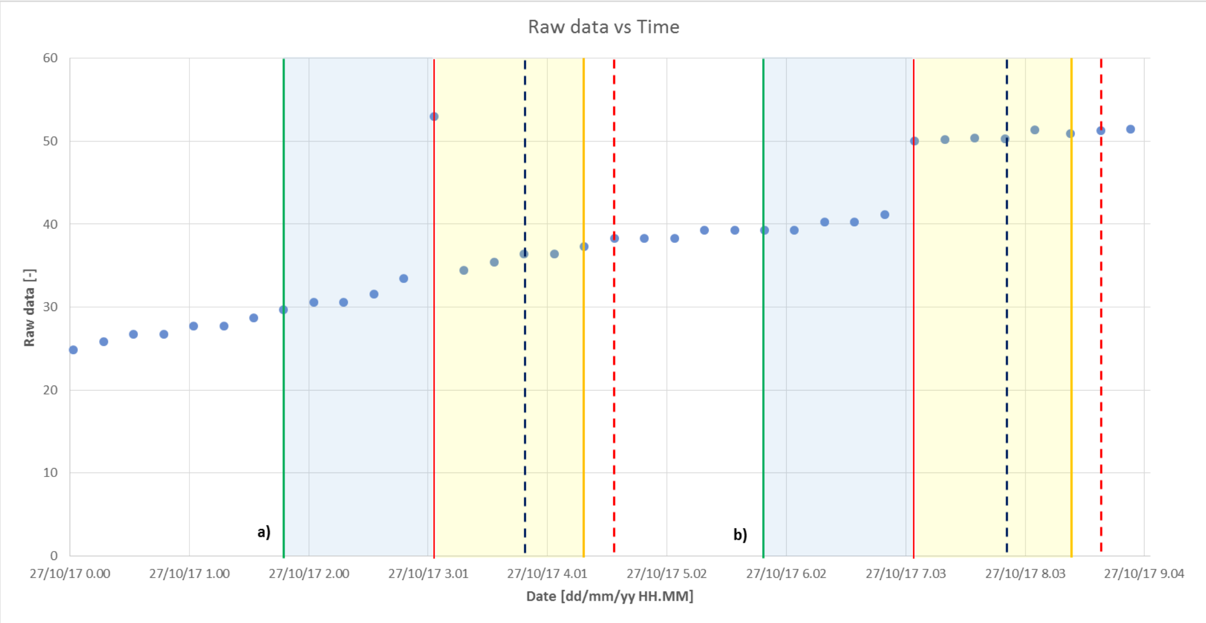

Fig. 3.41: Spike noise dataset referred to raw data represented by the red line, analysed using the dataset window which starts from the green line and terminates at the orange line. Transmission frequency is represented by red, dashed blue and dashed red lines.

In particular, when the information to be evaluated reaches the database, the calculation window starts 5 points before (green line) and only the left-weighted de-spiking process is possible (i.e. the outliers are evaluated only considering the data before). If this point does not follow the previous trend, two scenarios are possible: it is an outlier (case a) or a new movement trend is going on (case b). The software could not recognize the correct answer considering only the information provided by data before, due to the nature out of the trend of both possibilities. It follows that a possible displacement or outlier is highlighted for a) and b) situations, depending on the deviation from the median. This information has a reliability of the 50%. Then, 30 minutes later we have a new data transmission (blue dashed line) with 3 more sample data. Using the new dataset, the algorithm identifies the outliers in the case a), while case b) is evaluated as a displacement. The information obtained is quite confident (80%), but a small uncertainty still remain, because the dataset is not complete (2 data are still missing). The following data transmission (occurring 30 minutes later, red dashed line) complete the dataset (yellow line) and confirms the outcomes previously obtained with a level of confidence equal to 100%.

Eq. [3.116] summarizes the spike noise identification process.

$$out_i = f\left(t_{sp}, t_{ft}, d_w\right) \qquad [\ 3.116\ ]$$

Where:

- out_i is the identification process of outlier i;
- t_{sp} is the sampling period;
- t_{ft} is the frequency of data transmission;
- d_w is the dimension of dataset window.

t_{sp}, t_{ft} and d_w parameters should be defined accordingly to the monitoring needs. In particular, the sample period is related (Eq. [3.117]) to the expected evolution of the phenomenon: if a rapid movement may occur, t_{sp} has to be higher, highlighting and validating the displacement rate change in a short time. If the monitored landslide is a secondary creep, the sample period could be lower, able to identify the starting point of tertiary creep (as described in Chapter 5). t_{sp} is related to d_w and could change during the monitoring process, accordingly to the results or forecasted possibly dangerous events.

$$t_{sp} = f\left(v, d_w, e_p\right) \qquad [\ 3.117\ ]$$

Where:

- v is the displacement rate;
- e_p is the electrical power.

t_{ft} shows the same characteristics (Eq. [3.118]) of the previous parameter, with two more aspects. Frequency of data transmission determines the data elaboration, so should be higher (even equal to sample period) if the monitoring responsible requires a real time monitoring and an Early Warning System. Therefore, this process requires more electrical power than the sampling one (in particular in remote areas, where the 3G telephonic line is not well covered) and must be considered together with the design of the power supply.

$$t_{ft} = f\left(e_p, v, d_w, t_r\right) \qquad [\ 3.118\ ]$$

Where t_r represents the expected time period related to the providing of results to the monitoring responsible.

Finally the dimension of dataset window (d_w) is related to the phenomenon characteristics. In particular, it should be considered that a reduced dataset validates the raw data in a shorter time (Fig. 3.42) but could be not statistically valid. On the other hand, a large dataset improves the statistical processes and recognition of instrumental noise, causing a very long validation (and sometimes calculation) time. Therefore, it could be more permissive for outliers which are not very distant from the data trend. Fig. 3.42 reports the relationship between t_{sp} and d_w, considering $t_{ft} = t_{sp}$. In particular, a centred dataset of 11 data, like in the previous example, could be validated after 50 minutes, considering a sample period of 10 minutes, or 5 days, if the data are collected every 24 hours. A centred dataset of 25 data requires 2 hours for the validation, if the sample period equals 10 minutes, up to 10 days, for a daily reading of the sensors. Nevertheless the variation of results regards only sub-millimetre values for the majority of the cases. Due to the mentioned reasons, it is necessary to remind that the term "real time" is never correct in the monitoring field and should be substituted with "*near* real-time". It should also be noted that data of traditional tools are absolutely not consistent for a statistical validation of the outcomes and it is not possible to certificate the results considering the instrumental data trends. In this specific case, it is possible to assure the reliability of results only if there are other instruments providing a very similar and coherent information.

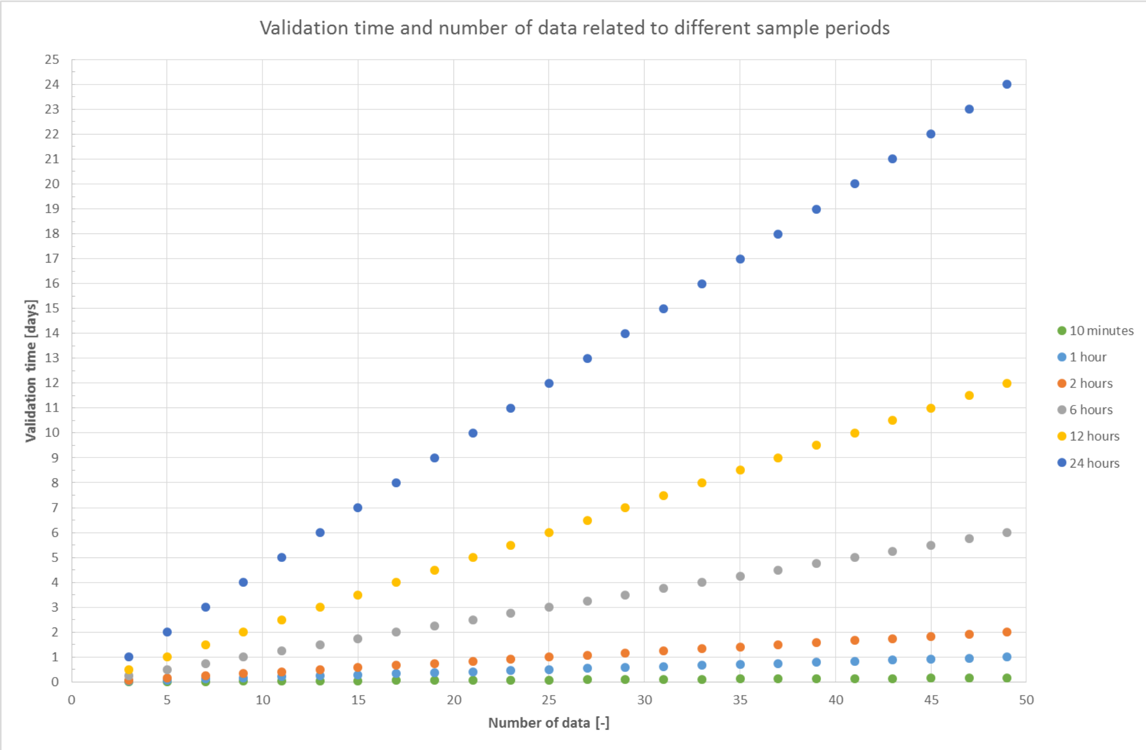

Fig. 3.42: Validation time and number of data related to different sample periods

The filter is not applied to temperature, pore and atmospheric pressures and quantities with an impulse nature, due to the more variable nature of the monitored physical entities.

Coherence of the gravity acceleration vector

Thanks to the 3D nature of MEMS that equips MUMS sensors Tilt Link V, Tilt Link H, Tilt Link HR 3D V & Tilt Link HR 3D H, it is possible to control the coherence of normalized gravity acceleration vector at every step of measures. In particular, the monitoring field regards static measures in which Earth gravity acceleration g is the only acceleration present. For this reason, instrumental data a_x, a_y, a_z has to verify Eq. [3.119]. The influence of earthquakes, vibrations, instrumental noise or malfunctions of the sensor is identified and removed according to Eq. [3.120], where Δ_g is the admitted variation from the gravity acceleration vector. The coherence of vector g has never been taking into account in literature due to the impossibility to reconstruct the gravity acceleration vector using 2D MEMS. The control is an innovative task of fundamental importance that characterizes MUMS system.

$$\frac{\sqrt{a_x^2 + a_y^2 + a_z^2}}{g} = 1 \qquad [\ 3.119\ ]$$

$$\left| 1 - \frac{\sqrt{a_x^2 + a_y^2 + a_z^2}}{g} \right| \geq \Delta_g \qquad [\ 3.120\ ]$$

Variability of the gravity acceleration vector

The acceleration recorded by MEMS sensor is subjected to instrumental noise that characterizes every electronic device. For this reason, a low variability of the instrumental gravity acceleration vector should be expected and analysed. An automatic filter (Eq. [3.121]) identifies variations between two measures higher than an admitted value (ε_g) and adjusts the related results. This control is complementary to the previous one: Eq. [3.120] represents the variation of instrumental gravity acceleration vector referring to the gravity field, while Eq. [3.121] analyses the variation of instrumental gravity acceleration vector itself, between two consecutive readings.

$$\left|\frac{\sqrt{a_{x_t}^2 + a_{y_t}^2 + a_{z_t}^2}}{g} - \frac{\sqrt{a_{x_{t-1}}^2 + a_{y_{t-1}}^2 + a_{z_{t-1}}^2}}{g}\right| > \varepsilon_g \qquad [\ 3.121\ ]$$

As an example, if we consider the a_x, a_y, a_z data reported in Tab. 3.9, $\Delta_g = 0.1$ and $\varepsilon_g = 0.0025$, the coherence control of gravity acceleration vector is activated only for case IV, while the variability of the gravity acceleration vector criterion is activated for cases III and IV.

Tab. 3.9: Comparison between coherence and variability of the gravity acceleration vector

	a_x	a_y	a_z	$\frac{\sqrt{a_x^2 + a_y^2 + a_z^2}}{g}$	$\left\|1 - \frac{\sqrt{a_x^2 + a_y^2 + a_z^2}}{g}\right\|$	$\left\|\frac{\sqrt{a_{x_t}^2 + a_{y_t}^2 + a_{z_t}^2}}{g} - \frac{\sqrt{a_{x_{t-1}}^2 + a_{y_{t-1}}^2 + a_{z_{t-1}}^2}}{g}\right\|$
I	0.018	0.015	0.995	0.995	0.005	-
II	0.017	0.012	0.993	0.996	0.004	0.001
III	0.017	0.009	0.991	0.991	0.009	0.005
IV	0.020	0.008	0.988	0.988	0.012	0.003

Coherence of the magnetic field vector

3D MEMS permits also to evaluate the coherence of the magnetic field recorded. Earth's magnetic field is not equivalent in every area, but, as already mentioned, it is a known variable (Campbell 1997) available on government or scientific institute websites. Starting from the Latitude, Longitude and altitude of the site, it is possible to reconstruct the resultant Earth magnetic field vector and to compare it with the instrumental resultant vector. In this way it is possible to identify anomalies of the local magnetic field and correct or ignore them in the calculation process.

Variation of the magnetic field vector

The filter is absolutely complementary to the variation of gravity acceleration vector and works in the same mode, starting from the definition of the tolerance value ε_m.

Coherence of node temperature

Due to the field of application and the fact that underground applications shows a temperature which is often around 10÷15 °C, node temperature should not exceed certain extreme values, where the electronic tools do not work. For this reason, if a node registers a temperature higher (T_h) or lower (T_l) with respect to the two defined parameters, the instrumental information are considered as not valid (as in Eq. [3.122]). Reasonable values for T_h should be 70÷80 °C, while T_l could be defined equal to -20 °C.

$$T_n < T_l \vee T_n > T_h \qquad [\ 3.122\ ]$$

Running average

The centred running average operation is complementary to the recognition of spike noise and it is able to identify and reduce instrumental noise, together with the definition of a specific data trend. This operation is of fundamental importance where very small movements are expected, if compared to instrumental sensibility and repeatability. For the same issues highlighted before, the considered running average window should not be too small or too large. Therefore, higher is the running average dataset, lower is the tilt of displacement trend. If a rapid movement occurs, the neighbouring average operation could strongly reduce the displacement rate, anticipating the date of activation and postponing the date of conclusion. Fig. 3.43 reports an example of a rapid displacement which is not subjected to running average process. It is possible to observe a swift increase of movement, followed by a stable series, only influenced by an instrumental noise of 1.7 mm.

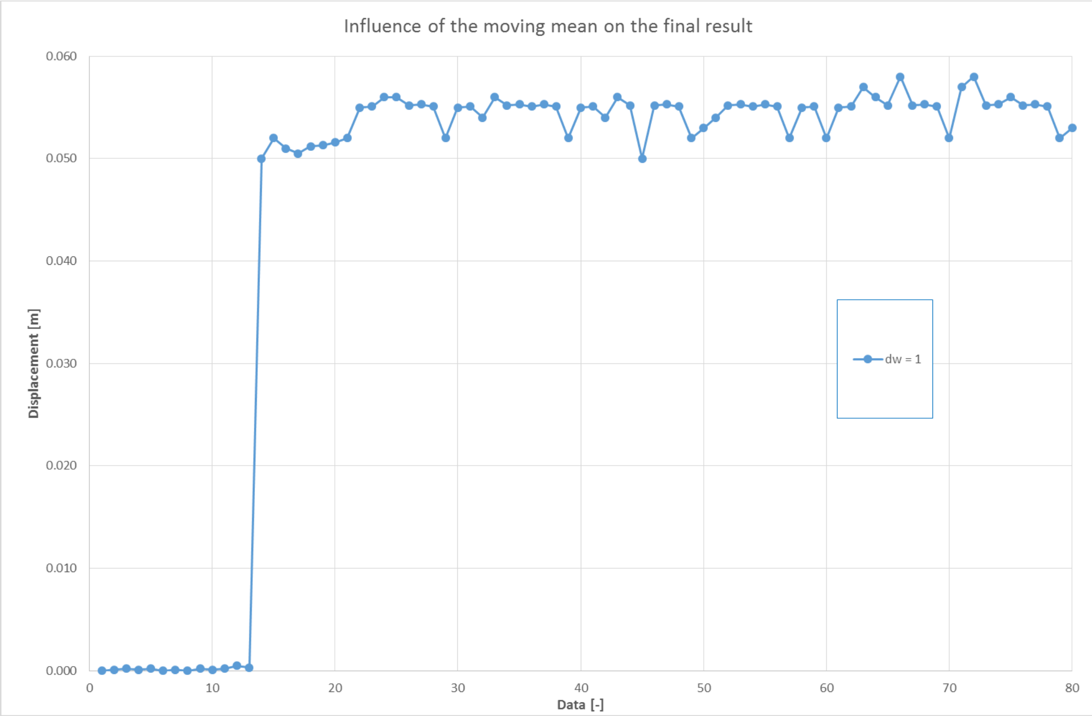

Fig. 3.43: Rapid displacement not subjected to running average process

Processing the same dataset using a centred running average of 3 elements (orange dots in Fig. 3.44) it is possible to observe that the movement apparently starts one data before and terminates one data after, for an event time of 3 data. The resultant instrumental noise equals 1.2 mm.

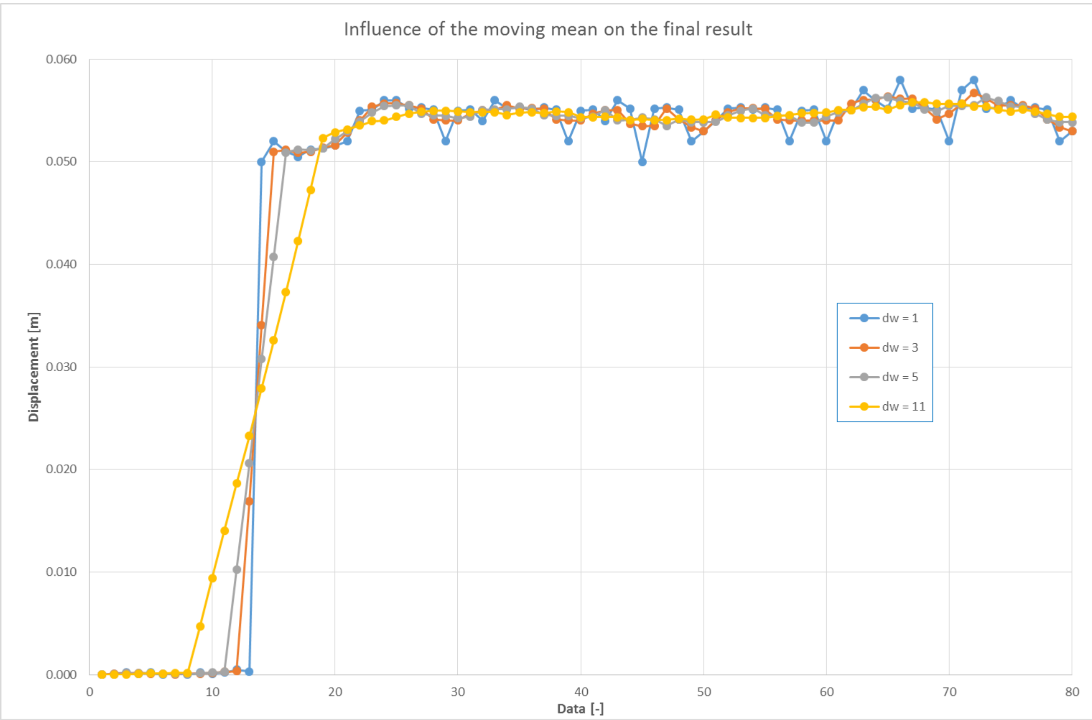

Fig. 3.44: Rapid displacement not subjected to running average process (blue) and analysed with a centred running average window of 3 (orange), 5 (grey) and 11 (yellow) points

The situation is amplified if the data set increases. A centred running average of 11 elements (yellow dots) anticipates the displacement of 5 data and terminates 5 data later, with an instrumental noise of 0.9 mm (two times lower than the dataset not subject to the running average operation). Increasing the dataset up to 99 data (dark blue dots in Fig. 3.45), the instrumental noise is of 0.1 mm (17 times lower than the original data) but the movement is anticipated of 49 data and apparently continues for other 49 data. It follows that the right balance of the running average window is expressed by the correct knowledge of the phenomenon and the aim of the monitoring.

If it is necessary to detect very small displacements that could be confused with instrumental noise, it is necessary to define a large dataset, accepting the risk to highly anticipate the accelerating phase (once the dataset is completely centred) and consistently reduce the displacement rate. In order to find a correct balance, it is suggested to increase the sampling period. If a consistent rapid movement is expected, a very low running average window should be used to the detriment of instrumental noise and data variability (Tab. 3.10). A balanced solution is required in the other cases.

Tab. 3.10: Example of instrumental noise reduction with the increasing of the running average dataset

	$d_w = 1$	$d_w = 3$	$d_w = 5$	$d_w = 11$	$d_w = 23$	$d_w = 51$	$d_w = 99$
Instrumental noise [mm]	0.0017	0.0012	0.0009	0.0006	0.0004	0.0002	0.0001

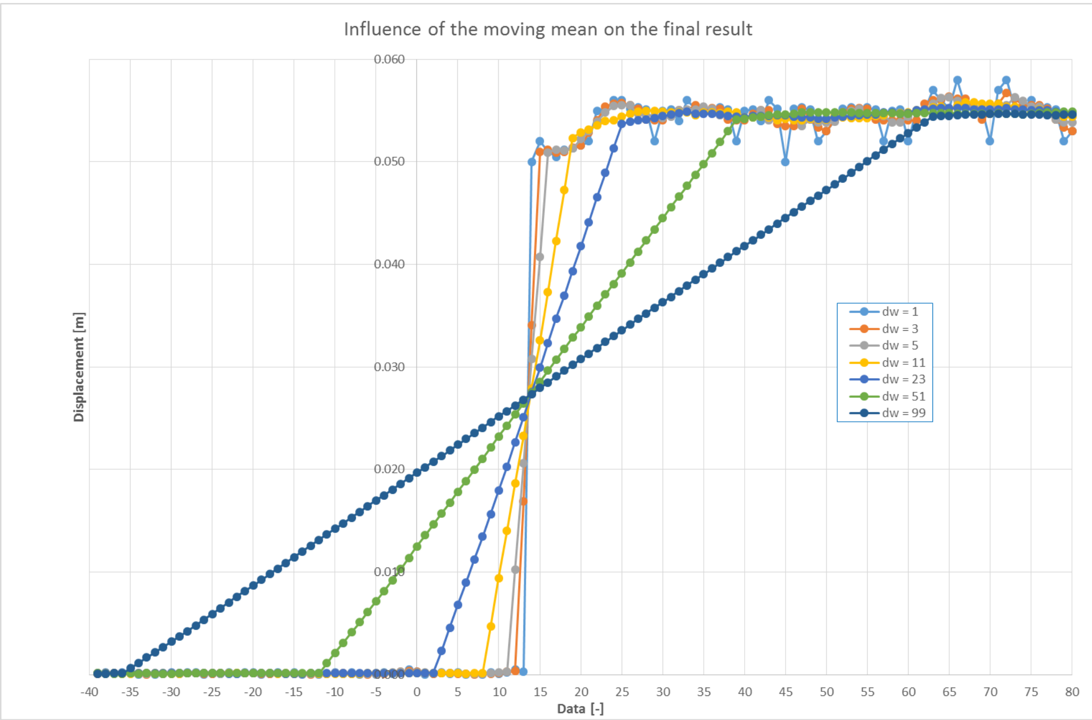

Fig. 3.45: Rapid displacement not subjected to running average process (light blue) and analysed with a centred running average window of 3 (orange), 5 (grey), 11 (yellow), 23 (blue), 51 (green) and 99 (dark blue) points

Recognition of instrumental noise

The recognition of instrumental noise task has been widely discussed in the previous paragraph. Due to the fact that every electronic tool is subjected to instrumental noise, it is necessary to detect and quantify it. After the definition of the data variability on site, the responsible of monitoring could identify the "real" sensibility and repeatability of the instrumentation, which has always a lower performance than the one derived from laboratory tests and optimistically declared in the data sheet. The definition of the real sensibility permits to recognize and validate (or not) the small displacements that may occur. Fig. 3.46 shows three (real) displacement data recorded by MUMS instrument (Tunnel Link sensor).

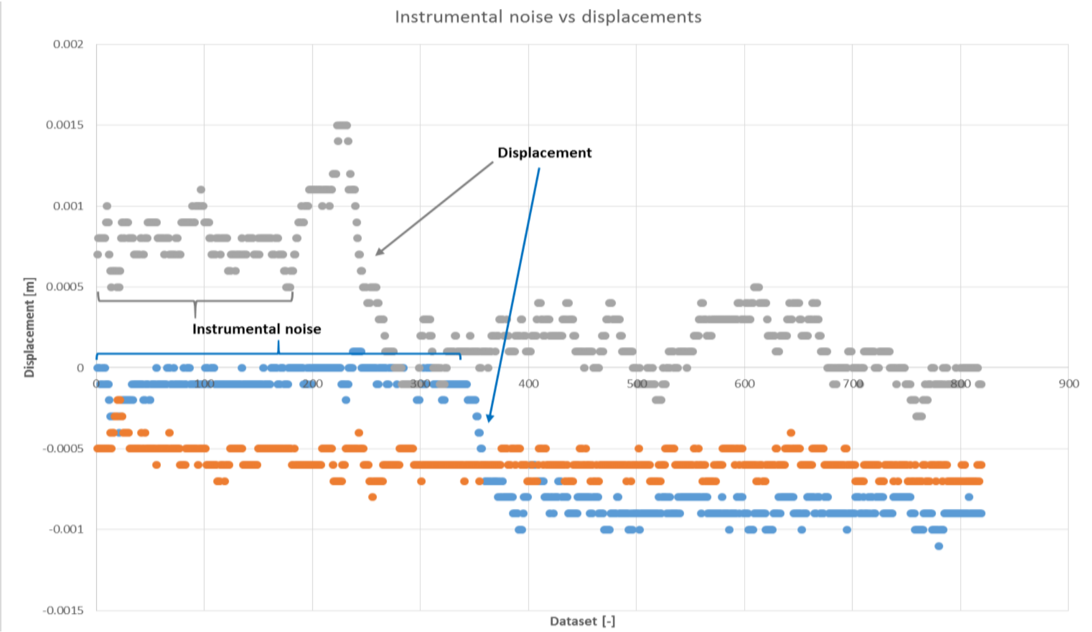

Fig. 3.46: Recognition of instrumental noise and displacements

The analysis of standard deviation highlights a data variability of 0.1 mm for the orange and blue datasets, while the grey points show an oscillation of 0.2 mm (that could be extended to 0.5 mm of instrumental noise, considering an adequate running average dataset). This could be related to many reasons, like for example the installation position and the excavation distance (the dataset is referred to the convergence measure just after the excavation of the considered section and during the digging of the following one). Once achieved this knowledge, a displacement of the grey series is validated only if it is superior to half a millimetre, while blue and orange samples information is valid if higher than 0.1 mm. The algorithm defines the instrumental noise (and consequently the validation threshold) for every single sensor.

Recognition of not-operating sensors

All the mentioned Self-check controls identify anomalies that could regard the values of a single or a series of sensor readings. It may happen that a sensor does not answer or is completely compromised for some reasons. In this case, control unit queries the node two times and, after that, continues the series of reading with the following one. Therefore, the Link returns an error text code related to the undergoing issue. This code could not be elaborated and causes the crash of the software, which can elaborate only numerical values. For this reason, when an error code is identified, the last working numerical value of the Link is reported to permit the elaboration of other sensors at that specific date. Anyway, the information about the malfunction is not lost and reported on the database (using a binary code, where 0 represents a working node and 1 identifies a malfunction) and finally on the web platform (Fig. 3.47). Here the responsible of the monitoring knowns that the specific information related to sensor i at the date j is not valid and should be ignored.

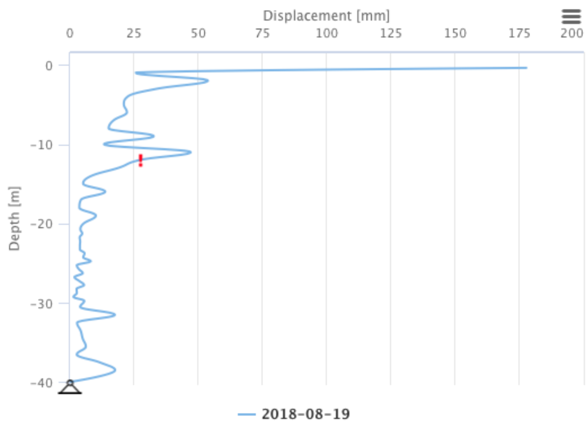

Fig. 3.47: Web platform representation of the malfunction that regards the node at 12 m depth

Chapter 4

"Knowledge is power, and the right knowledge lets man perform miraculous, almost godlike tasks."

Brown D. – The Lost Symbol

TIME OF FAILURE PREDICTION

During recent years, the forecast of landslide time of failure has been a particularly relevant task of natural hazard assessment. In particular, the definition of alert thresholds is a fundamental aspect for the risk management process, influenced by a high number of parameters and factors. Numerous articles highlight this difficulty presenting a site-specific approach, where thresholds are evaluated for each single case and sometimes also for different homogeneous areas on the same site. An accurate time of failure prediction could have a key role in the case of an Early Warning System (EWS) based on displacement sensors with an adequate sample period.
This chapter summarizes the studies reported in literature and the article of Segalini et al. (2018c), introducing an attempt to generalize the behaviour and the alert thresholds of the landslide when the collapse is approaching.

4.1. Literature

The first studies about landslide Time of Failure date back to the early 60s (Saito and Uezawa 1961). Their method is based on the comparison between displacements recorded and creep rupture curves, obtained from triaxle load-controlled laboratory tests. Other articles (Saito 1969, Saito 1979) report the application of the methodology. After two decades, Fukuzono (1985) developed a new approach based on large-scale laboratory tests. In particular, the article focuses his attention on the inverse of displacement rate, which decreases with time after the activation of the tertiary creep. The time of failure is provided by the interception between the x-axis (reporting time as independent variable) and the extension of monitoring data interpolation line. Fukuzono theory has been applied to numerous back analysis about different fields, like volcanic eruptions (Voight 1988, Voight 1989), catastrophic events (Kilburn and Petley 2003), man-made slopes (Petley 2004), open pit mines (Carlà et al. 2017a). During recent years, a new method (Mufundirwa et al. 2010) proposes to evaluate the time of failure determining the slope of a curve obtained through the elaboration of monitoring data. Together with the definition of time of failure, scholars have focused their attention on the definition of alert thresholds. At the end of 80s, three velocity thresholds levels were proposed (Cruden and Masoumzadeh 1987) in order to determine the critical time to start the evacuation of an open pit mine. The levels correspond to the accelerating creep stages. Intrieri et al. (2012) applied the concept to the Early Warning System of Torgiovannetto landslide, identifying the most critical periods of the monitoring dataset to define three displacement velocity thresholds. Voight's model has been applied (Crosta and Agliardi 2002) to create "characteristic velocity curves" that represent the behaviour of a monitored sub-area of the rock-mass approaching to failure. In the case study of Ruinon, authors defined 30, 15 and 7 days alert velocity thresholds. Manconi and Giordan (2015) proposed a EWS with alert levels integrated together with the time of failure prediction model, constantly updated by data of monitoring system. Some authors have investigated different methods and monitoring technologies (Federico et al. 2012, Herrera et al. 2013, Wasowski and Bovenga 2014, Wasowsky et al. 2014, Moretto et al. 2017). Intrieri and Gigli (2016) evaluated the application of Saito, Fukuzono and Mufundirwa methods to different cases with a Predictability Index (PI), ranging from 1 to 5. Results highlight the similarity between Fukuzono and Saito models, while Mufundirwa has a lower performance. In particular, the first two methods have a different quality referring to a specific case. For this reason, Fukuzono and Saito models could be considered as independent and non-redundant.

4.1.1. Creep Theory

The methods previously described approach the evaluation of time of failure in different ways using common principles. The main hypothesis relates to the assumption that displacements have a continuous acceleration approaching to failure, as discussed for the first time by Terzaghi (1950). This acceleration follows a hyperbolic trend, defined as "tertiary creep" (Varnes 1982). The creep is generally characterized with three steps (Fig. 4.1): if subjected to a constant load, the first one shows a decreasing of the strain rate, the second has a constant strain rate and finally the third evinces an increasing of the strain rate. Other authors (Ter-Stepanian 1980, Tavenas and Leroeuil 1981) observed the presence of relevant creep deformations before failure in some case studies.

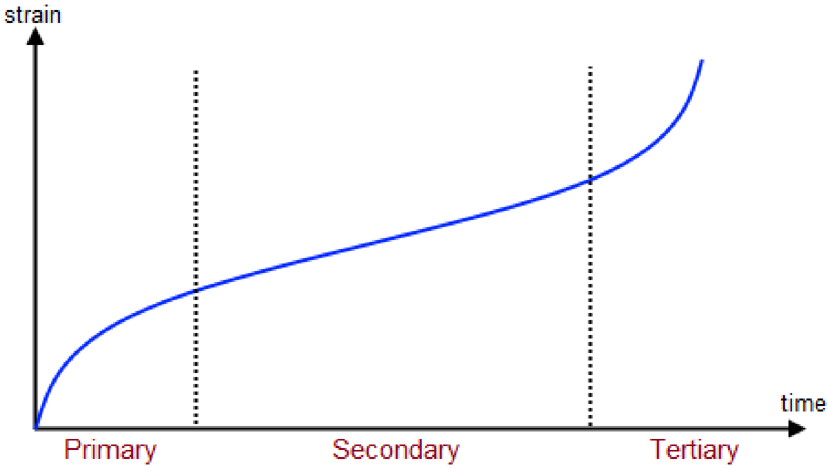

Fig. 4.1: Possible Creep behaviours under the same load conditions: decreasing of displacement with time (Primary), constant displacement rate (Secondary) or increasing of displacements with time (Tertiary)

4.1.2. Inverse Velocity Method

Thanks to its ease of application and the effectiveness of results in numerous cases, even with its limitations, author of this thesis has focused his attention on the Fukuzono method or Inverse Velocity Method (IVM). This model considers the data from the tertiary creep phase, relating the inverse of the displacement rate with time. Fukuzono studied small-scale models thus identifying a proportionality between acceleration and velocity, as in Eq. [4.1].

$$\frac{d^2x}{dt^2} = A\left(\frac{dx}{dt}\right)^{\alpha} \qquad [\ 4.1\ ]$$

Where:

- x represents the slope surface displacement at the point of measure;
- t is time;
- A and α are constant dimensionless parameters.

Then, landslide Time of Failure (T_f) is formulated through Eq. [4.2].

$$\frac{1}{v} = \left(A(\alpha-1)(T_f - t)\right)^{\frac{1}{\alpha-1}} \qquad [\ 4.2\ ]$$

Where:

- v is the surface displacement rate;
- T_f is the Time of Failure;
- t is the monitoring time.

α parameter governs the trend of inverse velocity vs time curve (Fig. 4.2) with a value that ranges between 1.5 and 2.2 for natural slopes (Fukuzono 1985, Fukuzono 1989). In particular, $\alpha = 2$ represents the linearity of

the relationship and is generally a good assumption to estimate T_f. Rose and Hungr (2007) observed that the hypothesis is particularly verified when considering data close to failure. Bozzano et al. (2014) underline that lower values of α are frequent in the case of slope influenced by man-made structures. A and α require a preliminary calibration in order to define the theoretical velocity versus time characteristic curve.
Voight (1988, 1989) studied in detail the Fukuzono model applying the equation as a more general fundamental law that governs materials failure. The result is the Eq. [4.3].

$$\ddot{\Omega} = A\dot{\Omega}^{\alpha} \qquad [\ 4.3\ ]$$

Where:

- $\dot{\Omega}$ is the displacement rate;
- $\ddot{\Omega}$ is the acceleration.

Voight (1988) considers Ω as conventional geodetic observations, seismic quantities or geomechanical observations. Eq. [4.3] was used to predict volcanic eruptions (Voight 1988, Voight 1990, Cornelius and Voight 1995) using $\alpha = 2$.

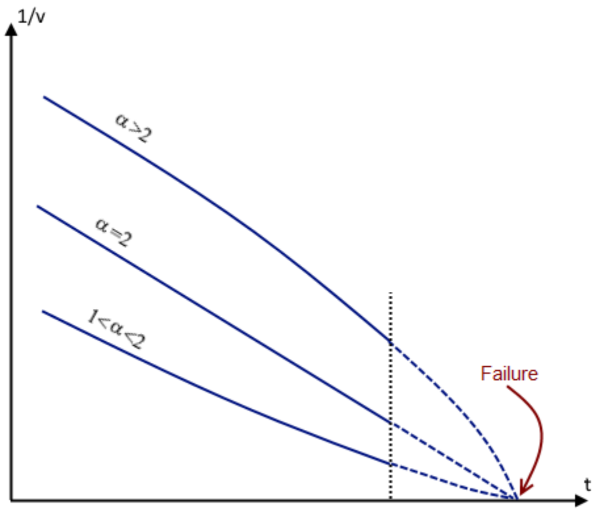

Fig. 4.2: Inverse velocity versus time relationship related to the variation of α (modified after Fukuzono 1985)

The applicability of IVM requires the availability of monitoring data with an adequate frequency. Rose and Hungr (2007) analysed the case of open-pit mines and highlighted that the update of the model with latest available information forecasts a more reliable collapse prediction. Authors also suggest to continue the monitoring activity until the proximity to failure.
A second major task is the quality of the monitoring activity in terms of sensitivity, precision and instrumental noise, in particular if it is comparable with the entities to be evaluated (Intrieri and Gigli 2016). Instrumental noise could be corrected with post-processing smoothing (Dick et al. 2015, Carlà et al. 2017b) that requires to be tested before. Finally, while the method has a demonstrated validity, it is fundamental to remember that its application has to be carefully evaluated by responsible authorities for each specific case. T_f should not be considered as a deterministic prediction of the collapse. It follows that the method is able to determine that the failure is approaching (Carlà et al. 2018) referring to a time window, which should be considered using short-time and long-time data running average (Carlà et al. 2017b). The method applicability has to take into account also the following tasks:

- The method is based only on monitoring displacements recorded, which is a single aspect of a complex phenomenon. Predisposing factors and driving forces are not taken into account by IVM. For this reason, responsible authorities should not apply it in isolation;

- The model is quite weak in the representation of brittle failure, due to the extremely rapid evolution of this kind of events. The uncertainties could be reduced with the installation of a high-frequency monitoring system, able to represent the acceleration in place (Carlà et al. 2017b);
- As mentioned before, it is highly recommended to identify and remove natural and instrumental noise through statistical tools;
- Unknown factors could unpredictably change the data trend.

IVM has a warning meaning and should not be considered as a closed box truth that predicts the hour and minute of collapse. However, the approach has proven to be successful and permits its integration in EWS applications (Atzeni et al. 2014, Manconi and Giordan 2016, Sättele et al. 2016).

4.1.3. Analysis of historical landslides

This paragraph reports the application of Fukuzono method (Fig. 4.3) to the dataset represented by some historical landslides reported in literature. In particular, pre-failure displacements and displacements ratio data have been recovered and digitalized from scientific literature using *Engauge Digitizer* software, converted into millimetres/day and reported in graphs. A and α parameters have been calibrated using first attempt values of $\alpha = 2$ and $A = -m$ (slope of the interpolating curve). Then it follows the fit of the monitoring data available with the Generalized Reduced Gradient (GRG) method (Lasdon et al. 1974), minimizing the Root Mean Square Error (RMSE), defined in Eq. [4.4] (Barnston 1992).

$$RMSE = \left[\sum_{i=1}^{N} \frac{\left(z_{f,i} - z_{o,i}\right)^2}{N} \right]^{\frac{1}{2}} \qquad [\ 4.4\ ]$$

Where:

- $z_{f,i}$ represents the forecasted value;
- $z_{o,i}$ is the measured value;
- N is the number of observations.

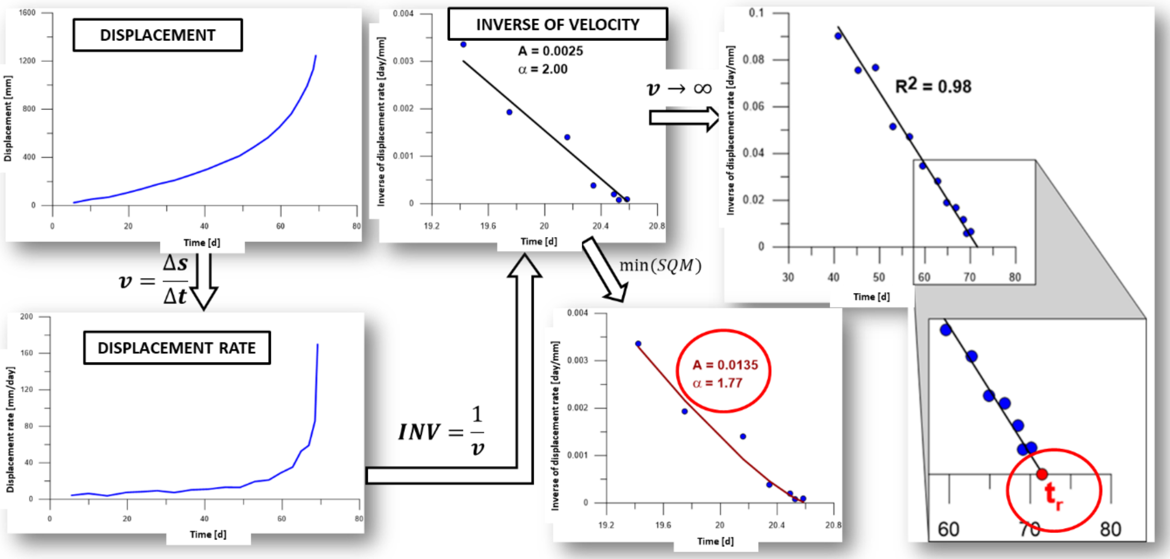

Fig. 4.3: Procedure followed in the analysis of historical landslides. After the evaluation of displacements over time, it is possible to calculate the displacement rate and consequently the inverse of velocity versus time. This information is useful to calibrate A and α parameters and to define the intersection between x-axis (time) and extension of dataset linear interpolation, which leads to the definition of Time of Failure

After the operation described, it has been possible to define a characteristic velocity curve. This curve represents the behaviour of the landslide starting from 30 days before the failure occurrence. Fig. 4.4 shows the curves related to Betze Post SW (Rose and Hungr 2007), Mt. Beni (Gigli et al. 2011) and Ooigawa (Saito 1969) case studies. This procedure identifies curves with very different displacement rate magnitudes which are not comparable in a single graph. Using this representation, it is not possible to generalize the criterion and extend the knowledge to other case histories.

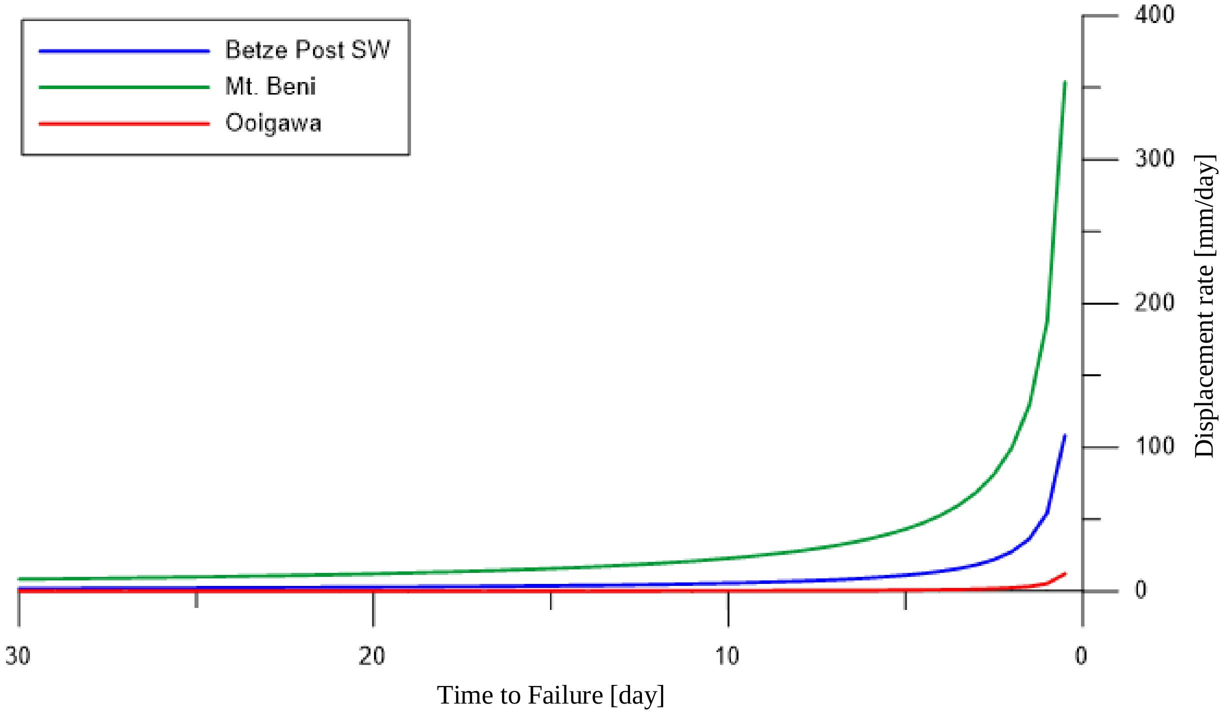

Fig. 4.4: Characteristic velocity curves related to three different case studies

Tab. 4.1 summarizes the considered dataset, including information about the volumes involved, the materials, the failure mechanisms, triggering factors, duration of the monitoring periods and references.

The cases have relevant differences about materials (rocks or soils), failure mechanisms (toppling, rock slide, earth flow, roto-translation, etc.) and triggering factors. It is also possible to observe a consistent variation in the quality and frequency of monitoring data. In particular, some applications recorded the transition between secondary and tertiary creep, while other sampled only the accelerating phase.

By applying the Fukuzono-Voight (FV) model (Voight 1988), as in Eq. [4.5], it is possible to obtain site-specific curves, with displacements and velocity order of magnitude that can not be compared.

$$v_{FV} = \left(A(\alpha - 1)(T_f - t)\right)^{\frac{1}{1-\alpha}} \qquad [\ 4.5\ ]$$

Starting from the collected data and Fukuzono method, a new generalized method has been studied in order to overcome the site specificity, as described in the following paragraph.

Tab. 4.1: Database of landslides collected from literature, including information about volumes involved, materials, failure mechanisms, triggering factors, durations of the monitoring and references

Name	Volume [m^3]	Material	Failure mechanism	Triggering Factor	Monitoring duration [days]	References
Afton Mine	$28x10^6$	Rock	Toppling	Excavation, Blasting	68	Glastonbury and Fell, 2002
Asamushi	$1x10^5$	Rock	-	Weathering	7	Saito, 1969
Betze Post SE	$18x10^6$	Rock	Compound	Groundwater	45	Rose and Hungr, 2007
Betze Post SW	$2x10^6$	Rock	Rock Slide	Rainfall	5	Rose and Hungr, 2007
Bomba	$12x10^6$	Soil	Slump	Excavation	1290	Urciuoli and Picarelli, 2008
Braced up Cliff	$1.2x10^4$	Rock	Toppling	Frost Action, Snow Melt	1886	Schumm and Chorley, 1964
Cavallerizzo	$5x10^6$	Rock, Soil	Rock Slide, Earth Flow	Rainfall, Snowfall	7	Iovine et al., 2006
Chuquicamata	$4.1x10^6$	Rock	Compound	Excavation, Seismic Actions	140	Voight and Kennedy, 1979
Delabole Quarry	-	Rock	Toppling	Rainfall	5900	Boyd et al., 1973
Dosan Line	$6x10^4$	Rock	-	-	3	Saito, 1969
Hogart Pit	$2x10^5$	Rock	Toppling	Rainfall, Snow Melt, Excavation	285	Brawner and Stacey, 1979
Huanglongxi	$3.9x10^5$	Rock	-	Rainfall, Human Activities	6	Li et al., 2012
La Chenaula	$1.6x10^6$	Rock	Roto-Translation	-	912	Engel et al., 1983
La Saxe	$8.4x10^6$	Rock	Rock Slide	Snow Melt	30	Manconi and Giordan, 2016
Maoxian	$18x10^6$	Rock	Rock Avalanche	Rainfall	1014	Intrieri et al., 2018
Mt Beni	$5x10^6$	Rock	Rock Slide, Toppling	Water and Snow	240	Gigli et al., 2011
Nevis Bluff	$3.2x10^4$	Rock	Rotation	Excavation	272	Brown et al., 1980
Ohto	$2x10^5$	Rock	-	Rainfall (Typhoon)	90	Suwa et al., 2010
Ooigawa	$6x10^4$	Soil	Earth Flow	Erosion	10	Saito, 1969
Preonzo	$2.2x10^5$	Rock	Rockfall	-	12	Geoprævent, 2012
Puigcercòs	$10.12x10^5$	Rock	Rockfall	Gradual Degradation	2217	Royàn et al., 2015
Selborne	$1.8x10^4$	Soil	Roto-Translation	Groundwater	400	Petley, 2004
Town of Peace River	-	Rock	Roto-Translation	Rainfall	180	Kim et al., 2010
Tuckabianna West	$1.25x10^6$	Rock	Translation	Excavation	37	Glastonbury and Fell, 2002
Vajont	$270x10^6$	Rock	Roto-Translation	Groundwater	70	Sornette et al., 2004
Xintan	$30x10^6$	Rock	Rock Slide	Rainfall, Groundwater	2550	Keqiang and Sijing, 2006

4.2. New generalized method

In order to overcome the site-specific concept, Segalini et al. (2018c) propose to normalize the velocity data obtained with the application of a new generalized model, as in Eq. [4.6].

$$v_n = \frac{v_{FV} - \mu_{v_{FV}}}{\sigma_{v_{FV}}} \qquad [\ 4.6\ ]$$

Where:

- v_n dimensionless velocity parameter;
- v_{FV} velocity obtained with the application of Fukuzono-Voight model, expressed as mm/d;
- $\mu_{v_{FV}}$ mean of the velocity dataset, obtained with the application of FV model;
- $\sigma_{v_{FV}}$ standard deviation of the velocity dataset, obtained with the application of FV model.

The new dimensionless velocity parameter v_n permits the comparison between data of different case studies, as in Tab. 4.1. The procedure application returns a normalized displacement rate vs time curve that could be of fundamental importance in the definition of a landslide behaviour approaching to failure and preliminary generalized alert velocity thresholds.

4.2.1. Results

The prediction of T_f has been computed applying IVM under the hypothesis of linear behaviour, providing reliable results, as expressed by R^2 index in Tab. 4.2.

Tab. 4.2: Observed and forecasted Time of Failure for considered landslide dataset

Name	Observed T_f [d]	Predicted T_f [d]	ΔT_f [d]	Linear regression			Non-linear regression		
				A	***α***	**R^2 [-]**	***A***	***α***	**R^2 [-]**
Afton Mine	69	69	0	0.0014	2.00	0.9554	0.0016	1.94	0.9588
Asamushi	7	7	0	0.0046	2.00	0.8511	0.0056	1.96	0.8534
Betze Post SE	45	45	0	0.0121	2.00	0.9981	0.0119	2.00	0.9981
Betze Post SW	5	5	0	0.0183	2.00	0.9948	0.0173	2.01	0.9950
Bomba	1,320	1,352	32	0.0041	2.00	0.8635	0.0038	2.15	0.8822
Braced up Cliff	1,910	1,904	-6	0.0529	2.00	0.9189	0.0548	1.53	0.9764
Cavallerizzo	6	6	0	0.0654	2.00	0.9937	0.0779	1.96	0.9998
Chuquicamata	263	263	0	0.0006	2.00	0.7693	0.0004	2.10	0.7788
Delabole Quarry	5,899	5,954	55	0.0218	2.00	0.7423	0.0205	1.96	0.7464
Dosan Line	3	3	0	0.0105	2.00	0.9725	0.0098	2.01	0.9726
Hogart Pit	291	286	-5	0.0022	2.00	0.9730	0.0024	1.97	0.9748
Huanglongxi	5	5	0	0.0151	2.00	0.9057	0.0109	2.00	0.9057
La Chenaula	884	890	6	0.0821	2.00	0.2955	0.0767	1.94	0.2966
La Saxe	21	21	0	0.0025	2.00	0.9492	0.0135	1.77	0.9572
Maoxian	1,018	1,020	2	0.0827	2.00	0.9446	0.0777	1.93	0.9476
Mt Beni	258	260	2	0.0002	2.00	0.9310	0.0015	2.13	0.9312
Nevis Bluff	287	279	-8	0.0191	2.00	0.9790	0.0191	2.00	0.9788
Ohto	92	91	-1	0.0303	2.00	0.9515	0.0400	1.90	0.9561
Ooigawa	9	9	0	0.1216	2.00	0.9960	0.2813	1.85	0.8468
Preonzo	13	13	0	0.0028	2.00	0.6057	0.0024	2.03	0.6065
Puigcercòs	2,198	2,264	66	0.0116	2.00	0.8776	0.0106	1.94	0.8822
Selborne	600	597	-3	0.1495	2.00	0.9690	0.1570	2.03	0.9695
Town of Peace River	178	181	3	0.1241	2.00	0.6015	0.1371	2.05	0.6043
Tuckabianna West	38	37	-1	0.0426	2.00	0.8858	0.0343	2.07	0.8897
Vajont	70	71	1	0.0307	2.00	0.9767	0.0319	1.97	0.9778
Xintan	2,800	2,805	5	0.0007	2.00	0.8831	0.0008	2.00	0.8831

In order to make a comparison in the evaluation of the governing parameters, non-linear behaviour has been taken into account only for the estimation of A and α. In particular, 11 cases of a total of 26 (42%) forecast the exact day of collapse, while 17 of 26 (66%) predict a T_f less or equal to the observed time of failure, with a mean anticipation of 1 day and 10 hours and a maximum anticipation of 8 days. 4 cases (15%) show a T_f overestimated of 3 days or less, which should be anyhow considered as a useful information for hazard assessment management. IVM method fails the prediction in the 19% of the cases, postponing the failure event of a mean value of 19 days. Moreover, A parameter shows a variability of three orders of magnitude. R^2 coefficient has a value higher or equal than 0.95 in the 42% (linear regression) or 46% (non-linear regression) of the dataset, while it is greater than 0.90, 0.80 and 0.70 respectively in the 62% (linear) or 58% (non-linear), 81% and 88% of the cases. Poor values of the linear regression coefficient could be attributed to various factors:

- Insufficient quantity or frequency of monitoring data;
- Inadequate quality of monitoring data;
- Excessive natural or instrumental disturbing noise and inadequate post processing;
- Incorrect interpretation of the data during the digitalization process;
- Landslide behaviour diverging from linearity (i.e. asymptotic).

The percentages obtained for R^2 highlight the slightly differences between linear and non-linear regressions and validate the application of the first one, due to its simplicity and efficacy, as mentioned in literature (Rose and Hungr 2006; Gigli et al. 2011; Dick et al. 2015).

In order to improve the representation of landslide behaviour and take into account a non-linear regression, the model requires a preliminary calibration of A and α parameters (reported in Tab. 4.2). An example of the procedure is shown in Fig. 4.5. α shows results that are consistent with the range of values (1.5÷2.2) reported in literature (Fukuzono 1985, Fukuzono 1989). In particular, 14 of 26 cases (54%) show a variation which is less than 0.05, 19 of 26 (73%) less than 0.1 and 24 of 26 (92%) feature $\Delta\alpha < 0.2$. Another important information obtained regards the concavity of the trend, which is convex ($\alpha < 2$) for the majority of the dataset (13 vs 9). After calibration, A has an increment in the variation related to the increase of divergence from the linearity. In particular, where a pronounced non-linear behaviour is observed, the difference could reach even one order of magnitude.

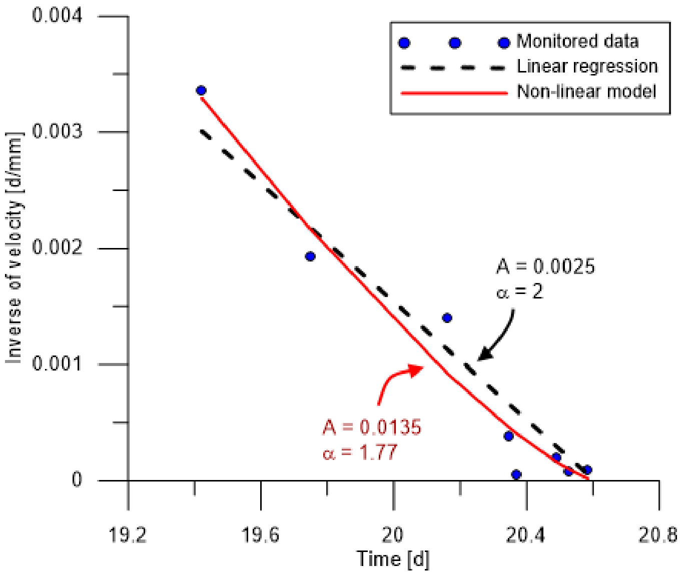

Fig. 4.5: Linear and non-linear regressions after the model calibration. La Saxe landslide (data source: Manconi and Giordan 2016)

After calibration, it is possible to apply Eq. [4.5] to define the site-specific velocity curve, starting from 30 days before the observed collapse. The graph describes the theoretical displacement rate assumed by the landslide some weeks or days before the failure. Due to the site-specific meaning of the curves, it is only possible to assess a unique set of alert thresholds for each case.

By applying the new generalized criterion, as expressed in Eq. [4.6], it is possible to identify a generalized trend which is valid for all the mentioned case histories (Fig. 4.6).

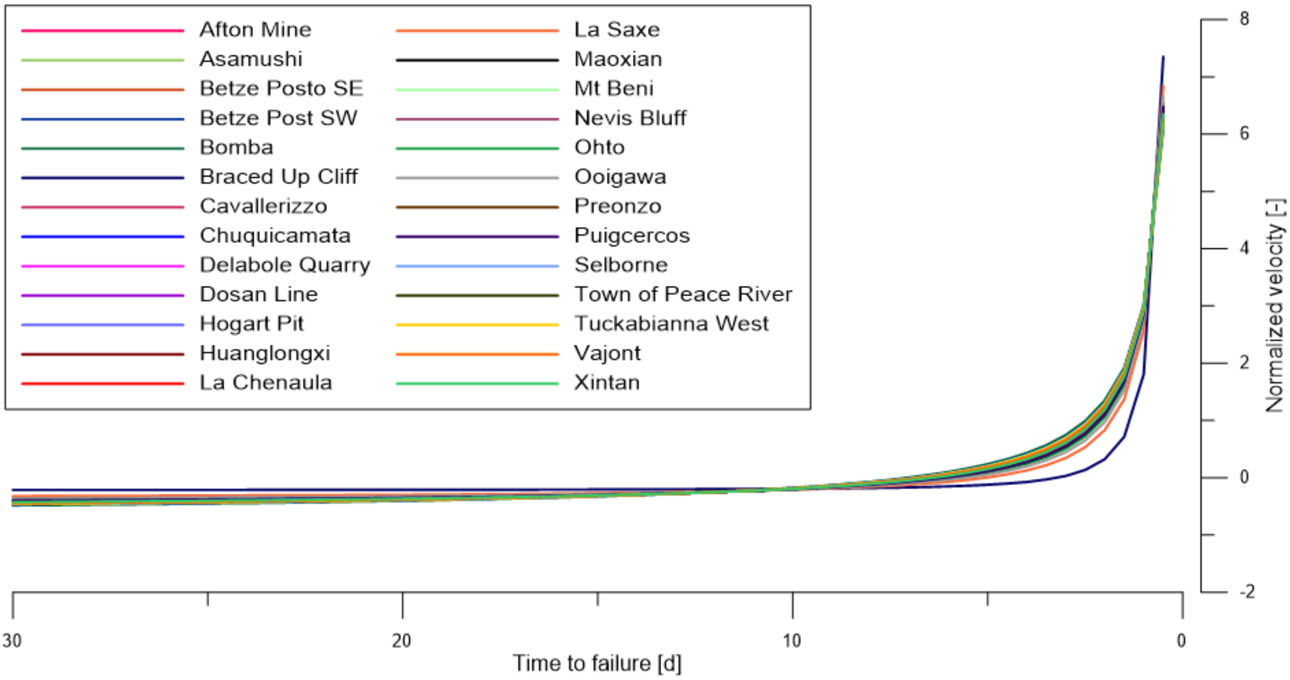

Fig. 4.6: Normalized velocity v_n versus time, including all the 26 case histories

The new introduced dimensionless parameter v_n increases its value approaching to failure, reaching a vertical asymptote for $t = 0$. Normalized velocity rescales the different orders of magnitude of observed displacement rates and permits a direct comparison, leading to the creation of an abacus. It is interesting to observe that all the 26 cases have a change in the sign of dimensionless velocity 10 days before failure. When $t < 10$ days, each curve start to show a peculiar behaviour. This appears more evident approaching the collapse and depends on α parameter. In particular, if the curve has a non-linear behaviour ($\alpha < 2$) the high acceleration phase appears later, while $\alpha > 2$ leads to an earlier velocity increasing (Fig. 4.7).

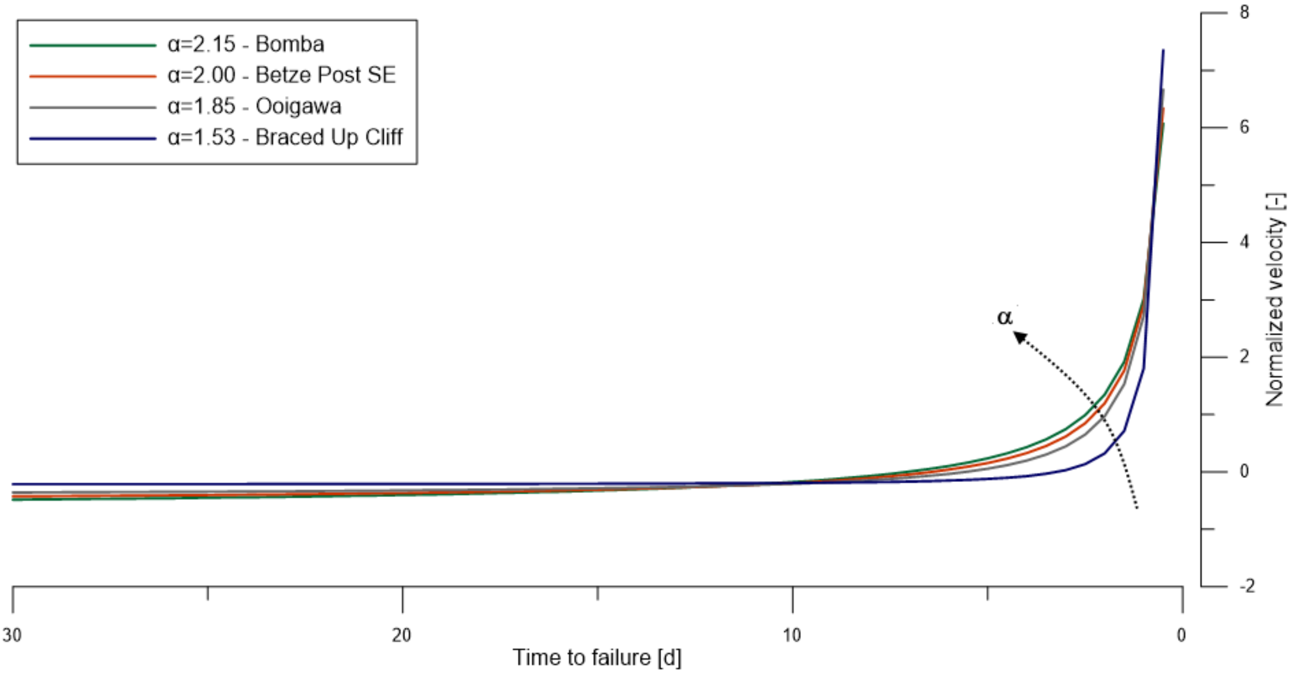

Fig. 4.7: Influence of the α parameter on the curves trend, displayed by four different case histories

An interesting consequence that regards the application of the new proposed method is the negligibility of A parameter. As mentioned above, this parameter could have a wide range of variability and it is possible to reduce the uncertainties of the model by removing it. It follows that each curve depends only on α, derived from the calibration of the Fukuzono model. Thanks to the abacus reported in Fig. 4.6, the authorities have a set of reference behaviours to assess preliminary alert thresholds, according to specific needs.

4.2.2. Application of the Inverse Velocity Generalized Method

The mentioned study has been developed using a back-analysis procedure and considering the whole data set achieved in the past, starting from 30 days before the failure. This approach is not representative for a real case, where data are gradually acquired and decisions have to been made in real-time. This paragraph considers two case studies not included in the landslide dataset mentioned before, simulating the progressive acquisition of monitoring data. This test wants to evaluate the efficiency of the proposed criterion and its ability and reliability in the recognition of a landslide which is approaching to collapse.

In particular, the procedure follows these steps:

a) After the recognition of the beginning of accelerating phase, the following three data are considered as the starting dataset;
b) The IVM method is applied in order to estimate the theoretical Time of Failure, under the hypothesis of a linear behaviour (α = 2);
c) The displacement rate is evaluated through Eq. [4.5];
d) Model is calibrated using monitoring data, by changing A and α parameters;
e) Definition of the theoretical velocity curve using the calibrated A and α parameters;
f) Evaluation of $\mu_{v_{FV}}$ and $\sigma_{v_{FV}}$ and application of Eq. [4.6];
g) Comparison with the abacus of normalized theoretical curves defined by a specific value of α;
h) Inclusion of new monitoring data in the dataset (as soon as they are available) and repetition of the procedure, starting from point b).

Letlhakane Landslide

The first case study is the Letlhakane Landslide (Kayesa 2006), occurred on 14 July 2005 in a diamond open pit mine in Botswana. The event was a toppling with an estimated volume of 233,000 m^3, monitored through a Total Station. Fig. 4.8 represents the digitized dataset used for the test.

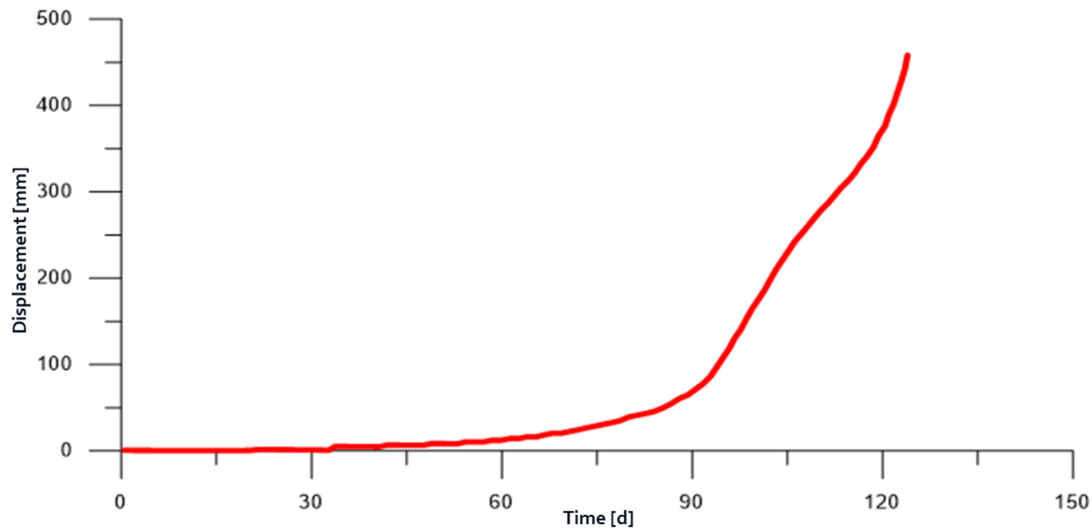

Fig. 4.8: Displacements digitized and used for the test, recorded at Letlhakane Landslide (Kayesa 2006)

Tab. 4.3 reports the predicted and observed Time of Failure, with the corresponding differences ΔT_f (a positive value indicates that the predicted T_f occurs later than the observed T_f) and warning time Δt. Fig. 4.9 shows the progressive evaluation of Time of Failure when a new data integrates the dataset. Both Tab. 4.3 and Fig. 4.9 highlight a correct prevision of T_f starting from 5 days and a half before, while since a period of 10 days to failure the evaluation ranges between ±1.5 days with respect to observed Time of Failure.

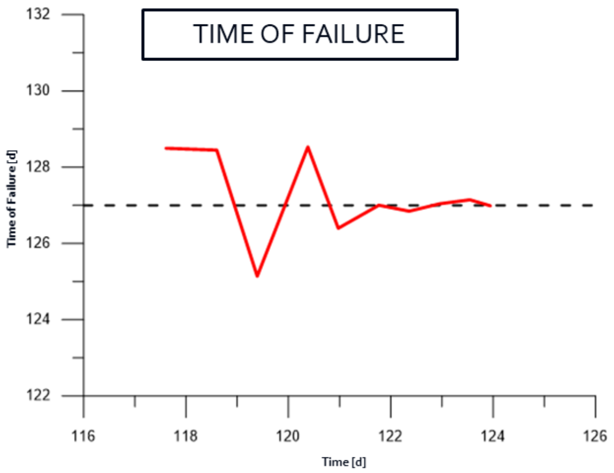

Fig. 4.9: Time of Failure forecast approaching to failure

Tab. 4.3: Time of Failure forecast, observed and differences

Time since the start of the monitoring [d]	Observed T_f [d]	Predicted T_f [d]	ΔT_f [d]	Δt [d]
117.6	127	128.5	1.5	10.9
118.6	127	128.4	1.4	9.8
119.4	127	125.1	-1.9	5.7
120.4	127	128.5	1.5	8.1
121.0	127	126.4	-0.6	5.4
121.8	127	127.0	0.0	5.2
122.4	127	126.8	-0.2	4.4
123.0	127	127.0	0.0	4.0
123.5	127	127.1	0.1	3.6
123.9	127	127.0	0.0	3.1

Fig. 4.10 shows the variation of A and α parameters approaching to failure. As the evaluation of T_f, the governing parameters of the model become stable at day 121 (6 days before landslide occurrence).

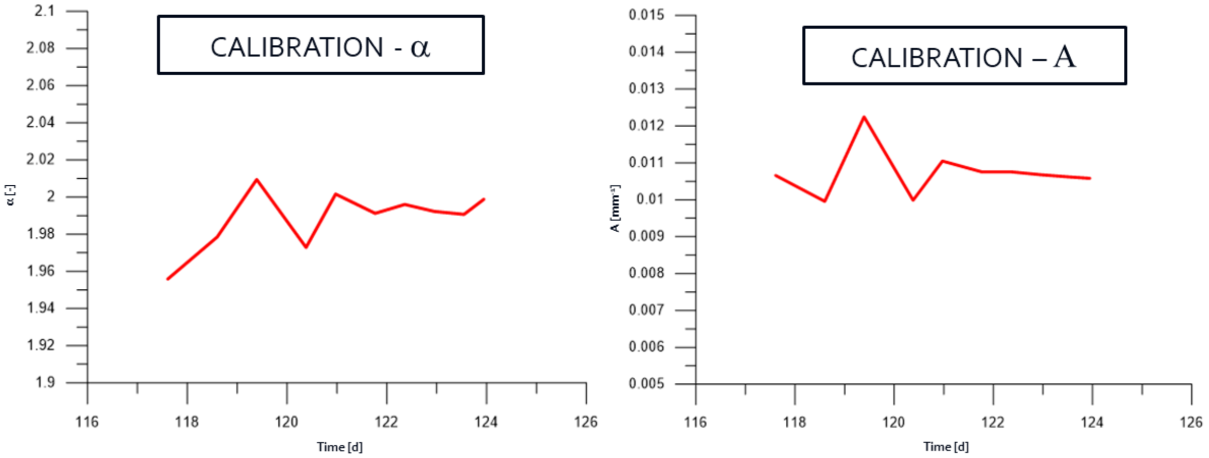

Fig. 4.10: Variation of A and α parameters approaching to failure

Fig. 4.11 shows the result obtained through the application of Eq. [4.6], considering the curve related to $\alpha = 1.99$. Monitoring data fit very well the theoretical curve and this permits to compensate the lack of displacements data after day 124 (3 days before failure) with the behaviour forecasted by the model. The generalized method is significant in the representation of the landslide behaviour and permits to activate an alert procedure.

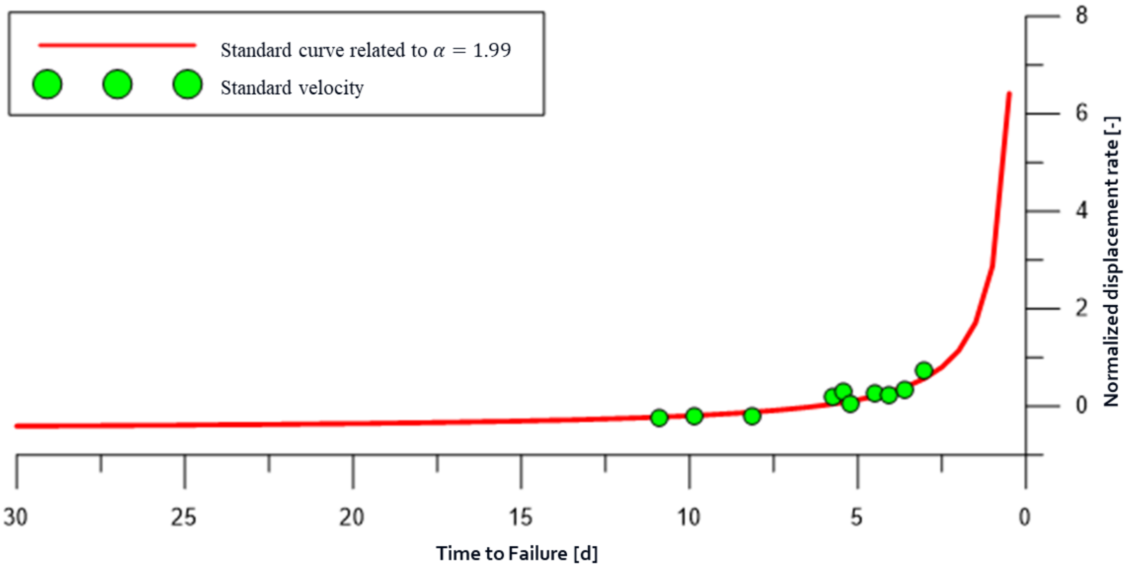

Fig. 4.11: Comparison between normalized displacement rate data and the generalized curve related to $\alpha = 1.99$

Kagemori Quarry Landslide

The second case study is the Kagemori Quarry Landslide, occurred on 20 September 1973 at Kagemori, Saitama prefecture, Japan. The event could be classified as a rockslide with an estimated volume of about 400,000 m^3 of limestone rock debris (Yamaguchi and Shimotani 1986). According to the authors, sliding surface observed after the collapse appeared as "irregular and complex", probably for the influence of secondary slides, which followed the main one. Fig. 4.12 represents the digitized dataset used for the test (Yamaguchi and Shimotani 1986).

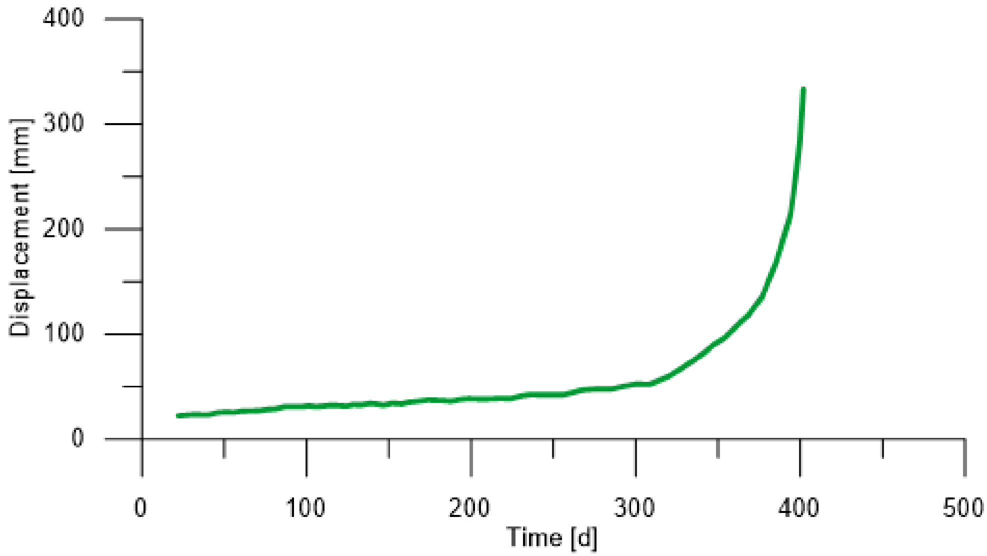

Fig. 4.12: Displacements digitized and used for the test, recorded at Kagemori Quarry Landslide (Yamaguchi and Shimotani, 1986)

Tab. 4.4 reports the predicted Time of Failure and corresponding A and α parameters, obtained through the calibration of the model. It is possible to observe that IVM increases its forecasting quality with the progressive addition of new monitoring data. In particular, the model has overestimated the T_f of only 1.2 days since the first iteration (19 days before). This result is very important for the risk management process because the model is advising the authorities that an accelerating phase is going on and has to be accurately controlled through monitoring data. At t = 397.2 days, T_f coincides with the observed Time of Failure, warning authorities that a potential failure is expected in a week. The two following monitoring data and consequent iterations of the model confirm the prediction, computing the same T_f.

Tab. 4.4: Time of failure forecast, model calibration and normalization procedure

Time since the start of the monitoring [d]	Observed T_f [d]	Predicted T_f [d]	$\Delta\, T_f$ [d]	Δt [d]	Linear regression		v_n [-]
					A	***α***	
385.5	404	405.2	1.2	19.7	0.0137	2.06	-0.3336
394.1	404	406.1	2.1	12.0	0.0141	2.04	-0.2567
397.2	404	404.3	0.3	7.1	0.0146	2.05	0.1721
399.6	404	404.2	0.2	4.6	0.0148	2.05	0.3056
401.8	404	404.3	0.3	2.5	0.0148	2.05	0.8886

The test demonstrates that the real-time application of the Fukuzono model during the accelerating phase of Kagemori Quarry landslide first identifies a potentially dangerous phenomenon about three weeks before the failure, then it estimates an accurate Time of Failure a week before the event. Finally, this result is confirmed respectively 4 and 2 days before the collapse, potentially giving the authorities the time to operate for an evacuation of the area. A and α parameters display a variation of respectively 0.0011 and 0.02. In particular, α has a constant value of 2.05 (very similar to the value which corresponds to the linear regression) for the last three model iterations, starting from a week before the failure.
After the application of the IVM, each monitoring data starting from t = 360 days is progressively consider in the dataset and normalized through the previously described procedure. The obtained value of v_n can be compared to the abacus of generalized theoretical velocity curves displaying the same α parameter. Fig. 4.13 reports the comparison, highlighting the efficacy of the generalized method in the representation of the landslide behaviour.

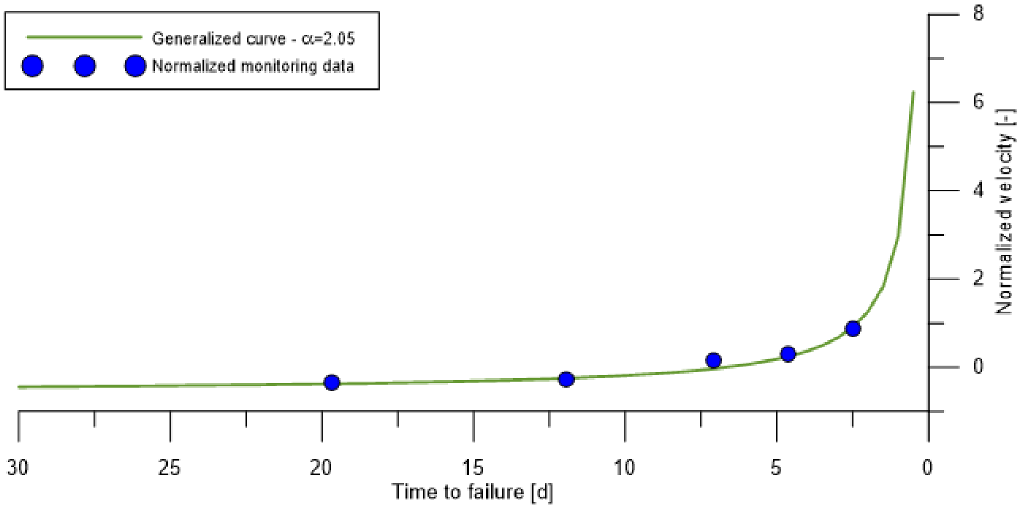

Fig. 4.13: Comparison between normalized monitoring data and the generalized curve featuring the corresponding α value

In particular, the abacus could also provide information about normalized velocity thresholds to be used together with monitoring data in order to activate alert procedures. Fig. 4.14 shows a possible application, where normalized displacement values thresholds are evaluated respectively for 14 and 7 days before the collapse.

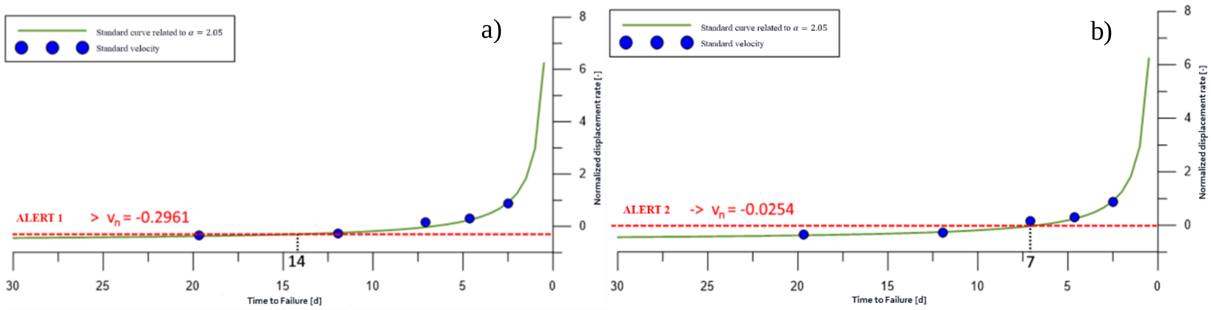

Fig. 4.14: Normalized velocity thresholds using the proposed abacus corresponding to a) 14 days and b) 7 days before the collapse

Tab. 4.5 reports the alert levels corresponding to 14, 7 and 4 days before the collapse. It is possible to observe that the first alert is activated when $v_n > -0.2961$, that for Kagemori landslide corresponds to the monitoring data registered 10 before failure. The second alert has a normalized velocity threshold equal to -0.0254 and it is activated a week before the event. Finally, selecting an alert to be activated 4 days before the event, $v_n = 0.3673$. This alert level is activated 2 days before the landslide. Through this analysis it is also possible to observe that a monitoring characterized by an adequate sampling period highly improve the application of the method (in particular for the estimation of α parameter) and do not delay the activation of alert procedures.

Tab. 4.5: Alert levels activated through the proposed abacus

Time since the start of the monitoring [d]	Observed T_f [d]	Predicted T_f [d]	v_n [-]	v_n threshold [-]	Alert [-]
385.5	404	405.2	-0.3336	-	-
394.1	404	406.1	-0.2567	-0.2961	1
397.2	404	404.3	0.1721	-0.0254	2
399.6	404	404.2	0.3056	-	-
401.8	404	404.3	0.8886	0.3673	3

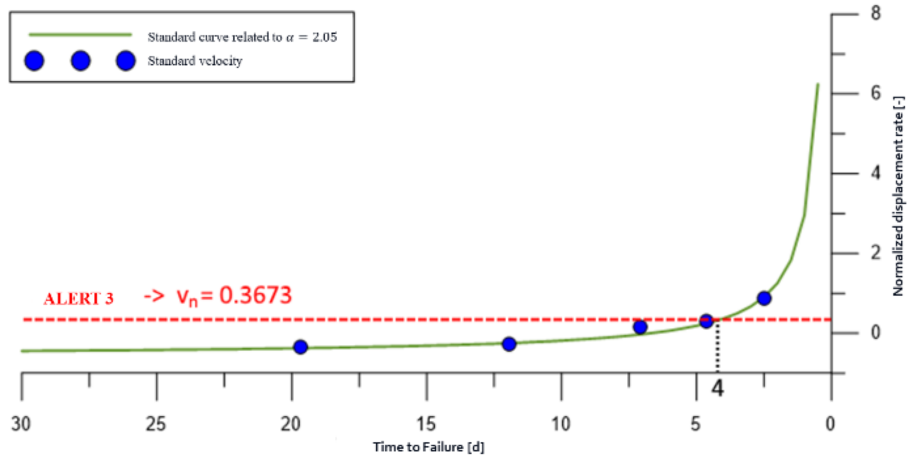

Fig. 4.15: Normalized velocity threshold using the proposed abacus corresponding to 4 days before the collapse

4.2.3. IVM activation criterion

As explained in the previous paragraph, the applicability of Fukuzono model has been successfully demonstrated under the hypothesis of a tertiary creep behaviour. For this reason, the dataset should contain only accelerating displacement data. This assumption is very important and highly influence the forecasting analysis, especially if only a few data are available. The identification of the tertiary creep could not be so difficult if there is a manual check made by an operator. The issue become harder and harder for EWS applications, where the software has to automatically recognize a continuous accelerating phase in real time. In order to implement Fukuzono model inside MUMS EWS, the author of this thesis suggests a new method able to identify the acceleration phase, mentioned as IVM activation criterion.

The method is based on the following hypothesis:

- The landslide undergoing to failure changes its behaviour from a secondary to a tertiary creep;
- The displacement rate should be increasing and positive between two consecutive readings. An increasing negative velocity is not considered (as for example a displacement rate equal to -3 m/s at *n-1* reading and -1 m/s at *n* data);
- The displacement rate – time graph is a curve with increasing concavity;
- The inverse velocity vs time regression is linear;
- The previous 30 days dataset is considered, starting from the last data achieved.

Concentrating on MUMS EWS system, the criterion (Fig. 4.16) is applied at both local and cumulative displacements in the resultant direction, which could be assumed as the maximum grade direction, along the whole depth. By considering the displacement rate as m/d, the velocity are calculated through Eq. [4.7] and [4.8].

$$v_{loc_{i,j}} = \frac{S_{loc_{i,j}} - S_{loc_{i,j-1}}}{t_j - t_{j-1}} \qquad [\ 4.7\ ]$$

$$v_{cum_{i,j}} = \frac{S_{cum_{i,j}} - S_{cum_{i,j-1}}}{t_j - t_{j-1}} \qquad [\ 4.8\ ]$$

Where:

- $v_{loc_{i,j}}$ is the local displacement rate in the resultant direction, recorded by sensor *i*, between *j* and *j-1* readings;
- $S_{loc_{i,j}}$ is the local displacement in the resultant direction, recorded by sensor *i* at reading *j*;
- $v_{cum_{i,j}}$ is the cumulative displacement rate in the resultant direction, recorded by sensor *i*, between *j* and *j-1* readings;
- $S_{cum_{i,j}}$ is the cumulative displacement in the resultant direction, recorded by sensor *i* at reading *j*;
- t_j is the date corresponding to reading *j*, expressed as a number.

Activation Criterion 0: positive displacement rate

The Activation Criterion 0 considers the signs of displacement rates (local, through Eq. [4.9] and cumulative through Eq. [4.10]). In particular, the method requires four consecutive positive velocities (referred to reading *j*) to proceed with the following tasks.

$$v_{loc_{i,j}} > 0 \ \& \ v_{loc_{i,j-1}} > 0 \ \& \ v_{loc_{i,j-2}} > 0 \ \& \ v_{loc_{i,j-3}} > 0 \qquad [\ 4.9\ ]$$

$$v_{cum_{i,j}} > 0 \ \& \ v_{cum_{i,j-1}} > 0 \ \& \ v_{cum_{i,j-2}} > 0 \ \& \ v_{cum_{i,j-3}} > 0 \qquad [\ 4.10\ ]$$

Activation Criterion 1: increasing displacement rate

If Criterion 0 has a positive result (C0 = 1), the Activation Criterion 1 investigates the variation between two consecutive positive velocities (related to local Eq. [4.11] or cumulative Eq. [4.12] displacements). The criterion is activated (C1 = 1) if $\Delta v > 0$ for at least three of four consecutive velocities.

$$\Delta v_{loc_{i,j}} = v_{loc_{i,j}} - v_{loc_{i,j}-1} \qquad [\ 4.11\ ]$$

$$\Delta v_{cum_{i,j}} = v_{cum_{i,j}} - v_{cum_{i,j}-1} \qquad [\ 4.12\ ]$$

Activation Criterion 2: parabolic criterion

If the Criterion 1 is activated, local and cumulative displacement rate data are interpolated using a parabolic fitting, as in Eq. [4.13]. The dataset considers ten data referring to reading *j*, as in Tab. 4.6 (the example is about local displacement rates).

Tab. 4.6: Dataset considered for the Activation Criterion 2 (case of local displacement rates)

Referring dataset	First reading considered in the dataset	Last reading considered in the dataset
j	$v_{loc_{i,j-9}}$	$v_{loc_{i,j}}$
j-1	$v_{loc_{i,j-10}}$	$v_{loc_{i,j-1}}$
j-2	$v_{loc_{i,j-11}}$	$v_{loc_{i,j-2}}$
j-3	$v_{loc_{i,j-12}}$	$v_{loc_{i,j-3}}$

If the a coefficient is positive for at least the 75% of the dataset represented by *j*, *j-1*, *j-2* and *j-3* readings, Criterion 2 is achieved (C2 = 1).

$$y = ax^2 + bx + c \qquad [\ 4.13\ ]$$

Activation Criterion 3: increasing concavity

The last criterion considers the variation of a coefficient for both local (through Eq. [4.14]) and cumulative (Eq. [4.15]) displacements. If Criterion 2 is activated at reading *j*, the method evaluates the variation of a starting from *j-3* reading. The Criterion 3 is activated (C3 = 1) if $\Delta a > 0$ for at least three of four consecutive data.

$$\Delta a_{loc_{i,j}} = a_{loc_{i,j}} - a_{loc_{i,j-1}} \qquad [\ 4.14\ ]$$

$$\Delta a_{cum_{i,j}} = a_{cum_{i,j}} - a_{cum_{i,j-1}} \qquad [\ 4.15\ ]$$

Activation of Fukuzono method

If Criterion 3 gives a positive result, Fukuzono method is activated considering the dataset *j-3* ÷ *j+1*. In this way, the algorithm evaluates the first attempt T_f. When a new data (*j+2*) reaches the Database, the Criterion 3 of *j+2* reading is considered. If $C3_{j+2} = 1$ or $C3_{j+1} = 1$, Fukuzono model re-calculates the T_f considering the dataset *j-3* ÷ *j+2* and results are reliable only if $R^2 > 0.8$. The procedure is repeated for every new data available until the Criterion 3 is not activated for both the last (*n*) and the previous (*n-1*) readings.

MUMS EWS is designed to recognize False Positives (FP) that may happen under certain conditions:

- If $T_f < 0$, the collapse date is in the past and the data is certainly a FP. Therefore the slope of the curve is positive;
- If the Fukuzono model estimates a $T_f > 0$ (for example at the date of 25 June 2018), corresponding to a date of failure (for example on 28 June 2018), which is previous than the last instrumental data recorded (continuing the example, on 29 June 2018) that is not returning an error. In this case it is supposed that the landslide did not collapse;
- If the last data of the dataset has an inverse velocity which is consistently increasing (i.e. the velocity is decreasing) referring to the previous one.

4.2.4. Final remarks

The proposed generalized normalized velocity method permits to compare the behaviours of landslide of very different nature, materials, mechanisms, displacement rates, etc.

The reported dataset refers to cumulated slope surface displacements, with any information about the underground behaviour, position of the sliding surface and pore pressure. This is an important factor in the case of a complex landslide, where the underground and soil behaviours could be significantly different. This theme will be analysed in a case study reported at Chapter 5.3.

The IVM method has demonstrated a successful applicability when the tertiary creep phase is correctly identified. A universal method able to highlight the turning point related to the beginning of the accelerating phase has not been developed yet. This thesis proposes a theoretical method developed by the author that requires further case studies evidences and applications on EWSs.

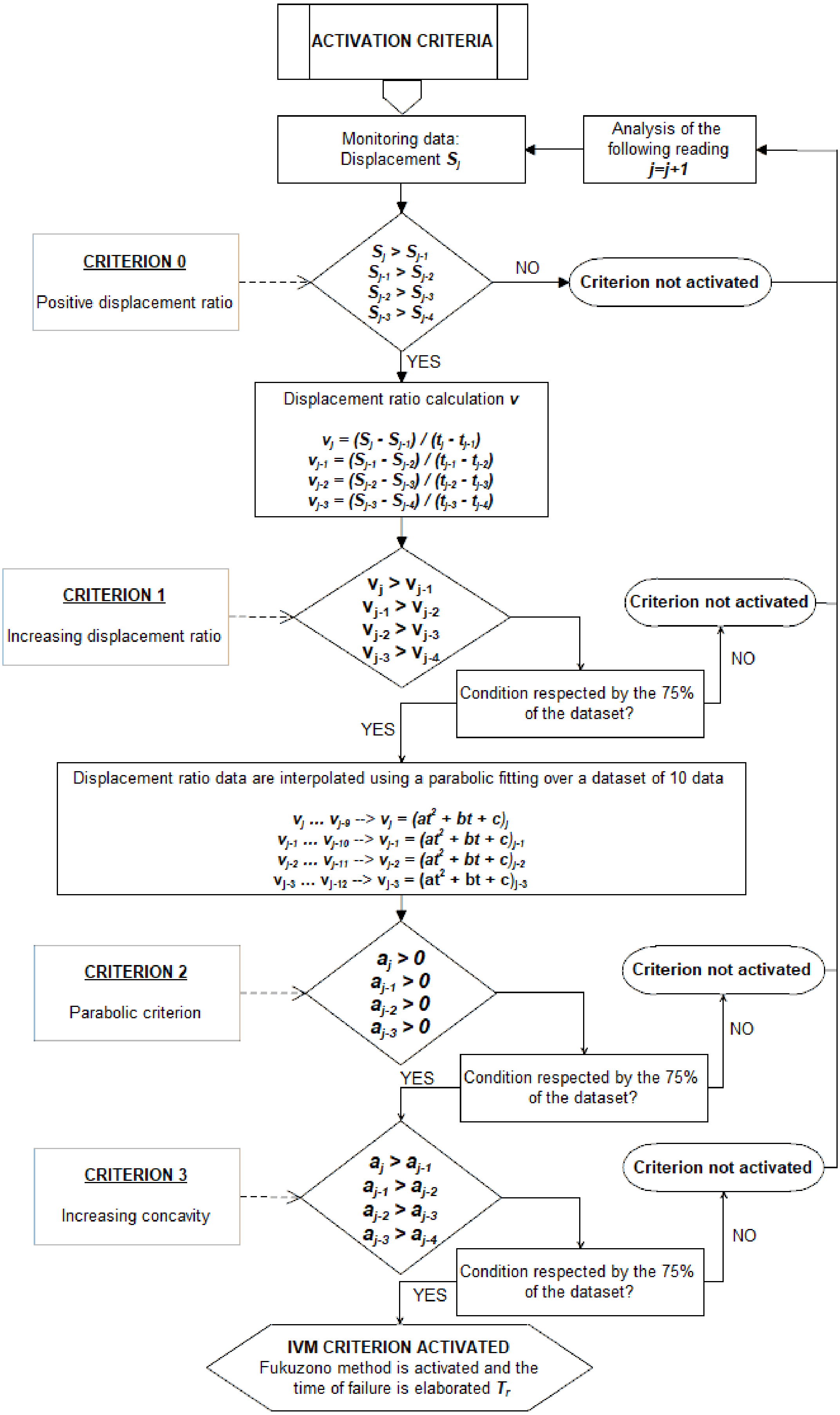

Fig. 4.16: Chart flow of the IVM Activation Criterion

Chapter 5

CASE STUDIES

5.1. Ferrari GES, Maranello, Italy

The first case study reported (Fig. 5.2) regards the monitoring of a geotechnical structure in the construction site of the new Ferrari GeS (Gestione Sportiva) in Maranello (MO), Italy (Fig. 5.1). The building has been constructed for 20 months, has a surface of about 9,000 m^2, which increases to 16,000 m^2 considering the green area and internal roads. The structure is composed by glass and steel, with underground floors that required excavations up to 15.5 m deep, supported by bulkheads. A MUMS system was installed during June 2013 inside one of the bulkheads to monitor the deformations occurred during construction and following year, and compare them with the design assumptions. The reference reading was taken on 18 of June 2013 and monitoring came to an end during August 2014.

Fig. 5.1: Construction site of Ferrari GeS

The system installed was a Vertical Array Structure, 16.5 m long, composed by 33 MEMS 1.0 sensors with a constant interspace of 0.5 m. Control Unit collected and saved data into a SD card. Raw Data were transmitted to the elaboration centre once a month, where a specifically designed software elaborated them.

Fig. 5.2: Maranello site (44°31’58.00 N, 10°51’46.00 E)

5.1.1. Results

The Array represents the fourth MUMS installation and the first Vertical Array Structure application. Starting from the reference reading, a direct comparison with GPS data was available for the first two months of monitoring. The system was not compensated in temperature and the results show consistent inaccuracies related to the thermal influence on the first meter of soil (Fig. 5.3). Excluding these information from the dataset, the difference between the data recorded by MUMS system at 1 m of depth and GPS at the ground level varies between 2 and 4 mm (Fig. 5.4). This variation could be related to the accuracy and sensibility of both MUMS and GPS, and finally to the (lost) information provided by superficial nodes of the Array.

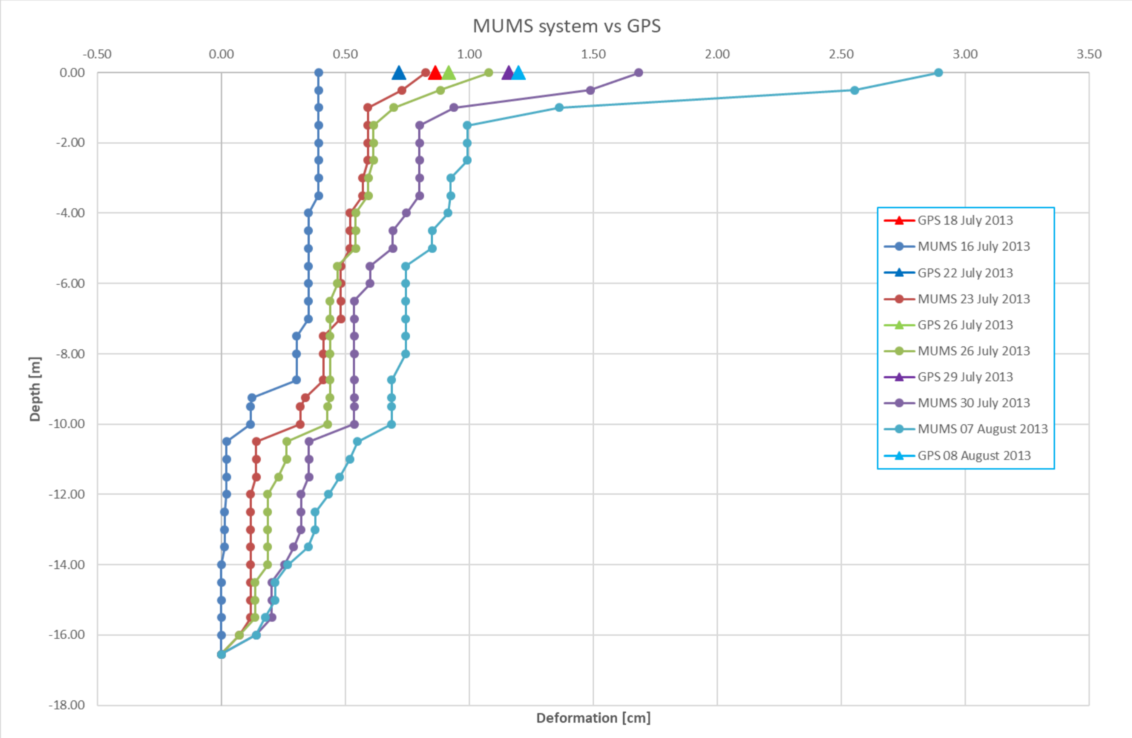

Fig. 5.3: Deformations recorded by MUMS system and GPS starting from 18 June 2013. MUMS system is not compensated in temperature and shows a relevant thermal dependence in the first meter of depth

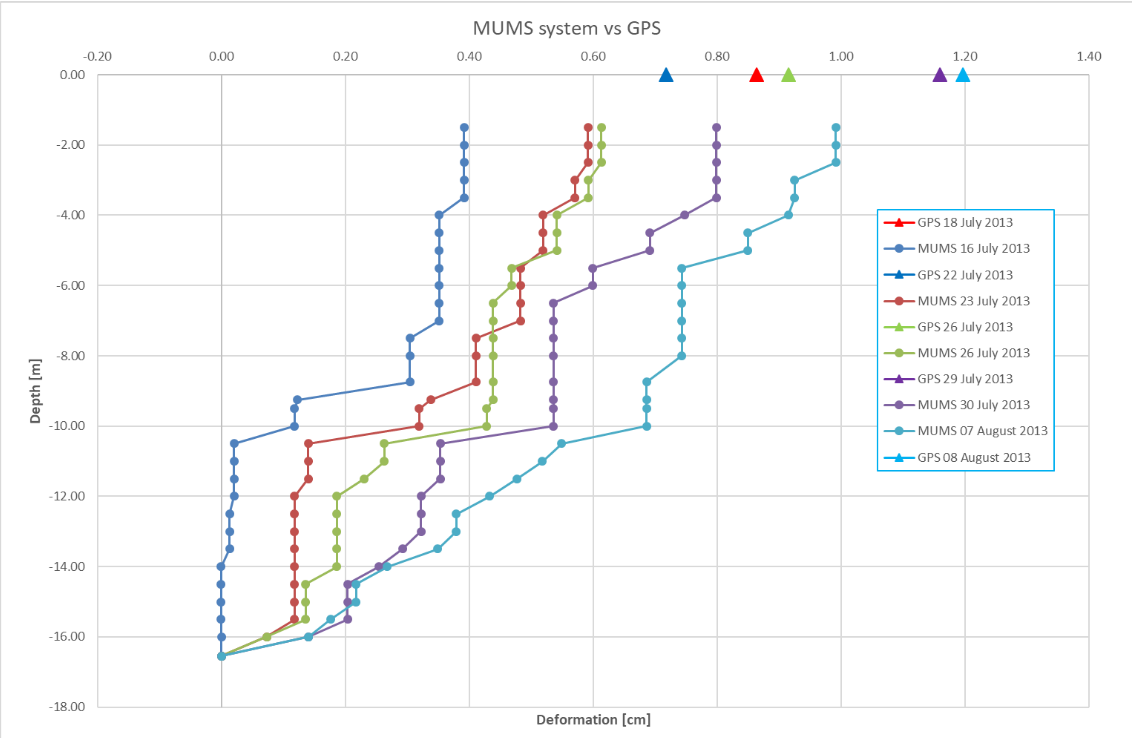

Fig. 5.4: Deformations recorded by MUMS system and GPS starting from 18 June 2013, excluding the inaccurate information related to the first meter of depth

During June 2013, a traditional inclinometer casing was installed, while the first available results date to the 10th of September 2013. The comparison between MUMS inclinometer (excluding the sensors influenced by thermal effects) and manual probe (Fig. 5.5) shows a good relationship regarding the stable zone, while the new tool identifies larger displacements in the excavation area.

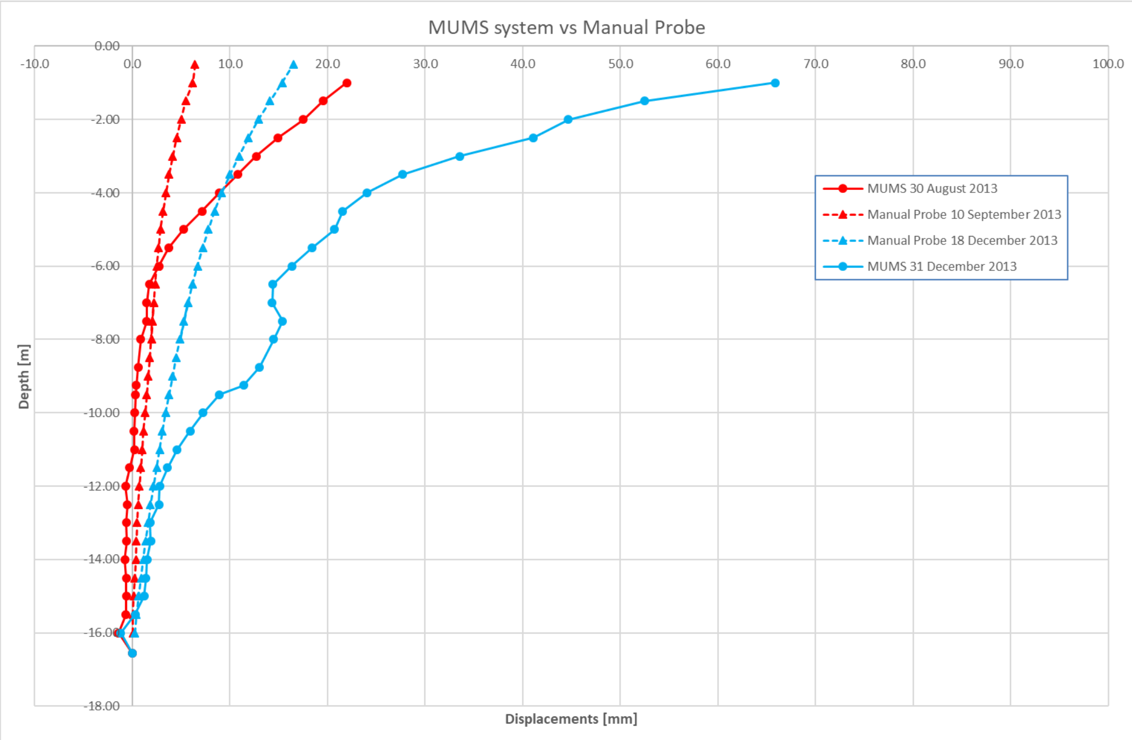

Fig. 5.5: Comparison between displacements recorded by Manual Probe and MUMS at the end of year 2013

After six months of monitoring (Fig. 5.6) MUMS highlights a relaxation of the structure, related to the change of boundary conditions, while Manual Probe measures did not react to this fact. The change of boundary conditions could be a consequence of the excavation execution on the horizontal plane perpendicular to the figure, together with the effects of seasonal temperature oscillations.

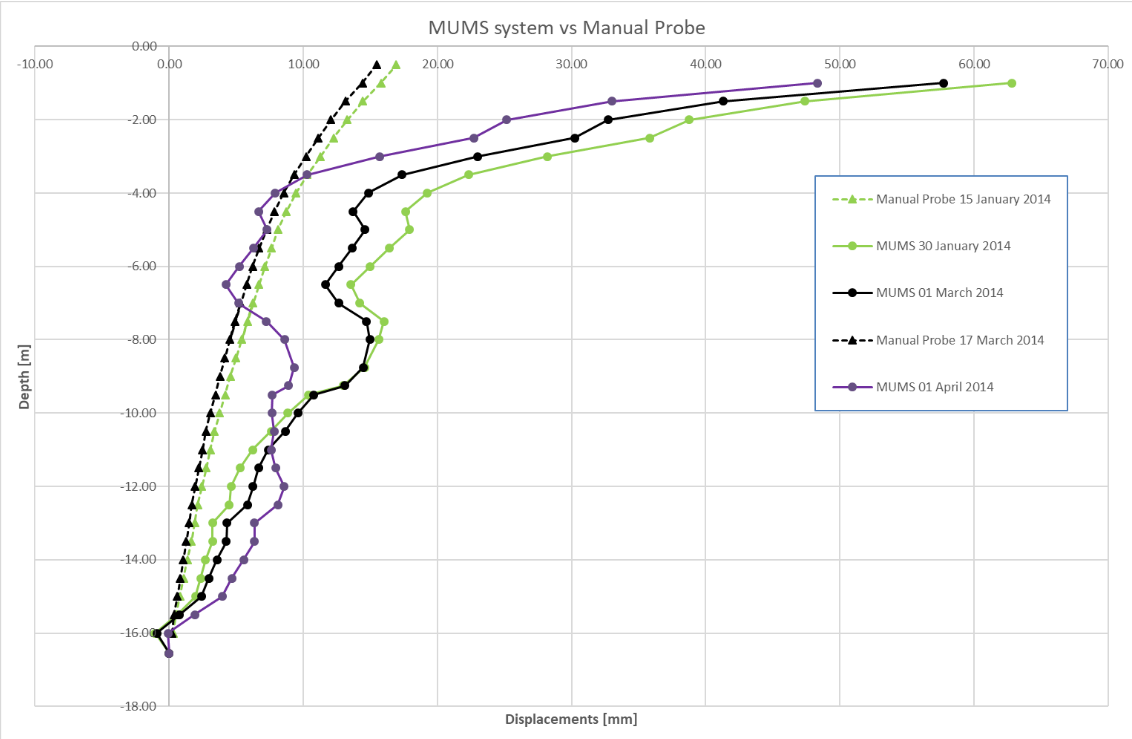

Fig. 5.6: Comparison between displacements recorded by Manual Probe and MUMS on April 2014

Finally, the monitoring came to an end on 9 August 2014, with the results reported in Fig. 5.7 and a cumulative deformation of 4.85 cm at the top.

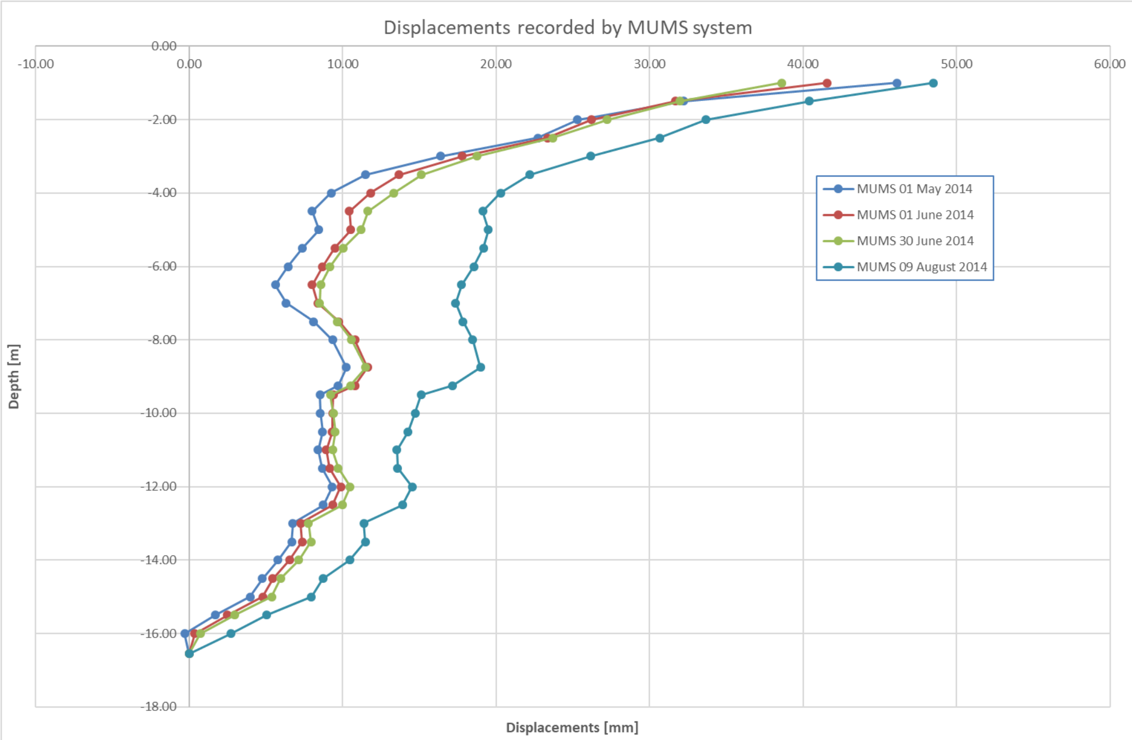

Fig. 5.7: Displacements recorded by MUMS system at the end of monitoring

5.1.2. Conclusions

The first application of a Vertical Array Structure MUMS system shows comfortable results. The instrument permitted to identify the excavation stages and the deformations related to seasonal oscillations and changes of boundary conditions. The comparison with a GPS system placed on the ground highlights the necessity to compensate the thermal effects with a specific calibrations that has been developed starting from this case study (described in Chapter 3.2.1). By comparing the results of Manual Probe Inclinometer with MUMS, it is possible to observe that the deformations recorded in the stable zone are very similar, while the differences regard the excavation area. In this case MUMS shows larger movements and the mentioned seasonal oscillations and changes of boundary conditions, related to excavation works on the perpendicular plane. The Manual Probe did not record this behaviour. Therefore, sensors installed were MEMS 1.0, characterized by electronic and thermal drifts, together with significant instrumental noise that required a consistent post processing. During recent years, the development of 2D electrolytic cells coupled with MEMS 2.0 (Tilt Link HR 3D V, as in Chapter 3.2.2) has highly improved the sensibility, repeatability and general applicability of the Vertical Array Structure.

The information obtained permits an evaluation and the validation of design assumptions. In particular, the expected movement for this specific case was 5 cm, which is very close to the value recorded by MUMS at the end of monitoring period (4.85 cm).

5.2. A16 Highway, Italy

The second case study proposed is the monitoring of a landslide that insists on a portion of A16 Highway (Fig. 5.8). The infrastructure crosses the Apennine connecting Campania and Puglia regions and has a relevant role in the trade between the gulf of Naples, the port of Salerno and the Adriatic Sea. The large presence of landslides in the zone has involved numerous scientists to study, test and evaluate new instrumentations, numerical models or methods for hazard assessment and management (Versace et al. 2014, Artese et al. 2015, Intrieri et al. 2017). The studied area is placed near the regional border, between A16 Km 97+450 and the Candela exit. The landslide phenomenon could be potentially dangerous for people, involving the infrastructure and some houses.

Site has been investigated since January 2015 through a series of site and laboratory tests, together with the definition and installation of a complex monitoring system, as described in the following paragraphs. A 2D FDM Time Dependent numerical model has been set up, calibrated and validated using monitoring data in order to reproduce the displacements recorded during the three years of surveys and perform a tentative forecasting analysis of the most probable future landslide behaviour. The obtained information is useful to check the compatibility of the structure with the potentially occurring deformations. The case study highlights two key aspects when dealing with elements at risk: the importance of monitoring data (Arbanas et al. 2014) and the continuous validation (also with self-learning ability) required by a numerical model (Bicocchi et al. 2016) to reproduce the dynamic changes eventually recorded during the study.

Fig. 5.8: A16 Highway site (41°5’20.33 N, 15°13’41.48 E)

5.2.1. Description of the Area

Several authors (Crostella and Vezzani 1964, Scandone 1967, Ippolito et al. 1973, Dazzaro et al. 1982 & 1984, Ciarcia and Vitale 2013, Carri et. al. 2017) have studied the area in the past fifty years. This paragraph reports a quick summary of the previous works in order to highlight the main information about lithostratigraphic units, geomorphology and geology, as reported in Carri et al. (2017).

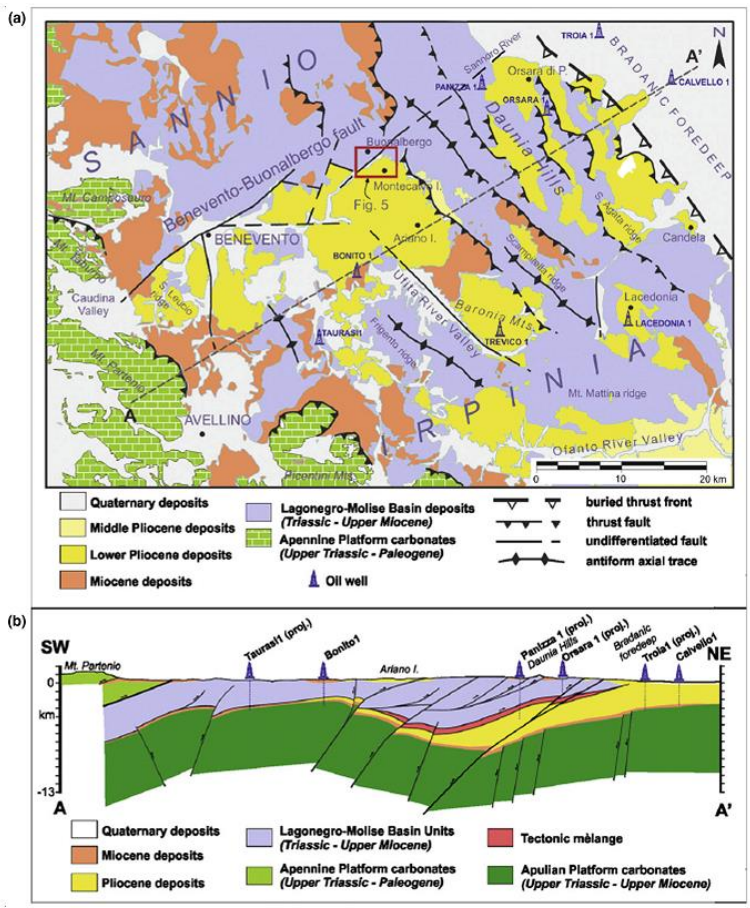

Fig. 5.9: a) Geological map and b) Cross section of the southern Apennines sector, Irpinia-Sunni (Source: Ciarcia and Vitale, 2013)

The area is placed in the Irpinia-Sunni, the southern sector of Apennines (Fig. 5.9), inside the wide valley of the Calaggio torrent, which follows a SW-NE path alongside the highway. The sector features a hilly physiography that can exceed 500 m a.s.l., as opposed to the Northern part, which mainly lays on levelled land. The morphology is characterized by the outcrops of the lithostratigraphic units, resistant to erosion. One of these outcrops is represented by the "pre-Quaternary" substrate terrains, related to the tectonic units Vallone del Toro, Lagonegro II (Scandone 1967) and Dauna (Dazzaro et al. 1982). They derive from the progressive deformation of Lagonegro-Molise Basin, topped by the deposits of the Pliocene basins (Ippolito et al. 1973, Ciarcia and Vitale 2013) constituted by sedimentary and evaporitic rock debris, that could be dated back to an age between the Upper Cretaceous and the Lower Pliocene, including limestone, sandstone, marl, argillite, clays, sands and conglomerates (Fig. 5.9). The whole territory is influenced by the presence of clayey successions which are affected by rotational sliding and/or shallow flow movements.

5.2.2. Lithostratigraphic Units

The site is located in the Dauno Apennines, whose genesis is connected to Apennine dynamics and still in progress. Thick portions of clay-marl composition characterize the majority of formations, including rare interbedded limestone beddings. Slope stability is influenced by the connection between clay units (dominant in the area) and the mentioned limestones. The Italian Geological map (Jacobacci and Martelli 1967) reports the stratigraphic description of each outcropping geological unit, available at "Foglio 174" (Ariano Irpino) and "Foglio 175" (Cerignola). The stratigraphic framework follows below, from bottom to top.

Pre-Orogenic Substrate Unit

- A succession of calcareous bio-clastic sediments of the Burdigalian characterizes Unit Lagonegro II (Scandone 1967). These are intercalated with clays and marl, red and green (Red Flysch). They are locally distinguishable in a limestone member at the bottom, an intermediate layer of mixed limestone and clayey-marl and an upper layer of limestone and clay-marl;
- Unit Daunia (Dazzaro et al. 1984) is characterized by turbidities and bio-clastic limestones, greenish-grey marl and clay marl with abundant planktonic foraminifera (Flysch of Faeto, Crostella and Vezzani 1964), related to the age of the Middle-Upper Miocene;
- A basin sequence of shales and polychrome marls defines the Unit Vallone del Toro. The sequence is intercalated with limestone, silicified marl and diatomite, with chalk upward.

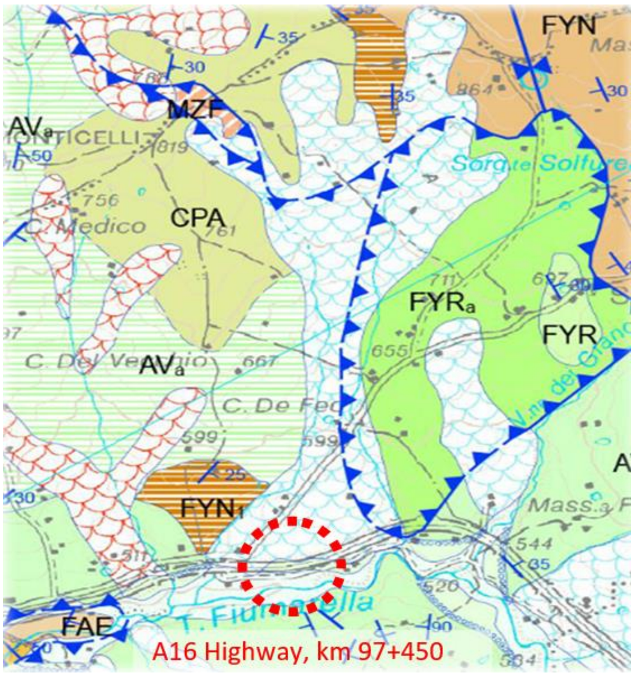

Fig. 5.10: Section of the geological map of Italy - project CARGO - Foglio 433 - Ariano Irpino. Detail of the km 97+450, scale 1:50,000. The formations represented are FYN (Numidian Flysch), FYR (Red Flysch), CPA (Corleto Perticara formation) and AV (clay marl and grey clay)

Deposits Basins Intramountains (wedge-top):
Conglomeratic clastic deposits, sandy and clayey, compose the Baronia formation (Ciarcia and Vitale 2013), organized in a complete transgressive-regressive sedimentary cycle. The conglomerate terms, members of the basal conglomerates, appear prevalently. Therefore, there are representative rock types of the other members (Ciarcia and Vitale 2013).
Lagonegro II, Dauna and Vallone del Toro are tectonic or kinematic units that progressively overlapped each other, partially outcropping. The Unit Lagonegro II presents a continuous stratigraphic series, which starts with Flysch Rosso at the bottom, followed by Numidian Flysch in accordant stratigraphic relationship. Unit Daunia is located on the Faeto Formation, superimposed on the Marne T. Capuana with stratigraphic relationships and lateral-vertical heterotopy. Unit Vallone del Toro shows Polychrome Calaggio argillite below with Limestone and Marne Serroni upwards. There are stratigraphic relationships with lateral-vertical heterotopy. The area of the case study is placed above the deposit of an ancient landslide (Fig. 5.10, light blue area), made of chaotic heterometric and heterogeneous debris, which is locally partially cemented (Holocene).

5.2.3. Geomorphology

The presence of described stratigraphic units influences the morphology. The soil is predominantly composed of clay and sand, with stratigraphic continuity and resistance to erosion. Slopes are subjected to gravitational phenomena like slow surface deformations, flows and deep instability movements. It is possible to observe elements linked to complex and different dynamics related to the coexistence of various landslides converging in the valley, such as erosional scarps, crowns, counterslopes and cracks. Sliding rotational surfaces can be identified between 8 and 15 meters depth. This datum is very important for the results showed in the following paragraphs.

5.2.4. Surveys

Surveys were carried out in order to define geotechnical parameters, water table levels and their variation related to rainfall and weather conditions. For this purpose, a monitoring system was designed and progressively installed in the area adjacent to the highway starting from the beginning of 2015. The information obtained is fundamental for the study of landslide dynamics and the definition of triggering causes, helping to establish mitigation measures.

Geotechnical investigations
Geotechnical investigations included (Fig. 5.11):
- Three borehole drillings (red dots) at a maximum depth of 30 m in order to determine the stratigraphy, followed by the installation of five IPIs;
- Four subsurface undisturbed samples (S1) for laboratory tests, which yielded the most important geotechnical parameters. These are natural water content, dry unit weight, void ratio, grain size distribution, Atterberg limits, Oedometric Modulus *E*, primary consolidation coefficient *Cv*, permeability coefficient *k*, cohesion *c'* and friction angle *ø'*;
- Twelve Standard Penetration Test (S3) in order to determine soil resistance to dynamic penetration, which can be related to the Young modulus, cohesion and other geotechnical parameters through empirical relationships;
- Five drillings at a maximum depth of 25 m, three of which equipped with Casagrande piezometers (yellow dots) and the remaining two with MUMS automatic inclinometers (green dots).

Hydrogeological investigations
Hydrogeological investigations were carried out with the installation of the following sensors (Fig. 5.11):
- Three Casagrande piezometers (PZ1, PZ2 and PZ3) installed in January, February and June 2015 respectively;
- Ten tensiometers (Idro UGM1_3 and UGM1_4) to detect suction;
- Ten TDR (Time Domain Reflectometry) systems (UGM1_3 and UGM1_4) to measure humidity;

- Two absolute piezometers along MUMS Inclinometers (CI1 and CI2) compensated with an absolute barometer, installed at the end of March 2015. These digital piezometers, together with Casagrande ones, record the variation of pore pressure along time.

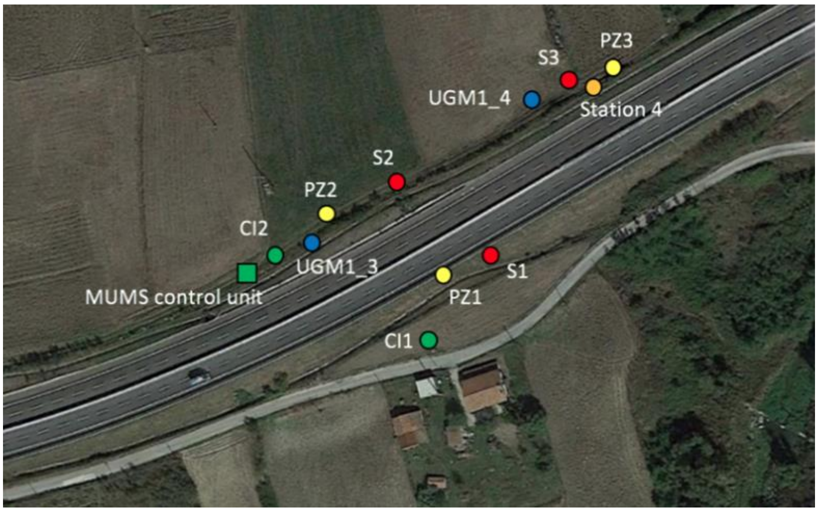

Fig. 5.11: Location of geotechnical surveys and monitoring instrumentations

Meteorological investigations
In order to evaluate the influence of rainfall and weather conditions on slope stability, a meteorological station (Station 4 in Fig. 5.11) was installed to record wind direction and velocity, rainfall, atmospheric pressure, temperature, humidity and solar radiation. After one year of monitoring, weather station resulted inactive and it was necessary to recover data from Greci (18 km far from the site) and Flumeri stations (6 km far).

Monitoring System
The monitoring system was composed by IPIs, MUMS, piezometers and meteorological station as already mentioned. In particular, the five IPIs (S1, S2 and S3 in Fig. 5.11) were installed in January, February and June 2015 respectively, while the two MUMS inclinometers (CI1 and CI2 in Fig. 5.11) at the end of March 2015. The instrumentation described is of fundamental importance to detect the depth and magnitude of displacements along vertical boreholes. In particular, IPIs are equipped with 2D MEMS (Micro Electro-Mechanical System) sensors installed along predetermined guides and able to detect the inclination of the borehole at a specified depth, monitoring also its variation along time. MUMS systems installed have 3D MEMS version 1.0 (25 for CI1 and 26 for CI2), 2D electrolytic cells (5 for CI1 and 4 for CI2), thermometers (30 for both verticals), pore (1 for each chain, version 1.0, as described in the previous paragraphs) and absolute (1) pressure sensors. Tab. 5.1 summarizes the described monitoring instrumentations installed, specifying the depth of each sensor.

Tab. 5.1 Monitoring instrumentations installed

Station	Sensor	Station	Sensor
Station 4	Weather station	S1	1 IPI at 17.5 m depth
UGM 1_3	5 tensiometers at 1.2 m depth; 5 TDR systems at 1.2 m depth	S2	1 IPI at 17 m depth
UGM 1_4	5 tensiometers at 1.2 m depth; 5 TDR systems at 1.2 m depth	S3	3 IPIs at 14, 17 and 20 m depth
CI1 – DT0008	MUMS automatic inclinometer, 23.5 m long (piezometer at 13 m depth)	PZ1	1 piezometer at 12 m depth
CI2 – DT0007	MUMS automatic inclinometer, 23.5 m long (piezometer at 13 m depth)	PZ2	1 piezometer at 12 m depth
MUMS control unit	Data logger for DT0007 and DT0008 MUMS systems	PZ3	1 piezometer at 15 m depth

Raw data were stored locally into a SD Card and then sent to the elaboration centre once a day through a UMTS router and GPRS line. As soon as a new dataset reached the central server, the proprietary software "Tilt" converted electrical data into physical units, elaborated those using statistical tools, stored the results in a MySQL database and made them available on a graphic and interactive web platform, with security controlled access.

Fig. 5.12: Installation of MUMS monitoring system

5.2.5. Models

Geotechnical Model

Results achieved with site and laboratory investigations (Tab. 5.2) permitted to establish a preliminary geotechnical model, constituted by four main layers:

- Layer I: upper layer of clayey silt, slightly sandy, above 6 m depth. Rare lithic inclusions of sandstones and marls, with a grain size that ranges between 0.5 and 1.2 cm;
- Layer II: intermediate layer of soft clay in different colours, between 6 and 16 m depth. Pebble grain size between 0.5 and 2 cm;
- Layer III: intermediate layer of marly clay, between 16 and 18 m depth. Pebble grain size between 0.5 and 1.5 cm;
- Layer IV: lower bedrock of marl flysch, over 18 m depth.

Mechanical parameters of Layer I, II and III were derived from available laboratory tests, while the parameters for Layer IV were estimated using the large literature database of RocData® software (Rocscience 2014). The following chapter analyses the calibration and validation of the parameters through a back-analysis process (Krkač et al 2014).

Tab. 5.2 Mechanical parameters and failure criterion

	Layer I Clayey silt	Layer II Soft clay	Layer III Marly clay	Layer IV Marl Flysch
Failure criterion	Mohr-Coulomb	Mohr-Coulomb	Mohr-Coulomb	Modified Hoek-Brown (Hoek et al. 2002)
Elastic modulus [MPa]	1.857	4.725	2.350	12000.000
Poisson's ratio [-]	0.30	0.33	0.30	0.30
Unit weight [kN/m^3]	20.19	20.85	21.00	26.00
Friction angle [°]	28.00	33.60	33.60	-
Cohesion [kPa]	9.30	9.30	9.30	-
m_b [-]	-	-	-	2.005
s [-]	-	-	-	0.007
a [-]	-	-	-	0.504
σ_{ci} [MPa]	-	-	-	2.413
σ_t [MPa]	-	-	-	0.100

5.2.6. Numerical Model

Once the geotechnical model of the slope was completed, a 2D numerical model was created in order to define the landslide triggering causes and propagation, supported and validated by geotechnical and hydrological investigations. The model has been developed using FLAC® - Fast Lagrangian Analysis of Continua software (FLAC Version 8.0, User's Guide 2016). This software is able to evaluate displacements, critical failure locations, settlements and stresses, using an explicit finite difference formulation. Previous studies reported in the literature (Segalini et al. 2009) focused their attention on the importance of FDM models in the analysis of landslide phenomena. In particular, this is highlighted when slopes have a slow-continuous displacement with time, occurring without appreciable variations of the effective stress state and often related to the presence of plastic clay portions. Model geometry (Fig. 5.13b) reproduces the section of major declivity for a total length of 267 m in order to avoid border effects. The grid has 22,040 nodes with an aspect ratio x/y = 2. MUMS inclinometers are included in this section (Fig. 5.13a) and placed respectively at the progressive of 72 m (DT0007 – CI2) and 103 m (DT0008 – CI1) along horizontal plane. The definition of ground surface geometry was obtained using satellite images first, then corrected and validated with cartography. Constrains for left and right boundaries are rollers, with only vertical movements allowed. The upper boundary is free to move in every direction, while the lower boundary is fixed.

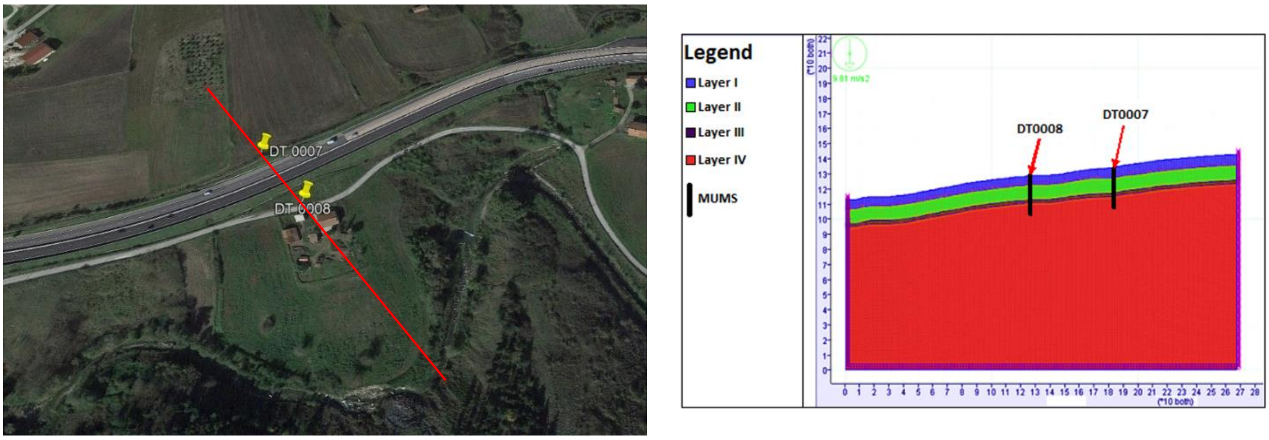

Fig. 5.13: a) Section of major declivity and MUMS inclinometers, b) model geometry

5.2.7. Results

Manual Inclinometers

Preliminary studies of the area took into consideration two surveys conducted in March and June 2015 with traditional inclinometer probes in two different boreholes. Both investigations identified the major displacement at 17.68 m depth, with movements that equalled 6.8 mm (Azimuth 162°, South-East direction) and 4.9 mm (Azimuth 132°), respectively. This preliminary knowledge could be relevant in the following interpretation of MUMS and IPIs data, installed between April and August 2015.

IPI

IPIs provide the displacements at a specific position only, with no information about other locations along the vertical direction. The instrument is useful to detect local movements, while it is not possible to evaluate cumulate displacements. For this reason, the results are quite difficult to interpret and strictly related to the correct planning of the monitoring, which requires to already know the position(s) of the sliding surface(s). Tab. 5.3 reports the movements registered by IPIs at two representative dates and the related depths, with the comparison between nodes of MUMS inclinometers at the corresponding depths. It is worth noting that DT0007-CI2 and DT0008-CI1 arrays are about 70 m apart, with 5 m of difference in height. A previous study (Carri et al. 2017) highlights the issues and the misleading interpretation related to the results of IPIs in the analysis. In particular, these are related to the different positions (Fig. 5.11) of the instrumentations on the slope, the lack of IPIs data along the vertical and finally a series of malfunctions with a substantial loss of information. As an example, MUMS DT0007-CI2 and IPI S3 are 125 m apart, with the first installed in a portion of the ground which is 3 m lower and on the western part of the landslide. At the same time the section which crosses IPIs S1 and S2 could be considered for the numerical model calibration, in opposition to the section that crosses both MUMS array. Nevertheless the results are related only to a single tilt angle for the whole depth, which is quite a poor information for the calibration and validation process. Considering all the issues mentioned, this study does not take into account the IPIs for the comparison with the 2D FDM model.

Tab. 5.3 Local displacements recorded by IPI and MUMS inclinometers at two dates, starting from 4 August 2015

Sensor	Depth [m]	Displacement at 04/10/2015 [mm]	Displacement at 30/04/2016 [mm]	Sensor	Depth [m]	Displacement at 04/10/2015 [mm]	Displacement at 30/04/2016 [mm]
S1	17.50	7.7	8.4	DT0007	16.25	0.1	10.2
S2	17.00	9.6	9.5	DT0007	17.25	0.8	0.8
S3	14.00	5.1	5.2	DT0007	18.00	0.7	0.7
S3	17.00	12.4	12.5	DT0008	13.00	0.0	3.0
S3	20.00	1.9	1.8	DT0008	15.50	0.4	0.4
				DT0008	16.25	0.0	2.4

MUMS inclinometers

MUMS inclinometers were installed at the end of April 2015 and the functionality had been tested for two months. After that period, the instrumentations started the monitoring on 30 June 2015, which was considered the zero-reference date for the following elaborations. The sample period was set to 6 hours, sending data to the elaboration centre once a day. The monitoring came to an end on 5 June 2018 due to the displacements recorded. The borehole was filled with cement at the bottom for about 1 meter, in order to fix the anchor to the stable portion, and gravel for the remaining part of the vertical, using the Spaggiari Installation method described at Chapter 3.3. The installation of both Arrays required one day. Data logger was powered through 12 V lead-acid battery and 5 W solar panel. Fig. 5.14a shows the battery level for the whole period of monitoring, highlighting the correct functionality of the powering system, while Fig. 5.14b represents the temperature of the data logger.

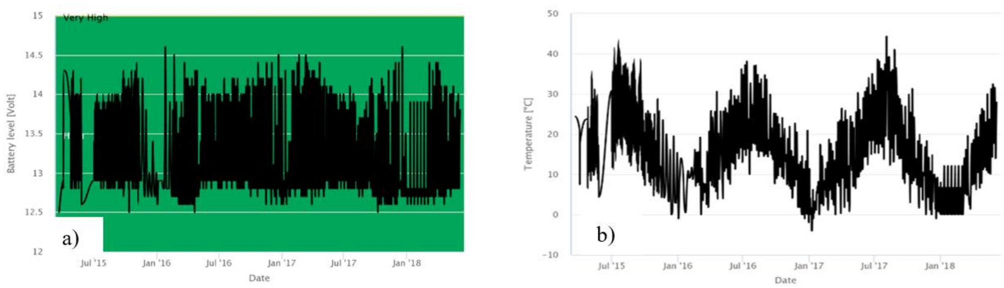

Fig. 5.14: a) Battery level and b) data logger temperature for the whole period of monitoring

MEMS 1.0 sensors were characterized by the presence of relevant signal disturbances, related to instrumental noise, drift and thermal influences. In particular, the array was calibrated manually (the procedure described in Chapter 3.2 was not implemented yet), correcting the thermal effects using three reference temperatures (0°, 20° and 40°) and assuming a linear behaviour of the gravity acceleration between the reference temperatures. This assumption was not completely correct and required a statistical validation obtained with a back-analysis of the first two months of the dataset. A filter was then applied to the displacement results, analysing the weekly trend of data for every sensor and considering only the statistically significant movements (i.e. movements that do not follow the typical behaviour of instrumental noise or temperature variations). The final result was quite comfortable and was considered for both MUMS arrays.

DT0007 chain highlights (Fig. 5.15) a primary slip surface at 16.25 m depth, with a displacement of about 58.5 mm at the end of November 2017 (Azimuth equal to 187°). The second major movement is equal to 16.4 mm and is located at 17.5 m depth. The depth of sliding surface is about the same highlighted during preliminary surveys with manual probes and corresponds to a layer composed by soft clay, including marl and sandstone.

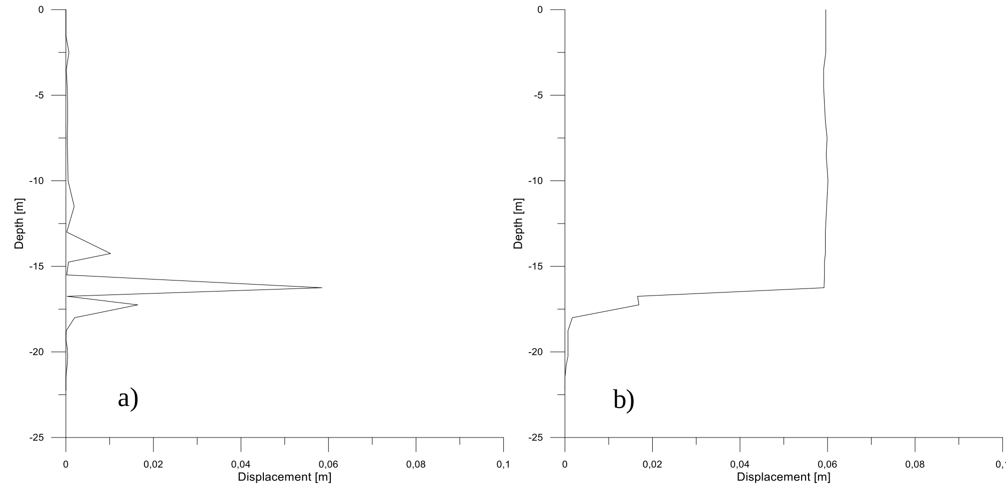

Fig. 5.15: Differential a) Local and b) Cumulative displacements recorded by DT0007 MUMS inclinometer at the end of the monitoring (June 2018), starting from the zero reference date of 30 June 2015

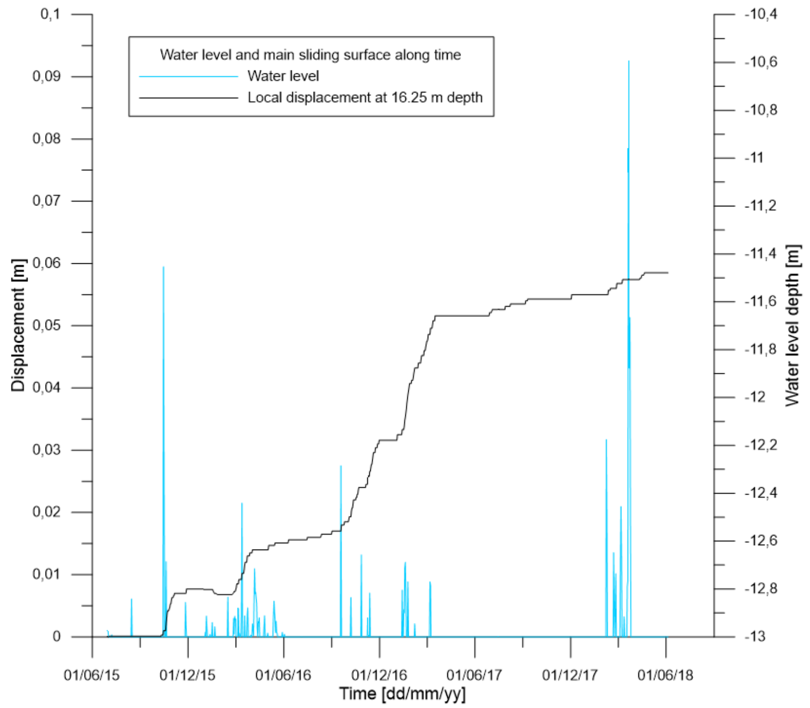

Fig. 5.16: Water level registered by piezometer located at 13 m depth and local displacement at 16.25 m depth, recorded by MUMS DT0007 during the period of monitoring

It is possible to observe (Fig. 5.16) the relationship between the variation of water level along time (recorded by the absolute piezometer at 13 m of depth along DT0007 chain) and displacement in correspondence of the sliding surface (registered along the same vertical of the piezometer). A first event, occurred between 14 October and 05 November 2015, activated the movement at 16.25 m depth, resulting in 6.7 mm shift in three weeks of observations (displacement rate of 0.3 mm/day, with a maximum of 1 mm/day). A second event took place during March 2016 with about 7 mm of displacement at the same depth, during one month of observations (displacement rate of 0.2 mm/day, with a maximum of 1 mm/day). A third event occurred in two different time intervals, between 18 September and 22 October 2016 and between 04 November and 30 November 2016 (displacement rate of 0.2 mm/day and 0.3 mm/day, with a maximum of 1 mm/day and 1.2 mm/day respectively). Finally a continuous constant displacement occurred between 03 January and 17 March 2017, for a total amount of 20 mm.

In particular, the trends and durations of the movements (Tab. 5.4) could suggest the presence of a creep behaviour, marginally influenced by seasonal oscillations of water level. This hypothesis needed a verification with a numerical model able to reproduce the site conditions.

Tab. 5.4: Periods of major displacements and displacement rates recorded by tilt sensor at 16.25 m depth

Date [dd/mm/yyyy]	Period [days]	Displacement [mm]	Displacement rate [mm/day]	Maximum displacement rate [mm/day]
14/10/2015 ÷ 05/11/2015	23	6.7	0.29	1.0
23/02/2015 ÷ 02/04/2015	40	7.2	0.18	1.0
18/09/2016 ÷ 22/10/2016	35	7.0	0.20	1.0
04/11/2016 ÷ 30/11/2016	27	7.6	0.28	1.2
03/01/2017 ÷ 17/03/2017	74	20.0	0.27	0.9

Fig. 5.17 shows the differential local and cumulative displacements at the end of March 2017 recorded by DT0008 MUMS chain starting from the reference reading. In this particular case, the situation is slightly different, since movements are concentrated on an area between 17.25 and 13 m depth, with a major sliding surface at 16.25 m below ground level (24.7 mm displacement at the end of March 2017, Azimuth 115°). The piezometer placed at 13 m depth broke at June 2016, for unknown reasons, while the instrumentation has been inactive since 20 March 2017, due to unknown causes that damaged the chain irreversibly.

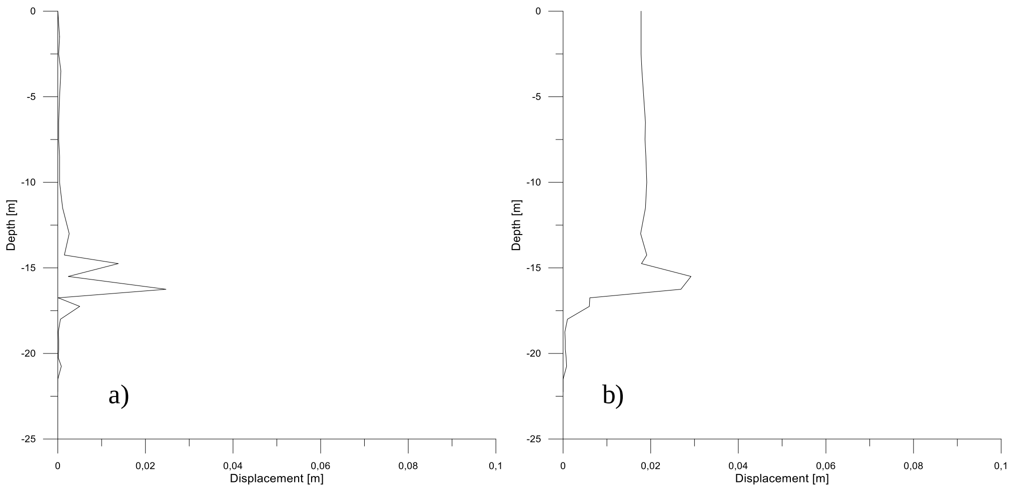

Fig. 5.17 Differential a) Local and b) Cumulative displacements, recorded by DT0008 MUMS inclinometer at the end of March 2017, starting from the zero reference date of 30 June 2015

Hydrogeological and meteorological investigations

Fig. 5.18 shows the relationship between the water level recorded by the piezometer of DT0007 chain (located at 13 m depth) and rainfall.

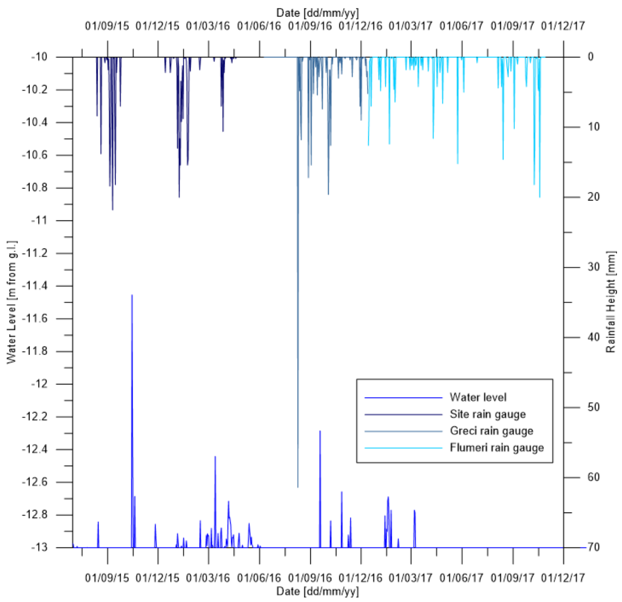

Fig. 5.18: Rainfall and water level recorded during the period of monitoring. After the first year, data have had to be retrieved from the stations in Greci and Flumeri

In particular, from July 2015 to July 2016 the rainfall was recorded by the meteorological station installed on site. Starting from 14 July 2016 data have had to be retrieved from literature. Notably, from July 2016 to January 2017 the nearest data available were from the meteorological station of Greci, 18 km far from the site, while data from Flumeri station (6 km far from the area) have been available since 02 January 2017. It is quite difficult to establish a valid and repeatable correlation between these two physical entities. This could be related to malfunctioning of the pluviometer installed on site or lack of direct evidences, which could suggest that there is not a direct relationship between rainfall and water level in the area.

Numerical Model

First year of monitoring

The numerical model described in the paragraph 6.2.6 was calibrated using the data related to the first three months of monitoring and was part of a preliminary study proposed at the 4th World Landslide Forum (Carri et. al. 2017). In particular, various simulations regarded the position of the water table, accordingly to the data registered by the piezometers. This was initially located at 17 m depth below ground level and then gradually raised up to 11 m depth. Fig. 5.19a shows the comparison between the displacements provided by the model and those recorded by DT0007 inclinometer, for a water level located at 17, 15, 13 and 11 meters below ground level. The highest level is the one recorded by the instrumentation at the end of October 2015. The same results were represented for DT0008 inclinometer (Fig. 5.20a).

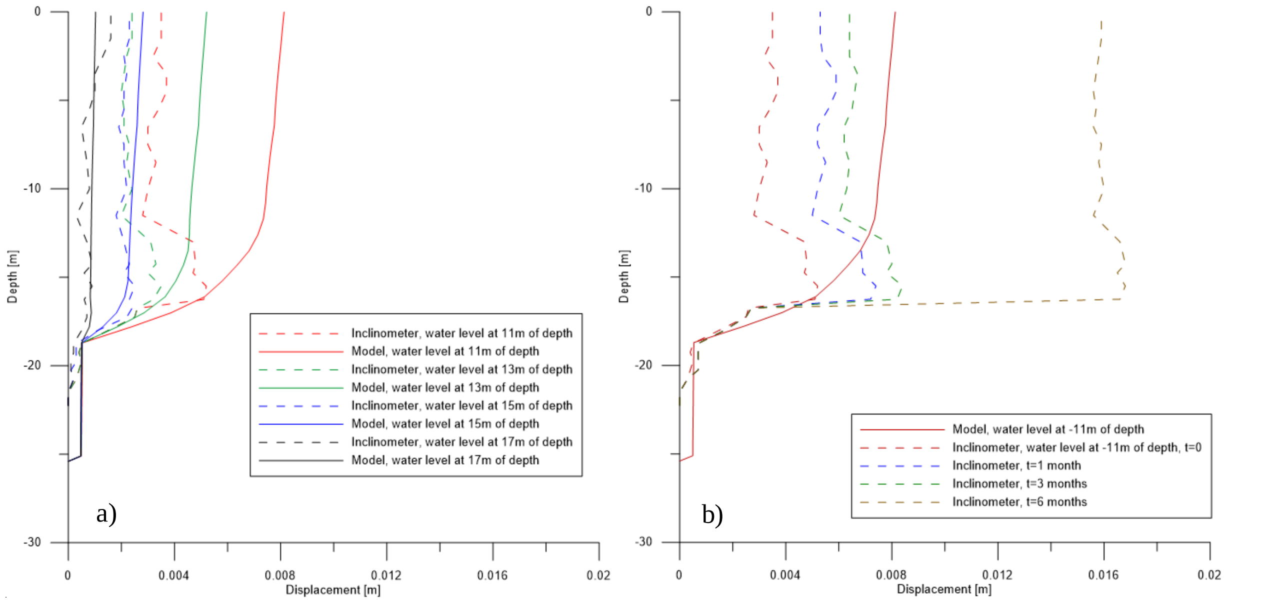

Fig. 5.19: a) Displacements recorded by DT0007 inclinometer and provided by the 2D FDM model at the end of October 2015 and b) Displacements provided by the 2D FDM model and recorded by MUMS at the end of the first year of monitoring (July 2016)

The data appeared to be in good agreement, and the sliding surface was correctly identified. Moreover, the computed displacements were comparable with the ones obtained from MUMS chain. Starting from November 2015, the landslide started to show a different behaviour, with relevant displacements occurring without appreciable variations of the water level. In particular, Fig. 5.19b and Fig. 5.20b show the comparison between the displacements provided by the model with water level at 11 m of depth and movements recorded by DT0007 and DT0008 respectively with the same water level (related to the date of 15 October 2015) and after one, three and six months.

The results do not agree with the hypothesis of an elastoplastic constitutive model, in particular for DT0007 inclinometer. Furthermore, the displacement rate (previously discussed) remained constant over long periods, being only slightly influenced by the variations in pore pressure. At the end of the first year of monitoring it became clear that the assumption of elastoplastic behaviour was not correct. Such displacements could be ascribed to secondary creep behaviour of the material surrounding the sliding surface, located at 16.25 m of depth. The new assumption needed to be verified with a time dependent numerical model, able to reproduce the observed mechanical behaviour. For this reason, the model was changed assigning the Burgers constitutive model to the layer corresponding to the sliding surface (Layer III).

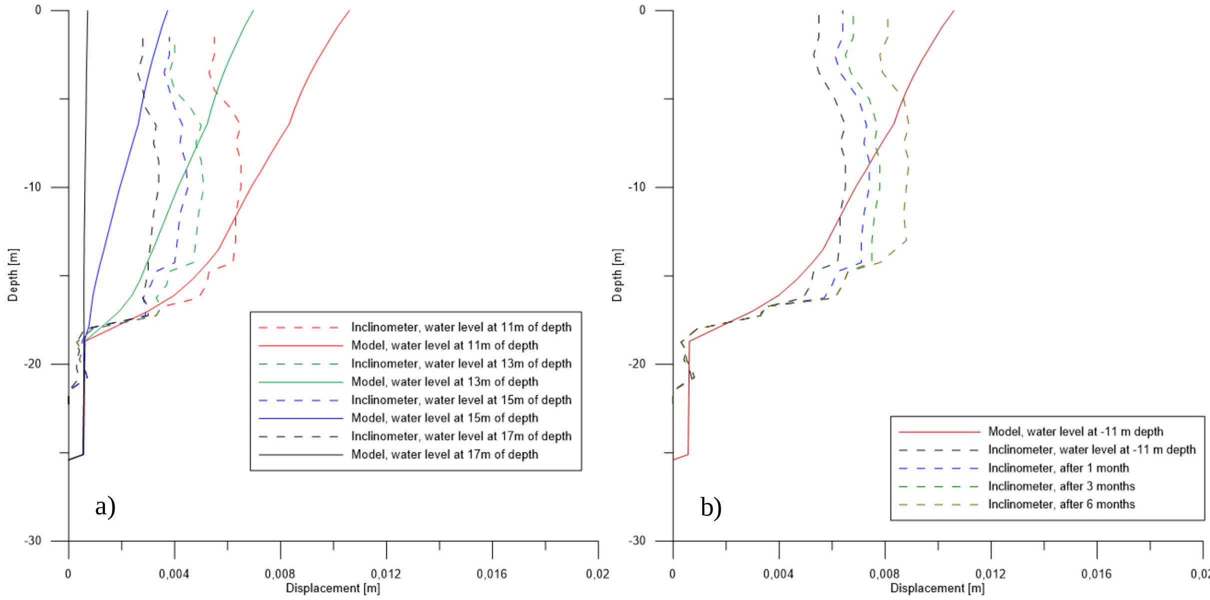

Fig. 5.20 a) Displacements recorded by DT0008 inclinometer and provided by the 2D FDM model at the end of October 2015 and b) Displacements provided by the 2D FDM model and recorded by MUMS at the end of the first year of monitoring (July 2016)

Burgers model (Fig. 5.21) combines Kelvin and Maxwell models acting in series (FLAC Version 8.0 Creep Material Models 2016). Kelvin model is represented by a linear spring and a dashpot in parallel, while Maxwell model shows the same elements in series. It was then necessary to define four parameters (K_{Ks}, C_{Ks}, K_{Ms}, C_{Ms}) corresponding to stiffness K of the linear spring and viscosity C of the dashpot for Kelvin (K_s) and Maxwell (M_s) models (Tab. 5.5). Fig. 5.21 reports the same parameters defined as K_{Kn}, C_{Kn}, K_{Mn}, C_{Mn} respectively.

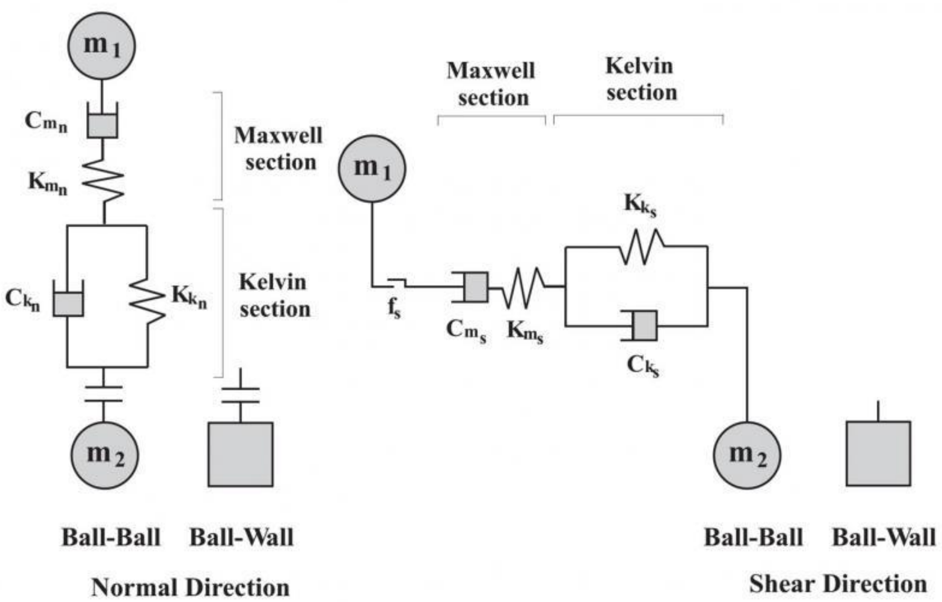

Fig. 5.21: Burgers model (source: FLAC website)

Laboratory tests are generally required to determine these parameters. This tests could last up to several months or years and were not possible in this specific case study, due to budget and time available. For this reason, data derived from similar case histories, where dynamics and materials involved were similar (Segalini 2001), were first introduced in the study. This assumption brings uncertainty into the model, because creep parameters are influenced by temperature and other site factors. As a consequence, the model required a calibration and a

validation through back analysis and comparison with monitoring data. In particular, expected values should have an order of magnitude of $10^7 \div 10^8$ Pa for parameters C, and $10^{10} \div 10^{14}$ for parameters K, which have higher variability (Lin et al. 2017, Segalini 2001).
The new 2D Time-Dependent FDM model considers the reference reading of MUMS inclinometers as its own starting time (t=0) and then simulates all the main variations of the water level recorded for both boreholes. During the monitoring, piezometers did not measure the pore pressure during most of the surveyed time. This means that the water table was at a higher depth that is over 13 m. Due to the low permeability of the materials involved and the pore pressure fluctuation recorded by the sensors, it was deemed appropriate to consider the starting position of the water table at 14 m below ground level. The small rapid increase of the water table during the 15 October event, which reached 11.5 depth in one day only, could also confirm the hypothesis. Tab. 5.5 reports the model mechanical parameters, while Fig. 5.22 shows the comparison between displacements provided by the Time-Dependent FDM model and instrumental data of DT0007 and DT0008 MUMS Vertical Arrays at the end of the first year of monitoring.

Tab. 5.5: Mechanical parameters and failure criterion – model used

	Layer I Clayey silt	Layer II Soft clay	Layer III Marl clay	Layer IV Marl Flysch
Model	Elastoplastic	Elastoplastic	Burgers	Elastoplastic
Failure criterion	Mohr-Coulomb	Mohr-Coulomb	-	Modified Hoek-Brown
Elastic modulus [MPa]	1.857	4.725	-	12000.000
Poisson's ratio [-]	0.30	0.33	-	0.30
Unit weight [kN/m^3]	20.19	20.85	-	26.00
Friction angle [°]	28.00	33.60	-	-
Cohesion [kPa]	9.30	9.30	-	-
m_b [-]	-	-	-	2.005
s [-]	-	-	-	0.007
a [-]	-	-	-	0.504
σ_{ci} [MPa]	-	-	-	2.413
σ_t [MPa]	-	-	-	0.100
K_{Ks} [MPa]	-	-	16.20	-
C_{Ks} [PI]	-	-	4.00 e^{11}	-
K_{Ms} [MPa]	-	-	84.60	-
C_{Ms} [PI]	-	-	1.50 e^{14}	-

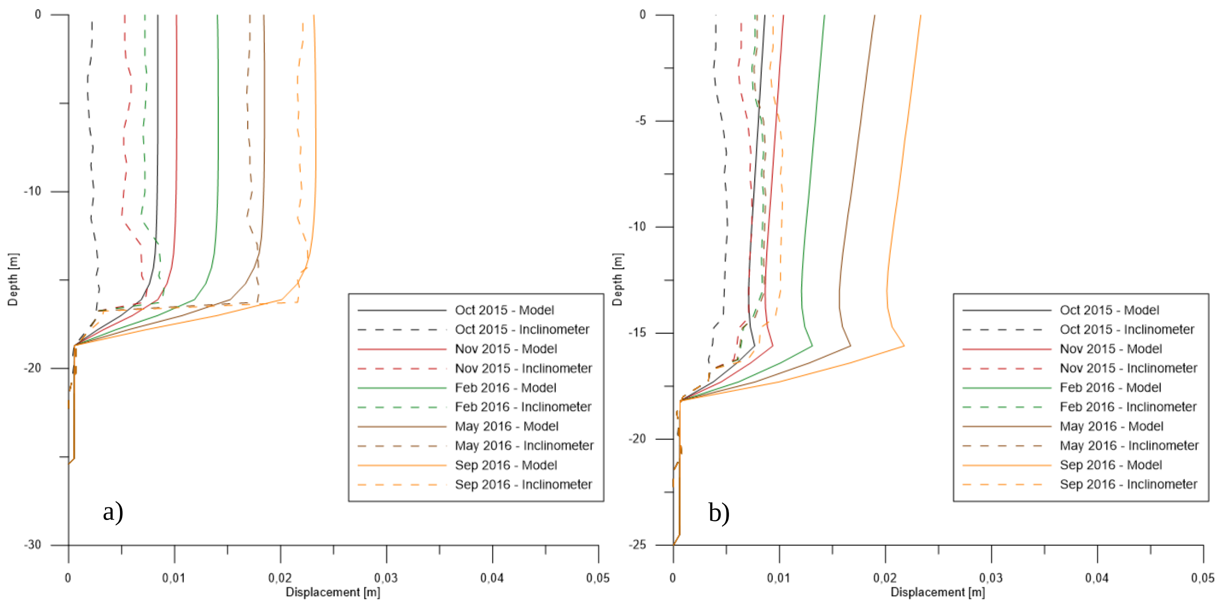

Fig. 5.22: Comparison between displacements provided by time-dependent FDM model and a) DT0007 and b) DT0008 data

Data of DT0007 are in good agreement with the model outcomes, while DT0008 displacements are overestimated. This result could suggest a different behaviour of the landslide above and below the highway.

This could be related to the position of DT0008 inclinometer, placed in a zone which is less steep and more lateral with respect to the active movement, close to the left side of the landslide. This hypothesis could be confirmed by the difference in azimuth between two inclinometers, with DT0008 that presents an azimuth towards the centre of the accumulation area (Carri et. al. 2017).

Second year of monitoring

Starting from the beginning of the second year of monitoring, the model began to underestimate the amount of movements related to the DT0007 inclinometer (Fig. 5.23), probably due to the acceleration observed in the displacement rate after the date of 13 November 2016. Some scholars have studied the terrain at a microscopic level identifying that micro-cracks could reduce the friction resistance along the sliding surface (Colleselli and Colosimo, 1977). Some examples of constitutive models which describe the progressive damage of the soil related to deformation phenomena are reported in literature (Singh and Mitchell 1968, Vyalov 1986).

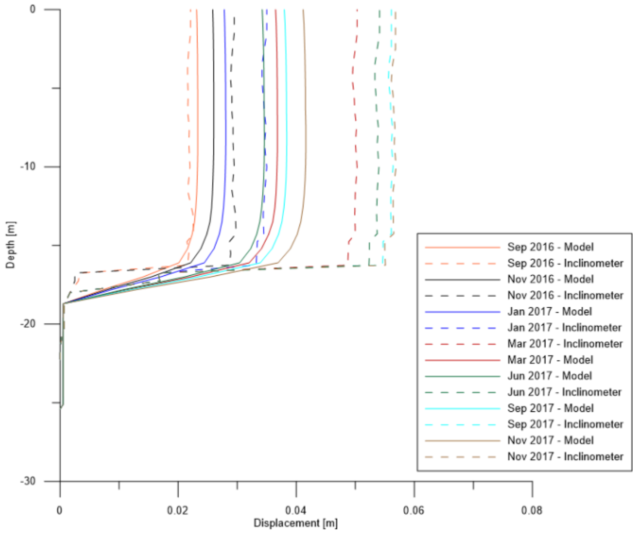

Fig. 5.23: Comparison between displacements provided by time-dependent FDM model and DT0007 inclinometer during the second year of monitoring

According to the hypothesis of a mechanical resistance degradation caused by the aforementioned progressive damage, Burgers model parameters were reduced, starting from the beginning of the second year of monitoring (t = 365 days). Tab. 5.6 reports the values of K_{Kn}, C_{Kn}, K_{Mn}, C_{Mn} obtained after the calibration of results with monitoring data at the end of the second year.

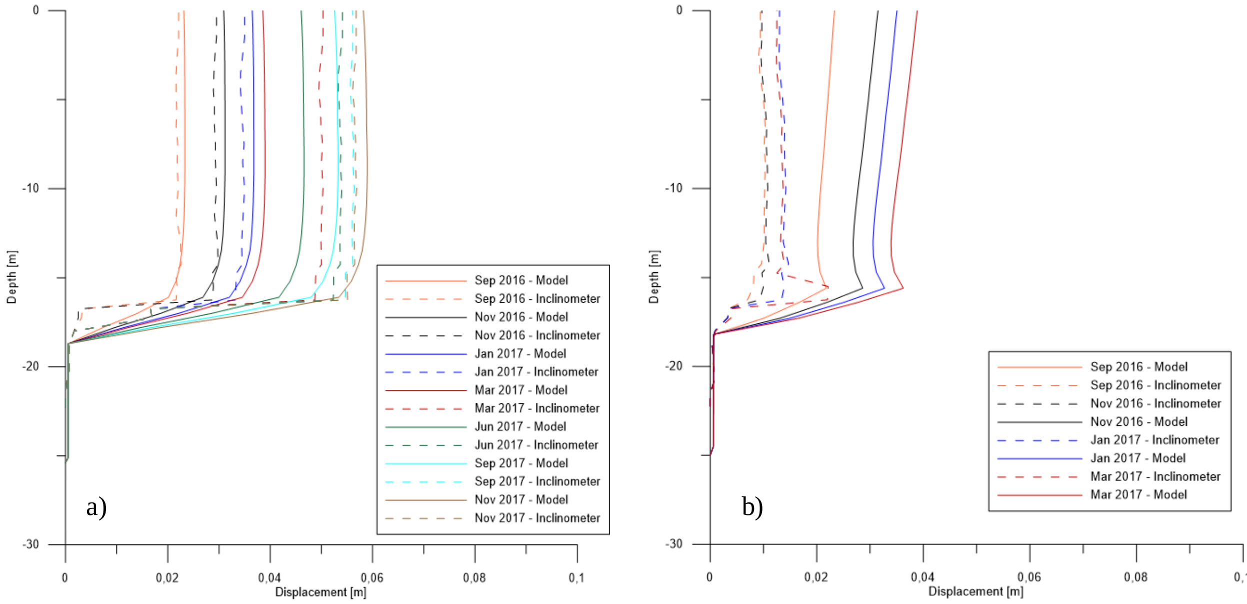

Fig. 5.24: Comparison between displacements provided by time-dependent FDM model, with reduced Burgers parameters, and a) DT0007 inclinometer at November 2017 and b) DT0008 inclinometer at March 2017

Tab. 5.6: Mechanical parameters adopted for Layer III of Burgers model in the simulation of the second year of modelling

K_{Ks} [MPa]	C_{Ks} [PI]	K_{Ms} [MPa]	C_{Ms} [PI]
9.23	2.28 e^{11}	48.22	8.55 e^{13}

As in the previous simulation, data of DT0007 are in perfect agreement with the model outcomes at November 2017, both from qualitative and quantitative points of view. DT0008 displacements are overestimated, but the model anticipates the behaviour between 15 and 17 m depth registered by the instrumentation at March 2017. It appears evident what already stated about the different behaviour of the landslide above and below the highway.

Forecasting analysis

Thanks to the knowledge achieved during two years of monitoring, two forecasting numerical simulations were carried out for the year 2018, based on the following hypotheses:

- The position of the water table was based on the observations of past events, with the water level below 13 m of depth;
- The first simulation considered the mechanical parameters of Layer III, reported in Tab. 5.6, which are the same used for the simulation of the second year of monitoring;
- The second simulation was carried out reducing stiffness and viscosity (Tab. 5.7) of the same trend observed between the first and the second year of monitoring;
- Due to the fact that the DT0008 chain has been inactive since March 2017, a comparison between forecasting analysis carried out at the end of 2017 and monitoring outcomes was possible only for DT0007 inclinometer.

Tab. 5.7: Mechanical parameters adopted for Layer III of Burgers model in the forecasting simulation for year 2018

K_{Ks} [MPa]	C_{Ks} [PI]	K_{Ms} [MPa]	C_{Ms} [PI]
5.26	12.99 e^{10}	27.49	48.73 e^{12}

The first simulation (Fig. 5.25a) highlighted a constant deformation that reached 8.7 cm in November 2018, while the second simulation (Fig. 5.25b) showed 11.4 cm. The same analysis applied at DT0008 vertical forecasted 8.7 and 11.4 cm of displacements, respectively. During 2018 it was possible to compare DT0007 inclinometer results with the model forecasts.

Unfortunately the MUMS array was interrupted at 16.75 m depth on 01 January 2018, probably due to displacements that regarded the sliding surface placed at 17 m depth. Starting from that date, data are available only for the upper part of the tool, over 16.25 m depth. For this reason, differential cumulative displacements are underestimated. MUMS inclinometer resulted permanently compromised on 5 June 2018 and monitoring came to an end due to excessive deformations. The comparison between the inclinometer readings at the end of February and May 2018 endorses the first model hypothesis, with a 9% and 17% difference at the top respectively (Fig. 5.25a). The difference could be related to the lack of instrumental information under the depth of 16.75 m and the position of the water table. As shown in Fig. 5.16, water table showed significant variations with respect to the simulation hypotheses, in particular at March 2018.

Further studies should involve the integration of other piezometers data, together with the restoration of weather station and inclinometer systems functionality. The installation of new instrumentations could lead to an automation of the numerical model, continuously validated through monitoring data, and consequent alert procedures to the authorities in charge.

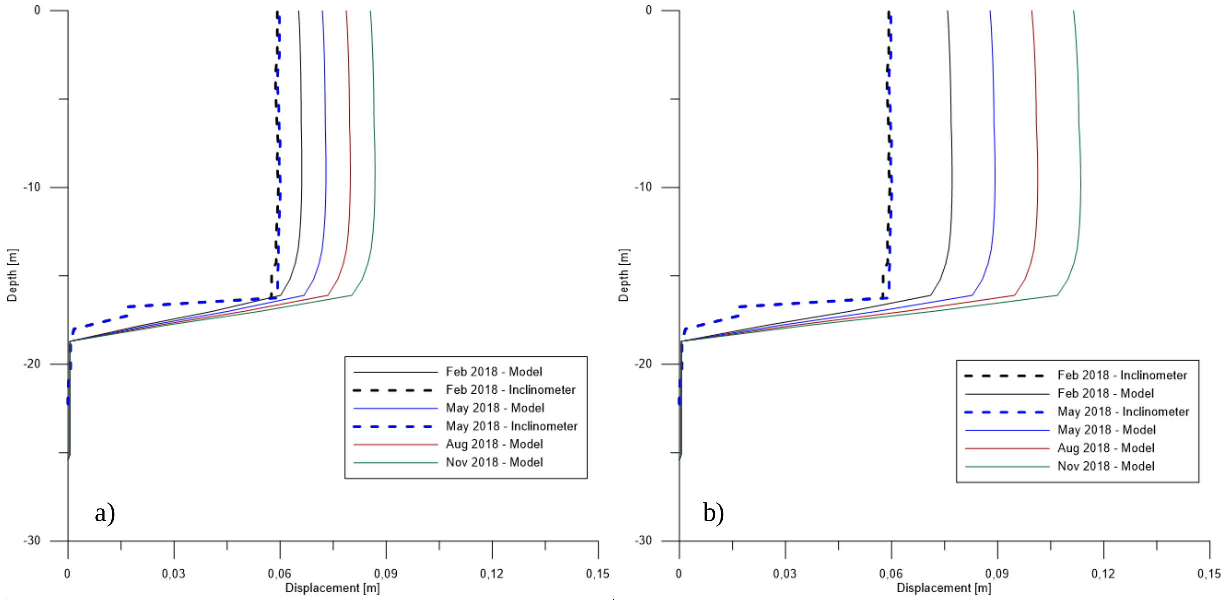

Fig. 5.25: Forecasting analysis for year 2018 a) with no degradation of mechanical resistance and b) reducing stiffness and viscosity with the same trend recorded between the first and the second year of monitoring

5.2.8. Conclusions

The case study focuses on understanding the landslide mechanism with the near real-time monitoring of displacements, pore pressures and rainfall, together with the development of a series of numerical models, calibrated and validated through site outcomes. The knowledge obtained is of primary importance in the risk management process and could vary along time, requiring a continuous verification of the hypothesis and updating of the results. In particular, this study started with the definition of a 2D FDM elastoplastic model, converted to a Time-Dependent FDM model at the end of the first year of monitoring. After the second year, mechanical parameters needed a reduction due to progressive degradation observed. The new validation permitted a forecasting analysis, partially verified through monitoring data. The results obtained could be used by the authorities in charge to evaluate the landslide possible behaviour and the compatibility of the forecasted deformations on the structural work, assessing the potentially required mitigation measures or implementing alert procedures. Finally, this study underlines the importance of a properly designed and timed monitoring system, coupled with appropriate and proactive numerical modelling to understand and safely manage landslide hazard. Further evolution of this conceptual approach should involve the objective and automated recognition of variations in landslide dynamics, and the related autonomous correction of the numerical model input parameters. This would allow a near real-time and continuous update of the landslide hazard assessment forecast, and the self-learning redefinition of the thresholds used to trigger the activation of each different management alert level.

5.3. SS652 Fondovalle Sangro Landslide, Italy

The third case study is about the monitoring of a landslide that insists on the construction site of State Road 652, an important infrastructure that connects Adriatic and Tyrrhenian Sea, through Abruzzo and Molise regions (Fig. 5.26). The results of the case study were included in Segalini et al. (2019)

Fig. 5.26: SS652 Fondovalle Sangro site (41°53’36.50 N, 14°15’14.90 E)

The realization of the road started in the first 60s and now the completion of the last 5.3 km is ongoing. The works have undergone several delays due to numerous landslides, the collapse of the viaduct Le Barche near the town of Bomba (Fig. 5.27) and bureaucratic problems. The completion works have a cost of 190,433 million euros for a period of 30 months (Strade & Autostrade 2018).

Fig. 5.27: Le Barche viaduct

During the preliminary surveys, a series of MUMS systems (Fig. 5.28) have been installed (Tab. 5.8). In particular, this discussion focuses on DT0014 inclinometer and the event of March 2017.

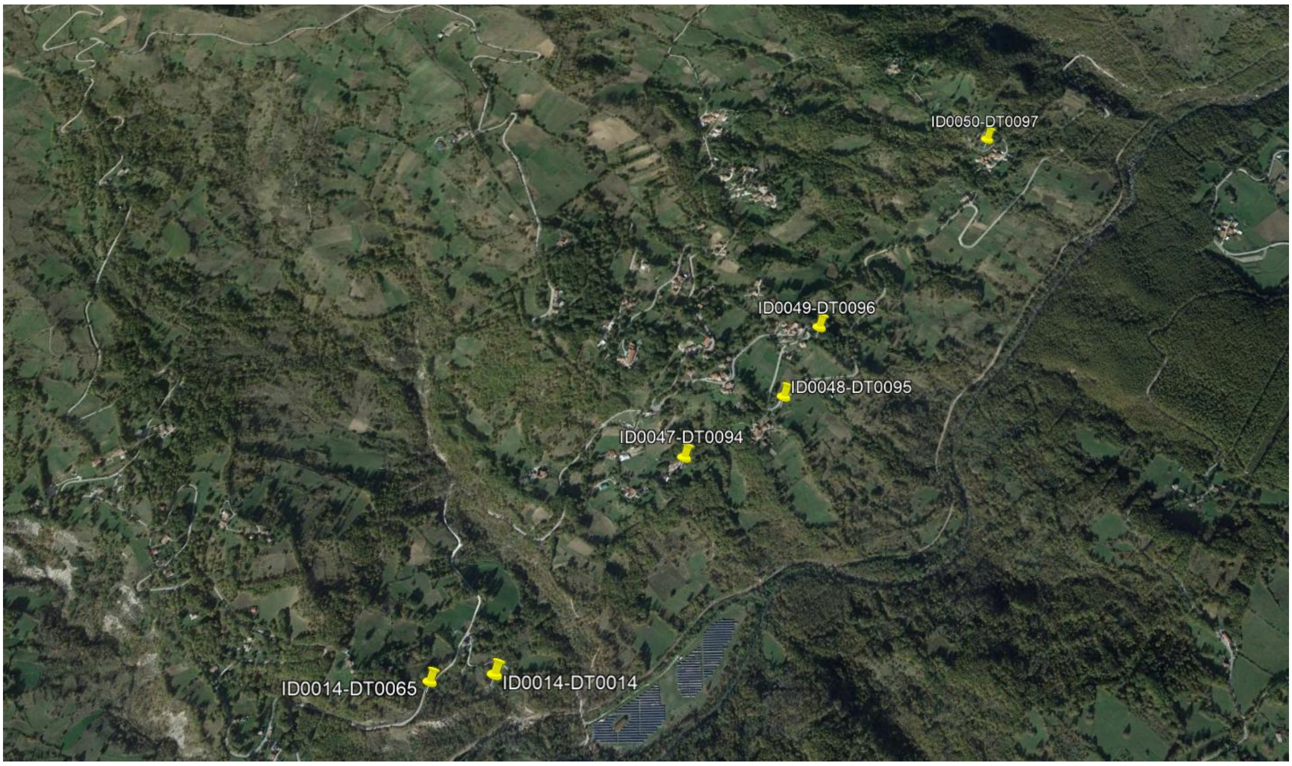

Fig. 5.28: Location of MUMS inclinometers

Tab. 5.8: MUMS inclinometers installed on SS652 construction site at September 2018

ID	DT0014	DT0065	DT0094	DT0095	DT0096	DT0097
Installation date	18/11/2016	07/09/2017	19/09/2018	18/09/2018	20/09/2018	19/09/2018
Reference reading	19/11/2016	09/09/2017	22/09/2018	22/09/2018	22/09/2018	22/09/2018
End of monitoring	13/03/2017	Ongoing	Ongoing	Ongoing	Ongoing	Ongoing
Array typology	Vertical Array	Vertical Array	Vertical Array	Vertical Array	Vertical Array	Vertical Array
Length [m]	35	35	69	95	111	66
Sensors typology	Tilt Link HR 3D V	Tilt Link HR 3D V	Tilt Link HR 3D V	Tilt Link HR 3D V	Tilt Link HR 3D V	Tilt Link HR 3D V
Number of sensors [-]	50	48	34	47	55	33
Interspace between sensors [m]	0.70	0.70	2.00	2.00	2.00	2.00

5.3.1. Introduction

DT0014 inclinometer was installed on 18 November 2016 (Fig. 5.30) and the following day was considered as the elaboration reference date. The sample period was set to 1 hour, sending data to the elaboration centre once a day. The monitoring came to an end on March 13th, 2017 due to excessive deformations. The borehole was filled with cement at the bottom for about 1 meter, in order to fix the anchor to the stable portion, and a mixture of bentonite for the remaining part of the vertical, using the Spaggiari method described in Chapter 3.3. The installation required a couple of hours. Data logger was powered through 12 V lead-acid battery and 5 W solar panel. Fig. 5.29a shows the battery level for the whole period of monitoring, highlighting the correct functionality of the powering system, while Fig. 5.29b represents the temperature of the data logger.

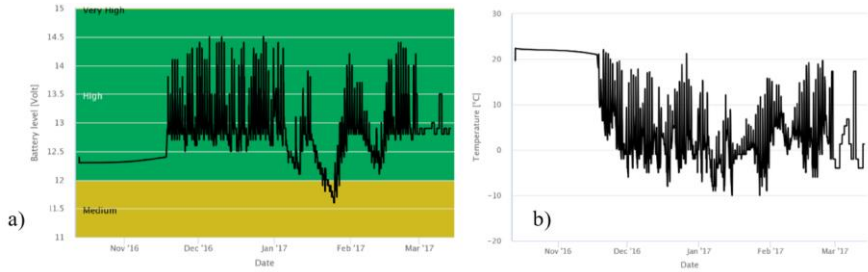

Fig. 5.29: a) Battery level and b) data logger temperature for the whole period of monitoring

Sensors used were Tilt Link HR 3D V, equipped with MEMS 2.0 and Electrolytic Cells, calibrated through the procedure described in Chapter 3.2. The Array was 35 m long, with nodes every 70 cm.

Fig. 5.30: MUMS DT0014 after installation on site

5.3.2. Description of the Area

The site is characterized by the presence of clayey and sandy silt and Flysch, with several landslides that show fast kinematics and sliding surfaces between 8 and 10 m depth. The area has been analysed through seismic tests, geophysics and geo-mechanical surveys that permitted to define the soil category E, accordingly to $v_{s_{30}}$ seismic classification, the Poisson coefficient, the shear strength, the elastic and the compressibility modules.

Fig. 5.31: Movements recorded in the area during surveys before MUMS installation

During preliminary surveys that anticipated the installation of MUMS, some instability events were recorded:

- An inclinometer casing was interrupted at 8 m depth, with 40 cm of settlements of the surrounding soil;
- Two landslide bodies invaded an old railway line.

5.3.3. Results

During the period of monitoring, the automatic inclinometer recorded the displacements reported in Fig. 5.32. In particular, the instrumentation showed two significant changes in displacement rate starting from the 23th of January 2017 and the 7th of March 2017 respectively that interested the first 6 m of soil (Fig. 5.34a). The phenomenon led to the progressive breaking of the Array, as reported in Tab. 5.9. For this reason, the cumulative movements at the end of monitoring, reported in Fig. 5.32b, are underestimated after the 27 of February 2017, while the local ones over 5.65 m depth could be considered as correct. Moreover, sensor at 0.75 m depth registered a settlement, which is observable in Fig. 5.33 as a negative displacement (the node moved on the opposite direction with respect to the landslide, realigning itself to the vertical).

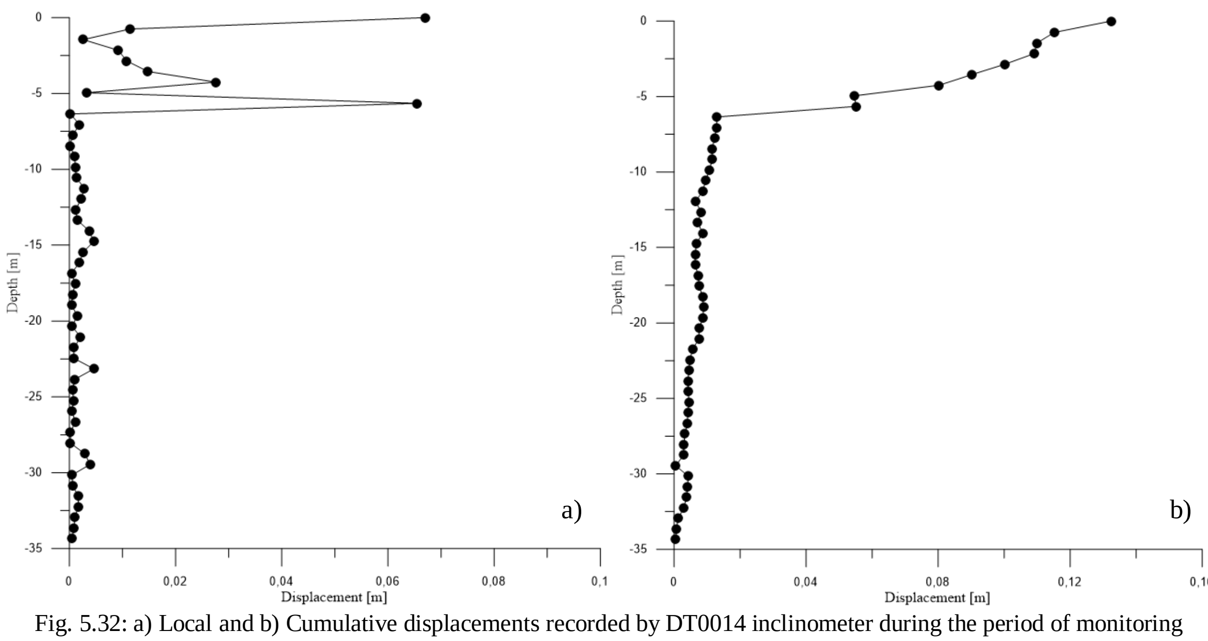

Fig. 5.32: a) Local and b) Cumulative displacements recorded by DT0014 inclinometer during the period of monitoring

Tab. 5.9: Progressive damage of the array with related last raw data available

Links	Date and hour of the last raw data available	Date and hour of the first inactive reading	Depth [m]
1÷84	27/02/2017 12:45	27/02/2017 13:45	-5.65
85÷86	08/03/2017 20:32	08/03/2017 21:32	-4.95
87÷100	13/03/2017 13:56	13/03/2017 14:56	0.00

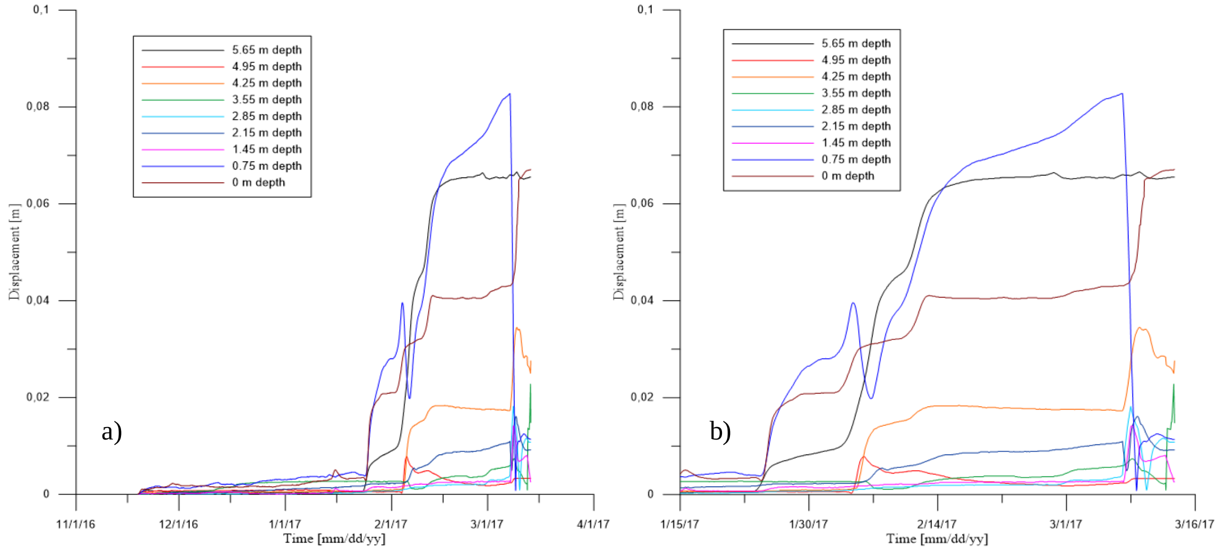

Fig. 5.33: Local displacements versus time starting from 5.65 m depth for a) the whole period of monitoring and b) starting from the 15 of January 2018

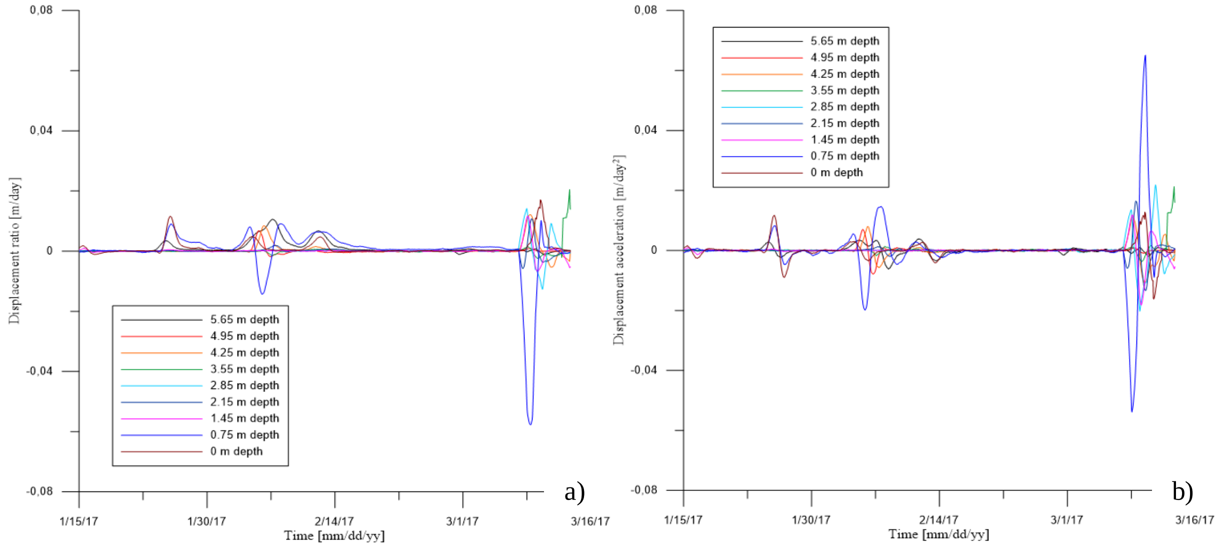

Fig. 5.34: a) Displacement rates and b) accelerations versus time starting from 5.65 m depth recorded after the 15 of January 2018

MUMS inclinometer resulted completely inactive on March 13th, 2017. During the last days of monitoring, Fukuzono method (described in Chapter 4.1.2) was activated several times through IVM activation criterion (Chapter 4.2.3) and an alert procedure was processed reporting the ongoing event to the responsible of monitoring. After an on-site inspection (Fig. 5.35), a landslide event was clearly identified, with a complex dynamic characterized by several breakings, major and minor events, settlements and displacements. Fig. 5.36 shows the area surrounding MUMS Vertical Array. During the inspection, all the traditional inclinometer casings were inaccessible. Moreover, any traditional measure resulted impossible, giving no information at all. In particular, some vertical boreholes were drilled recently and never read, resulting in a loss of money and time. MUMS has been the only instrumentation able to identify and report the landslide event, also providing a measure of its magnitude. This to demonstrate, if necessary, the importance of an automated tool in the detection of hazardous phenomena instead of traditional manual technologies.

Fig. 5.35: Situation reported during the on-site inspection

Fig. 5.36: Area surrounding MUMS Vertical Array as observed during on-site inspection

Tab. 5.10 summarizes all the Alarms and False Alarms detected during the period of monitoring, based on IVM activation criterion described in Chapter 4.2.3 and application of Fukuzono method. In particular, it is important to remind some concepts:

- The sampling period was set to 1 hour. For this reason, the sensibility of the T_f definition is ±1 hour;
- Data reached the elaboration centre once a day, at 12:00;
- As previously reported, MUMS EWS is designed to recognize False Positives that may happen under certain conditions:
    - T_f < 0 (negative Time of Failure, i.e. date of collapse is in the past, reported in Tab. 5.10 as reason #1);
    - T_f > 0 & $T_f < T_{rd}$, where T_{rd} is the time of the last raw data available represented by a numerical value. In detail, the date of failure precedes the last instrumental data recorded, which is not returning an error (i.e. the sensor is working correctly);
    - The last dataset value has an inverse velocity which is consistently increasing, referring to the previous one.
- The activation of Fukuzono method does not imply an automatic alarm to the responsible of monitoring. This is validated through a series of preliminary analysis that regard:
    - The number of points in the dataset (reported in Tab. 5.10 as reason #3). The minimum dataset considered is composed by 5 points. If this value increases, it means that a consistent trend of data is respecting the IVM activation criterion;
    - R^2: the linear regression index points out the ability of the linear model to reproduce the observed data. Model is activated for R^2 > 0.8. Higher values indicates an increasing confidence level;
    - Nature of displacements (Cumulative or Local). The algorithm analyses the number (reported in Tab. 5.10 as reason #4) and the typology of alarms referring to the presence of cumulative, local or both cumulative and local displacements (reason #2),
    - Number of alarms previously sent (reported in Tab. 5.10 as reason #5): this parameter verifies the presence of previous alarms during days before and characterizes the so defined "Conditioned Alarms".

Tab. 5.10: Alarms and False Alarms activated during the period of monitoring, based on IVM activation criterion and Fukuzono method

Node [-]	Depth [m]	Displacement typology	Acceleration date [dd/mm/yyyy HH:MM]	T_f prediction [dd/mm/yyyy HH:MM]	Considered dataset [-]	R^2 [-]	Automated validation response	Reason of validation response
99	0.4	Cumulative	24/01/2017 15:42	24/01/2017 22:36	5	0.8997	False Alarm	#1 & #2
87	4.6	Local	04/02/2017 13:37	04/02/2017 19:47	6	0.8853	False Alarm	#1 & #2
97	1.2	Cumulative	05/02/2017 19:44	06/02/2017 09:29	5	0.9200	False Alarm	#1 & #2
93	2.5	Cumulative	07/03/2017 14:26	07/03/2017 21:11	5	0.8980	False Alarm	#1
95	1.8	Cumulative	07/03/2017 14:26	07/03/2017 23:57	5	0.8889	False Alarm	#1
95	1.8	Local	07/03/2017 15:26	08/03/2017 04:14	7	0.9441	False Alarm	#1
93	2.5	Cumulative	08/03/2017 02:28	09/03/2017 00:55	7	0.8515	Alarm	#3 & #4
95	1.8	Cumulative	08/03/2017 02:28	08/03/2017 22:48	7	0.9578	Alarm	#3 & #4
99	0.4	Cumulative	08/03/2017 17:31	09/03/2017 06:00	6	0.9675	False Alarm	#1
99	0.4	Local	08/03/2017 21:32	09/03/2017 23:59	5	0.8802	Conditioned Alarm	#5
99	0.4	Local	09/03/2017 05:34	09/03/2017 16:48	5	0.9117	Conditioned Alarm	#5
91	3.2	Cumulative	09/03/2017 23:38	10/03/2017 12:05	5	0.9081	Conditioned Alarm	#5
93	2.5	Cumulative	09/03/2017 23:38	10/03/2017 10:53	5	0.9421	False Alarm	#1
89	3.9	Cumulative	12/03/2017 13:51	12/03/2017 19:56	5	0.8350	False Alarm	#1
95	1.8	Cumulative	12/03/2017 13:51	12/03/2017 18:57	5	0.8301	False Alarm	#1
89	3.9	Cumulative	13/03/2017 06:54	13/03/2017 16:06	5	0.9400	Conditioned Alarm	#5

#1 Date of collapse is in the past;
#2 A single alarm is not significant;
#3 Significant dataset;
#4 Multiple alarms activated at the same time;
#5 Information closely linked to the site history and outcomes of the previous days.

In this particular case, due to the fact that data reach the elaboration centre only once a day, a series of False Alarms were identified because the date of predicted collapse was in the future, referring to the acceleration date, but in the past, referring to the transmission date and hour. As an example, the activation of Fukuzono method, occurred for local displacement of node 95 on 07 March 2017 at 15:26, predicted a potentially dangerous event on 08/03/2017 at 04:14. The data transmission took place on 08/03/2017 at 12:00 and the sensor was still reading correctly. If the data transmission had been in real time, the False Alarm would have not been recognize based on #1 hypothesis. Real time analysis implies a severe cross check validation procedure.

Condition #2 indicates that a EWS should not refer to a single alarm of a single sensor. In particular, the alert procedure of DT0014 MUMS application investigates 50 local and 50 cumulative conditions, which are independent one to each other (remembering that cumulative displacements are related, because they add the information at a specific depth to the information obtained for the deeper part of the array). An email is sent to the responsible of monitoring only if there is an evidence of an event going on, i.e. Fukuzono method is activated for different nodes and possibly for different displacement typologies (local and cumulative), as in condition #4.

Condition #3 is about the number of points included in the linear regression model, thanks to IVM activation criterion (4.2.3). A larger dataset implies that the abovementioned hypotheses are more solid, i.e. the landslide is accelerating and the linear regression reliability improves. As previously discussed, the minimum dataset required by the algorithm to detect the Time of Failure is composed by 5 values. Cases defined by 7 points, like the Alarms identified by cumulative displacements of nodes 93 and 95 activated on 08 March at 02:28, are more consistent for the analysis and certify an enhanced accuracy in the final result.

Finally, there are some situations that could be classified as not significant if considered alone, which become worthy of note if analysed together with previous information. For example this is the case of the Alarm identified by local displacements of node 99 on 09/03/18 05:34. If the result is considered alone, it could be classified as a False Alarm because it is composed of 5 points (standard dataset), the information related to cumulative displacements is classified as a False Alarm (for date of collapse in the past) and there are no further information about other sensors. Considering the series of alarms activated the day before, it is possible to define a new category, closely related to condition #5, which is defined as “Conditioned Alarm”. A Conditioned Alarm is an alarm that could be classified as a False Alarm or an Alarm to be ignored if considered alone, which become a “real” alarm if related to site alarm history.

Thanks to the on-site inspection and a series of back analysis, it was possible to classify two main landslide events, occurred on 08 March 2017, between 20:32 and 21:32, and on 13 March 2017, between 13:56 and 14:56. The uncertainty that regards the precise time is related to the sampling period of instrumentation: the first value (for example 20:32) indicates the last available instrumental reading characterized by a numerical value, while the second one (21:32) the first reading returning an error code (i.e. the breaking of the instrumentation after landslide event).

Tab. 5.11 reports the comparison between Time of Failure predictions and Time of Failure observed for Alarm or Conditioned Alarm events. The first activation (Links 93 and 95) resulted in a very comfortable result, evaluating the Time of Failure only 3 hours and 1 hour later respectively (which could be considered as 2 hours and 15 minute respectively considering 20:32 as collapse hour). The meaning of the algorithm is not to be a magical crystal ball that identifies the day & hour of collapse perfectly, but is intended to provide useful information about potentially dangerous phenomena that are going on and a period where the collapse should be expected and carefully monitored. The first alert procedure gave a correct response, with a warning time of 10 hours (time between the data transmission & elaboration and collapse) that could have been of 19 hours in case of a real-time data transmission. The operator that received the notification assumed that the warning time was of 11 hours (time between the data transmission & elaboration and predicted time of failure) which is very close to the observed one. After this event, two conditioned alarms were activated on 09 March at 12:00, predicting a possible collapse some hours later. This second alert procedure, like the following one (10 March 12:00), is quite difficult to evaluate, because it could refer to the collapse observed on 08 March or it could express the first symptoms of the following collapse, occurred on 13 March. In any case, the information should be considered as “*you observed a collapse and something is still going on, be careful and monitor the situation*”. Finally, the last alert procedure (Conditioned Alarm) was activated on 13 March at 12:00, forecasting a potentially collapse 4 hours later. A main landslide event was effectively observed 3 hours later, with the breakout of all the instrumentations on-site. The forecasting error was of only 1 hour, giving the necessary time for a risk management procedure.

Tab. 5.11: Comparison between predicted and observed T_f and related warnings time

Node [-]	Depth [m]	Acceleration date [dd/mm/yyyy HH:MM]	T_f prediction [dd/mm/yyyy HH:MM]	T_f observed [dd/mm/yyyy HH:MM]	Forecasting error [h]	Theoretical warning time [h]	Observed warning time [h]
93	2.5	08/03/2017 02:28	09/03/2017 00:55	08/03/2017 21:32	3 hours later	13 (22*)	10 (19*)
95	1.8	08/03/2017 02:28	08/03/2017 22:48	08/03/2017 21:32	1 hour later	11 (20*)	10 (19*)
99	0.4	08/03/2017 21:32	09/03/2017 23:59	08/03/2017 21:32	postponed of 1 day and 2 hours	12 (26*)	-14 (0*)
99	0.4	09/03/2017 05:34	09/03/2017 16:48	08/03/2017 21:32	postponed of 19 hours	5 (11*)	-14 (-8*)
91	3.2	09/03/2017 23:38	10/03/2017 12:05	?	not clear	0 (12*)	?
89	3.9	13/03/2017 06:54	13/03/2017 16:06	13/03/2017 14:56	1.5 hour later	4 (9*)	3 (8*)

* value that indicates the warning time if the data transmissions were in real-time

During the alert procedures, the responsible of monitoring received information about the Link, depth, displacement typology, acceleration date and Time of Failure prediction, together with two graphs for each sensor. In particular, the first one shows the Inverse of Velocity (expressed as day/mm) versus Time, together with the Index of Linear Regression, while the second reports the Velocity (mm/day) versus Time. The purpose of the figures is to help the decision maker in his final evaluation, which is always required. By observing the graphs of the first alert (Fig. 5.37 and Fig. 5.38) two main information are available: the dataset is consistent (7 points for both Links) and the Indexes of Linear Regression show a reliable fitting, in particular for node 95 (0.95779). Last point of Node 95 dataset seems to slightly diverge from the linear trend evidenced by the previous ones, and probably this is the cause of the 1 hour delay in the Time of Failure prediction. The displacement rate is consistent (Node 95 has a final velocity of 43 mm/day) and the average acceleration (lasted 7 hours) ranges between 24 and 45 mm/day^2. In particular, the displacement rate clearly indicates that a potentially dangerous phenomenon is going on, if compared to standard quantities recorded between the installation date and the end of February, which have a value of 0.093 mm/day and 0.025 mm/day respectively.

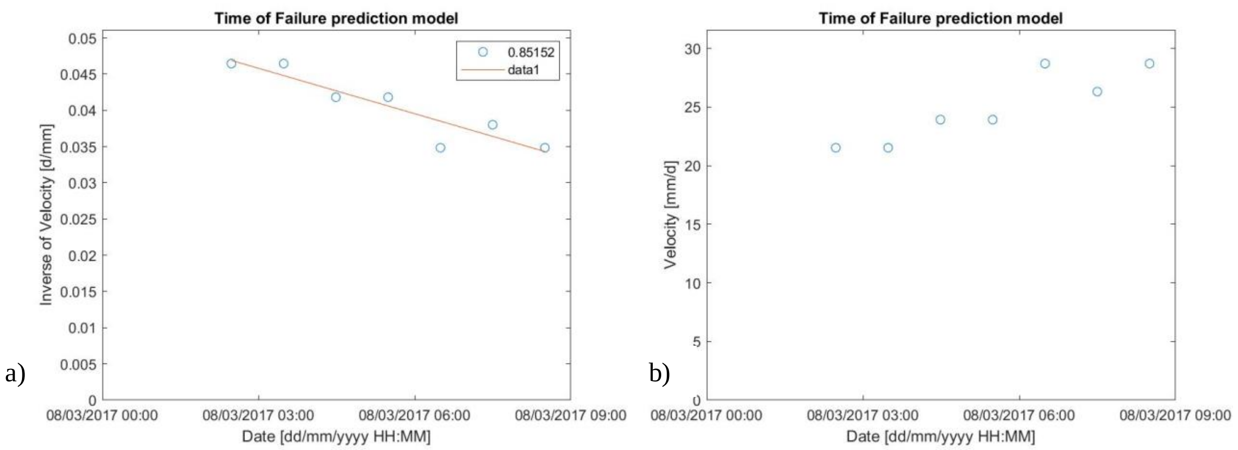

Fig. 5.37: a) Inverse Velocity vs Time and b) Velocity vs Time for cumulative displacements of node 93 with acceleration date on 08 March 2017 02:28 and Time of Failure forecasted on 09 March 2017 00:55

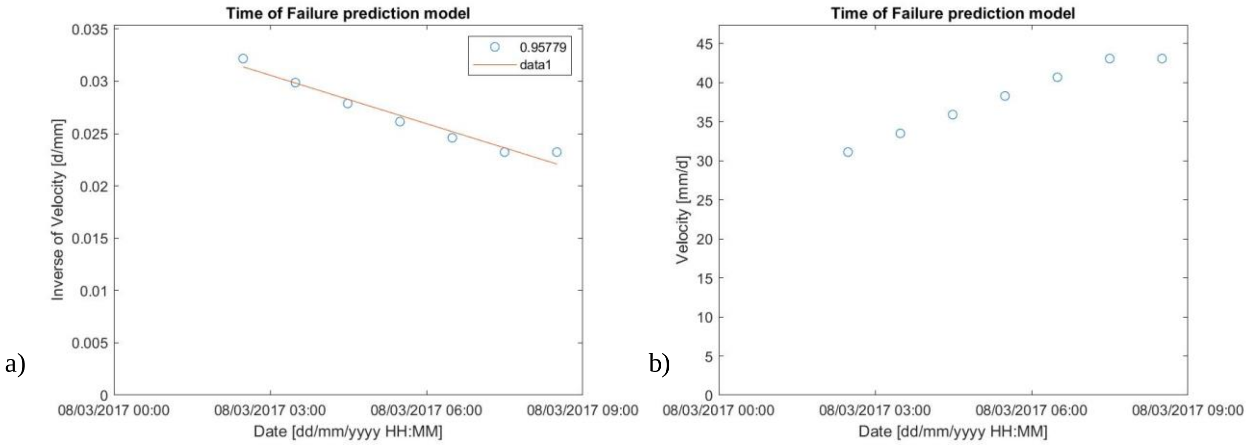

Fig. 5.38: a) Inverse Velocity vs Time and b) Velocity vs Time for cumulative displacements of node 95 with acceleration date on 08 March 2017 02:28 and Time of Failure forecasted on 08 March 2017 22:48

Finally, considering the distances between Links, it is possible to state that the movement has not a single shear plane but interests a zone where different sliding surfaces are present. This could be identified observing the values of displacement rate and acceleration.

The second alert (Fig. 5.39 and Fig. 5.40) shows a lower dataset (5 points) with good Indexes of Linear Regression (0.88 and 0.92) related to local superficial displacements (node 99).

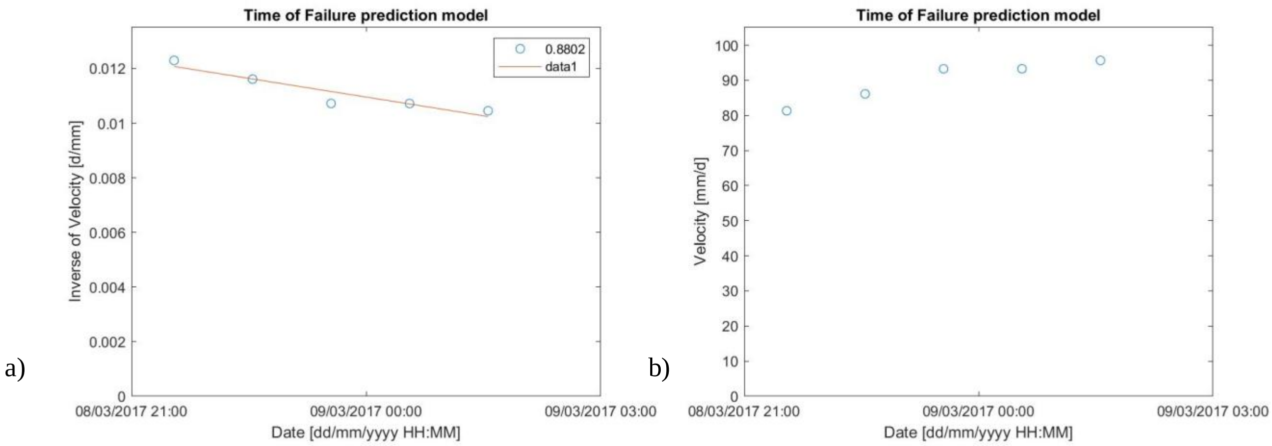

Fig. 5.39: a) Inverse Velocity vs Time and b) Velocity vs Time for local displacements of node 99 with acceleration date on 08 March 2017 21:32 and Time of Failure forecasted on 09 March 2017 23:59

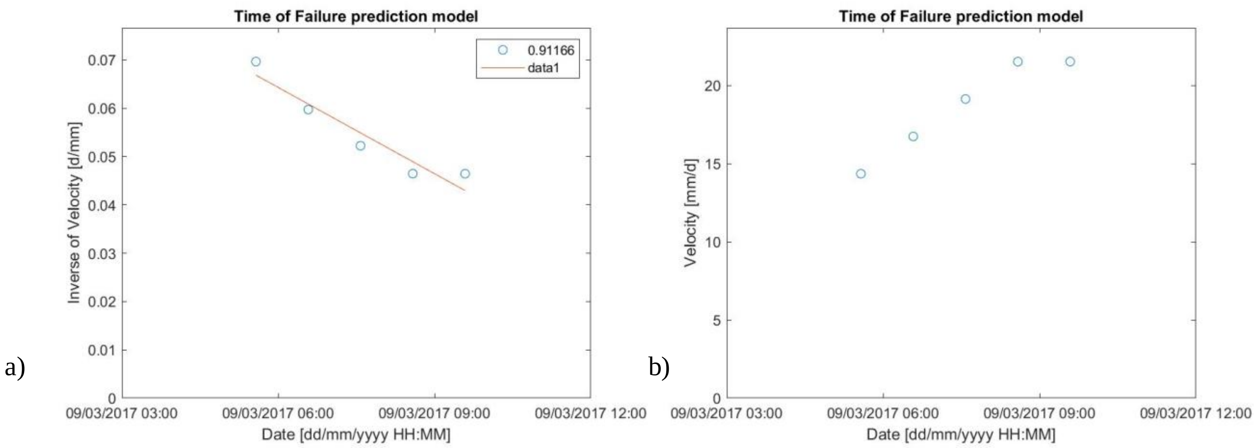

Fig. 5.40: a) Inverse Velocity vs Time and b) Velocity vs Time for local displacements of node 99 with acceleration date on 09 March 2017 05:34 and Time of Failure forecasted on 09 March 2017 16:48

The concavity that characterizes the last part of the dataset tends to a horizontal asymptote for both cases and this could be an index of a decelerating movement. The information obtained is only related to a single portion of the vertical (the superficial one) and indicates a dynamic that interests the ground level, probably caused by the adjustment of soil after the landslide event occurred on 08 March. Displacement rate is very high and this confirms that the situation has not stabilized yet.

The third alert procedure features 5 points, with $R^2 = 0.91$, and an increasing concavity for cumulative movements at 3.2 m depth. This outcome should not be underestimated, even if associated with a single event. It probably does not indicate a collapse, but highlights the predisposing factors for a subsequent event.

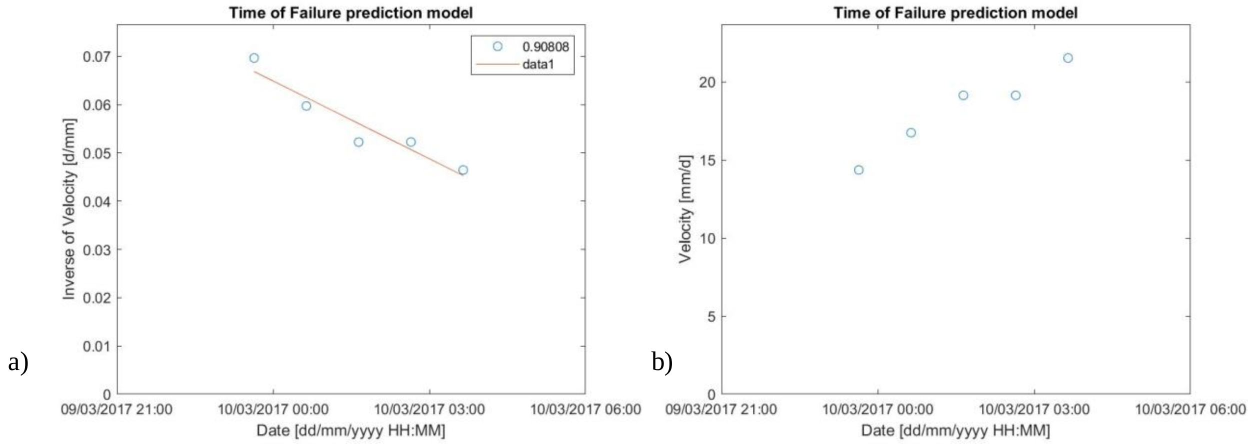

Fig. 5.41: a) Inverse Velocity vs Time and b) Velocity vs Time for cumulative displacements of node 91 with acceleration date on 09 March 2017 23:38 and Time of Failure forecasted on 10 March 2017 12:05

Finally, the fourth and last alert procedure leads to the final collapse of the slope. It is characterized by 5 points, with $R^2 = 0.94$. The most important information about this event is the constant increasing of acceleration (i.e. the increasing concavity of the velocity vs time curve) that regards the last part of the dataset, resulting in 58 mm/day^2, which is the higher value registered for the whole period of monitoring. This result, even if associated with the cumulative displacements of a single point, should activate every risk management procedure necessary for the site.

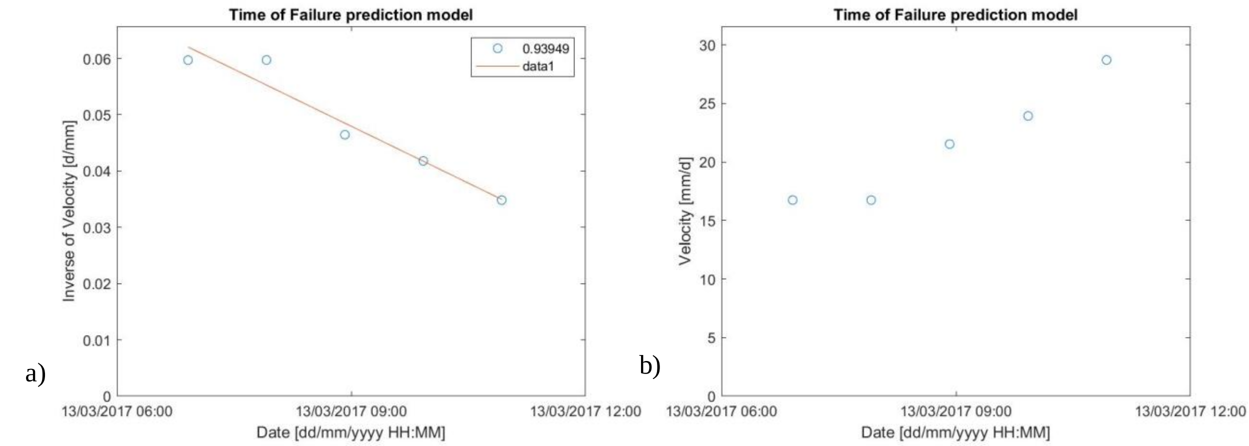

Fig. 5.42: a) Inverse Velocity vs Time and b) Velocity vs Time for cumulative displacements of node 89 with acceleration date on 13 March 2017 06:54 and Time of Failure forecasted on 13 March 2017 16:06

In this case study, IVM activation criterion and Fukuzono method showed high performances. Nevertheless, could the algorithm work even better? In order to answer this question, a back analysis has been performed, analysing the results after the event (i.e. conditioned by the knowledge about date & hour of collapse). In particular, the back analysis was executed using Microsoft Excel® and selecting the best dataset of cumulative displacements available for the application of Fukuzono method. This procedure reproduces what is usually done manually by an operator, as reported in literature.

Tab. 5.12 shows the results of the back-analysis procedure. The landslide event occurred on 08 March is identified by three sensors placed at 2.5, 1.8 and 0 m depth respectively. In particular, the datasets are composed by 8 points for Links 95 and 99 and 16 points for Link 93. The acceleration dates are estimated during the night between 07 and 08 March (nodes 93 and 95) or the morning of 08 March. Time of Failure predictions are very consistent, with a mean estimation error of 24 minutes in advance. In particular, combining the three information in a unique representation (Fig. 5.43) they lead to a consistent result where a collapse should be expected between 20:50 and 21:20 (collapse effectively observed between 20:32 and 21:32).

Tab. 5.12: Comparison between T_f predicted with a back-analysis and observed, with related warning time

Node [-]	Depth [m]	Acceleration date [dd/mm/yyyy HH:MM]	T_f prediction [dd/mm/yyyy HH:MM]	T_f observed [dd/mm/yyyy HH:MM]	Forecasting error [h]	Theoretical warning time [h]	Real warning time [h]
93	2.5	07/03/2017 20:27	08/03/2017 20:54	08/03/2017 21:32	38 minutes in advance	9 (24.5*)	9 (25*)
95	1.8	08/03/2017 01:28	08/03/2017 21:17	08/03/2017 21:32	15 minutes in advance	9 (20*)	9 (20*)
99	0.0	08/03/2017 11:30	08/03/2017 21:13	08/03/2017 21:32	19 minutes in advance	9 (10*)	9 (10*)
89	3.9	13/03/2017 06:54	13/03/2017 16:06	13/03/2017 14:56	1.5 hour later	4 (9*)	3 (8*)
91	3.2	13/03/2017 06:54	13/03/2017 16:56	13/03/2017 14:56	2 hours later	5 (10*)	3 (8*)
93	2.5	13/03/2017 06:54	13/03/2017 15:14	13/03/2017 14:56	18 minutes later	3 (8*)	3 (8*)
95	1.8	13/03/2017 06:54	13/03/2017 15:06	13/03/2017 14:56	10 minutes later	3 (8*)	3 (8*)

* value that indicates the warning time if the data transmissions were in real-time

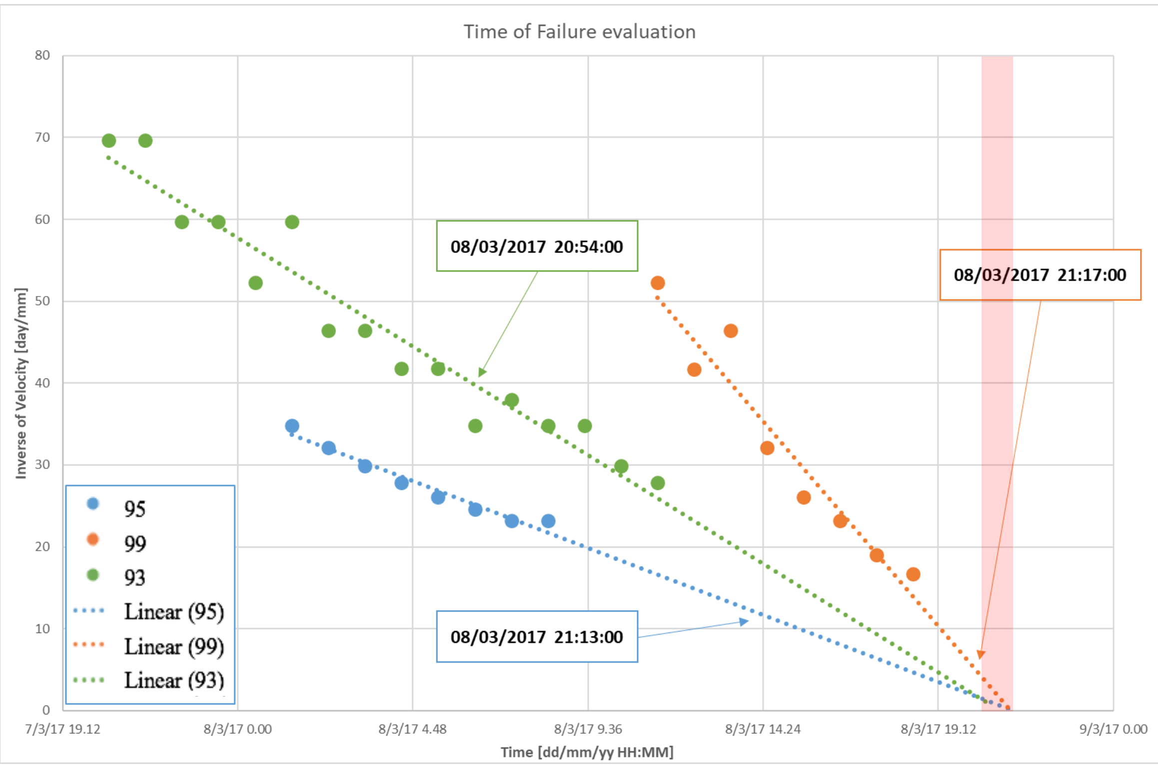

Fig. 5.43: Time of Failure evaluation using Excel® for the event occurred on 08 March 2017

The landslide event occurred on 13 March is identified by four sensors (Tab. 5.12) placed at 3.9, 3.2, 2.5 and 1.8 m depth respectively, with a dataset of 5 points each. Link 89 was correctly included also by the IVM activation criterion (Tab. 5.15) and the time prediction was exactly the same. The back analysis highlights also some interesting results provided by Links 91, 93 and 95. Node 91 shows a forecasting error of 2 hours, while nodes 93 and 95 evaluate the Time of Failure with only 18 and 10 minutes of error respectively, with a warning time of 3 hours (8 if the data transmission was in real-time). As for the event occurred on 08 March, a collapse is expected in a time window that ranges between 15:00 and 17:00 (collapse observed on site between 13:56 and 14:56).

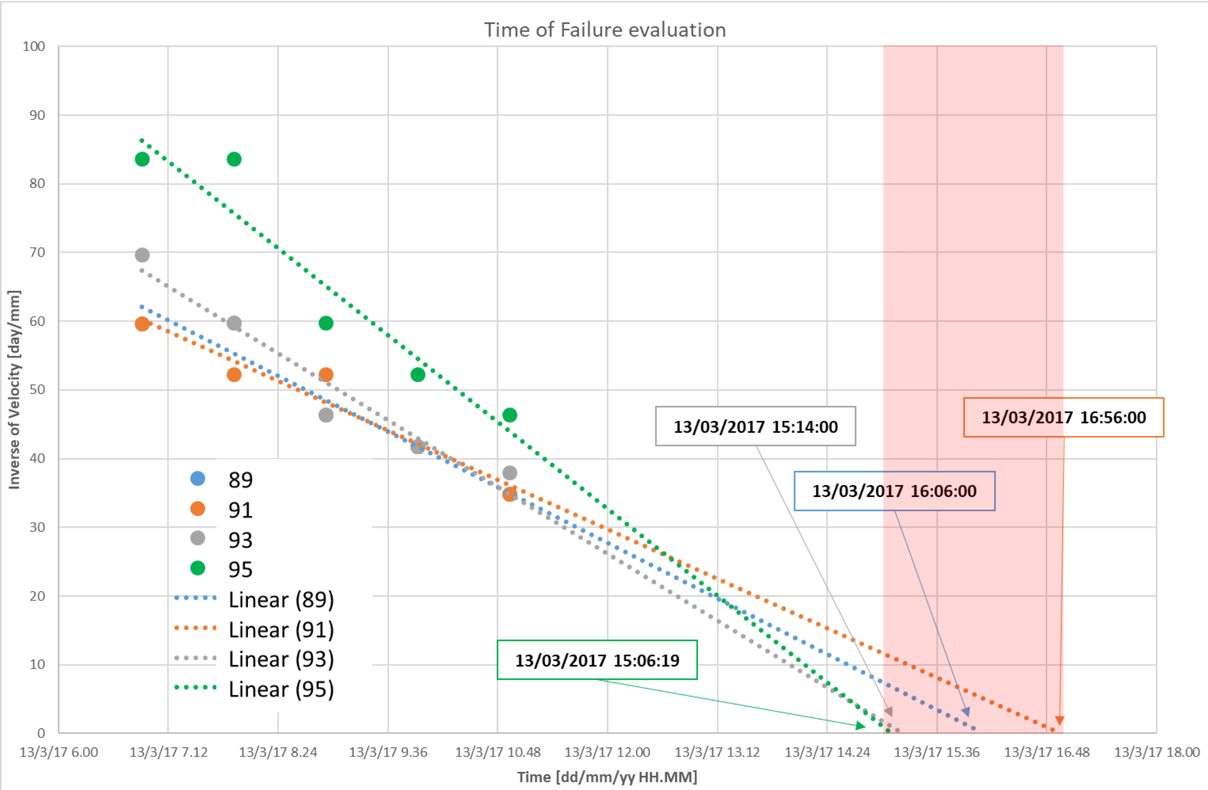

Fig. 5.44: Time of Failure evaluation using Excel® for the event occurred on 13 March 2017

Tab. 5.13: Comparison between algorithm and Microsoft Excel® T_f analysis of the event occurred on 08 March 2017

Node [-]	Analysis	Acceleration date [dd/mm/yyyy HH:MM]	T_f prediction [dd/mm/yyyy HH:MM]	T_f observed [dd/mm/yyyy HH:MM]	Forecasting error [h]	Theoretical warning time [h]	Real warning time [h]
93	Excel®	07/03/2017 20:27	08/03/2017 20:54	08/03/2017 21:32	38 minutes in advance	9 (24.5*)	9 (25*)
95	Excel®	08/03/2017 01:28	08/03/2017 21:17	08/03/2017 21:32	15 minutes in advance	9 (20*)	9 (20*)
93	Algorithm	08/03/2017 02:28	09/03/2017 00:55	08/03/2017 21:32	3 hours later	13 (22*)	10 (19*)
95	Algorithm	08/03/2017 02:28	08/03/2017 22:48	08/03/2017 21:32	1 hour later	11 (20*)	10 (19*)
99	Excel®	08/03/2017 11:30	08/03/2017 21:13	08/03/2017 21:32	19 minutes in advance	9 (10*)	9 (10*)

Tab. 5.13 reports the comparison of Time of Failure evaluation regarding the 08 March event using Excel® or algorithm developed during this thesis. In particular, Link 93 was activated by both methods, with Excel® estimation that starts 5 hours in advance, resulting in a more complete dataset and prevision. The algorithm

dataset is lower due to the parabolic criterion (as in Tab. 5.14). Analysis of Link 95 made with the algorithm has a forecasting error of only 1 hour, which improves with Excel® back analysis up to 15 minutes in advance. As in the previous case, differences in the number of points considered are related to parabolic criterion. The minimum dataset condition (5 points are required to activate the Time of Failure estimation) caused a 1-hour delay in the first application of Fukuzono method. Finally, node 99 is not considered by Tilt software, as evidenced in Tab. 5.14, due to increasing concavity criterion.

Tab. 5.14: Application of IVM activation criterion at the event occurred on 08 March 2017. Dates in red correspond to the Acceleration Date highlighted by Tilt software, related to the alert activation (last column) in red.

Node [-]	Date [dd/mm/yy HH:MM]	Activation Criterion 0 [=1 if verified]	Activation Criterion 1 [=1 if verified]	Activation Criterion 2 [=1 if verified]	Activation Criterion 3 [=1 if verified]	Alert system [1 if activated]
93	07/03/17 20:27	1	1	1	0	0
	07/03/17 21:27	1	1	0	0	0
	07/03/17 22:27	1	1	0	0	0
	07/03/17 23:28	1	1	0	0	0
	08/03/17 00:28	1	1	0	0	0
	08/03/17 01:28	1	1	0	0	0
	08/03/17 02:28	1	1	0	0	0
	08/03/17 03:29	1	0	0	0	0
	08/03/17 04:29	1	0	0	0	0
	08/03/17 05:29	1	1	1	1	0
	08/03/17 06:29	1	1	1	1	**1**
	08/03/17 07:29	1	1	1	1	**1**
	08/03/17 08:30	1	1	1	0	**1**
	08/03/17 09:30	1	0	0	0	0
	08/03/17 10:30	1	0	0	0	0
	08/03/17 11:30	1	1	0	0	0
95	08/03/17 01:28	1	1	0	0	0
	08/03/17 02:28	1	1	0	0	0
	08/03/17 03:29	1	1	0	0	0
	08/03/17 04:29	1	1	0	0	0
	08/03/17 05:29	1	1	1	1	0
	08/03/17 06:29	1	1	1	1	**1**
	08/03/17 07:29	1	1	1	1	**1**
	08/03/17 08:30	1	1	1	0	**1**
99	08/03/17 11:30	1	0	0	0	0
	08/03/17 12:30	1	0	0	0	0
	08/03/17 13:30	1	1	1	1	0
	08/03/17 14:31	1	1	1	0	0
	08/03/17 15:31	1	1	1	0	0
	08/03/17 16:31	1	1	0	0	0
	08/03/17 17:31	1	1	0	0	0
	08/03/17 18:32	1	1	0	0	0

Tab. 5.15 reports the comparison of Time of Failure evaluation regarding the final collapse occurred on 13 March. Link 89 was activated in the same way with both methods. This information confirms the validity of "Conditioned Alarm" concept, together with the IVM activation criterion hypothesis. The Excel® back analysis regards also nodes 91, 93 and 95. These sensors are not considered by Tilt software, as evidenced in Tab. 6.15, due to positive displacement rate (91) and increasing displacement rate (93 and 95) criteria. In particular, displacement occurred on 13 March is too rapid if related to the sampling period to respect the proposed model activation hypothesis.

Tab. 5.15: Comparison between algorithm and Microsoft Excel® T_f analysis of the event occurred on 13 March 2017

Node [-]	Analysis	Acceleration date [dd/mm/yyyy HH:MM]	T_f prediction [dd/mm/yyyy HH:MM]	T_f observed [dd/mm/yyyy HH:MM]	Forecasting error [h]	Theoretical warning time [h]	Real warning time [h]
89	Excel®	13/03/2017 06:54	13/03/2017 16:06	13/03/2017 14:56	1.5 hour later	4 (9*)	3 (8*)
89	Algorithm	13/03/2017 06:54	13/03/2017 16:06	13/03/2017 14:56	1.5 hour later	4 (9*)	3 (8*)
91	Excel®	13/03/2017 06:54	13/03/2017 16:56	13/03/2017 14:56	2 hours later	5 (10*)	3 (8*)
93	Excel®	13/03/2017 06:54	13/03/2017 15:14	13/03/2017 14:56	18 minutes later	3 (8*)	3 (8*)
95	Excel®	13/03/2017 06:54	13/03/2017 15:06	13/03/2017 14:56	10 minutes later	3 (8*)	3 (8*)

Tab. 5.16: Application of IVM activation criterion at the event occurred on 13 March 2017. Dates in red correspond to the Acceleration Date highlighted by Tilt software, related to the alert activation (last column) in red.

Node [-]	Date [dd/mm/yy HH:MM]	Activation Criterion 0 [=1 if verified]	Activation Criterion 1 [=1 if verified]	Activation Criterion 2 [=1 if verified]	Activation Criterion 3 [=1 if verified]	Alert system [1 if activated]
89	**13/03/17 06:54**	0	0	0	0	0
	13/03/17 07:54	0	0	0	0	0
	13/03/17 08:55	0	0	0	0	0
	13/03/17 09:55	1	1	1	1	0
	13/03/17 10:55	1	1	1	0	**1**
91	13/03/17 06:54	0	0	0	0	0
	13/03/17 07:54	0	0	0	0	0
	13/03/17 08:55	0	0	0	0	0
	13/03/17 09:55	1	1	1	0	0
	13/03/17 10:55	1	1	1	0	0
93	13/03/17 06:54	1	0	0	0	0
	13/03/17 07:54	1	0	0	0	0
	13/03/17 08:55	1	0	0	0	0
	13/03/17 09:55	1	0	1	0	0
	13/03/17 10:55	1	0	1	0	0
95	13/03/17 06:54	1	0	0	0	0
	13/03/17 07:54	1	0	0	0	0
	13/03/17 08:55	1	0	0	0	0
	13/03/17 09:55	1	0	1	0	0
	13/03/17 10:55	1	0	1	0	0

Finally, Tab. 5.17 shows displacement rate, acceleration, *a* coefficient, the variation of *a* coefficient and the inverse of velocity for nodes 93, 95 and 99, related to the event occurred on 08 March 2017, and sensors 89, 91, 93 and 95, related to the collapse observed on 13 march 2017.

Further studies should investigate these parameters in detail, concentrating on their application in the analysis of IVM activation criterion.

Tab. 5.17: Displacement rate, acceleration, a coefficient, Δa and $1/v$ for back analysis with Excel®

Node [-]	Date [dd/mm/yyyy HH:MM]	Displacement rate [mm/day]	Acceleration [mm/day²]	a coefficient [mm/day³]	Δa [mm/day³]	$1/v$ [day/mm]
93	07/03/17 20:27	0.014	0.002	-0.037	-0.099	71.429
	07/03/17 21:27	0.014	0.000	-0.110	0.000	71.429
	07/03/17 22:27	0.017	0.002	-0.119	0.000	58.824
	07/03/17 23:28	0.017	0.000	-0.026	0.000	58.824
	08/03/17 00:28	0.019	0.002	-0.011	0.000	52.632
	08/03/17 01:28	0.017	-0.002	-0.062	0.000	58.824
	08/03/17 02:28	0.022	0.005	-0.010	0.052	45.455
	08/03/17 03:29	0.022	0.000	0.005	0.016	45.455
	08/03/17 04:29	0.024	0.002	0.016	0.011	41.667
	08/03/17 05:29	0.024	0.000	0.021	0.005	41.667
	08/03/17 06:29	0.029	0.005	0.052	0.031	34.483
	08/03/17 07:29	0.026	-0.002	0.026	-0.026	38.462
	08/03/17 08:30	0.029	0.002	0.000	-0.026	34.483
	08/03/17 09:30	0.029	0.000	-0.025	0.000	34.483
	08/03/17 10:30	0.033	0.005	-0.020	0.000	30.303
	08/03/17 11:30	0.036	0.002	0.051	0.000	27.778
95	08/03/17 01:28	0.029	0.000	0.000	0.000	34.483
	08/03/17 02:28	0.031	0.002	-0.021	-0.021	32.258
	08/03/17 03:29	0.033	0.002	0.000	0.021	30.303
	08/03/17 04:29	0.036	0.002	0.021	0.021	27.778
	08/03/17 05:29	0.038	0.002	0.031	0.010	26.316
	08/03/17 06:29	0.041	0.002	0.021	-0.010	24.390
	08/03/17 07:29	0.043	0.002	0.036	0.016	23.256
	08/03/17 08:30	0.043	0.000	0.010	-0.026	23.256
99	08/03/17 11:30	0.019	0.012	0.286	0.045	52.632
	08/03/17 12:30	0.024	0.005	0.297	0.011	41.667
	08/03/17 13:30	0.022	-0.002	0.120	-0.177	45.455
	08/03/17 14:31	0.031	0.010	0.063	-0.057	32.258
	08/03/17 15:31	0.038	0.007	-0.015	-0.078	26.316
	08/03/17 16:31	0.043	0.005	-0.049	0.000	23.256
	08/03/17 17:31	0.053	0.010	-0.011	0.037	18.868
	08/03/17 18:32	0.060	0.007	0.041	0.052	16.667
89	**13/03/17 06:54**	0.017	0.019	0.098	0.098	58.824
	13/03/17 07:54	0.017	0.000	0.103	0.005	58.824
	13/03/17 08:55	0.022	0.005	0.124	0.020	45.455
	13/03/17 09:55	0.024	0.002	0.072	-0.052	41.667
	13/03/17 10:55	0.029	0.005	0.036	-0.036	34.483
91	13/03/17 06:54	0.017	0.019	0.124	0.124	58.824
	13/03/17 07:54	0.019	0.002	0.119	-0.005	52.632
	13/03/17 08:55	0.019	0.000	0.077	-0.042	52.632
	13/03/17 09:55	0.024	0.005	0.083	0.005	41.667
	13/03/17 10:55	0.029	0.005	0.031	-0.052	34.483
93	13/03/17 06:54	0.014	0.017	0.104	0.104	71.429
	13/03/17 07:54	0.017	0.002	0.088	-0.016	58.824
	13/03/17 08:55	0.022	0.005	0.114	0.026	45.455
	13/03/17 09:55	0.024	0.002	0.067	-0.047	41.667
	13/03/17 10:55	0.026	0.002	0.010	-0.057	38.462
95	13/03/17 06:54	0.012	0.017	0.130	0.130	83.333
	13/03/17 07:54	0.012	0.000	0.093	-0.036	83.333
	13/03/17 08:55	0.017	0.005	0.067	-0.026	58.824
	13/03/17 09:55	0.019	0.002	0.020	-0.047	52.632
	13/03/17 10:55	0.022	0.002	-0.016	-0.036	45.455

5.3.4. Conclusions

SS652 case study represents the first real-time application of proposed IVM activation criterion and Fukuzono method, as described in Chapter 5. In particular, the algorithm is aimed to substitute the manual check for a preliminary analysis and alert procedure, especially if related to the real time monitoring of several landslides, like for example the work of regional authorities. In this specific case, two landslide events were automatically identified and related alert procedures activated by the software. After on-site inspection, the previsions resulted effective with only some minor inaccuracies (with a mean value of one hour) related to the exact time of collapse. The application should be considered as a great result, if thinking about the warning significance of the method. A back analysis executed through Excel® software confirms the outcomes, improving the information related to the exact date & hour of collapse. The differences between two methods are related to the definition of IVM activation criterion versus the manual check executed by an operator. Further studies should investigate and improve this final topic.

5.4. French Alps, France

The last case study is about the stability monitoring of a reinforced soil wall placed on the French Alps at 1263 m a.s.l. The wall is about 12 m height and has shown instability phenomena since its construction. The site location could not be specified due to the sensitive nature of the data.

The site has been investigated through topographic readings, Casagrande piezometers, traditional inclinometer surveys and MUMS system. In particular, two 15 meters long Vertical Arrays are installed on the soil wall, 3 m far one from each other and with a sensor interspace of 1 m. Both Arrays are equipped with 15 Tilt Link HR 3D V (MEMS 2.0) and 1 Piezo Link (model 2.0, at 13 m depth) sensors, while the first one (DT0080) has a barometer installed inside the data logger case and the second one (DT0081) has a High Resolution Thermometer, located 1 m below the top margin of the wall.

Both MUMS systems were installed on 29 August 2017 (Fig. 5.45) using the new installation method described in Chapter 3.3. In detail, a 16 m long PVC pipe with a diameter of 60 mm was inserted in the borehole and then MUMS plastic pipe placed inside. The borehole was filled with cement at the bottom for about 1 meter, in order to fix the anchor to the stable portion, and gravel with small diameter for the remaining part of the vertical, using sand for the piezometer portion. The installation required less than one hour.

Fig. 5.45: Installation of DT0080 and DT0081 MUMS Vertical Arrays

The zero-reference date has been set on the 30 of August 2017 and the sample period to 2 hours, sending data to the elaboration centre once a day. The monitoring is still ongoing. Data logger is powered through 12 V lead-acid battery and 5 W solar panel. Fig. 5.46a shows the battery level for the whole period of monitoring, highlighting the correct functionality of the powering system, while Fig. 5.46b represents the temperature of the data logger.

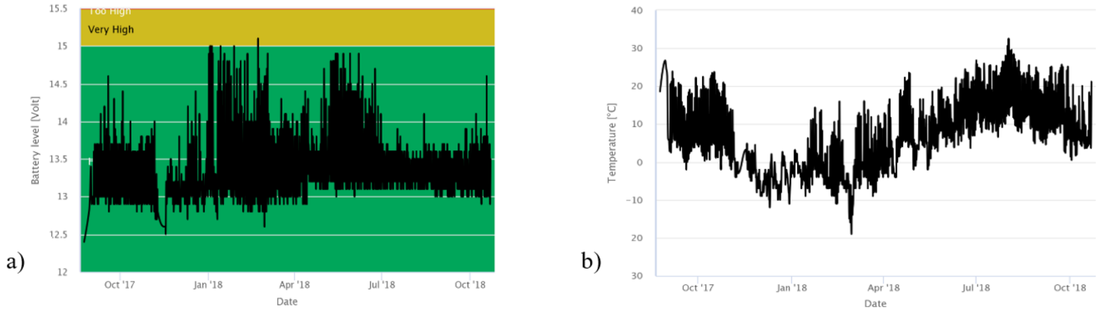

Fig. 5.46: a) Battery level and b) data logger temperature for the whole period of monitoring

5.4.1. Results

During the monitoring, atmospheric pressure has showed a mean value that ranges between 0.95 and 0.96 atm, according to the seasons (Fig. 5.47a). In particular, Tab. 5.18 reports the standard deviation evaluated over summer, autumn, winter and spring periods. This result is influenced by many factors and could be a gross interpretation of sensor repeatability. Fig. 5.47b shows the temperature recorded 1 m below the top margin of the reinforced soil wall. This value is quite constant over time.

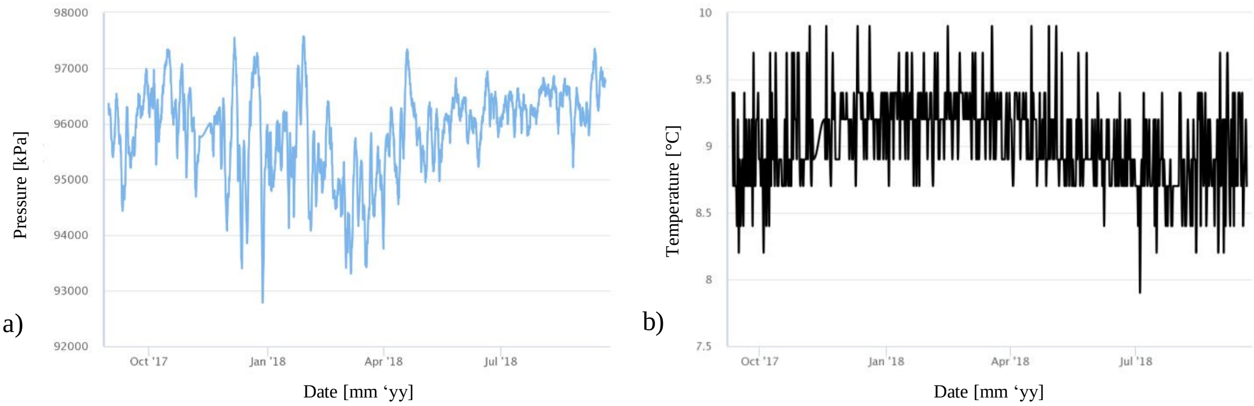

Fig. 5.47: a) Atmospheric pressure on site and b) Temperature 1 m below the top margin of the reinforced soil wall

Tab. 5.18: Standard deviation of atmospheric pressure recorded by the Baro Link, calculated over season periods

Season	σ atmospheric pressure [Pa]
Summer 2017	504
Autumn 2017	773
Winter 2017	956
Spring 2018	616
Summer 2018	225

DT0080

DT0080 Vertical Array is the upstream inclinometer that has started to record data the day after the installation. Due to the fact that preliminary displacements are influenced by the adjustment of filling material, it was necessary to define the reference date, as in Fig. 3.26. This was set on 11/09/2017, according to Fig. 5.48. Fig. 5.49a shows the local displacements starting from the reference date, while Fig. 5.49b reports the cumulative ones. A sliding surface is clearly identifiable at a depth of 5 m, resulting in 11 mm of movements over the period. The cumulative displacement at the top equals 31 mm. Fig. 5.50 shows the local (a) and cumulative (b) displacements over time. It is clearly identifiable the oscillation of the structure, bound to weather conditions. In particular, the major displacement occurred during May 2018 (55 mm at the top), followed by a relaxation which is still in progress.

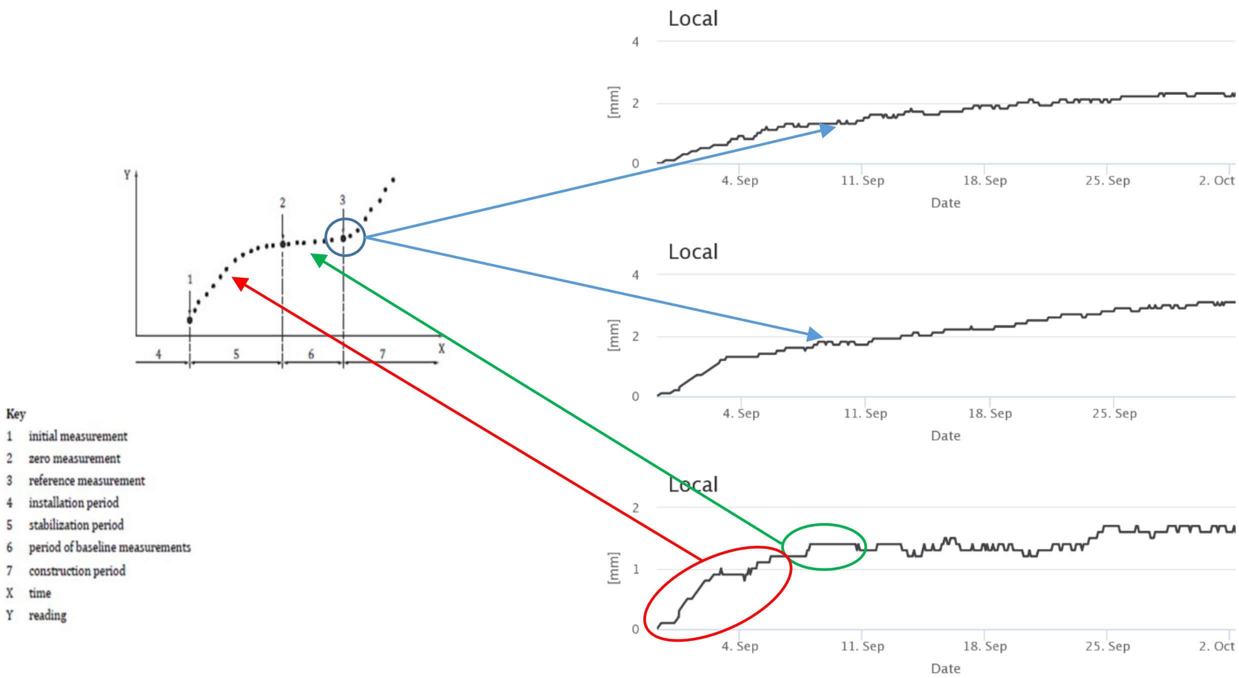

Fig. 5.48: Zero reading, baseline measure and reference date evaluated using Link 1, 3 and 11 of DT0080 MUMS Vertical Array

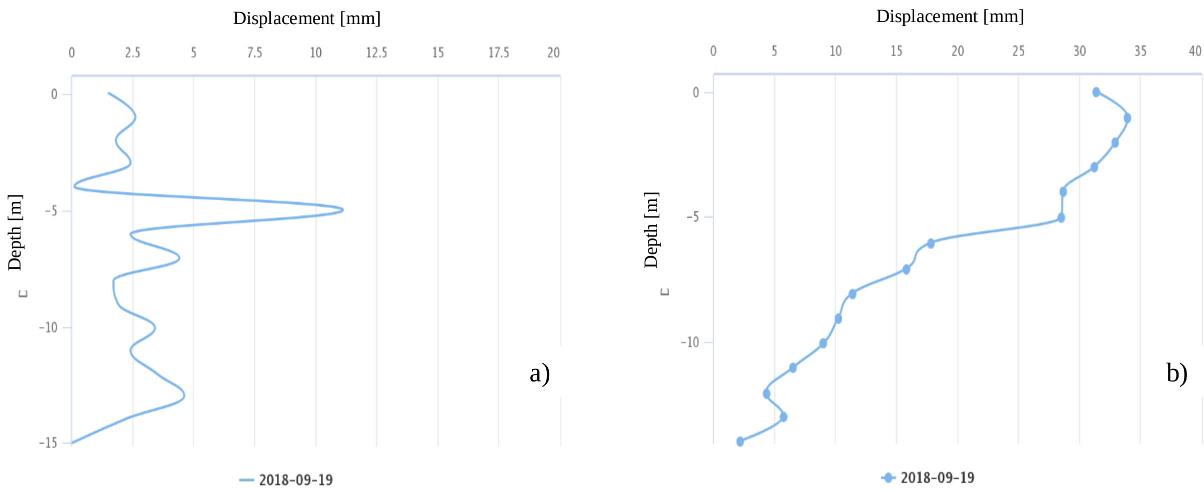

Fig. 5.49: a) Local and b) Cumulative displacement recorded by DT0080 MUMS inclinometer on 19/09/2018 starting from the reference reading

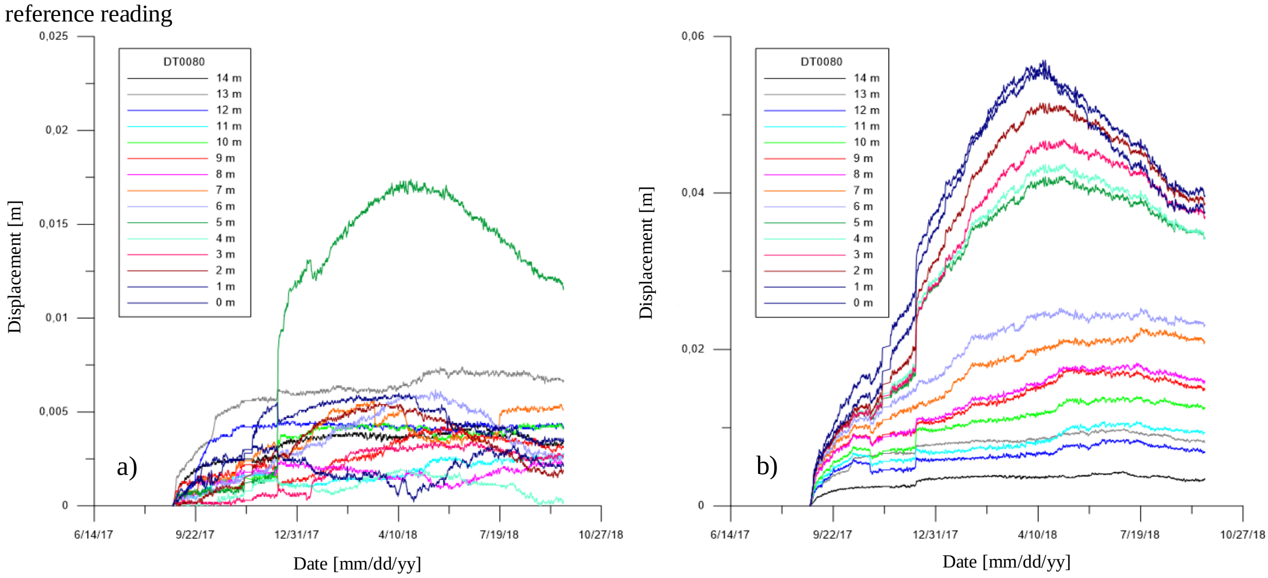

Fig. 5.50: a) Local and b) Cumulative displacements over time, recorded by DT0080 inclinometer starting

Displacement rate (Fig. 5.51a) and acceleration (Fig. 5.51a) registered during the period of monitoring highlight a major event occurred on 11 December 2017, with a speed up to 6.3 mm/day and a rapid acceleration of 6.4 mm/day^2, followed by a deceleration of 5.7 mm/day^2. The analysis of pore pressure (Fig. 5.52) shows a primary maximum at that date, repeated on 04 and 05 of May 2018. The second event did not cause displacements, probably due to the realization of drains on the wall.

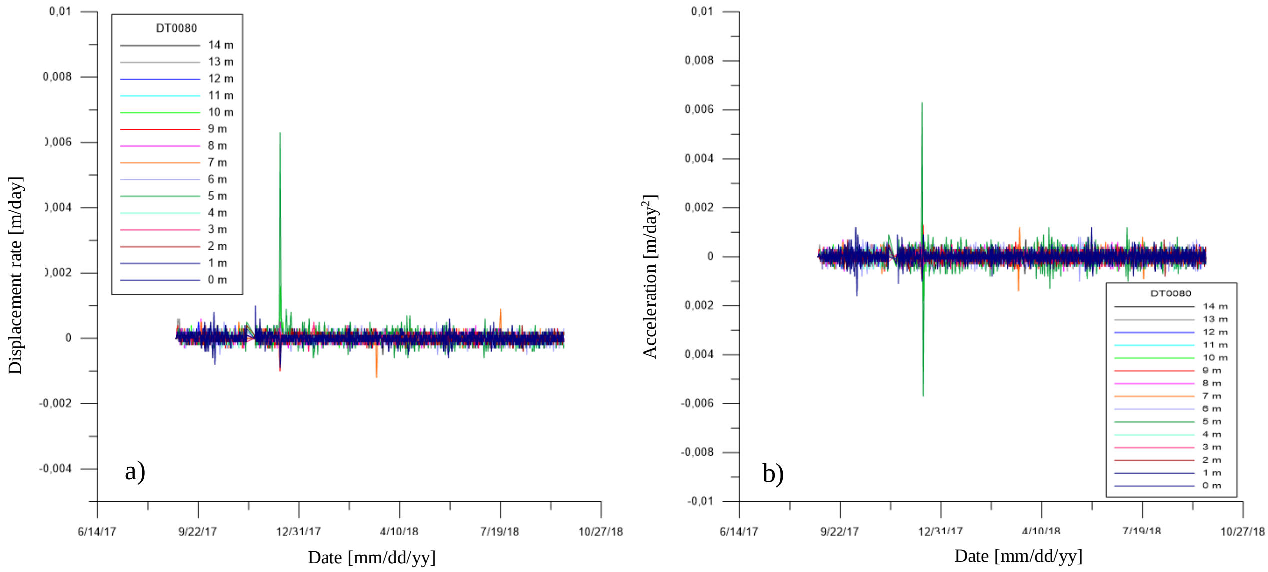

Fig. 5.51: a) Displacement rate and b) Acceleration recorded by DT0080 inclinometer starting from the reference reading

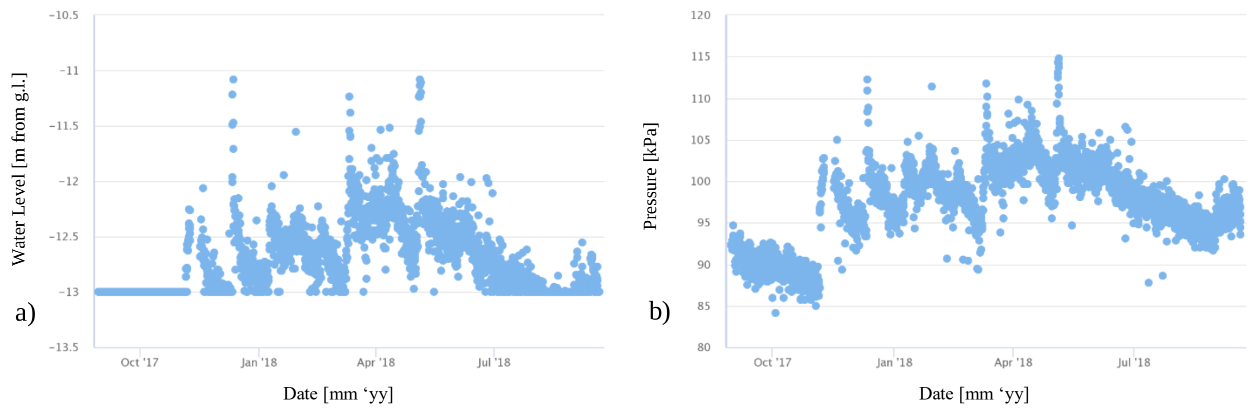

Fig. 5.52: a) Water level and b) Pore pressure recorded by the Piezo Link of DT0080 inclinometer starting from the reference reading

As in Fig. 5.53, the first rapid increasing of pore pressure clearly triggered the movements at 10 and 5 m of depth. The second event, occurred on May, did not cause displacements, as well as the event of March. This fact could be related to a more stable configuration of the wall, related to maintenance works. This representation emphasizes the importance of automated tools in the detection of cause-effect relationships and efficacy control of works related to geotechnical field, as well as the definition of triggers. Tab. 5.19 reports the standard deviation of pore pressure and water level evaluated over summer, autumn, winter and spring periods. This result is influenced by water circulation and other factors. It could be interpreted as an indicative index of sensor repeatability, as for the Baro Link.

Tab. 5.19: Standard deviation of pore pressure recorded by the Piezo Link, calculated over season periods

Season	σ pore pressure [Pa]	σ water level [m]
Summer 2017	1524	0.00
Autumn 2017	5006	0.25
Winter 2017	2868	0.27
Spring 2018	2661	0.28
Summer 2018	1905	0.16

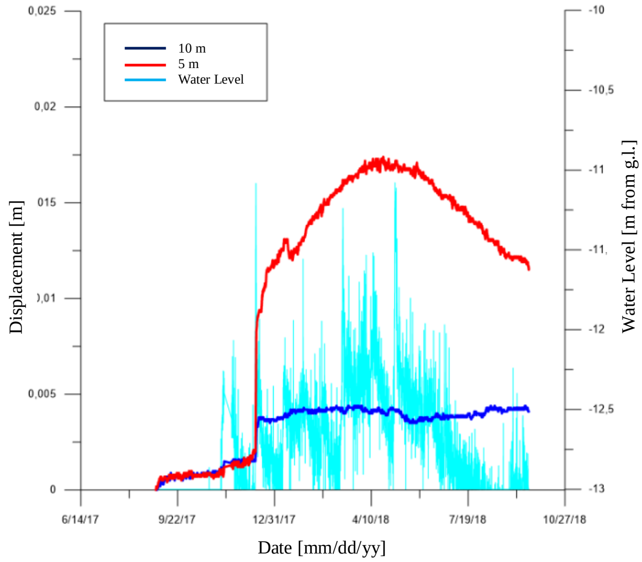

Fig. 5.53: Displacements recorded at 10 and 8 m depth and water level versus time

Azimuth of displacements (Fig. 5.54) equals 198° (South South-West direction). This information is quite coherent with the maximum grade direction of the slope (South). Finally, Fig. 5.55 shows the temperatures recorded during the period of monitoring and their variations along time.

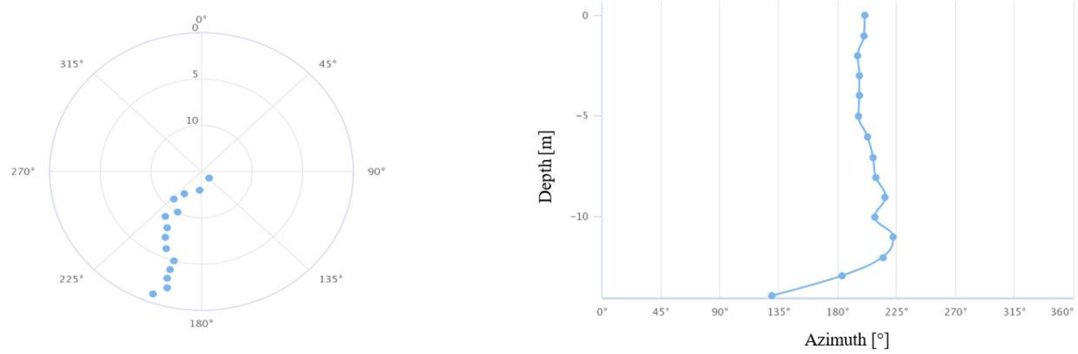

Fig. 5.54: Azimuth of displacements recorded by DT0080 inclinometer starting from the reference reading

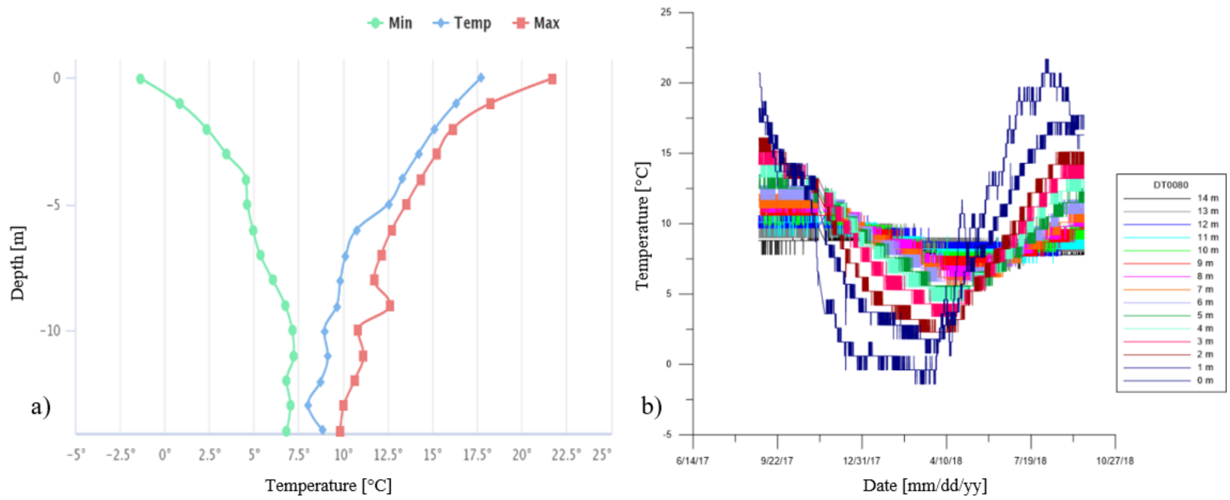

Fig. 5.55: a) Minimum, maximum and actual temperature and b) temperature over time recorded by thermometer sensors of DT0080 inclinometer, starting from the reference reading

DT0081

DT0081 Vertical Array is the downstream inclinometer that has started to record data the day after the installation, as DT0080 one. As in the previous case, the reference date was set on 11/09/2017. Here the situation is quite different, with a rapid and huge displacement (18.6 mm) occurred on 05 July 2018 at 14 m depth (Fig. 5.56a, Fig. 5.57), which was considered as a stable zone.

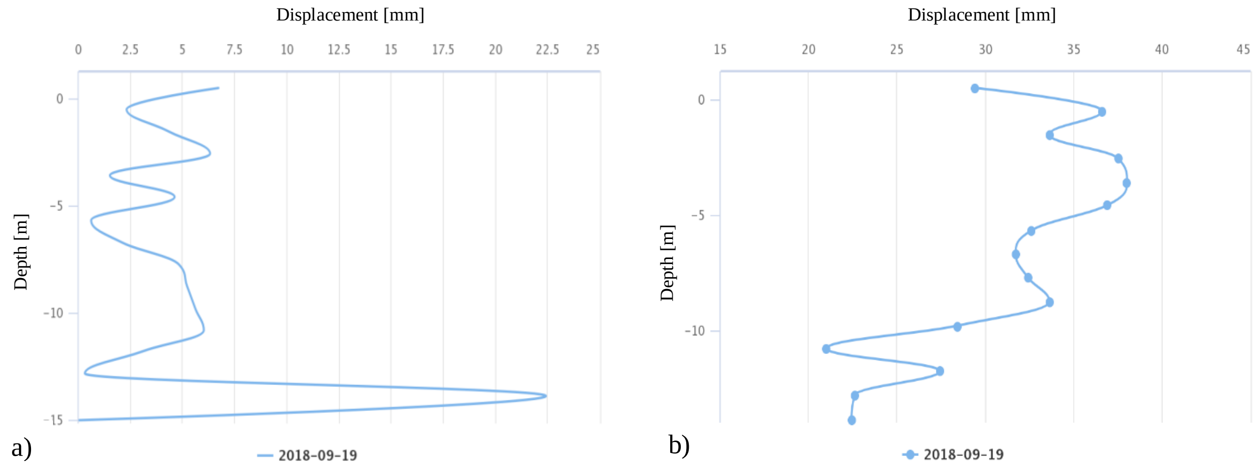

Fig. 5.56: a) Local and b) Cumulative displacement recorded by DT0081 MUMS inclinometer on 19/09/2018 starting from the reference reading

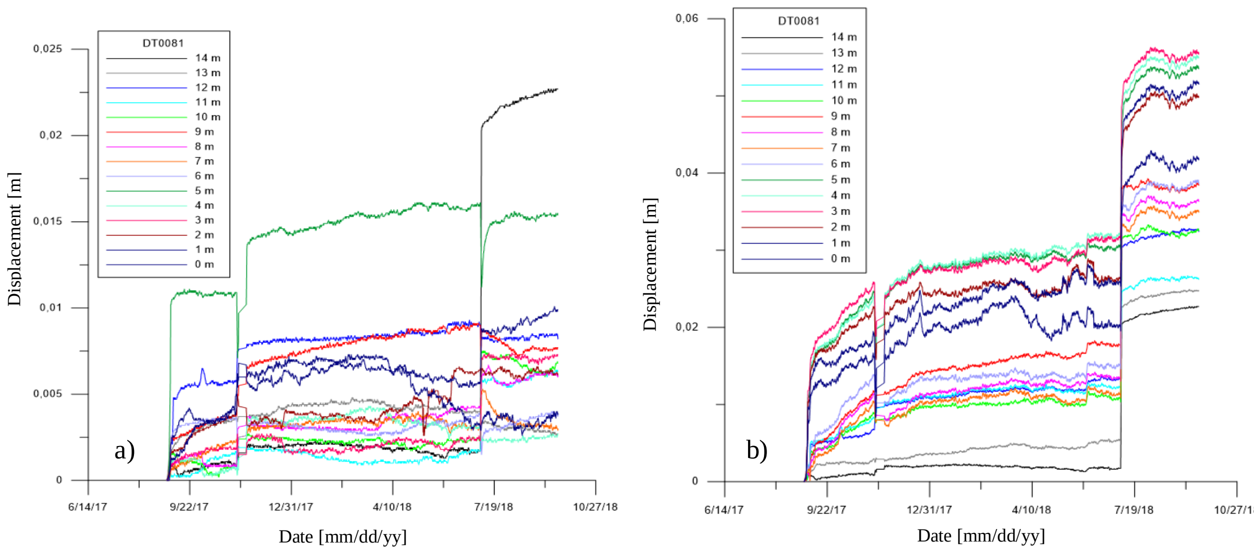

Fig. 5.57: a) Local and b) Cumulative displacements over time, recorded by DT0081 inclinometer

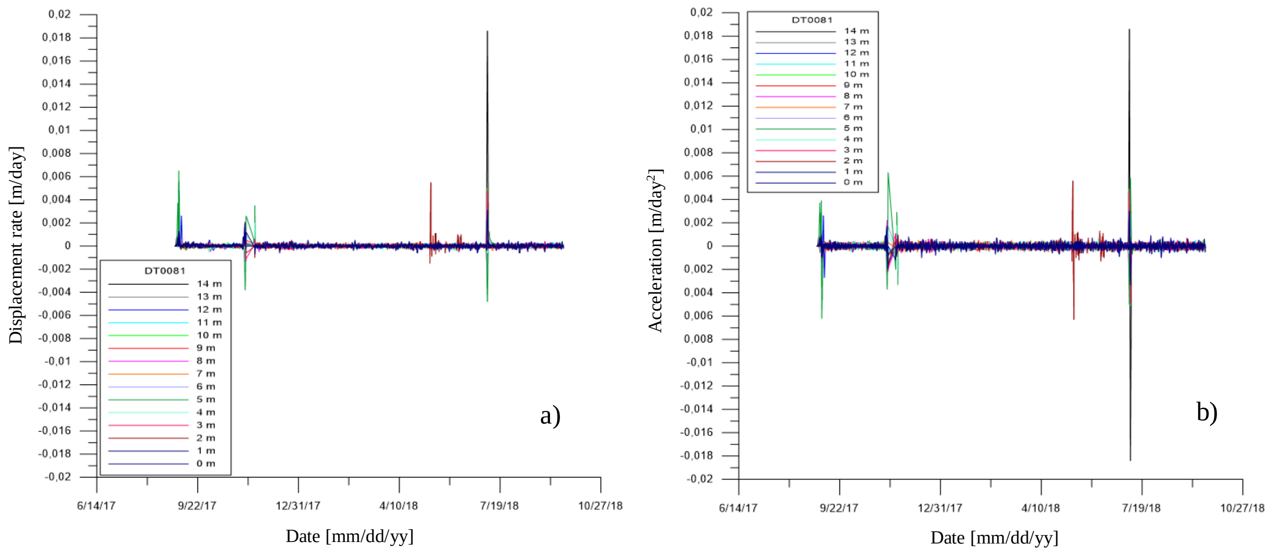

Fig. 5.58: a) Displacement rate and b) Acceleration recorded by DT0081 inclinometer starting from the reference reading

Fig. 5.58a shows a speed and an acceleration of about 19 mm/day and 19 mm/day^2, followed by a rapid deceleration of the same value. The cumulative displacement at the top equals 29 mm (Fig. 5.56b), while the inclinometer did not register the structure oscillation as in the previous case.

The analysis of pore pressure (Fig. 5.59) highlights a behavior which is very different if compared to data of DT0080 inclinometer, despite the distance of 3 m one to each other. In particular, water level reached 4.64 m of depth on November 2017, causing 2 mm of displacement at ground level (and generally along the whole vertical). Then, secondary maximums were registered on April (6.48 m depth) and July (6.86 m) 2018. This last one caused the observed rapid displacement at 14 m of depth, as in Fig. 5.53. The situation is quite complex and interesting, because apparently it is not the water level that triggers the displacements, but the rapid increase of water level: in fact this is the main difference between the two secondary maximums. Nevertheless, the primary maximum has a rapid increase too and caused lower displacements.

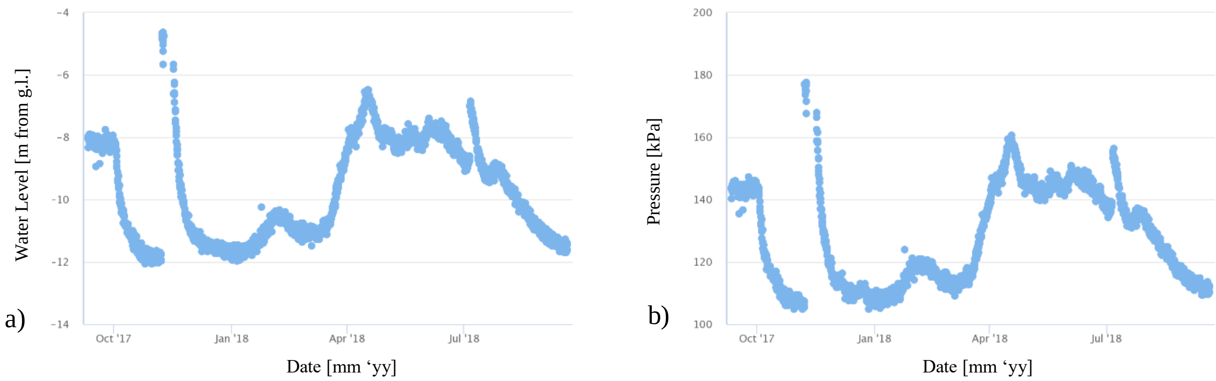

Fig. 5.59: a) Water level and b) Pore pressure recorded by the Piezo Link of DT0081 inclinometer starting from the reference reading

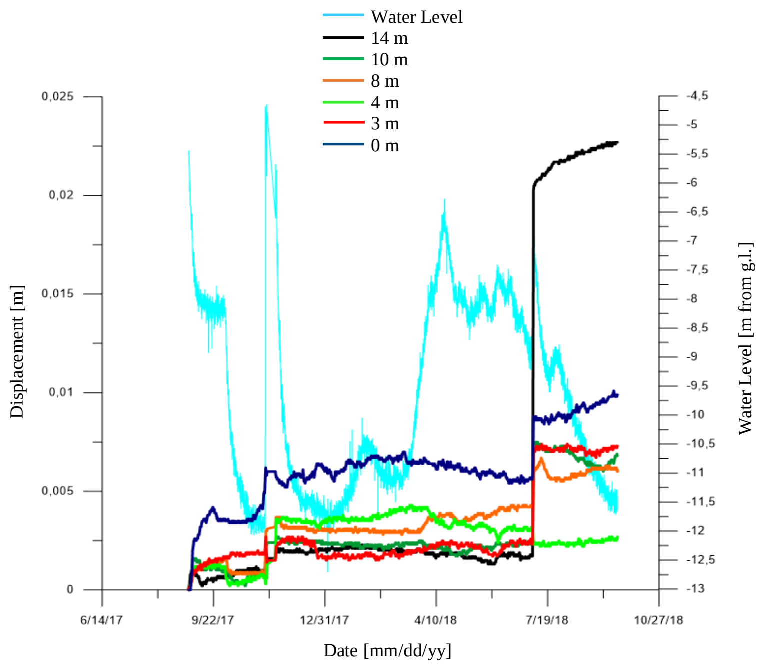

Fig. 5.60: Displacements recorded at 10 and 8 m depth and water level versus time

Taking into account the strange behavior of the displacement, occurred for a secondary maximum of the water level and in a portion which was considered as stable, and the fact that the upwards inclinometer did not record a movement, the responsible of monitoring could have doubts about this information. For this reason Tilt Link HR 3D V sensors are very useful and innovative, because they provide a double independent information at the same depth. Having a look at the local displacements data of electrolytic cell (Fig. 5.61a), it is possible to find a behavior which is exactly the same recorded by MEMS (Fig. 5.61b) for the whole period of monitoring, with slight differences related to the sensibility of sensors. Moreover, focusing on 06 of July event, both Links

(Fig. 5.62) highlight a rapid movement, started at about 10 AM and ended at about 7 AM on the day after. The amount of displacements is of 18.6 mm and 16.9 mm respectively, with a difference of 1.7 mm. The result gives a positive feedback about data interpretation and delete any doubt related to sensors functionality.

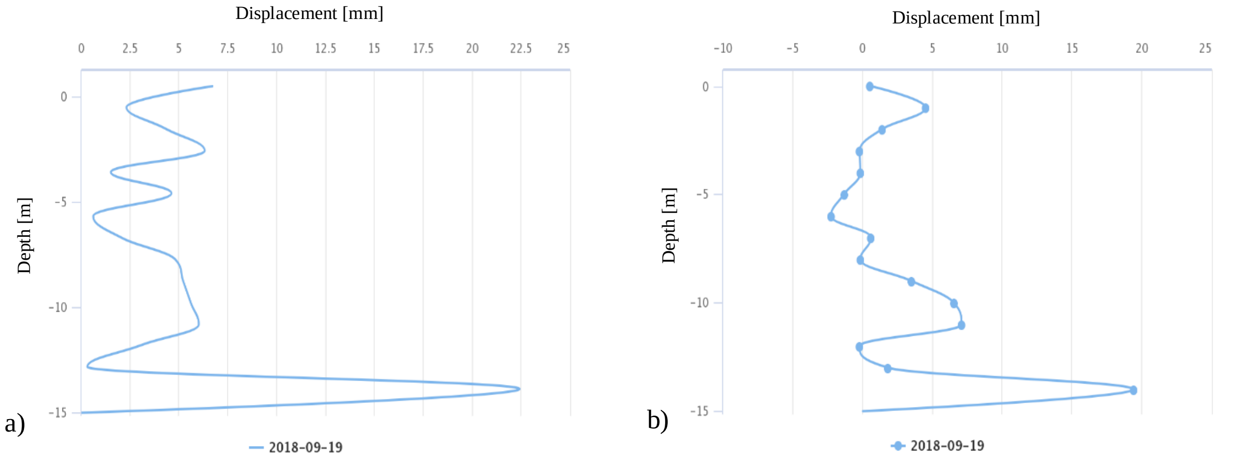

Fig. 5.61: Local displacements recorded by a) 3D MEMS and b) 2D electrolytic cell of DT0081 during the period of monitoring

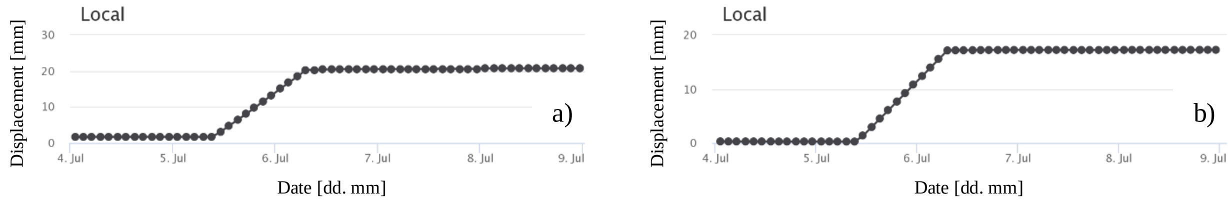

Fig. 5.62: Local displacements versus time recorded by a) 3D MEMS and b) 2D electrolytic cell of DT0081 between the 4th and the 9th of July 2018

Tab. 5.20 reports the standard deviation of pore pressure and water level for DT0081, as in Tab. 5.19 (related to DT0080)

Tab. 5.20: Standard deviation of pore pressure recorded by the Piezo Link, calculated over season periods

Season	σ pore pressure [Pa]	σ water level [m]
Summer 2017	5656	0.56
Autumn 2017	15904	1.61
Winter 2017	4014	0.42
Spring 2018	6692	0.65
Summer 2018	5921	0.60

Fig. 5.63 shows the azimuth of displacements, which is South (181°), corresponding to the maximum grade direction, which differs of 17° from the DT0080 one.

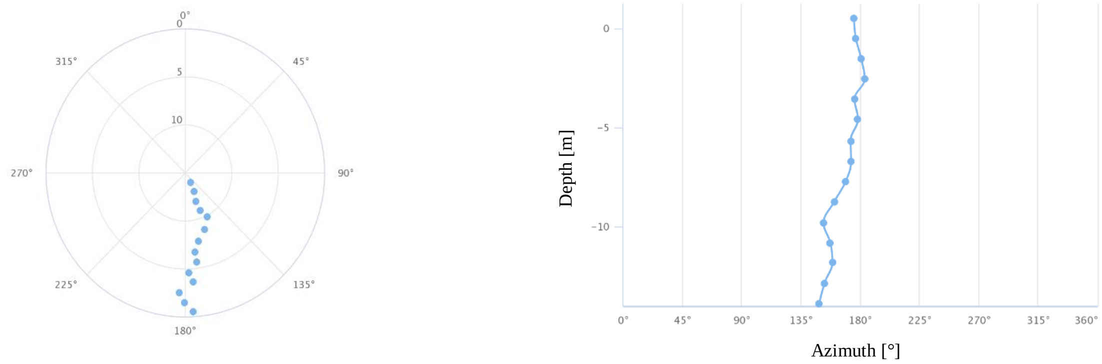

Fig. 5.63: Azimuth of displacements recorded by DT0081 inclinometer starting from the reference reading

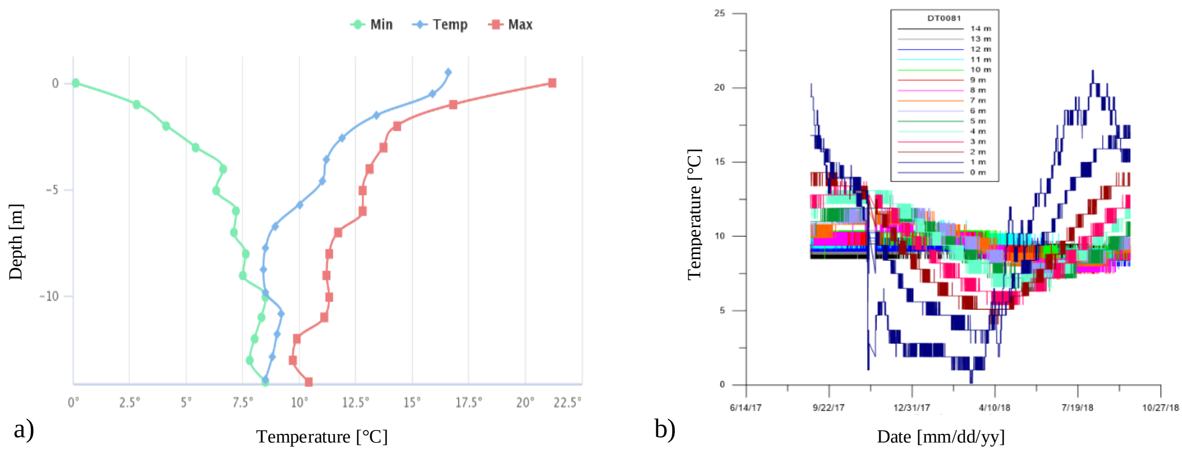

Fig. 5.64: a) Minimum, maximum and actual temperature and b) temperature over time recorded by thermometer sensors of DT0081 inclinometer, starting from the reference reading

Finally, Fig. 5.64 reports the minimum, the maximum and the last temperatures recorded by MEMS sensor of DT0081 Vertical Array, which are about the same reported by DT0080, remembering the ±0.96 °C sensibility of the thermometers that equip Tilt Link HR 3D V.

5.4.2. Conclusions

The applications of two MUMS systems inside a reinforced soil wall in the French Alps highlighted the importance of high frequency automated tools in the detection of cause-effect factors. In particular, the two inclinometers showed different behaviours of displacements and pore pressure regimes, despite the distance of only 3 meters one to each other. The case study points out the importance of Tilt Link HR 3D V nodes, related to the redundancy of information at the same depth, provided by two independent sensors. An indicative tentative has been performed in order to reconstruct the repeatability of Piezo Link 2.0 on-site, highlighting a mean value of 19 cm for DT0080 and 77 cm for DT0081. This measure is influenced by many factors, like the natural oscillations of water level, the water circulation, infiltration and the weather conditions.

Chapter 6

CONCLUSIONS

6.1. Summary and conclusions

This work concentrates on the development of a new innovative multi-parametric monitoring system, whose application regards landslides, civil and geotechnical structures as well as underground excavations. The tool starts from traditional and innovative instrumentations present in literature, improving some fundamental characteristics and reducing uncertainties. In particular, it removes the presence of an operator on-site, it saves time and money and it permits a high-frequency sampling, disconnected from site accessibility conditions, consequently allowing a meaningful statistical validation. In addition, it collects multi-parametric data and acts as an Early Warning System. Other characteristics are related to the removal of any rigid mechanical connection between sensors, creating a more flexible and cheaper instrument, with low electrical consumption. The aim of the new tool was to increment the knowledge about evolution of slopes, both for natural conditions and artificial changes.

Then, the thesis describes the introduction of software filters, which is an innovative elaboration philosophy, in opposition to hardware filters, which characterizes the tool available on the market. Software filters permit to control malfunctions, spike noises, inaccuracies and every disturbing factor which could influence the elaboration, together with a complete knowledge of instrumentation performance on-site. The new philosophy allows to establish "real" sensibility and repeatability characteristics, together with the discharge of instrumental noise. The SW is implemented with a self-learning philosophy: after a training period, the algorithm knows how to elaborate the raw data. A calibration procedure has been defined for every sensor, together with his related calculation algorithm.

Part of the work presents a new installation method, with related encouraging results. This method has been defined in order to simplify the whole procedure, reducing time and sources of error.

The study concentrates also on the creation of a new redundant double sensor exploiting different technologies, able to be installed at the same depth and independently calculate the resulting displacement.

The IoT approach is applied, in order to facilitate and speed up the result accessibility, in particular for big data management. Through a specifically designed dynamic web platform it is possible to view all the main sensors outcomes using any device with an internet connection.

The last part of the work investigates the evaluation of Time of Failure prediction. In particular, starting from methods described in literature and in particular the Fukuzono-Voight model, a new generalized criterion has been proposed. The new theory overcomes the site-specific applicability and evaluates landslide Time of Failure for a wide range of landslide behaviors and characteristics, allowing to compare the behaviours of landslide of very different nature, materials, mechanisms, displacement rates, etc. The study permitted the creation of an abacus which reports the expected landslide behavior approaching failure, starting from the definition of the governing parameter. Then, the thesis investigates the real time applicability, with the implementation of the method within a self-learning algorithm and the automatic definition of the point of activation. For this purpose, a multi-criteria activation procedure is proposed. The literature concentrates on cumulated slope surface displacements, while the new method analyses both local and cumulative underground movements along the whole vertical direction.

Finally, the tool has been applied to numerous case histories. Four of them are reported in this thesis.

The first one regards the application to a geotechnical structure and the comparison between MUMS, GPS and traditional inclinometer data. The new instrument permitted to recognise the excavation stages and the deformations related to seasonal oscillations and changes of boundary conditions. The evaluation of GPS results highlights the thermal influence on MEMS sensors and the necessity to compensate them with a specific calibration procedure. The traditional inclinometer identifies deformations which are very similar in the stable zone and quite different in the excavation area. In this case MUMS displays larger movements, also related to seasonal oscillations and changes of boundary conditions, which the Manual Probe did not record at all. The result has permitted an evaluation and validation of design assumptions. Despite the encouraging outcomes, the application of more precise and sensible sensors could improve the measure and reduce the complexity of post processing. For this reasons, a 2D electrolytic cells coupled with a new version of MEMS has been developed, improving the sensibility, repeatability and general applicability of the Vertical Array Structure.

The second case study is aimed to study the landslide mechanism through the near real-time monitoring of displacements, pore pressures and rainfall, together with the development of a series of numerical models. In particular, after the definition of a 2D FDM elastoplastic model, it has been necessary to convert it to a Time-Dependent FDM model at the end of the first year of monitoring. Then, mechanical parameters needed a reduction due to progressive degradation observed during the second year. This permitted a preliminary forecasting analysis for the upcoming year that requires a verification through monitoring data. The results obtained are very useful in the assessment of potentially required mitigation measures, related to the landslide possible behaviour and the compatibility of the forecasted deformations on the structural work. The study also highlights the necessity to automatically recognize the variations in landslide dynamics and correct the input parameters of FDM numerical model, allowing a continuous update of the alert levels.

The third case study is about the first real-time application of the new IVM activation criterion and Fukuzono method. In particular, it is stressed the efficiency of the algorithm in the preliminary analysis and detection of potentially hazardous events. Software was able to automatically identify two landslide events and activate related alert procedures. The subsequent on-site inspection confirmed the previsions, evidencing some minor inaccuracies related to the exact evaluation of Time of Failure. The execution of a back analysis through Excel® software confirmed the results, further refining the collapse prevision. The variances between two methods are related to the automatic recognition of acceleration date. Further studies should investigate and improve this topic.

Finally, the fourth case history regards the applications of two MUMS systems inside a reinforced soil wall. The results show the importance of high frequency automated monitoring in the detection of trigger factors. In particular, the two instrumentations presented diverse displacements and pore pressure behaviours, despite the difference in position of only 3 meters. The significance of redundant Tilt Link HR 3D V results is evidenced in correspondence of an unexpected movement that occurred in a “stable” zone.

6.2. Future researches

Future researches should involve the range of applicability of the new tool, extending its use to other sectors like, for example, the monitoring of environmental quality, concentrating on physical entities (e.g. pollution, dusts and noise). Therefore, already designed tools, like the RockFall Safety Network, should be tested and applied on-site.

The Vertical Array could implement new kind of sensors, such as tensiometers or humidity sensors.

A possible innovation could regard the web platform, where new sensors could be represented, together with new dynamic graphs. The self-learning algorithm should automatically recognize increasing displacement rates and consequently reprogram the control unit sampling period through the web platform, also in case of atypical water levels or rainfall heights. At the end of the alert period, the sampling should be reprogrammed to previous standard settings.

Due to market reasons, it could be interesting to study a method to recover the Vertical Array and make it reusable.

The calibration procedure should be evolved in order to define the absolute position of sensors.

An interesting task could be the automatic integration of MUMS results inside commercial or scientific numerical models, in order to re-calibrate and validate them in real-time.

Further studies should involve the Time of Failure method, firstly improving the IVM activation criterion. Moreover, the collapse estimation could involve a time window assessment, instead of a specific date & time, simulating different possible behaviours of displacement rates starting from monitoring data. Other methodologies and models should be investigated and the analysis could recognize the landslide typology starting from displacement data and apply the corresponding model which best reproduces the site outcomes. Finally, a new criterion could be evaluated, putting together information about displacements, displacement rates, water level, rainfall height and consider them all together with a weighted approach.

Acknowledgements

"The science of today is the technology of tomorrow."

Teller E. – To Have or to Be?

Three years ago I started this work with strong motivations. These were linked to my love for science, my strong conviction in the work of ASE and the admiration I had for the team I would work with. During these three years I have experienced very pleasant moments, as well as some great and necessary difficulties. I have seen places, met professionals, participated in conferences and lived in full what I dreamed of doing.

For all of this, I am incredibly grateful to prof. Andrea Segalini, to his trust, his ability to motivate me constantly and his innovative ideas born in the middle of the night.

During the project I was lucky enough to meet the GEI elettronica team, colleagues and friends who made me feel at home and with whom I shared pleasant moments, made of dinners and business challenges. I thank them in particular for having taught me a new work and life philosophy, in which even in the most difficult moments, a laugh precedes every other word.

A heartfelt thanks to the colleagues of ASE S.r.l. for the hard work done together during these three years, made also of recreational activities and aperitifs. I can really say that we had fun. We have so many developments to do and we know that the best is yet to come.

A special thanks to Alessandro Valletta for the excellent work done together on the Time of Failure prediction. You've been a bit like my Gandalf.

I would also like to thank Prof. Giovanna Capparelli of the University of Calabria and Dott. Maurizio Martino of ANAS for the kind collaboration in the case studies.

This thesis is dedicated to my family, to the scientific vocation that has always distinguished us.

"Now I think that all of us are born with a hole in our hearts, and we go around looking for the person who can fill it" (King S., The Dark Tower: Wolves of the Calla). Dedicated to you, your tenacity, your smile, your eyes.

References

AirVision website, www.airvision.it [Last accessed 10 July 2018]

Allasia P., Lollino G., Godone D., Giordan D. (2018) *Deep displacements measured with a robotized inclinometer system*. 10th International Symposium on Field Measurement in Geomechanics. FMGM2018, 17-20 July 2018, Rio de Janeiro

Arbanas Z., Sassa K., Nagai O., Jagodnik V., Prodan M. V., Jovančević S. D., Peranić J., Ljutić K. (2014) *A Landslide Monitoring and Early Warning System Using Integration of GPS, TPS and Conventional Geotechnical Monitoring Methods.* Landslide Science for a Safer Geoenvironment. Vol. 2. doi https://doi.org/10.1007/978-3-319-05050-8_98

Artese G., Perrelli M., Artese S., Meduri S., Brogno N. (2015) *POIS, a Low Cost Tilt and Position Sensor: Design and First Tests*. Sensors 2015, 15, 10806-10824; doi: 10.3390/s150510806

Atzeni C., Barla M., Pieraccini M., Antolini F. (2015) *Early warning monitoring of natural and engineered slopes with Ground-Based Synthetic-Aperture Radar*. Rock Mechanics and Rock Engineering (2015) 48:235-246. doi: https://doi.org/10.1007/s00603-014-0554-4

Barnston A. (1992) *Correspondence among the Correlation, RMSE, and Heidke Forecast Verification Measures; Refinement of the Heidke Score*. Notes and Correspondence, Climate Analysis Centre, NMC/NWS/NOAA, Washington DC, December 1992, pp.699-709

Beninati L., Brunetti A., Caruso C., Mazzanti P. (2015) *Structural Health Characterization of an Old Riveted Iron Bridge By Remote Sensing Techniques*. Proceedings of the 7th International Conference on Structural Health Monitoring of Intelligent Infrastructure, Turin, Italy, 2015

Bennett V. G. (2010) *Development of a MEMS-Based In-Place-Inclinometer-Accelerometer Array for Monitoring and Evaluation of Geotechnical Systems*. Thesis for the degree of Doctor of Philosophy. Faculty of Rensselaer Polytechnic Institute, Troy, New York, May 2010

Bicocchi G., D'Ambrosio M., Rossi G., Rosi A., Tacconi-Stefanelli C., Segoni S., Nocentini M., Vannocci P., Tofani V., Casagli N., Catani F. (2016) *Geotechnical in situ measures to improve landslides forecasting models: A case study in Tuscany (Central Italy).* Landslides and Engineered Slopes. Experience, Theory and Practice. Aversa et. al (eds.)

Boyd J. M., Hinds D. V., Moy D., Rogers C. (1973) *Two simple devices for monitoring movements in rock slopes*. Quarterly Journal of Engineering Geology and Hydrogeology (1973), 6(3-4), pp. 295-302

Bozzano F., Cipriani I., Mazzanti P., Prestininzi A. (2014) *A field experiment for calibrating landslide time-of-failure prediction functions*. International Journal of Rock Mechanics & Mining Sciences 67 (2014), pp. 69-77

Brawner C. O., Stacey P. F. (1979) *Hogart Pit slope failure, Ontario, Canada*. In Rockslides and Avalanches, B; Elsevier: Amsterdam, The Netherlands, 1979: pp. 691-707

Brown I., Hittinger M., Goodman R. (1980) *Finite element study of the Nevis Bluff (New Zealand) rock slope failure*. Rock Mechanics, 12, pp. 231-245 (1980)

Campbell W. H. (1997) *Introduction to geomagnetic fields*. Cambridge University Press, Cambridge. ISBN: 571936

Cardellini S., Osimani P. (2008) *Living with landslide: the Ancona case history and early warning system*. First World Landslide Forum, 18-21 November 2008, United Nation University, Tokio, Japan, Session n.13, 2008

Carlà T., Farina P., Intrieri E., Botsialas K., Casagli N. (2017a) *In the monitoring and early-warning of brittle slope failures in hard rock masses: Examples from an open-pit mine*. Engineering Geology 228 (2017) pp. 71-81

Carlà T., Intrieri E., Di Traglia F., Nolesini T., Gigli G., Casagli N. (2017b) *Guidelines on the use of inverse velocity method as a tool for setting alarm thresholds and forecasting landslides and structure collapses*. Landslides (2017) 14, pp. 517-534

Carlà T., Macciotta R., Hendry M., Martin D., Edwards T., Evans T., Farina P., Intrieri E., Casagli N. (2018). *Displacement of a landslide retaining wall and application of an enhanced failure forecasting approach*. Landslides (2018) 15, pp-. 489-505. doi: https://doi.org/10.1007/s10346-017-0887-7

Carri A., Grignaffini C., Segalini A., Capparelli G., Versace P., Spolverino G. (2017) *Study of an Active Landslide on A16 Highway (Italy): Modeling, Monitoring and Triggering Alarm*. M. Mikoš et al. (eds.), Advancing Culture of Living with Landslides, doi https://doi.org/10.1007/978-3-319-53487-9_28

Ciarcia S., Vitale S. (2013) *Sedimentology, stratigraphy and tectonics of evolving wedge-top depozone: Ariano Basin, southern Apennines, Italy*

CNR website, www.cnr.it [Last accessed: 09 July 2018]

Colleselli F., Colosimo P. (1977) *Comportamento di argille plio-pleistoceniche in una falesia del litorale adriatico*. Rivista Italiana di Geotecnica. 5. pp. 5-21

Cornelius R., Voight B. (1995) *Graphical and PC-software analysis of volcano eruption precursors according to the Material Failure Forecast Method (FFM)*. Journal of Volcanology and Geothermal Research, 64 (1995), pp. 295-320

Crosta G.B., Agliardi F. (2002) *How to obtain alert velocity thresholds for large rockslides*. Physics and Chemistry of the Earth 27 (2002), pp. 1557-1565

Crosta G., Agliardi F., Rivolta C., Alberti S., Dei Cas L. (2017) *Long-term evolution and early warning strategies for complex rockslides by real-time monitoring*. Landslides, 2017, pp. 1-18

Crostella A., Vezzani L. (1964) *La geologia dell'Appennino Foggiano*. Bollettino Società Geologica Italiana. 83 p., pp. 121-141

Cruden D.M., Masoumzadeh S. (1987) *Accelerating creep of the slopes of a coal mine*. Rock Mechanics and Rock Engineering 20, pp. 123-13

CSG S.r.l. website, www.csgsrl.eu [Last accessed: 01 June 2018]

Curtaz M., Ferrero A. M., Roncella R., Segalini A., Umili G. (2013) *Terrestrial Photogrammetry and Numerical Modelling for the Stability Analysis of Rock Slopes in High Mountain Areas: Aiguilles Marbrées* *case*. Rock Mechanics and Rock Engineering, vol. 47, 2013, pp. 605-620, ISSN: 0723-2632, doi: https://doi.org/10.1007/s00603-013-0446-z

Dasenbrock D. D. (2010) *Automated Landslide Instrumentation Programs on US Route 2 in Crookston, MN*. Proceedings of the University of Minnesota 58th Annual Geotechnical Engineering Conference, 2010, pp. 165-185

Dazzaro L., Rapisardi L. (1982) *Le Bentoniti dell'Appennino Dauno tra Castelnuovo Monterotaro e Motta Montecorvino (FG)*. Geologia Applicata e Idrogeologia. Bari. 17 p., pp. 151-160

Dazzaro L., Rapisardi L. (1984) *Nuovi dati stratigrafici, tettonici e paleogeografici della parte settentrionale dell'Appennino Dauno*. Bollettino Società Geologica Italiana. 103 p., pp. 51-58

Dick G. J., Eberhardt E., Gabrejo-Liévano A. G., Stead D., Rose N. D. (2015) *Development of an early-warning time-of-failure analysis methodology for open-pit mine slopes utilizing ground-based slope stability radar monitoring data*. Canadian Geotechnical Journal 52, pp. 515-529 (2015)

Dunnicliff J. (1988) *Geotechnical Instrumentation for Monitoring Field Performance*. Wiley-Interscience, page 117, ISBN: 0-471-00546-0

Dusense LLC website, www.dusense.ae [Last accessed: 05 July 2018]

Earth System S.r.l. website, www.earthsystem.it [Last accessed: 04 July 2018]

Eledia research center website, www.eledia.science.unitn.it [Last accessed: 10 July 2018]

Engel T., Noverraz F., Oboni F. (1983) *Glissement de la Chenaula*. Ingènieurs et architectes suisses n°22, 27 octobre 1983 (in French)

Federico A., Popescu M., Elia G., Fidelibus C., Internò G., Murianni A. (2012) *Prediction of time to slope failure: a general framework*. In Environmental Earth Sciences (2012) 66, pp. 245-256

Fell R. (1994) *Landslide risk assessment and acceptable risk*. In: Canadian Geotechnical Journal, 31(2), pp. 261-272. doi: https://doi.org/10.1139/t94-031

Ferrero A. M., Migliazza M., Roncella R., Segalini A. (2011) *Rock cliffs hazard analysis based on remote geostructural surveys: The Campione del Garda case study (Lake Garda, Northern Italy)*. Geomorphology, vol. 125, 2011, pp. 457-471, ISSN: 0169-555X, doi: https:/doi.org/10.1016/j.geomorph.2010.10.009

Ferrero A. M., Migliazza R., Segalini A., Gullì D. (2013) *In situ stress measurements interpretations in large underground marble quarry by 3D modeling*. International Journal of Rock Mechanics and Mining Sciences, vol. 60, 2013, pp. 103-113, ISSN: 1365-1609, doi: https://doi.org/10.1016/j.ijrmms.2012.12.0089

FLAC® Version 8.0, Creep Material Models (2016)

FLAC® Version 8.0, User's Guide (2016)

FLAC® website, http://www.itascacg.com/software/flac [Last accessed: 11 June 2018]

FLIR Systems Inc. website, www.flir.it [Last accessed 10 July 2018]

Fowler M. (2013) *Inclinometers, the good, the bad and the future*. Australian Center for Geomechanics, December 2013 Newsletter, pp. 21-24

Fukuzono T. (1985) *A new method for predicting the failure time of a slope*. In Proceedings of the Fourth International Conference and Field Workshop on Landslides (Tokyo; 1985). Tokyo University Press. 1985, pp. 145–150

Fukuzono T. (1990) *Recent studies on time prediction of slope failure*. Landslide News 4: pp. 9-12

Geokon® Inc. website, www.geokon.com [Last accessed: 28 August 2018]

Geoprævent (2012) *Rockfall monitoring Preonzo: Detailed monitoring and analysis of rock movements by interferometric radar (GB-InSAR)*. Available online at: www.geopraevent.ch

Geoscience Australia website, www.ga.gov.au [Last accessed 10 July 2018]

Geosense® Ltd website, www.geosense.co.uk [Last accessed: 03 July 2018]

Gigli G., Fanti R., Canuti P., Casagli N. (2011) *Integration of advanced monitoring and numerical modelling techniques for the complete risk scenario analysis of rockslides: The case of Mt. Beni (Florence, Italy).* Engineering Geology 120 (2011), pp. 48-59

Glaisher J. W. L. (1871) *On a class of definite integrals*. London, Edinburgh and Dublin Philosophical Magazine and Journal of Science. 4. Taylor & Francis

Glastonbury J., Fell R. (2002) *Report on the analysis of the deformation behaviour of excavated rock slopes*. School of Civil and Environmental Engineering, University of New South Wales, Report n° R403

Hoaglin D. C., Mosteller F., Tukey J. W. (1983) *Understanding Robust and Exploratory Data Analysis*. John Wiley & Sons. pp. 404-414. ISBN: 0-471-09777-2

Hoek E., Carranza-Torres C., Corkum B. (2002) *Hoek-Brown Failure Criterion – 2002 Edition*. Proc. NARMS-TAC Conference, Toronto, 2002, 1, pp. 267-273

IDS GeoRadar S.r.l. website, www.idsgeoradar.com [Last accessed 10 July 2018]

Intrieri E., Gigli G., Mugnai F., Fanti R., Casagli N. (2012) *Design and implementation of a landslide early warning system*. Engineering Geology 147-148 (2012), pp. 124-136

Intrieri E., Gigli G. (2016) *Landslide forecasting and factors influencing predictability*. Natural Hazards and Earth System Sciences, 16, 2501-2510, 2016

Intrieri E., Bardi F., Fanti R., Gigli G., Fidolini F., Casagli N., Costanzo S., Raffo A., Di Massa G., Capparelli G., Versace P. (2017) *Big data managing in a landslide early warning system: experience from a ground-based interferometric radar application*. Natural Hazards Earth Syst. Sci., 17, pp. 1713-1723, 2017. https://doi.org/10.5194/nhess-17-1713-2017

Intrieri E., Raspini F., Fumagalli A., Lu P., Del Conte S., Farina P., Allievi J., Ferretti A., Casagli N. (2018) *The Maoxian Landslide as seen from space: detecting precursor of failure with Sentinel-1 data*. Landslide, January 2018, Vol.15, Issue 1, pp. 123-133

Iovine G., Petrucci O., Rizzo V., Tansi C. (2006) *The March 7th Cavallerizzo (Cerzeto) Landslide in Calabria – Southern Italy*. IAEG Congress, Nottingham, UK 2006 Paper number 785

Ippolito F., Ortolani F., Russo M. (1973) *Struttura marginale dell'Appennino Campano: reinterpretazione di dati di antiche ricerche di idrocarburi*. Memorie della società geologica italiana. v. 12, pp. 227-250

Ishizawa T., Sakai N., Morohoshi T., Fukuzono T. (2013) *Effectiveness of underground displacement measurement using inclinometer for prediction of slope failure*. Landslides – Journal of the Japan Landslide Society Vol.50, n°6 (2013), November, pp. 256-267 (in Japanese). doi: https://doi.org/10.3313/jls.50.256

ISO 18674-1:2015 (2015) *Geotechnical investigation and testing. Geotechnical monitoring by field instrumentation. General rules.* BS EN ISO 18674-1:2015, BSI, ISBN: 978-0-580-83379-3

ISPRA (Istituto Superiore per la Protezione e la Ricerca Ambientale) (2007) *Rapporto sulle frane in Italia*. APAT, Rapporti, 78/2007, ISBN: 978-88-448-0310-0

ISPRA (Istituto Superiore per la Protezione e la Ricerca Ambientale). (2018) *Dissesto idrogeologico in Italia: pericolosità e indicatori di rischio*. ISPRA, Rapporti, 287/2018, ISBN: 978-88-448-0901-0

Jacobacci A., Martelli G. (1967) *Note illustrative della Carta Geologica d'Italia. Foglio 174, Ariano Irpino.* Roma, La Litograf, 1967

Kayesa G. (2006) *Prediction of slope failure at Letlhakane Mine with the Geomos Slope Monitoring System.* Proceedings of the International Symposium on Stability of Rock Slopes in Open Pit Mining and Civil Engineering, Cape Town, South Africa, 3-6 April 2006. South African Institute of Mining and Metallurgy, Johannesburg, pp. 605-622

Keqiang H., Sijing W. (2006) *Double parameter threshold and its formation mechanism of the colluvial landslide: Xintan landslide, China*. Environmental Geology 2006, 49, pp. 696-707

Kilburn C.R.J., Petley D.N. (2003) *Forecasting giant, catastrophic slope collapse: lessons from Vajont, Northern Italy*. Geomorphology 54 (2003), pp. 21-32

Kim T. H., Cruden D. M., Martin C. D., Froese C. R., Morgan J. (2010) *Landslide movements and their characteristic, Town of Peace River, Alberta*. Conference Paper, form 63th Canadian Geotechnical Conference and 6th Canadian Permafrost Conference, at Calgary, Alberta

Krkač M., Arbanas S. M., Arbanas Ž., Bernat S., Špehar K., Watanabe N., Nagai O., Sassa K., Marui H., Furuya G., Wang C., Rubinić J., Matsunami K. (2014) *Review of Monitoring Parameters of the Kostanjek Landslide (Zagreb, Croatia).* Landslide Science for a Safer Geoenvironment. pp. 637-643

Lasdon L. S., Fox R. L., Ratner M. W. (1974) *Nonlinear optimization using the generalized reduced gradient method*. RAIRO-Operations Research – Recherche Opérationelle Vol.8 Issue 3, pp. 73-103

Lee Y., Jang H., Kim D., Kim C. (2012) *Development of a mirror mounted fiber optic inclinometer*. Sensors and Actuators A: Physical. Vol. 184, September 2012, pp. 46-52

Leica Geosystems AG website, www.leica.com [Last accessed 10 July 2018]

Li X., Jiming K., Zhenyu W. (2012) *Landslide displacement prediction based on combining method with optimal weight*. Natural Hazards (2012) 61, pp. 635-646

Lin S. S., Lo C. M., Lin Y. C. (2017) *Investigating the deformation and failure characteristics of argillite consequent slope using discrete element method and Burgers model*. Environmental Earth Science. doi https://doi.org/10.1007/s12665-017-6401-7

Lollino G. (1992) *Automated inclinometric system*. Proceedings of the 6th international symposium on landslides, Christchurch, New Zealand, 10-14 Feb. 1992. Bell David H (ed). A.A. Balkema, Rotterdam, pp. 1147-1150

Lollino G., Arattano M., Cuccureddu M. (2002) *The use of the automatic inclinometric system for landslide early warning: the case of Cabella Ligure (North-Western Italy)*. Physics and Chemistry of the Earth, 27, 2002, pp. 1545-1550

Lollino G., Arattano M., Allasia P., Giordan D. (2006) *Time response of a landslide to meteorological events*. Natural Hazards Earth Syst. Science, pp. 179-184

Lollino G., Allasia P., Filippa F., Riba A. (2008) *Apparecchiatura automatizzata di misurazione in perforazioni sotterranee di tipo perfezionato, in particolare per misurazioni inclinometriche*. 2008, Italian Patent filed UIBM 0001391881 - 2012

Lunardi P. (1988) *ADECO-RS Analisi delle deformazioni controllate nelle rocce e nei suoli*. Seminar on "Design and construction of Tunnels", ISMES, Bergamo, 1988

Mayne P. W., Barry R. C., DeJong J. (2011) *Manual on Subsurface Investigations*. National Highway Institute, Publication No. FHWA NHI-01-031, Federal Highway Administration, Washington DC, 2011

Manconi A., Giordan D. (2015) *Landslide early warning based on failure forecast models: the example of the Mt. de la Saxe rockslide, northern Italy*. Natural Hazards and Earth System Sciences, 15, pp. 1639-1644, 2015. doi: https://doi.org/10.5194/nhess-15-1639-2015

Manconi A., Giordan D. (2016) *Landslide failure forecast in near-real time*. Geomatics, Natural Hazards and Risk, 2016, Vol.7, n°2, pp. 639-648. doi: https://doi.org/10.1080/19475705.2014.942388

Margottini C., Spizzichino D., Crosta G. B., Frattini P., Mazzanti P., Scarascia Mugnozza G., Beninati L. (2015) *Rock fall instabilities and safety of visitors in the historic rock cut monastery of Vardzia (Georgia)*. Proceedings of the Volcanic Rocks and Soils Workshop, Isle of Ischia, Italy, 24-25 September 2015

Martino S., Mazzanti P. (2014) *Integrating geomechanical surveys and remote sensing for sea cliff slope stability analysis: the Mt. Pucci case study (Italy)*. Natural Hazards and Earth System Sciences, Vol. 14, 2014, pp. 831–848, doi: https://doi.org/10.5194/nhess-14-831-2014

Mazzanti P., Bozzano F., Brunetti A., Esposito C., Martino S., Prestininzi A., Rocca A., Scarascia Mugnozza G. (2015) *Terrestrial SAR Interferometry Monitoring of Natural Slopes and Man-Made Structures*. Engineering Geology for Society and Territory, Vol. 5, Springer International Publishing, Switzerland, 2015, pp. 189-194

Measurand Inc. website, www.measurand.com [Last accessed: 11 July 2018]

Minardo A., Picarelli L., Avolio B., Coscetta A., Papa R., Zeni G., Di Maio C., Vassallo R., Zeni L. (2014) *Fiber optic based inclinometer for remote monitoring of landslides: On site comparison with traditional inclinometers*. 2014 IEEE Geoscience and Remote Sensing Symposium, 13-18 July 2014, Quebec City, Canada

Moretto S., Bozzano F., Esposito C., Mazzanti P., Rocca A. (2017) *Assessment of landslide pre-failure monitoring and forecasting using satellite SAR interferometry*. Geosciences 2017, 7, 36

Mufundirwa A., Fujii Y., Kodama J. (2010) *A new practical method for prediction of geomechanical failure-time.* International Journal of Rock Mechanics & Mining Sciences 47 (2010), pp. 1079–1090

Nilsson L. E., Zetterlund E., Krüger B. (2007) *Fiber optic inclinometer*. Poster, Optik i Sverige, Skellefteå, Sweden, November 2007

NOAA website, www.ngdc.noaa.gov [Last accessed: 04 June 2018]

Peck R. B. (1969) *Advantage and limitations of the observational method in applied soil mechanics*. Géotechnique. 19 (2), pp. 171-187

Peck R. B. (1988) Foreward of *Geotechnical Instrumentation for Monitoring field performance*. John Dunnicliff, with the assistance of Gordon E. Green. ISBN: 0-471-00546-0

Petley D. N. (2004) *The evolution of slope failures: mechanisms of rupture propagation*. Natural Hazards and Earth System Science, Copernicus Publications on behalf of the European Geosciences Union, 2004, 4 (1), pp. 147-152

Raspini F., Bianchini S., Ciampalini A., Del Soldato M., Solari L., Novali F., Del Conte S., Rucci A., Ferretti A., Casagli N. (2018) *Continuous, semi-automatic monitoring of ground deformation using Sentinel-1 satellites*. Scientific Reports (2018) 8:7253, Nature. doi: https://doi.org/10.1038/s41598-018-25369-w

Rose N. D., Hungr O. (2006) *Forecasting potential rock slope failure in open pit mines – contingency planning an remediation.* International journal of Rock Mechanics and Mining Science, February 17, 2006

Rose N. D., Hungr O. (2007) *Forecasting potential rock slope failure in open pit mines using the inverse-velocity method*. International Journal of Rock Mechanics and Mining Science 2007; 44, pp. 308–32

Rocscience website, www.rocscience.com [Last accessed: 11 June 2018]

Roncella R., Forlani G., Fornari M., Diotri F. (2014) *Landslide monitoring by fixed-base terrestrial stereo-photogrammetry*. ISPRS Annals of the Photogrammetry, Remote Sensing and Spatial Information Sciences, Vol. 2, 2014, pp. 297-304 DOI:10.5194/isprsannals-II-5-297-2014, ISSN:2194-9050

Roncella R., Forlani G. (2015) *A fixed terrestrial photogrammetric system for landslide monitoring*. Modern Technologies for Landslide Monitoring and Prediction, Springer Berlin Heidelberg, 2015, pp 43-67

Royán M. J., Abellán A., Vilaplana J. M. (2015) *Progressive failure leading to the 3 December 2013 rockfall at Puigcercós scarp (Catalonia, Spain)*. Landslides (2015) 12:585-595

rst Ltd website, www.rstinstruments.com [Last accessed: 05 July 2018]

Sättele M., Kautblatter M., Bründl M., Straub D. (2016) *Forecasting rock slope failure: how reliable and effective are warning systems?* Landslides (2016) 13:737. doi: https://doi.org/10.1007/s10346-015-0605-2

Saito M. (1969) *Forecasting time of slope failure by tertiary creep*. In Proceedings of the Seventh International Conference on Soil Mechanics Foundation Engineering, 1969; 2, pp. 677–683

Saito M. (1979) *Evidential study on forecasting occurrence of slope failure*. Trans. of the Dept. of Geomech. - Armenian Academy of Sciences, Yerevan, URSS

Saito M., Uezawa H. (1961) *Failure of soil due to creep*. In Fifth International Conference on Soil Mechanics and Foundation Engineering, 1, pp. 315-318, Paris

Scaioni M., Feng T., Lu P., Qiao G., Tong X., Li R., Barazzetti L., Previtali M., Roncella R. (2015) *Close-range photogrammetric techniques for deformation measurement: Applications to landslides*. Modern Technologies for Landslide Monitoring and Prediction, Springer Berlin Heidelberg, 2015, pp. 13-41

Scandone P. (1967) *Studi di geologia lucana: la serie calcarea-silico-marnosa e i suoi rapporti con l'Appennino calcareo*. Bollettino Società Naturalisti Napoli. Napoli. 76 p., pp. 301-469

Schumm S. A., Chorley R. J. (1964) *The fall of Threatening Rock*. American Journal of Science, Vol. 262, November 1964, pp. 1041-1054

Segalini A. (2001) *Numerical monitoring of time dependant - slow moving – landslides in colluvium*. Flac and Numerical Modelling in Geomechanics. D. Billaux, C. Detournay, R. Hart, X. Rachez Eds. CRC Press. ISBN 9789026518591 pp. 171-178

Segalini A., Giani G. P., Ferrero A. M. (2009) *Geomechanical studies on slow slope movements in Parma Apennine*. Engineering Geology, 109 (1-2), pp. 31-44

Segalini A., Carini C., Cristalli L. (2011) *Monitoring Underground Landslide Displacement: A New MUMS Based Device*. Slope Stability 2011: International Symposium on Rock Slope Stability in Open Pit Mining and Civil Engineering, Vancouver, Canada (September 18-21, 2011)

Segalini A., Carini C. (2013) *Underground landslide displacement monitoring: A new MMES based device.* Landslide Science and Practice: Early Warning, Instrumentation and Monitoring 2. pp. 87-93

Segalini A., Carri A., Savi R. (2017) *Role of Geotechnical Monitoring: state of the art and new perspectives*. Geo-Expo 2017, Sarajevo, 26th and 27th October 2017

Segalini A., Carri A., Grignaffini C., Capparelli G. (2018a) *Definition of landslide risk scenarios using underground monitoring data and numerical models: conceptual approach, analysis and evolution of a case study in Southern Italy.* Submitted to Landslide Journal, Accepted for publication

Segalini A., Carri A., Savi R., Cavalca E., Alessio C., Kalamaras G. (2018b) *Tunnel restoration in unstable rock masses: numerical analysis and validation of monitoring data from innovative instrumentation.* Geomechanics and Geodynamics of Rock Masses.

Segalini A., Valletta A., Carri A. (2018c) *Landslides time of failure forecast and alert thresholds assessment: A generalized criterion.* Engineering Geology. Elsevier. doi: https://doi.org/10.1016/j.enggeo.2018.08.003

Segalini A., Valletta A., Carri A. (2018d) *Application of a generalized criterion: time of failure forecast and alert thresholds assessment for landslides.* 6° Convegno Nazionale AIGA, 27-29 June 2018, Courmayer (AO), Italy

Segalini A., Carri A., Valletta A., Martino M. (2019) *Innovative Monitoring Tools and Early Warning Systems for Risk Management: A Case Study*. Geosciences 2019, Vol. 9, Issue 2, 62. doi: https://doi.org/10.3390/geosciences9020062

Singh A., Mitchell J. K. (1968) *General stress-strain-time function for soils*. J. Soil Mech. Found. Engrg. Div. ASCE, 94(1), pp 21-46

SISGEO S.r.l. website, www.sisgeo.com [Last accessed: 16 October 2018]

Sornette D., Helmstetter A., Andersen J. V., Gluzman S., Grasso J. R., Pisarenko V. (2004) *Towards landslide predictions: two case studies*. Physica A 338 (2004), pp. 605-632

Spaggiari L. (2015) *Calibration and installation improvements of MUMS inclinometers*. Thesis for the master degree in Environmental Engineering. DICATeA, University of Parma, March 2015

STMicroelectronics website, www.st.com [Last accessed: 13 September 2018]

Strade & Autostrade website, www.stradeeautostrade.it [Last accessed: 18 September 2018]

Suwa H., Mizuno T., Ishii T. (2010) *Prediction of a landslide and analysis monitoring of slide motion with reference to the 004 Ohto slide in Nara, Japan*. Geomorphology 124 (2010), pp. 157-163

Taylor J. R. (1999) *An Introduction to Error Analysis: The Study of Uncertainties in Physical Measurements*. University Science Books, 1999, pp. 128-129, ISBN: 0-935702-75-X

Tavenas F., Leroueil S. (1981) *Creep and failure of slopes in clays*. Canadian Geotechnical Journal, 18 (1), pp. 106-120

TBT Scietech website, www.tbt-scietech.com [Last accessed: 16 October 2018]

Ter-Stepanian G. (1980) *Creep on natural slopes and cutting*. In Proceedings of the third International Symposium on Landslides, 2, pp. 95-108, New Delhi

Terzaghi K. (1950) *Mechanism of landslides*. In Application of Geology to Engineering Practice (Berkeley Volume); Geological Society of America: Washington, DC, USA, 1950; pp. 83–123

Urciuoli G., Picarelli L. (2008) *Interaction between landslides and man-made works*. Landslides and Engineered Slopes – Chen et al. (eds) 2008, Taylor & Francis Group, London

Varnes D. J. (1982) *Time-deformation relations in creep to failure of earth materials*. In: Proceedings of the Seventh Southeast Asian geotechnical conference, Hong Kong, pp 107–130

Versace P., Artese G., Autiero M., Avolio M. V., Bardi F., Borgia A., Cancelliere A., Capparelli G., Capuozzo M., Caruso A., Casagli N., Cavallaro L., Cianciosi O., Conforti M., Conte E., Costanzo A., Costanzo S., De Marinis M., Di Gregorio S., Di Massa G., De Luca D. L., De Santis D., Donato A., Fanti R., Fidolini F., Formetta G., Foti E., Intrieri E., La Sala G., Luci A., Maletta D., Mannara G., Moreno D., Morrone L., Mungari T., Muto F., Paoletti F., Peres D. J., Raffo A., Rago V., Rigon R., Spadafora F., Spataro W., Troncone A., Trunfio G. A., Vena M., Viggiani G. (2014) *An integrated system for landslide monitoring, Early Warning and risk mitigation along lifelines*. PON01_01503, Cosenza 25th-28th of November 2014

Voight B., Kennedy B. A. (1979) *Slope failure of 1967-1969, Chuquicamata mine, Chile*. In Developments of Geotechnical Engineering, Volume 14, part B, 1979, pp. 595-632

Voight B. (1988) *A method for prediction of volcanic eruptions*. Nature 1988; 332, pp. 125-130

Voight B. (1989) *A relation to describe rate-dependent material failure*. Science 1989; 243, pp. 200–203

Voight B. (1990) *The 1985 Nevado del Ruiz volcano catastrophe: anatomy and retrospection*. Journal of Volcanology and Geothermal Research, 44 (1990), pp. 349-386

Vyalov S. S. (1986) *Rheological fundamentals of soil mechanics*. Elsevier Amsterdam.

Wasowski J., Bovenga F. (2014) *Investigating landslides and unstable slopes with satellite Multi Temporal Interferometry: Current issues and future perspectives*. Engineering Geology 174 (2014), pp. 103-138. doi: https://doi.org/10.1016/j.enggeo.2014.03.003

Wasowski J., Bovenga F., Dijkstra T., Xingmin M., Nutricato R., Chiaradia M. T. (2014) *Interferometry provides insight on slope deformations and landslides activity in the mountains of Zhouqu, Gansu, China*. In Sassa K., Canuti P., Yin Y. (eds) Landslide Science for a Safer Geoenvironment. Springer, Cham. doi: https://doi.org/10.1007/978-3-319-05050-8_56

Yamaguchi U., Shimotani T. (1986) *A case study of slope failure in a limestone quarry*. International Journal of Rock Mechanics and Mining Sciences & Geomechanics Abstracts, Volume 23, Issue 1, February 1986, pp. 95-104. doi: https://doi.org/10.1016/0148-9062(86)91670-0

Yun X., Bachmann E. R., McGhee B. (2008) *A Simplified Quaternion-Based Algorithm for Orientation Estimation From Earth Gravity and Magnetic Field Measurements*. IEEE transactions on instrumentation and measurement, vol. 57, No. 3, March 2008